JPL Report D-31794

Ultra Stable Microwave Radiometers for Future Sea Surface Salinity Missions

Instrument Incubator Program
Final Report

William. J. Wilson, Alan B. Tanner
Jet Propulsion Laboratory, California Institute of Technology
Pasadena, California

Fernando A. Pellerano, Kevin A. Horgan
NASA Goddard Space Flight Center
Greenbelt, Maryland

April 2005

Jet Propulsion Laboratory
California Institute of Technology
Pasadena, California

ABSTRACT

The NASA Earth Science System Pathfinder (ESSP) mission Aquarius will measure global sea surface salinity with 100-km spatial resolution every 8 days with an average monthly salinity accuracy of 0.2 psu (parts per thousand). This requires an L-band low-noise radiometer with the long-term calibration stability of < 0.1 K over 8 days. This three-year research program on ultra stable radiometers has addressed the radiometer requirements and configuration necessary to achieve this objective for Aquarius and future ocean salinity missions. The system configuration and component performance have been evaluated with radiometer testbeds at both JPL and GSFC. The research has addressed several areas including component characterization as a function of temperature, a procedure for the measurement and correction for radiometer system non-linearity, noise diode calibration versus temperature, low noise amplifier performance over voltage, and temperature control requirements to achieve the required stability. A breadboard radiometer, utilizing microstrip-based technologies, has been built to demonstrate this long-term stability. This report also presents the results of the radiometer test program, a detailed radiometer noise model, and details of the operational switching sequence optimization that can be used to achieve the low noise and stability requirements. Many of the results of this research have been incorporated into the Aquarius radiometer design and will allow this instrument to achieve its goals.

CONTENTS

1. Introduction

The purpose of this NASA Instrument Incubator Project (IIP) research task was to develop sensitive stable microwave radiometers for precision measurements of sea surface salinity (SSS) for current and future space missions. To measure SSS to the required accuracy of 0.1 parts per thousand (0.1 practical salinity units) requires a radiometer with a very low noise performance and a calibration stability of 0.05 K for up to 8 days.

The design and observational techniques developed during this research program have demonstrated the radiometer performance required for spaceborne measurements of SSS. The results of this program have been incorporated into the design and operation of the Aquarius microwave radiometers. Aquarius was selected by NASA as an Earth System Science Pathfinder (ESSP) mission in 2002 and is currently under development with a launch planned in 2009. Aquarius will be the first NASA mission to provide global observation of SSS.

The research done under this IIP was a joint project between JPL and GSFC. This report will summarize the work performed at each institution and show how it has been applied to the Aquarius radiometers.

2. JPL Ultra Stable Radiometer Research

2.1 JPL Radiometer Testbed

At JPL, a testbed L-band radiometer was built to test out different designs necessary to achieve the low noise and high stability required for SSS measurements. A block diagram of this radiometer is shown in Fig. 2-1 and a photograph of the laboratory set-up is shown in Fig. 2-2. All the radiometer components were mounted on a temperature-controlled baseplate to provide the required temperature stability. (Typically, this baseplate was controlled to ± 0.1 °C, although in some tests we found performance improvements by letting it adjust to the stable laboratory temperature.) Two detector, amplifier, voltage-to-frequency converter circuits were built for the testbed and were used to verify that these circuits did not add noise to the measurements. A detailed description of the testbed is given in Section 1 of the 19 Feb 2003 memo, which is included in Appendix 1.

2.2 Calibration

The radiometer was calibrated using stable current-controlled noise diode sources. Two noise diode sources (near the input and after the Dicke switch) were used to cross-check calibration stability. Precision current supplies, which had a stability of ~6×10^{-5} per °C, were used to power the noise diodes. The calibration and Dicke switching sequences were easily changed to test different observing schemes to achieve the minimum noise and maximum stability. With the temperature controlled baseplate, it was possible to achieve calibration stabilities within 0.1 K over periods up to 8 days. These results are discussed in Section 4 of this report.

Ultra Stable Microwave Radiometers for Future Sea Surface Salinity Missions

Instrument Incubator Program
Final Report

Jet Propulsion Laboratory

April 2005

Prepared by:

William J. Wilson — 28 April 2005

William J. Wilson
Principal Investigator — Date

Approved by:

Robert T. Menzies — 4/28/05

Robert T. Menzies
Manager Microwave Systems Section - 385 — Date

5.10.05

Thomas S. Luchik
Manager, Instruments and Science Data Systems Division — Date

5/11/05

Thomas A. Cwik
Manager, Earth Science Instrument & Technology Office — Date

5/6/05

Kenneth C. Anderson
Manager, Instrument Incubator Program — Date

ACKNOWLEDGMENTS

This study was sponsored by the Instrument Incubator Program (IIP) of the NASA Earth-Sun System Technology Office (ESTO). The authors thank George Komar, Ken Anderson, and Tom Cwik of the ESTO Program Office for their support and guidance of the study. The authors also thank our colleagues Steve Dinardo, Jeff Piepmeier, and Terence Doiron for all their help and useful discussions on this subject.

The research described in this publication was carried out at the Jet Propulsion Laboratory, California Institute of Technology, under a contract with the National Aeronautics and Space Administration.

Reference herein to any specific commercial product, process, or service by trade name, trademark, manufacturer, or otherwise, does not constitute or imply its endorsement by the United States Government or the Jet Propulsion Laboratory, California Institute of Technology.

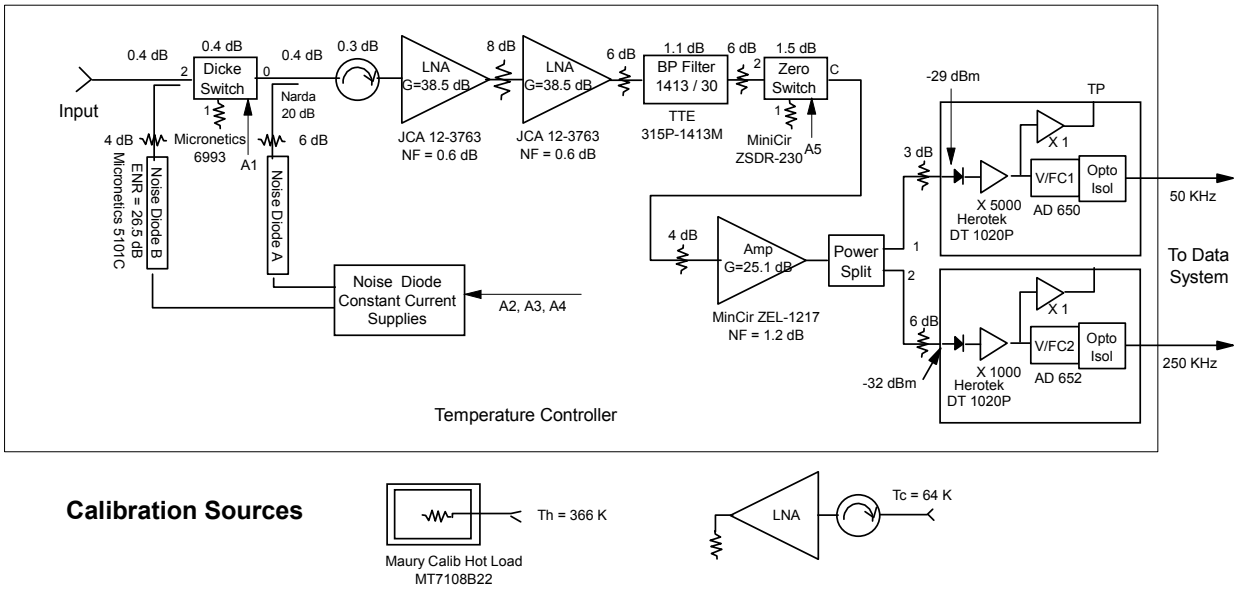

Figure 2-1. Block diagram of JPL ultra stable radiometer testbed. All components were mounted on a temperature controlled baseplate and multiple noise diodes were used to cross-check the calibration stability. The calibration sources, which included a hot load and a cold load, are also shown.

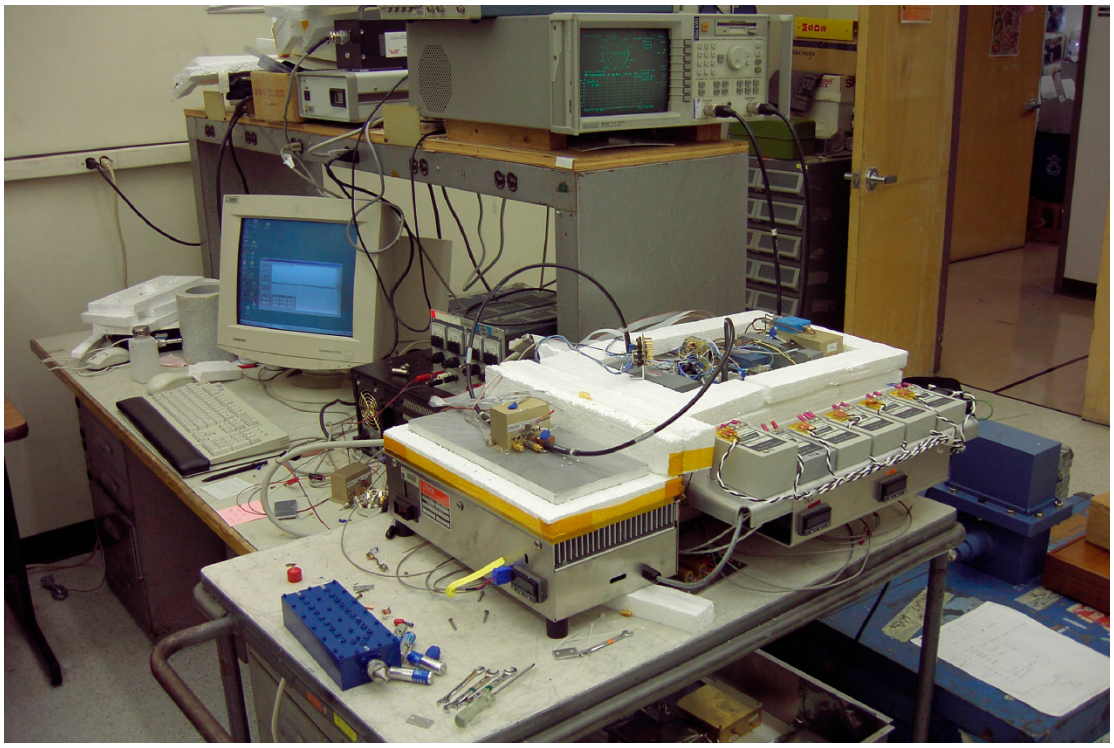

Figure 2-2. Photograph of the JPL ultra stable radiometer testbed.

2.3 Component Thermal Tests

The radiometer testbed was also used for a number of component thermal sensitivity tests, and these are described in Section 2 of the memo in Appendix 1 and in the 11 Jul 2003 memo in Appendix 2. In these tests the component temperature was varied from 0 to 60°C while the radiometer was held at a constant temperature. These tests were used to identify thermal stability problems in specific components; examples are shown in Fig. 2-3. For example, these tests identified the temperature stability problems in the isolator and the frequency diplexer.

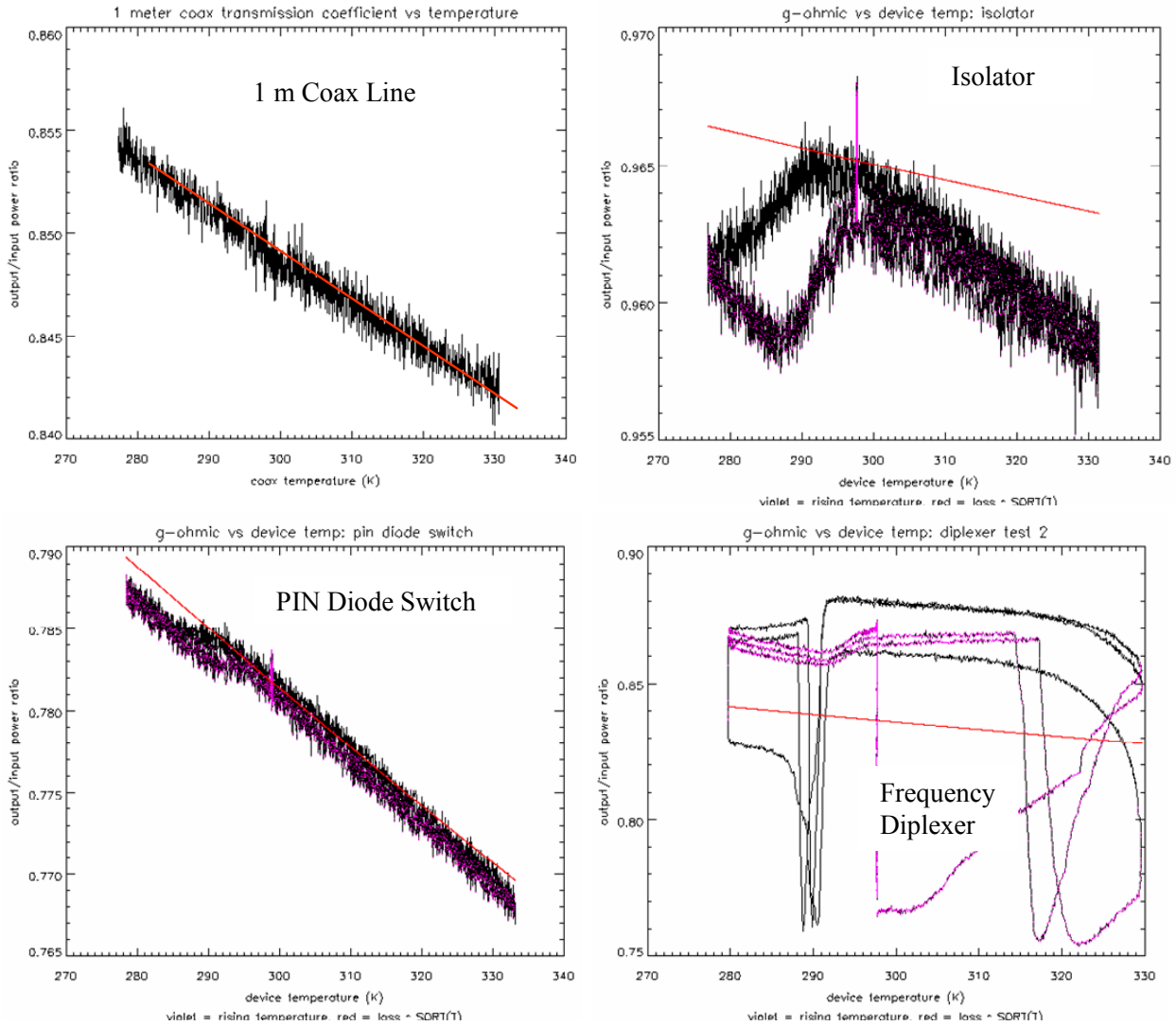

Figure 2-3. Component loss measurements versus temperature using the ultra stable radiometer testbed. The red lines represent a trend predicted by the copper conductivity alone.

2.4 Noise Diode Thermal Sensitivity

One interesting result from the temperature tests was the measurement of the noise diode output power versus its physical temperature. These results are described in Section 2 of the memo in Appendix 1. These thermal sensitivity tests reveal noise diode temperature coefficients of 400 to 1100 parts per million of output power per degree Celsius (ppm/°C) within a few

degrees of 23°C. The directional couplers exhibit sensitivities of about 400 to 600 ppm/°C in the coupled power versus temperature near 23°C. Combined, the net sensitivity is about 900 to 1700 ppm/°C, depending on the specific parts. Both of these devices, the noise diode and coupler, are found to be highly nonlinear outside of a narrow range of just a few degrees from 23°C as illustrated in Fig. 2-4. Inside this range the thermal sensitivities are repeatable to about 100 ppm/°C under a variety of test conditions with different length coaxial cables. This repeatability indicates that the thermal coefficients are not strongly affected by changes to the standing waves or port impedances when the coaxial cables are modified. It was also observed that changes to the noise diode bias current did not improve the temperature sensitivities of the noise diodes. The conclusion from these tests is that it is necessary to measure the noise diode and coupler temperature sensitivity, and then correct for these changes in the data analysis. Keeping the noise diode and coupler at a nearly constant temperature will minimize the errors of this correction.

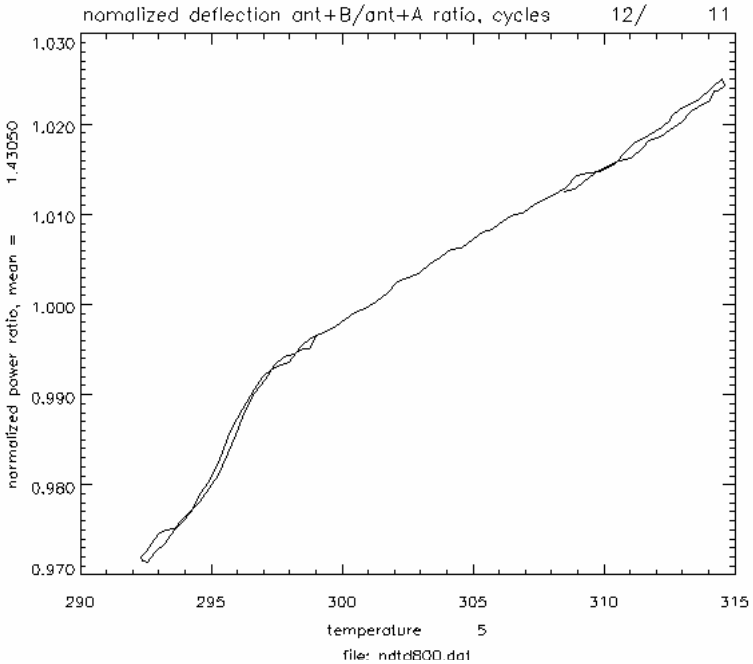

Figure 2-4. Noise diode B and coupler output versus physical temperature; bias current = 8.00 mA. The slope = 1840 ppm/°C @300 K.

2.5 Radiometer Thermal Requirements

Based on these tests, as described in Section 3 of the memo in Appendix 1, it is possible to summarize the thermal requirements for a stable radiometer as follows:

1. Time-variable temperature gradients are bad and will result in large errors.
2. Device temperature coefficients can be applied, but our experience indicates a limit of about 100 ppm/°C in such corrections, which imposes a 1 K requirement in the stability of the radiometer temperature: 100 ppm * 200 K (reference temperature − antenna temperature) = 0.02 K.
3. Thermal requirements can also be stated in terms of temporal and spatial scales.

For example, for a 0.05 K radiometric stability goal, these requirements could be stated as:

1. Initial set point temperature of 15 ± 15°C.
   - Any reasonable initial temperature appropriate for the spacecraft environment and radiometer components.
2. Soak temperature variations and fixed large scale gradients: 1°C RMS on >1-meter spatial/ >1-day temporal scales
   - We can correct for such changes, assuming the temperature gradients are constant.
3. Large scale time-variable gradients, measured in the difference of thermistors distributed throughout the major subassemblies of the radiometer: 0.1°C RMS on 10-cm spatial/ 1-hour temporal scales.
   - We can tolerate and possibly correct some variability in these gradients.
4. Small scale time-variable gradients: 0.01°C RMS on <3-cm spatial/ <10-minute temporal scales.
   - Such errors cannot be tracked with thermistors.

2.6 Non-Linearity Measurement

Another result from this research is a technique to measure and correct the non-linearities in the entire radiometer system. This is done using the internal noise diode on/off ratio versus the input noise level. The basic configuration of the radiometer linearity test is shown in Fig. 2-5. The linearization formula used was: $V_{linear} = V_c * \ln[V_{nonlinear} / V_c + 1]$, where $V_{nonlinear}$ is the detected voltage, and V_c is the correction factor. Note that a larger V_c corresponds to less correction since it would imply that the detector goes nonlinear at a higher voltage. A sample of the results of this radiometer correction is shown in Fig. 2-6 for noise diode A, showing that this technique provides a linearity within 0.2%. Additional detail of this procedure and the tests are described in the three memos of 4 Oct 2002, 24 Oct 2002, and 17 Aug 2004, which are included in Appendix 3.

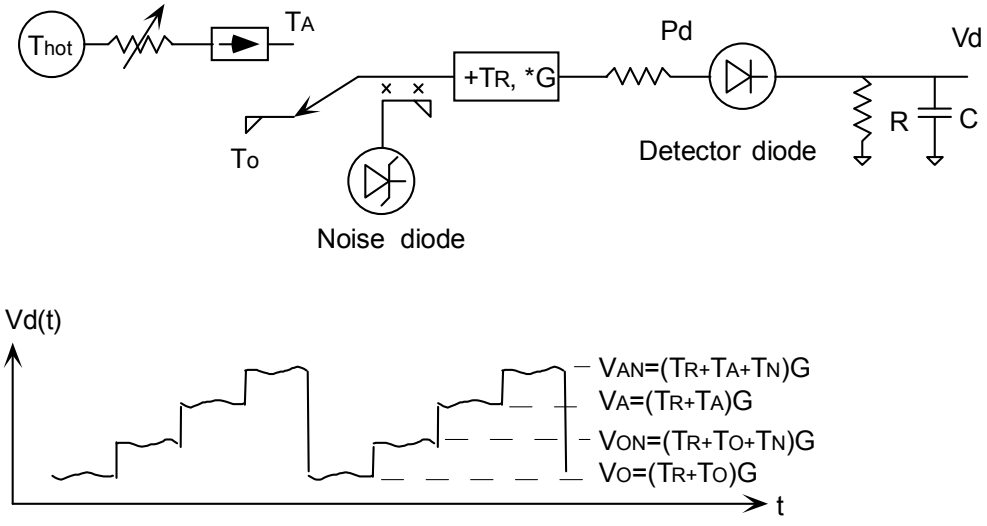

Figure 2-5. Layout of the radiometer linearity test and measurement sequence. T_{hot} is a variable noise source and the ratio of the noise diode on and off is measured as a function of this noise level.

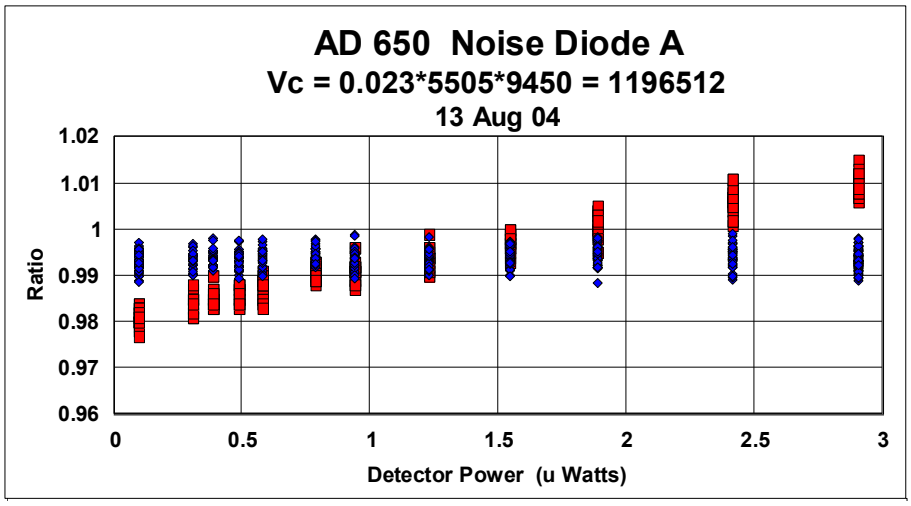

Figure 2-6. Plots of the noise diode A antenna/reference deflection ratios before (red) and after (blue) the nonlinearity correction was applied as a function of the input power for the AD 650 V/F converter.

2.7 Radiometer Observing Sequences

One of the main results of this research has been the verification of the running average technique used to reduce the radiometer NEDT while maintaining the required stability. This was proposed by Al Tanner in his 10 May 2002 memo, which is included in Appendix 4. This technique provides lower noise performance than either the two-position or three-position Dicke switching technique since it is a method that observes the input signal most of the time and only uses a small amount of the time to measure the gain, G, the radiometer noise, T_r, and the zero offset. Running averages of G and T_r are used to reduce the errors in their estimates and thus reduce the error in the calculation of the input signal. This technique takes advantage of the fact that the radiometer noise temperature is very stable over long time periods and that the gain is stable compared to the time of an individual measurement. The length of the running averages is set by the stability of G and T_r measurements, which can be determined for any switching sequence by measuring the power spectra of these quantities and noting at what frequency their 1/f noise becomes dominant. The 1/f point is a function of the switching sequence used and the temperature stability of the radiometer components. Section 4 of this report discusses a noise model for the microwave radiometer, and compares different observing schemes. A summary of the results of the long term stability tests (5–8 days) with the testbed radiometer is also presented in Section 4 and compared to the model analysis.

3. GSFC Ultra Stable Radiometer Research

3.1 GSFC Testbed

An L-band radiometer testbed was built at GSFC with the primary objective of assessing the long-term stability of the radiometers. The radiometer topology was similar to the JPL testbed, as shown in Fig. 2-1. That allowed us to compare results while at the same time trying complementary test scenarios. This testbed was built with a cryogenic load and operated in a thermal vacuum chamber, as shown in the block diagram and picture in Fig. 3-1.

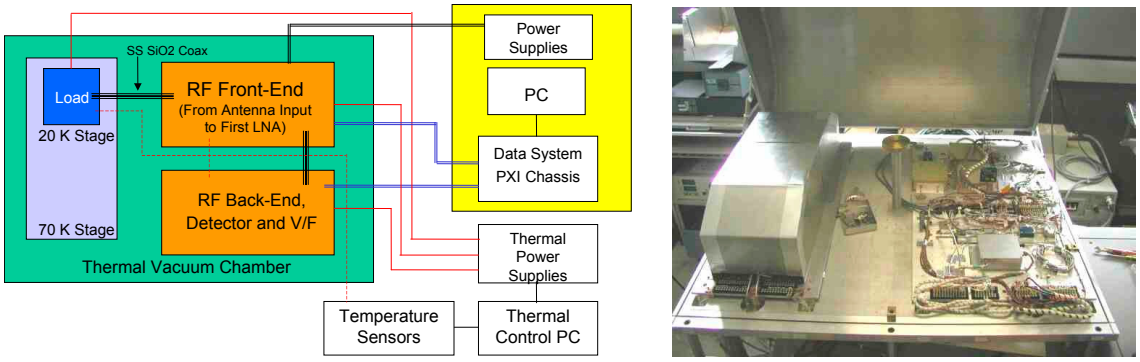

Figure 3-1. The testbed at GSFC provides three independently controlled temperature zones, including a cryogenic load capable of simulating ocean-like radiometric temperatures from 70K–120K.

A critical part of the system is the noise diode used for internal calibration. The noise diodes are operated under current control for optimum stability. To maintain good stability, the system employs current steering as opposed to turning the current on and off. The detected signal is digitized using a voltage-to-frequency converter and the output of the radiometer is a pulse train with a frequency F proportional to the input temperature. The noise diode control, as well as the overall switching sequence and output data acquisition, is done through a National Instruments PXI data system running on LabView programming.

The radiometer components are mounted in two plates that can be independently temperature controlled. The RF front-end plate includes the noise injection couplers, Dicke switch, and the first LNA. The RF back-end plate includes two more LNAs, bandpass filter, zero switch, detector, and video circuitry. The plates can be set to either a constant set point in the range of approximately room temperature ±10°C, or applied with a sinusoidal variation of user determined amplitude and period. We used this feature to simulate orbital temperature variations in the radiometer. The temperature control system is based on a proportional-integration-derivative (PID) loop. Underneath each plate is a set of four thermo-electric coolers (TEC). These devices have a varying heat flux as a function of voltage. The controller measured several thermistors in the plate. It would then average the temperature and apply the necessary voltage to maintain temperature control. Each of these plates demonstrated average temperature stability to better than $0.01°C_{rms}$, and $<0.1°C_{rms}$ in any component, over periods as long as two weeks.

3.2 Cryogenic Cold Load

The input calibration source to the radiometer was a matched load located on a 20-K cryogenic stage (see Fig. 3-2). This setup is capable of simulating radiometer input temperatures in the range 70–120 K, which is the expected range over the open ocean, over periods of months. The RF load was embedded in a copper block with two cartridge heaters on either side. The block in turn is mounted to the cryogenic stage via standoffs so it is only loosely thermally coupled. This allows for the block to be cold-biased, both through conduction and radiation, but can be heated quickly, providing good control authority. The block has embedded silicon diode temperature sensors and thermistors. The temperature controller is also PID-based and applies the necessary voltage to the heaters to maintain control. The controller can also simulate a fast transition (for example from ocean to land) by ramping the load temperature from 70 K to 300 K in about 60 seconds. Temperature sensors are also located along the 24-inch long coaxial cable. The coaxial cable is made of stainless steel with a silicon dioxide dielectric to provide good thermal isolation between the load and the radiometer. Fig. 3-3 shows a typical distribution of the sensors and the cable temperatures. The temperature control at the load is <0.002 K and ~0.1 K at the radiometer end of the cable.

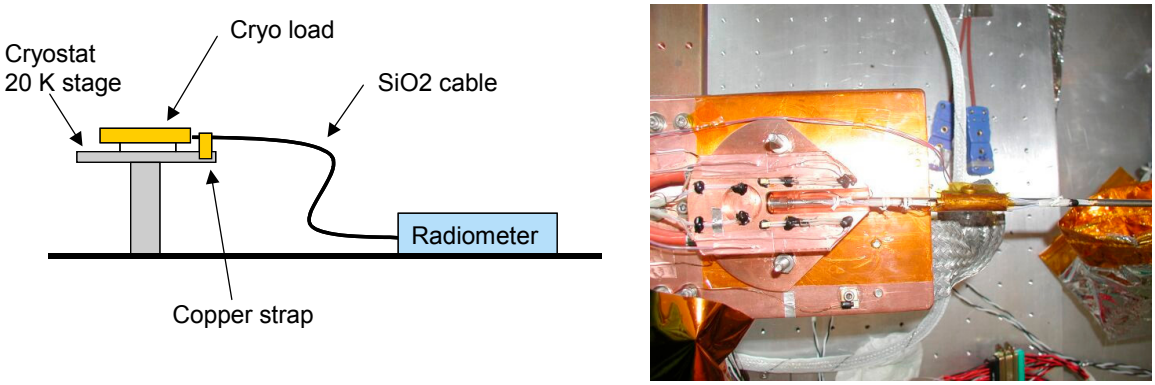

Figure 3-2. The cryogenic load is embedded in a copper block with heaters, which allows for very accurate control as well as rapid changes in temperature.

3.3 Cold Load Model

To assess the long-term radiometer calibration stability, the testbed must provide radiometric inputs more stable than the radiometer itself. For our case this implies knowledge of input radiometric temperature to <0.05 K. To achieve this, we apply both active control of the load and corrections based on a model for the input cable losses and emissions. This model breaks the cable into small sections and computes the cascaded system noise temperature based on the cable physical temperature distribution and includes the effects of connector losses and mismatches. This model is shown in Fig. 3-4. The model was tested against room temperature measurements of cables in the laboratory and vendor supplies data with very good correlation. No data, however, was available regarding the temperature sensitivity of the connector loss and impedance mismatch. A test was devised where a connector pair was locally cooled rapidly with freeze spray and the changes measured with a Vector Network Analyzer. The observed changes were within the VNA error of <0.02 dB / 30 K. A numerical sensitivity analysis to all

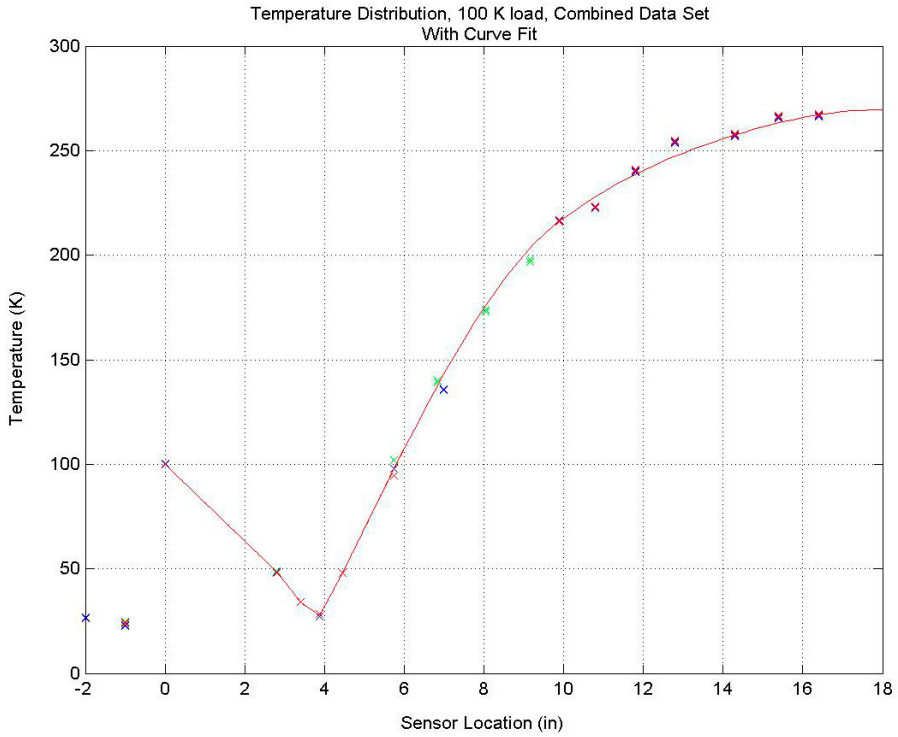

Figure 3-3. Typical temperature distribution along the coaxial cable. Due to the non-linear distribution, a model within a smaller spatial scale was developed.

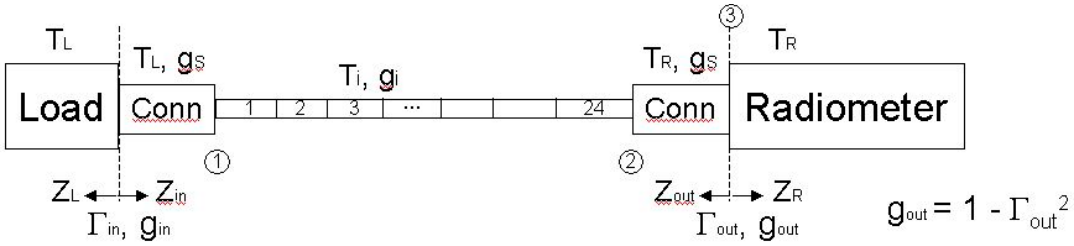

① $inputnoise = T_L\left[g_S g_{in} + (1 - g_S)\right]$

② $cablenoise = (inputnoise + T_{N1})\prod_{i=2}^{24} g_i + T_{N2}\prod_{i=3}^{24} g_i + \ldots$

③ $outputnoise = \left[cablenoise \times g_C + T_o(1 - g_C)\right] g_{out}$

Figure 3-4. The effective input brightness temperature model takes into account the temporal and spatial temperature variation of the coaxial cable as well as impedance mismatches at the connector interfaces.

parameters in the model was also performed. Given the low sensitivity of the connector loss and mismatch to temperature, the bias is largely driven by initial parameters uncertainty, while the coax temperature sensors drive the stability. These results suggests that the input temperature to the radiometer can be known with a bias of up to 1.85 K, and a stability or uncertainty due to random effects of ~0.01 K RSS, which is adequate for the radiometer stability testing. Fig. 3-5 shows the load and brightness temperatures of a 4-day test.

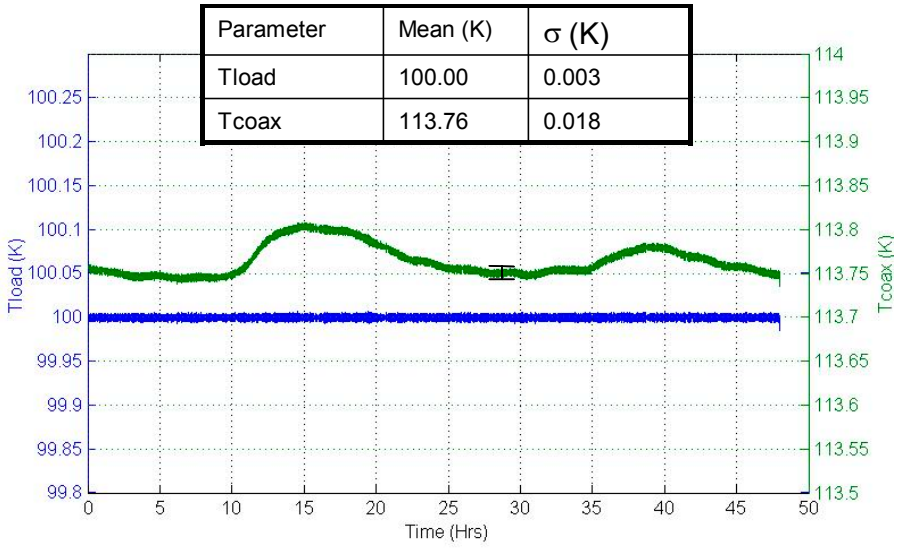

Figure 3-5. The variation of the brightness temperature was very small (0.018 K rms) and the uncertainty of any given point per the uncertainty analysis is 0.01 K rms.

3.4 Radiometer Linearity

A constant-deflection method was used to measure and characterize the radiometer linearity. Using this approach, nonlinearities are observed as deviations of the noise diode deflection when the antenna noise temperature changes. This method offers the advantage that it can be applied to the complete radiometer system, as opposed to just the final detector circuit, and because it is a ratio it is independent of radiometer calibration. In fact, this method can often be applied without any special accommodations or tests since the routine data from any noise-adding radiometer may be sufficient to characterize the linearity of the system.

Fig. 3-6 shows the laboratory configuration of the deflection test. The antenna in this case was replaced with a cold source and an injected noise source, which could be adjusted between ~30 K and 4700 K, well below and above the expected operational range. Also, the noise diode was injected after the Dicke switch so that the deflection can be measured in both the 'antenna' and 'reference' modes of the switch. With both of these measurements we can normalize the antenna deflections and examine the linearity with the deflection ratio:

$$D = \frac{V_{AN} - V_A}{V_{ON} - V_O}, \tag{3-1}$$

where the four voltages represent the response to the antenna (VA), antenna plus noise diode (VAN), ambient temperature reference (VO), and reference plus noise diode (VON). In a linear system with no impedance mismatches, D should always be unity. If the system is nonlinear, then D will change as the antenna noise temperature changes.

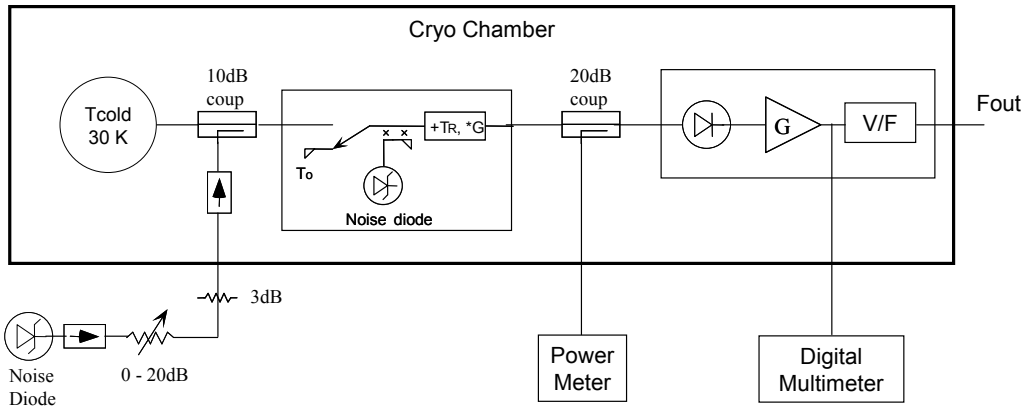

Figure 3-6. This setup for linearity tests using the deflection method allows the radiometer input to vary from 30 K – 4700 K without changing any radiometer circuitry.

As shown by the red '+' in Fig. 3-7, the system has a gain expansion behavior, as expected from the detectors, at low power levels up to approximately 2 mW, and gain compression at the higher levels. The response can be linearized very successfully with an error < 0.04% using a third order polynomial fit, as shown by the blue 'x'. These results also showed a bias in the deflection ratio due to the impedance mismatch of the Dicke switch between the antenna and load ports. This effect arises due to the coupler's imperfect isolation. Placing an isolator between the Dicke switch and the coupler eliminated this problem.

Tests were also performed to assess the linearity as a function of temperature. Two different scenarios were used. In the first one the radiometer front- and back-ends were held at equal temperatures in five temperature steps, 280 K, 289 K, 290 K, 291 K, and 300 K. The second scenario held the temperature of the front-end at a constant 290 K while the back-end was stepped through the above temperatures. In each of these tests the radiometer was allowed to settle and temperature-stabilize. The results show that for either of these cases the change in linearity as a function of temperature is very small. Fig. 3-8 shows the results of the first scenario, plotted in units of radiometer output frequency (i.e., counts). The system nonlinearity is very small and is virtually non-perceptible until large-enough signals, for example, near the noise diode, injected power. If uncorrected, however, they would lead to a significant error in the radiometer retrieval. The variation of the non-linearity as a function of physical temperature is even smaller. With a radiometer gain of approximately 0.1 K/Hz, the variation of the linearity is on the order of 0.04 K/°C in the expected ocean temperature range, and 0.15 K/°C in the noise diode injected temperature range. These effects become negligible given that the radiometer physical temperature is stable to <0.1°C RMS. Similar results were obtained for the second scenario of split temperatures. It is actually remarkable that we can detect these very small variations with this radiometer and the deflection technique.

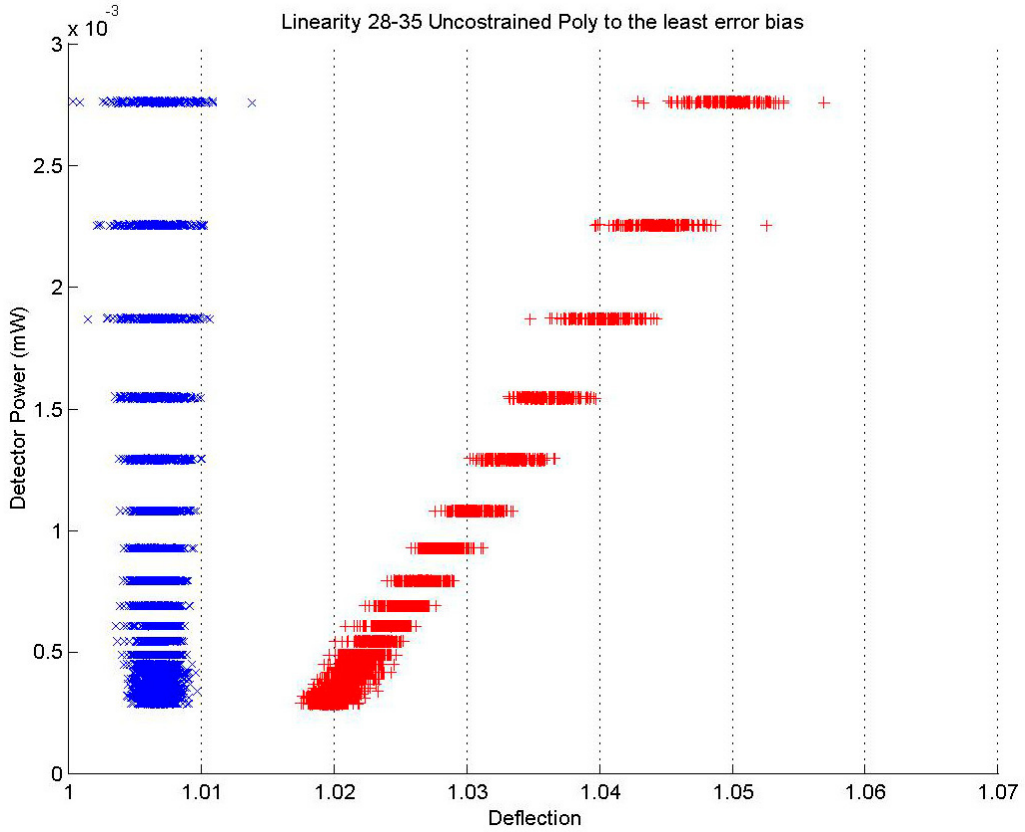

Figure 3-7. The radiometer can be linearized very successfully with a 3rd order polynomial.

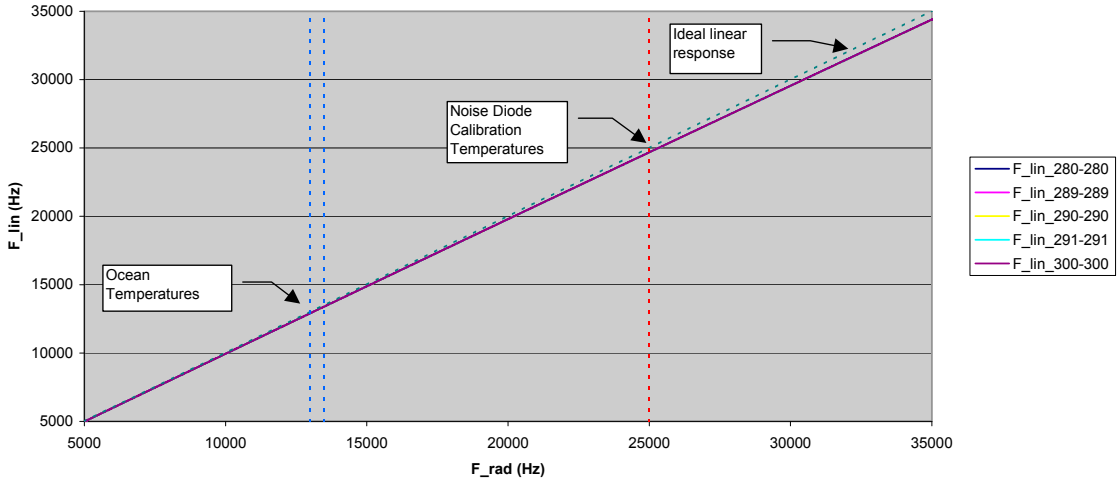

Figure 3-8. Changes in radiometer linearity as a function of physical temperature were very small and can easily be corrected.

3.5 Microstrip Radiometer Design

The results of device measurements previously made during this research clearly demonstrate that thermal control of the radiometer is the single-most dominant factor in obtaining long-term calibration stability. Corrections due to device temperature coefficients can only be applied successfully up to a point. Time-variable gradients, however, are significantly harder to correct. As a result we have determined that thermal control of the radiometer to within ±0.1 K is necessary to achieve the required calibration stability. A microstrip implementation of the radiometer was developed to minimize the size and improve thermal stability by allowing every device and transmission line to be in intimate contact with a temperature-controlled surface. This approach, while not the most size-efficient compared to, for example, a MMIC design, is very cost-efficient. Therefore, it seems to be a good compromise between size, thermal mass, and cost.

One key element of the design is the coupler used for noise injection. This coupler needs to exhibit very good stability since the radiometer calibration depends entirely on our ability to know the level of noise injected. A measurement at JPL of a commercial coupler showed that the stability of the coupling factor as a function of temperature was only about 600 ppm/°C (see Fig. 2-4), which is not sufficiently stable for our radiometer requirements. Investigating this issue with the vendor, it was concluded that the dielectric materials used were the primary source of the instability. Moreover, most commercial devices are designed for broadband performance, which means compromising on performance over our otherwise narrow frequency range—in particular, the coupler directivity, which our application needs in excess of 50 dB. It was decided to design a coupler with Duroid 6002, which is a very thermally stable dielectric. The design is based on a traditional coupled-lines approach. It capitalizes, however, on our narrow band requirements to obtain a measured directivity of ~55 dB in frequencies of interest. Several prototypes were built and characterized as a function of temperature. It successfully realized a coupling factor with variations of 60 ppm/°C, as shown in Fig. 3-9.

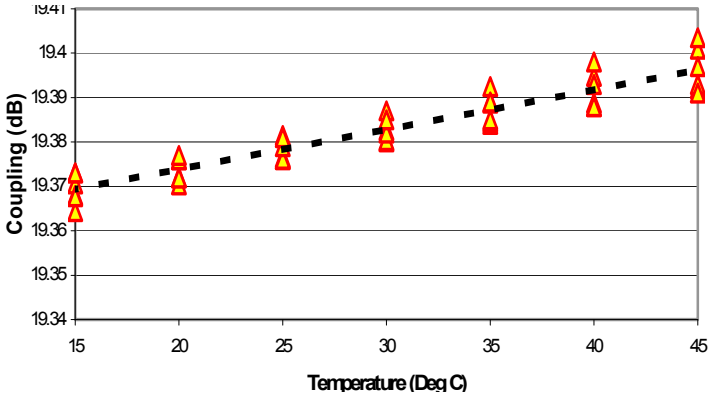

Figure 3-9. A 20-dB coupler was designed that exhibits only a 60 ppm/°C change in coupling over temperature.

The microstrip circuit housing itself is an important aspect of the design. It must carefully consider the broadband performance of devices to avoid interference and instabilities for the active devices, such as the low noise amplifiers. Circuit cavities behave like waveguides and must be designed with the appropriate cutoff frequency. In this design the cavities provide a

margin of >30 dB between gain stages. Additionally, filtered connectors are used at every DC or low frequency input/output (I/O) as well as internal connections. Fig. 3-10 shows pictures of prototypes for the microstrip front-end and back-end electronics. The microstrip radiometer has been functionally tested successfully and is undergoing long-term tests by the Aquarius development team.

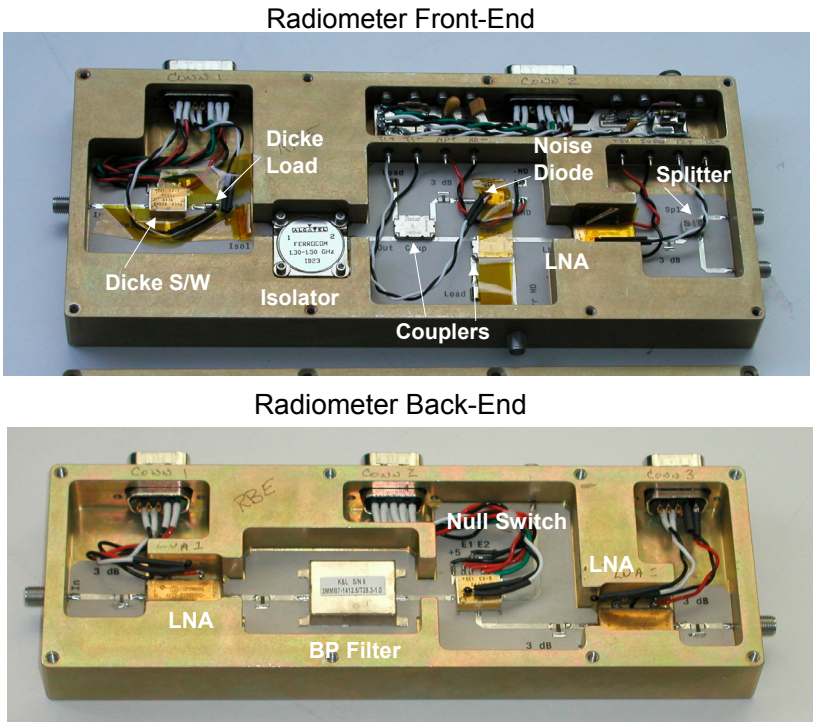

Figure 3-10. The microstrip radiometer achieves reduction in size and allows for good temperature control of devices and transmission lines.

3.6 Performance of Low Noise Amplifier over Voltage

Another area, in addition to temperature, that may affect the stability of the radiometers is the stability of the supply voltage. To study these effects several tests were performed to assess the performance of the low noise amplifier (LNA) as a function of voltage. These tests not only helped us understand these effects but also served to derive requirements for Aquarius. Two setups were performed, a stepped DC voltage test, and an AC noise test.

The LNAs used in our radiometer setup do not have an internal voltage regulator. This is desirable because, to achieve the precision temperature control, the power dissipation must be minimized. Including a regulator internal to the device increases the dissipation of the radiometer but also the localized heating. If a LNA without regulator is used instead, the necessary regulation can be shared by several components and located in an area where it can be more easily temperature-controlled. The non-regulated LNAs use a supply voltage of 5 V. This voltage is then stepped down to the necessary FET voltage by means of a resistor network.

In the stepped DC voltage test the supply voltage to the LNA was changed between 4.5 V and 5.5 V in 0.1-V steps. Fig. 3-11 shows the retrieved input antenna temperature (T_a) as a function of LNA voltage. It can be seen that the device is tuned at around 4.95 V, not 5 V. Fortunately,

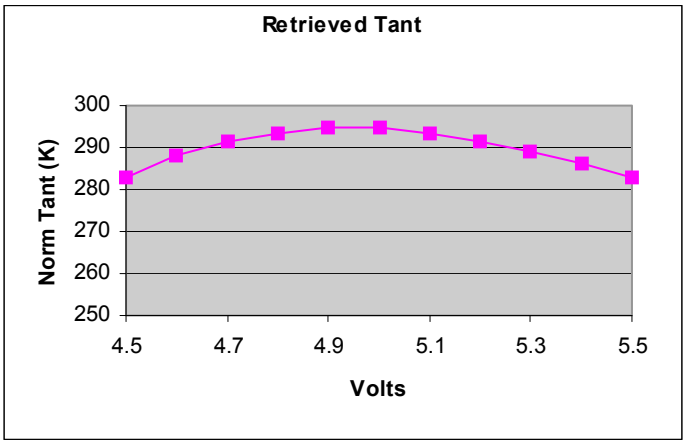

Figure 3-11. DC supply voltage to the LNA must be stable to 1 mV to maintain effects to <10% of NEDT.

the LNA gain is least sensitive to voltage changes in that range. To maintain the T_a variations to less than 10% of our desired NEDT (~0.003 K), then the peak-to-peak variation in voltage should be ≤ 1 mV. This test, however, did not consider the effect of frequency in the voltage variations.

The radiometer operates with a basic integration time of 10 msec. Those 10-msec samples are then averaged to form the desired observation time—in the case of Aquarius, 6 seconds.

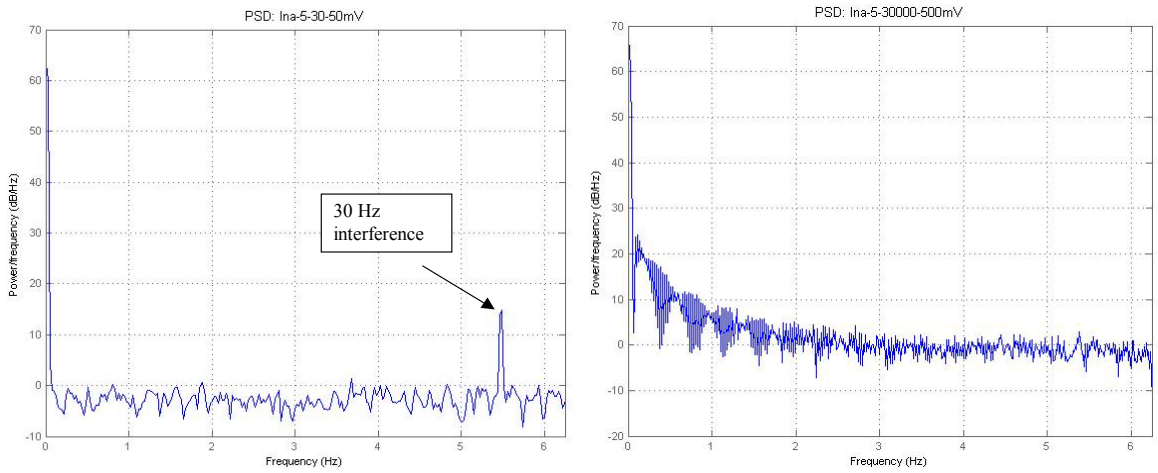

(a) **(b)**

Figure 3-12. Supply voltage low-frequency noise below the radiometer sampling rate of 100 Hz can be clearly seen in power spectral density plots of radiometer data (a), while not present at the higher frequencies (b).

Furthermore, the radiometer can average some values as long as 1000 seconds, for example, the radiometer noise temperature. In principle, high frequency fluctuations in the voltage supply will average out, while low frequency ones (in the scale of integration and calibration times) will affect the performance. To verify this, we performed a test where AC noise was injected into the DC supply voltage at various frequencies and voltage levels. The range of voltages and frequencies was limited to 30 Hz, 300 Hz, 3 kHz, and 30 kHz, at 50 mV, 100 mV, 250 mV, and 500 mV each. Radiometer data was obtained for each of those combinations and power spectral densities were computed for the retrieved antenna temperature. Fig. 3-12a shows an example PSD for 30 Hz-50 mV. It clearly shows the 30-Hz noise peaking above the radiometer's noise floor. Fig. 3-12b shows the PSD for 30 kHz-500 mV, where no supply noise is detected. In fact, the same is true for all the tests at frequencies higher than 30 Hz, confirming the hypothesis that high frequency supply noise will average out. Note, however, that these tests demonstrate that symmetrical sinusoidal noise and asymmetric high frequency noise from switching regulators should still be a concern and minimized as much as possible. If we then consider the frequency range of interest to be from 0.001 Hz (from 1000 seconds of calibration averaging) to 1000 Hz (radiometer 100 Hz sampling × 10) then the supply voltage has to meet a 1 μV/root Hz noise criteria.

3.7 Radiometer Performance Testing

To verify the objectives of long-term stability we ran the radiometer testbed virtually uninterrupted for a month. Two conditions were of primary interest. One, where the entire radiometer was under tight temperature control, allows us to investigate radiometer performance under the best possible conditions. In the second, the radiometer front-end was under tight temperature control while the back-end was varied sinusoidally ±1°C and ±2°C within a 90-minute period to simulate orbital variations.

Our data analysis demonstrates that we can improve the radiometer NEDT by employing long-time averages (up to 1000 seconds) of radiometer gain and temperature. A detailed discussion of the running average technique is in Section 4 and in Appendices 2 and 5. Fig. 3-13a shows one such case where the NEDT was approximately three times better than would be obtained with a three-position Dicke algorithm (no long-term averaging). Another conclusion is that we can largely remove the effects of back-end temperature variations. This is possible because the calibration signals (Dicke load and noise diode injection) are in the thermally stable front-end. Therefore, any radiometer changes due to temperature in the back-end are being tracked by the radiometer internal calibration. This can be seen in Fig. 3-13b where the back-end temperature oscillations have been removed from the retrieved data. This has significant implications because it simplifies the thermal control requirement of future instruments of this kind. More details of the stability results are discussed in Section 4 of this report and in the memo in Appendix 5.

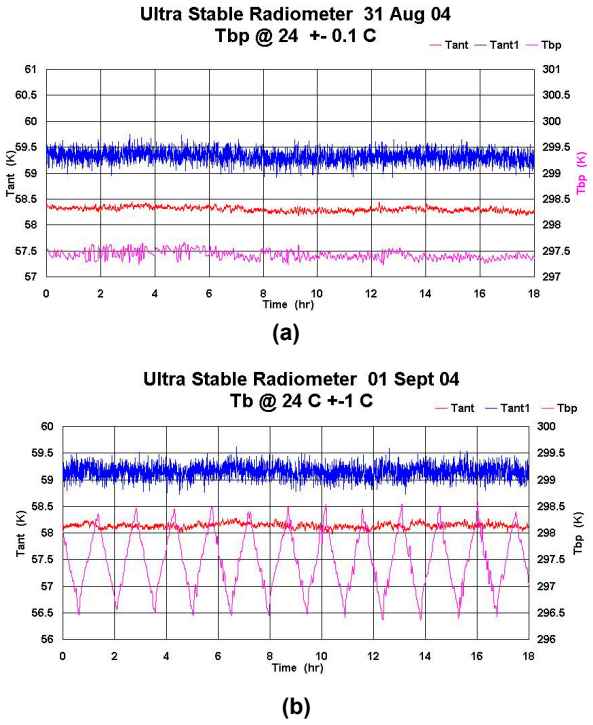

- Pink = Baseplate temperature
- Blue = 3-position Dicke
- Red = Smoothed average
  - Trad = 900 secs
  - Gain = 75 secs

Radiometer NEDT

	Red	Blue
±0.1C	0.044	0.123
±1.0C	0.044	0.130

Figure 3-13. The radiometer NEDT shows an almost three-times improvement using long averages of gain and receiver temperature over the three-position Dicke approach (a). Variations of the back-end temperature can also be removed as shown in (b).

4. Microwave Radiometer Model and Noise Analysis

This section describes a model for a microwave radiometer and derives the RMS noise from this radiometer model using various measurement switching schemes such as total power, two- and three-position Dicke switching and the running-average method. The purpose of this analysis is to show that the running average technique minimizes the RMS noise and maintains the required stability. This sequence is based on the measured properties of the radiometer; i.e., the power spectra of the gain and radiometer noise. The results of this analysis are compared to the measurements with our ultra stable laboratory radiometer. A more general analysis of the radiometer duty-cycle optimization with the running average technique is included in the memo in Appendix 4, which incorporates characterization using the radiometer's 1/f spectra.

4.1 Radiometer Model

A block diagram of a typical microwave radiometer is shown in Fig. 4-1. In this configuration, the radiometer is calibrated using the noise sources and the reference load connected to the Dicke switch. This configuration has the advantages of a stable and well-controlled calibration. (The analysis that follows is also applicable for calibration through the antenna feed, which has the advantage of calibrating some front-end components. However, this external calibration also has the disadvantage of additional complexity with external loads and the uncertainties in their calibration.)

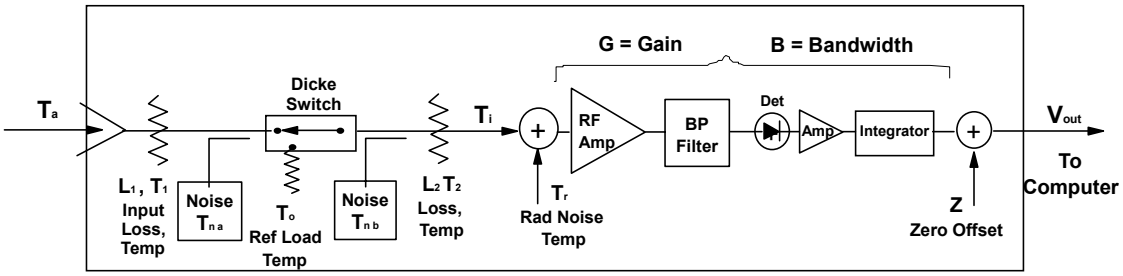

Figure 4-1. Microwave Radiometer Model

To simplify the following calculations, the input temperature to the first RF amplifier, T_i, is defined by the following expression:

$$T_i = \frac{T_a}{L_1 * L_2} + \frac{T_1}{L_2}\left[1 - \frac{1}{L_1}\right] + T_2\left[1 - \frac{1}{L_2}\right], \qquad (4\text{-}1)$$

where L_1, L_2 = input losses,
T_1, T_2 = physical temperatures of losses L_1 and L_2 (K),
T_a = antenna temperature (K).

When T_i is measured, T_a can be calculated using the measured quantities of loss and physical temperatures in (4-1). However, Ta will have some small additional noise because of the errors in the loss and their temperatures. The RMS error of the antenna temperature is given by

$$\Delta T_a = \sqrt{(L_1 * L_2 * \Delta T_i)^2 + (\Delta T_1 * (L_1 - 1))^2 + (\Delta T_2 * L_1 * (L_2 - 1))^2}\ , \qquad (4\text{-}2)$$

where ΔT_i, ΔT_1, and ΔT_2 are the errors in these temperatures.

In the model discussed below, it is assumed that the input losses (L_1, L_2), the physical temperatures, (T_1, T_2, T_o), the noise source temperatures, (T_{na}, T_{nb}) and the bandwidth B can be measured and their errors are small. Errors in the losses and the bandwidth can be assumed to be fixed, and thus will only add a constant bias. Based on our laboratory data and data from other space instruments, the noise source temperatures can be assumed to be constant over the monthly time scales and long-term drifts can be calibrated out using targets on the Earth. However, there is a question on how to accurately measure the temperatures of the losses L_1 and L_2, since in many cases these will be distributed losses. Also, when L_1 and L_2 include reactive losses (i.e., due to reflections), the source of emission is often poorly characterized by a single temperature sensor. Therefore, the most accurate way to determine these temperatures is to temperature-control the parts, so that the temperature gradients are small and the temperature sensors will provide accurate measurements.

Three of the unknown random quantities in this model are the radiometer gain, G, the radiometer noise temperature, T_r, and the zero offset, Z. To accurately calculate the input antenna temperature, T_a, they must be continuously measured. The procedure for these measurements is described below.

When the radiometer is switched to the input with the Dicke switch, the output voltage is given by the following equation:

$$\mathbf{V_i = (V_i' - Z) = G*(T_i + T_r)}, \tag{4-3}$$

where G = radiometer gain,
T_i = input temperature, see (4-1) (K),
T_r = radiometer noise temperature (K),
Z = zero offset voltage from detector and digitizer circuits (V).

To measure the zero offset, Z, the RF detector power is turned off and the offset voltage is measured. This offset voltage is then subtracted from the all the output voltages as noted in (4-3). In general, $Z << V_i$, and is nearly a constant value, especially with good temperature control. Thus Z can be measured for a small amount of the time, at intervals when the temperature is nearly constant. In this model, it is assumed that the subtraction of the offset will not add any noise to the overall measurements.

To measure G and T_r requires additional measurements. If the Dicke switch is switched to the reference load, the output voltage is

$$\mathbf{V_o = G*(T_o + T_r)}, \tag{4-4}$$

where T_o = reference load temperature measured through L_2 (K).

A second measurement is made by turning either of the noise sources on with the Dicke switch either in the input or load position:

$$\mathbf{V_{na} = G*(T_i + T_{na} + T_r)} \tag{4-5a}$$

or

$$\mathbf{V_{nb} = G*(T_o + T_{nb} + T_r)}, \tag{4-5b}$$

where T_{na} = noise temperature of noise source A, (K),
T_{nb} = noise temperature of noise source B, (K).

To calculate the RMS of these measurements, a small noise approximation will be used. In this technique, each voltage measured is set equal to its expected value plus a small noise term. The noise is a small fraction of the expected value and can be modeled as an additive Gaussian random variable with zero mean. Each voltage is modeled with the following expression:

$$\mathbf{V_j = <V_j>*(1 + \delta_j)}, \tag{4-6}$$

where j represents the measured voltage as noted in (4-2)–(4-4) above.

For a microwave radiometer, the expectation of the random variable is

$$\left\langle \delta_j^2 \right\rangle = \frac{1}{B * \tau_j}, \tag{4-7}$$

where B = radiometer bandwidth, (Hz),
τ_j = measurement integration time, (sec).

An analysis of four common radiometer switching sequences follows and derives the measurement RMS noise using the small-noise analysis technique.

4.2 Total Power

In an "ideal" total power radiometer, the radiometer is always switched to the input, and it is assumed that G and T_r are known. With a total power radiometer, T_i is calculated using the expression in (4-3):

$$\hat{T}_i = \frac{V_i}{G} - T_r . \tag{4-8}$$

If we assume that G and T_r are known, the value of T_i, using the small noise approximation, is

$$\hat{T}_i = T_i + \delta_i * (T_i + T_r) . \tag{4-9}$$

The RMS value of this measurement is then

$$\Delta\hat{T}_i = \frac{(T_i + T_r)}{\sqrt{B * \tau_i}} , \tag{4-10}$$

where τ_i = measurement time on the input (sec).

This is the standard expression for the RMS of a total power radiometer and gives the lowest possible measurement noise. The assumption that G and T_r are known perfectly is, of course, not correct, and techniques, described below, have been implemented to measure these quantities. However, it is useful to compare the RMS noise from the other techniques to this "ideal" value to determine the lowest noise technique.

4.3 Two-Position Dicke Switching

A traditional measurement technique is the two-position Dicke switching, where the radiometer is alternately switched between the input, V_i, and the reference load, V_o, using the Dicke switch. The input temperature is then calculated using the expression:

$$\hat{T}_i = T_o - \frac{(V_o - V_i)}{V_o} * (T_o + T_r) = T_i + \Delta T_i . \tag{4-11}$$

Using the small noise approximation, the estimate for T_i is then

$$\hat{T}_i = T_i + (T_i + T_r) * \delta_i - (T_i + T_r) * \delta_o + \frac{(T_i - T_o)}{(T_o + T_r)} * \Delta T_r . \tag{4-12}$$

Since the integration time on the reference load, τ_o, is equal to the integration time on the input, τ_i, and $< \delta_o >^2 = < \delta_i >^2 = 1 / (B*\tau_o)$, the RMS value of T_i is

$$\Delta T_i = \sqrt{\frac{2 * (T_i + T_r)^2}{B * \tau_o} + \frac{(T_i - T_o)^2}{(T_o + T_r)^2} * \Delta T_r^2} , \tag{4-13}$$

where ΔT_r = RMS error in the measurement of T_r (K).

Note that if there is no error in T_r, e.g., $\Delta T_r = 0$, and $\tau_o = \tau/2$, then ΔT_i is the standard expression for a Dicke-switched radiometer.

In a typical radiometer measurement sequence T_r is measured during part of the total integration time τ using the noise source A. In this case, a running average of the measurements of T_r can be used to reduce ΔT_r. Expressions for the error in T_r, $(\Delta T_r)_a$ using the running average technique are derived in Section 4.5 (4-18a). Using (4-13), it is possible to calculate the number of T_r measurements, N_r, which are required to not increase the ΔT_i noise. This is given by the condition:

$$\frac{(T_i - T_o)^2}{(T_o + T_r)^2} * (\Delta T_r)_a^2 \ll \frac{2 * (T_i + T_r)^2}{B * \tau_o} . \qquad (4\text{-}14)$$

Using the system parameters representative of our ultra stable radiometer testbed, as shown in Table 4-1, this condition is satisfied for values of $N_r > 10$ over an input temperature range from 150 K to 500 K.

Table 4-1. Laboratory Radiometer Characteristics

Parameter	Value
T_o	300 K
T_r	50 K
T_{na}	400 K
T_{nb}	400 K
B	25×10^6 Hz
τ	4 sec
τ_n	0.2 sec

To illustrate the behavior of ΔT_i, as a function of the input temperature and the number of averaged radiometer temperatures using noise source A, the value of ΔT_i is shown in Fig. 4-2. Also plotted is the ΔT_i for the ideal total power radiometer. These curves illustrate how the error in T_r influences the radiometer noise.

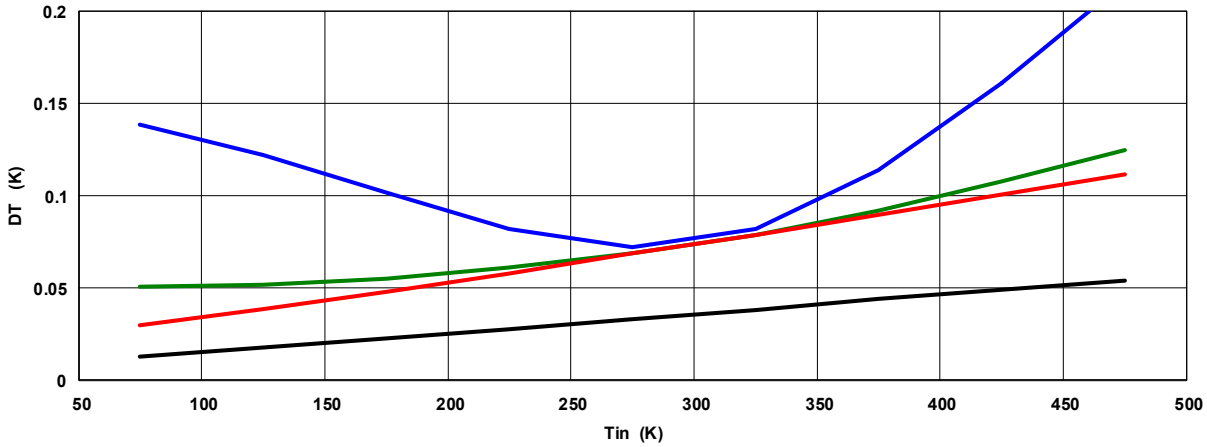

Figure 4-2. ΔT_i for two-position Dicke switching for different values of N_r, the number of T_r measurements averaged. The blue curve is for $N_r = 1$, the green curve is for $N_r = 10$, and the red curve is for $N_r = 100$. The black curve is the ΔT_i for the ideal total power radiometer.

4.4 Three-Position Dicke Switching

Another common radiometer switching technique is using a three-position switching sequence to effectively measure G, T_r, and Z in real time at the Dicke switching rate. In this sequence, the radiometer is switched between the input, the load, and a position with the noise source on. The input temperature is computed using the following expression if noise source A is used:

$$(\hat{T}_i)_a = T_o - \left[\frac{V_o - V_i}{V_{na} - V_i}\right] * T_{na} . \tag{4-15a}$$

If noise source B is used, the input temperature is

$$(\hat{T}_i)_b = T_o - \left[\frac{V_o - V_i}{V_{nb} - V_o}\right] * T_{nb} . \tag{4-15b}$$

Using the small noise approximation, the RMS noise for each of these measurements is

$$(\Delta T_i)_a = \frac{1}{\sqrt{B}}\left[\frac{(T_o + T_r)^2}{\tau_o} + \frac{(T_i + T_r)^2}{\tau_i}\left(1 - \frac{T_o - T_i}{T_{na}}\right)^2 + \frac{(T_o - T_i)^2}{\tau_n}\left(\frac{T_i + T_r + T_{na}}{T_{na}}\right)^2\right]^{\frac{1}{2}}, \tag{4-16a}$$

$$(\Delta T_i)_b = \frac{1}{\sqrt{B}}\left[\frac{(T_o + T_r)^2}{\tau_o}\left(1 + \frac{T_o - T_i}{T_{nb}}\right)^2 + \frac{(T_i + T_r)^2}{\tau_i} + \frac{(T_o - T_i)^2}{\tau_n}\left(\frac{T_o + T_r + T_{nb}}{T_{nb}}\right)^2\right]^{\frac{1}{2}} . \tag{4-16b}$$

In this case, $\tau_o = \tau_i = \tau_n = \tau/3$. These RMS noise values for the three-position Dicke switching technique are plotted in Fig. 4-3 as a function of the input temperature.

The advantages of the three-position Dicke switching sequence is that it cancels G, T_r, and the zero-offset variations at the Dicke switching rate to provide the best stability. The long-term stability is then only dependent on the stability of the noise source, the front-end losses, and the

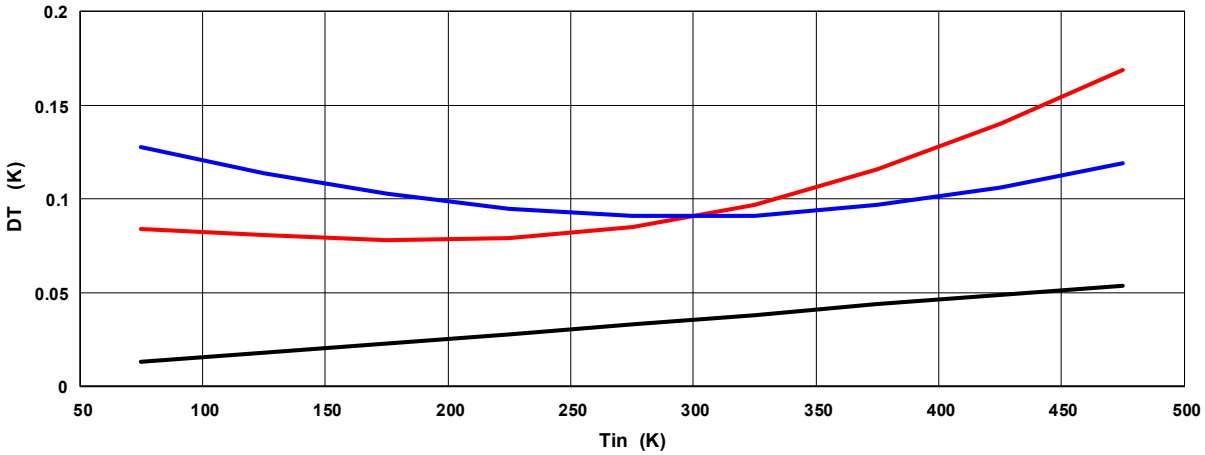

Figure 4-3. ΔT_i for three-position Dicke switching. The red curve is $(\Delta T_i)_a$ using noise source A, and the blue curve is $(\Delta T_i)_b$ using noise source B. The black curve is ΔT_i for the ideal total power radiometer.

accuracy of their measured temperatures. The disadvantage of this technique is that the RMS noise is ~3 times larger than with an ideal total power radiometer and ~1.5 times larger than the two-position Dicke-switching radiometer. However, in situations where it is not possible to achieve good temperature control, this may be the best technique.

As discussed in the next section, the Dicke switching rate must be faster than the 1/f point of the noise spectra of G or T_r to eliminate the additional noise from the slow changes in these quantities due to temperature variations.

4.5 Running Average Technique

A radiometer operational technique that provides lower noise performance than either the two- or three-position Dicke switching technique is a method that observes the input signal most of the time and only uses a small amount of the time to measure G, T_r, and the zero offset. Running averages of G and T_r are used to reduce the errors in these estimates. The length of the running averages is set by the stability of G and T_r measurements, which can be determined by measuring their power spectra and noting at what frequency their 1/f noise becomes dominant. This 1/f point is a function of the switching sequence used and the temperature stability of the radiometer components. In our laboratory radiometer system, which had 60% of the time spent on the input and was temperature controlled to ± 0.1°C, the 1/f point of G was >150 seconds. As noted earlier, T_r is a much more stable quantity and its 1/f point had values > 3,000 seconds. Using these long-running averages in the measurements of G and T_r then reduces the RMS noise in ΔT_i while still achieving the long-term stability. The radiometer switching sequence used in our laboratory radiometer tests was a 10-step sequence: V_0, V_{na}, V_{nb}, 6 × V_i, Z.

The expression in (4-3) is used to calculate T_i. However, the first step in the data analysis is to compute a running average of T_r, with noise sources A and B. With noise source A we compute:

$$(\hat{\mathbf{T}}_r)_a = \frac{\mathbf{V_o} * \mathbf{T_{na}}}{\mathbf{V_{na}} - \mathbf{V_i}} - \mathbf{T_o} = \mathbf{T_r} + (\Delta \mathbf{T_r})_a \,. \tag{4-17a}$$

Using noise source B we compute:

$$(\hat{\mathbf{T}}_r)_b = \frac{\mathbf{V_o} * \mathbf{T_{nb}}}{\mathbf{V_{nb}} - \mathbf{V_o}} - \mathbf{T_o} = \mathbf{T_r} + (\Delta \mathbf{T_r})_b \,. \tag{4-17b}$$

Using the small noise approximation, the RMS values of the running average of these measurements are:

$$(\Delta T_r)_a = \frac{1}{\sqrt{N_r * B}}\left[\frac{T_o + T_r}{T_{na}}\right]\sqrt{\frac{T_{na}^{\,2}}{\tau_o} + \frac{(T_i + T_r + T_{na})^2}{\tau_{na}} + \frac{(T_i + T_r)^2}{\tau_i}}\,, \tag{4-18a}$$

$$(\Delta T_r)_b = \frac{1}{\sqrt{N_r * B}}\left[\frac{T_o + T_r}{T_{nb}}\right](T_o + T_r + T_{nb})\sqrt{\frac{1}{\tau_o} + \frac{1}{\tau_{nb}}}\,, \tag{4-18b}$$

where N_r = number of T_r measurements averaged,
τ_o = time in switching cycle on the reference load (sec),
τ_n = time in switching cycle with the noise source on (sec),
τ_i = time in switching cycle on the input (sec).

If the measurements of $(T_r)_a$ and $(T_r)_b$ are averaged using a weighted average, the estimate of T_r is given by

$$\hat{T}_r = w * (T_r)_a + (1 - w) * (T_r)_b\,, \tag{4-19}$$

$$\text{where the weight } w = \frac{(\Delta T_r)_b^{\,2}}{(\Delta T_r)_a^{\,2} + (\Delta T_r)_b^{\,2}}\,. \tag{4-20}$$

The RMS value of this quantity is

$$(\Delta T_r)_{ab} = \sqrt{(\Delta T_r)_a^2 * w^2 + (\Delta T_r)_b^2 * (1 - w)^2}\,. \tag{4-21}$$

The next step in the data analysis is computing the running average of the radiometer gain. When the radiometer is switched to the reference load, the gain is given by

$$\hat{G}_o = \frac{V_o}{T_o + T_r} = G + \Delta G_o\,. \tag{4-22}$$

The RMS value of this running average gain measurement is

$$\Delta G_o = G\sqrt{\frac{1}{N_g} * \left[\frac{1}{B * \tau_o} + \left[\frac{(\Delta T_r)_{ab}}{T_o + T_r}\right]^2\right]}\,, \tag{4-23}$$

where N_g = number of gain measurements averaged together.

The gain can also be calculated during the time the noise source B is on, and this is given by

$$\hat{G}_b = \frac{V_{nb}}{T_o + T_r + T_{nb}} = G + \Delta G_b\,. \tag{4-24}$$

The RMS value of this gain measurement is

$$\Delta G_b = G\sqrt{\frac{1}{N_g} * \left[\frac{1}{B * \tau_{nb}} + \left[\frac{(\Delta T_r)_{ab}}{T_o + T_r + T_{nb}}\right]^2\right]}. \quad (4\text{-}25)$$

Averaging these two gain estimates,

$$\hat{G} \approx 0.5 * (\hat{G}_o + \hat{G}_b), \quad (4\text{-}26)$$

reduces the RMS noise in G by ~ √2,

$$\Delta G = \frac{\sqrt{\Delta G_o^2 + \Delta G_b^2}}{2}. \quad (4\text{-}27)$$

Using the running average estimates of these two parameters, the input temperature is given by the expression from (4-2):

$$\hat{T}_i = \frac{V_i}{\hat{G}} - \hat{T}_r = T_i + \Delta T_i. \quad (4\text{-}28)$$

Using the small noise approximation, the RMS of this measurement of T_i is

$$\Delta T_i = \sqrt{(T_i + T_r)^2\left[\frac{1}{B * \tau_i} + \left(\frac{\Delta G}{G}\right)^2\right] + \Delta T_r^2}. \quad (4\text{-}29)$$

A plot of ΔT_i versus the input temperature T_i is shown in Fig. 4-4 along with the total power result. This analysis shows that using the running averages of G and T_r to continuously calibrate the radiometer, the ΔT_i is only increased by a factor of ~1.3 compared to an "ideal" total power radiometer. This technique has a ΔT ~1.6 times lower than the standard two–position Dicke-switched radiometer and ~2 times lower than the three-position Dicke-switched radiometer. The two dots plotted represent the results for the radiometer testbed measurements discussed in the next section.

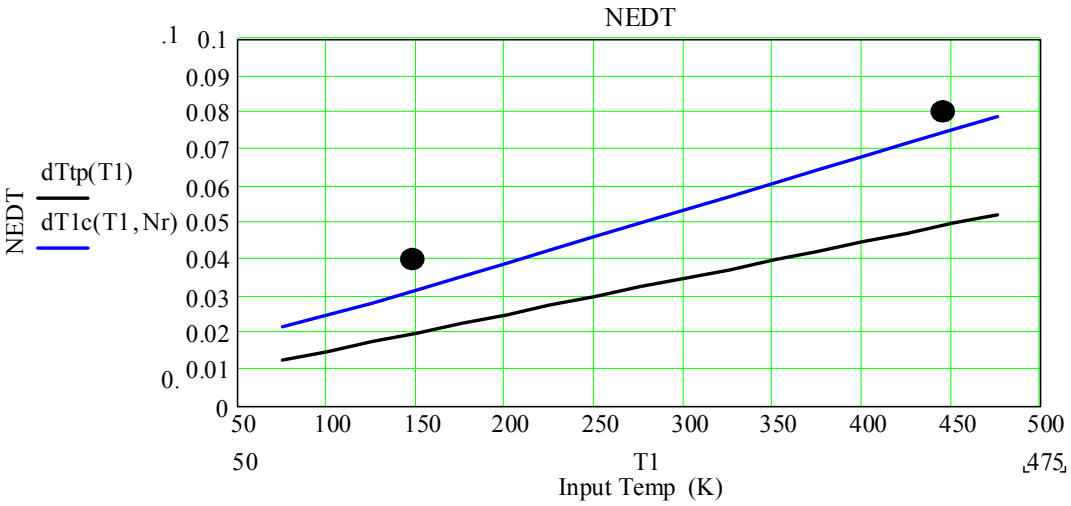

Figure 4-4. The blue curve is the calculated ΔT_i using the running average technique for 4.5 second integration with a 10-step switching sequence with 60% of the time on the input signal using the radiometer values in Table 4-1. The T_r measurements were made using noise sources A and B. The ΔT_i was near its minimum value with $N_g = 7$ and $N_r = 100$, which had gain averages of 35 seconds and radiometer noise averages of 500 seconds. The two dots are the measured results from the JPL radiometer testbed discussed in the next section. The black curve is ΔT_i for the ideal total power radiometer.

Using the expressions for the noise added to T_i by the measurements for T_r and G in (4-29), it is possible to derive requirements for the values of N_r and N_g to minimize the noise in T_i. These requirements are given by the two conditions:

$$\Delta T_r^2 << \frac{(T_i + T_r)^2}{B * \tau_i} \tag{4-30}$$

and

$$\left(\frac{\Delta G}{G}\right)^2 << \frac{1}{B * \tau_i}. \tag{4-31}$$

Using the laboratory radiometer parameters shown in Table 4-1, it is found that N_r must be ≥100 samples and $N_g \geq 7$ samples to achieve a near minimum of ΔT using an integration time of 4.5 seconds with a 10-step switching sequence and with 60% of the time spent on the input. With this switching sequence, the running average of T_r is ~500 seconds and G ~35 seconds. One important point to note in using the running average technique is to ensure that the running average time is smaller than the time when the power spectra of the measured quantities (G, T_r) increases due to their low frequency 1/f noise.

4.6 Model Comparison with Laboratory Radiometer Long Term Stability Tests

In November and December 2005, four long-term stability tests each of 5 to 8 days' length were made with the JPL laboratory testbed radiometer. Two calibration sources were used: a temperature controlled hot load with an effective temperature of ~366 K, and a temperature-controlled LNA, which was the cold load with an effective temperature of ~64 K. Both the hot and cold loads were used with the testbed radiometer in two temperature environments. The first was a ±0.1°C temperature controlled environment and the second was the ambient laboratory environment where the radiometer temperature variations were typically ±0.5°C.

Results from the hot load during the ±0.1°C tests for 7.6 days are shown in Figures 4-6 and 4-7. Plots of the power spectra of the gain, T_r, and T_a versus 1/f are shown in Fig. 4-6. The 1/f point where the power starts to increase is also noted in the figure. Note that at the longer time scales (lower frequencies), the increase in gain and T_r is proportional to 1/f. (The increase in these power spectra at ~500 seconds is due to the switching of the ±0.1°C temperature controller.) Plots of the physical temperatures of the baseplate and input coax, the averaged gain and T_r, and the radiometer antenna temperature, T_a, are shown in Fig. 4-7. Both the gain and baseplate temperature reflect the switching of the temperature controller. The RMS of the radiometer antenna temperature over the entire 8-day period is 0.10 K for the 5-sec samples. The model calculations presented in Section 4.5 predict that the RMS should be 0.08 K. This slightly larger measured value may be due to instability in the hot-load temperature controller and the small error in the correction that was used for the input coaxial line.

Fig. 4-8 is a plot of the power spectra of gain, T_r, and T_a versus 1/f for the hot-load case with the radiometer at the ambient laboratory temperature for 6.8 days. Fig. 4-9 is a plot of the temperatures, gain and T_r averages, and T_a for this case. (The radiometer was insulated with layers of Styrofoam and thus its temperature changes were slow.) Even though the RMS value of the radiometer baseplate temperature is larger than in the ±0.1°C temperature-controlled measurement, the 1/f point where the gain power increases is ~700 seconds, or a factor of 4 larger than the ± 0.1°C temperature-controlled case. This shows that the slower temperature changes do provide better radiometer stability. Also, the RMS of the measured Ta is 0.07 K, which is lower than 0.10 K in the ±0.1°C temperature-controlled test. Note that the low frequency increase in the gain and T_r spectra are larger than the 1/f increase due to the slower larger ambient temperature changes, whereas the T_a spectrum increase is proportional to 1/f.

Data from the cold load measurements are shown in figures 4-10 through 4-13. The cold load power spectra in the ± 0.1°C temperature-controlled case, shown in Fig. 4-10, also shows the increase in power at ~500 seconds due to the temperature controller. However, this does not have any effect on the measured ΔT since the running average time of the gain was 75 seconds. The 1/f point of the ambient temperature environment gain (500 sec) is lower than that for the hot load (700 sec), which may be due to the less stable radiometric temperature of the LNA. In this cold load case, there was no significant difference in the NEDT between the ±0.1°C temperature-controlled case (0.05 K) and the ambient temperature case (0.06 K).

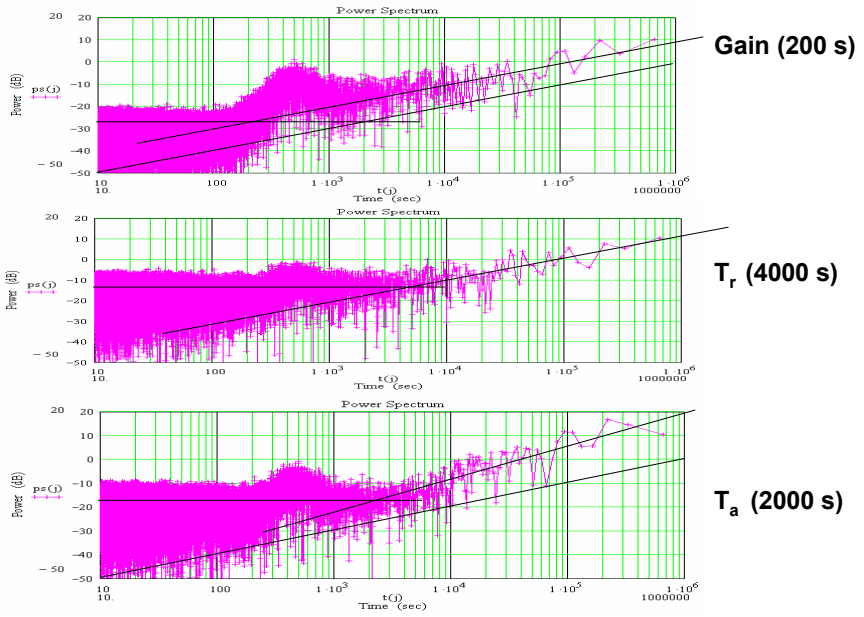

Figure 4-6. Power spectra for the Gain, T_r, and T_a plotted versus 1/f (sec) for the hot load with ±0.1°C radiometer temperature control for 7.6 days. The "1/f" points where the power increases for lower frequencies are noted on the right. The black lines through the low frequency values are proportional to 1/f, except for T_a, which increases slightly faster.

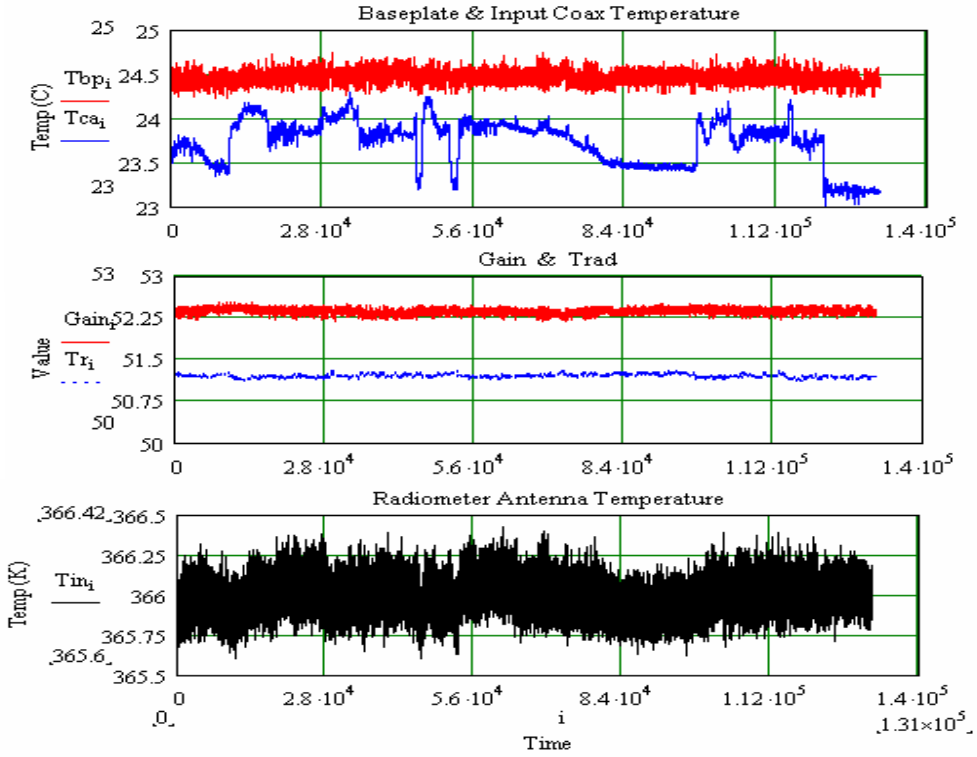

Figure 4-7. 5-second sample data from the 7.6-day test with the hot load with ± 0.1°C radiometer temperature control. The RMS of the baseplate temperature (top red) was 0.08°C. The gain average (lower red) is 75 seconds and was offset by 30. The T_r average is 1275 seconds. The RMS of the radiometer antenna temperature is 0.10 K over the full 7.6 days.

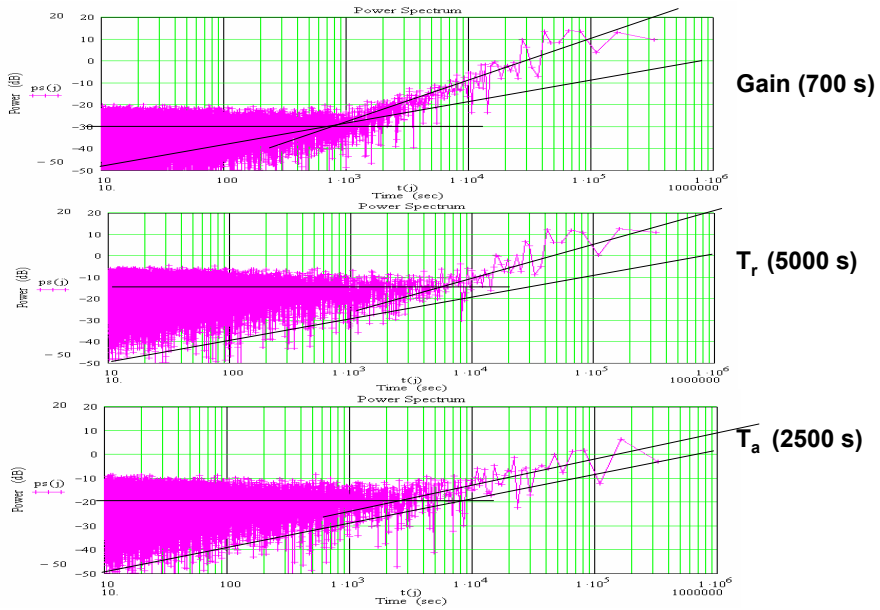

Figure 4-8. Power spectra for the Gain, T_r, and T_a plotted versus 1/f (sec) for the hot load with the radiometer at the ambient laboratory temperature for 6.8 days. The "1/f" points where the power increases for lower frequencies are noted on the right. The black lines through the low frequency values increase faster than 1/f, except for T_a, which is proportional to 1/f.

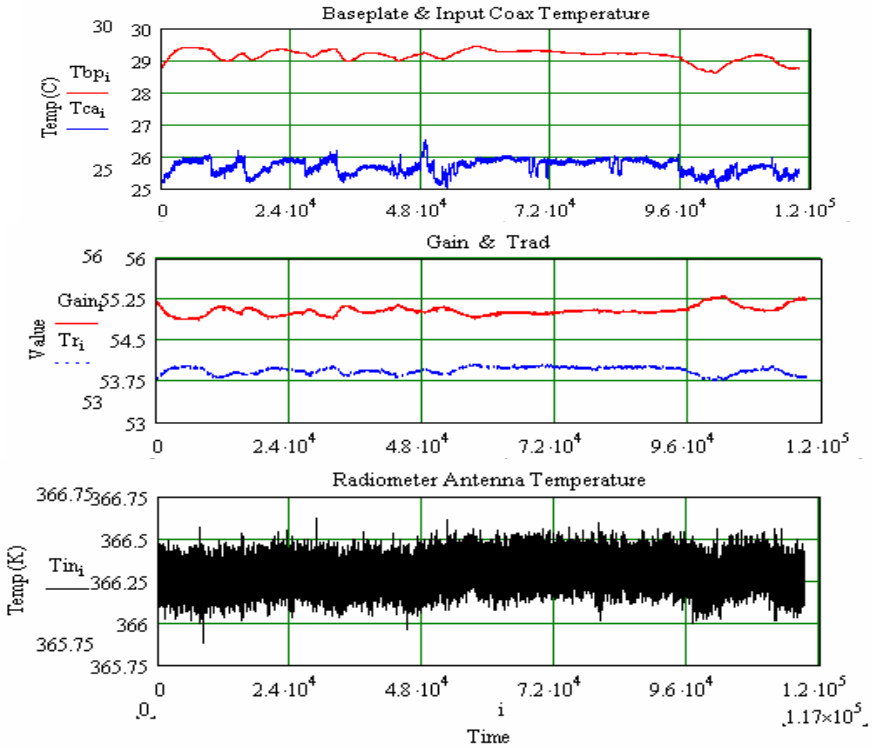

Figure 4-9. 5-second sample data from the 6.8-day test with the hot load with radiometer at the ambient laboratory temperature. The RMS of the baseplate temperature (top red) was 0.17°C. The gain average (lower red) is 75 seconds and was offset by 30. The T_r average is 1275 seconds. The RMS of the radiometer antenna temperature is 0.07 K.

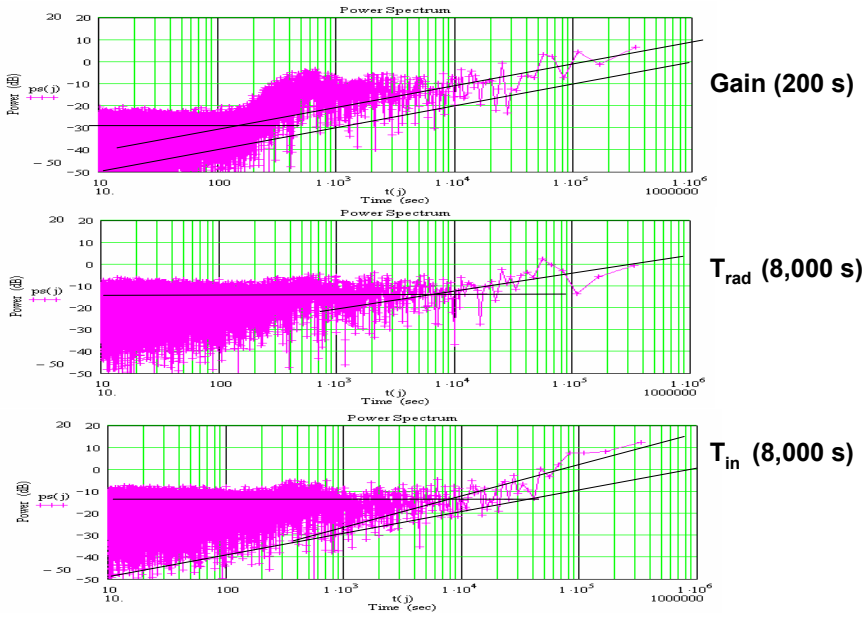

Figure 4-10. Power spectra for the Gain, T_r, and T_a plotted versus 1/f (sec) for the cold load with ±0.1°C radiometer temperature control for 6.2 days. The "1/f" points where the power increases for lower frequencies are noted on the right. The black lines through the low frequency values are proportional to 1/f, except for T_a, which increases slightly faster.

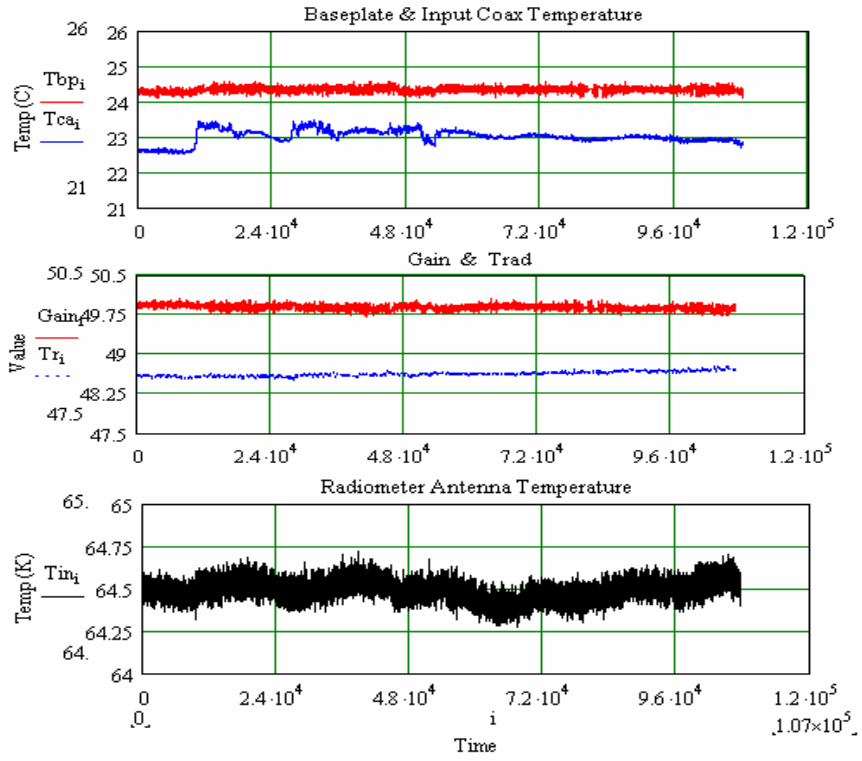

Figure 4-11. 5-second sample data from the 6.2-day test with the cold load with ± 0.1°C radiometer temperature control. The RMS of the baseplate temperature (top red) was 0.08°C. The gain average (lower red) is 75 seconds and was offset by 30. The T_r average is 1275 seconds. The RMS of the radiometer antenna temperature is 0.05 K.

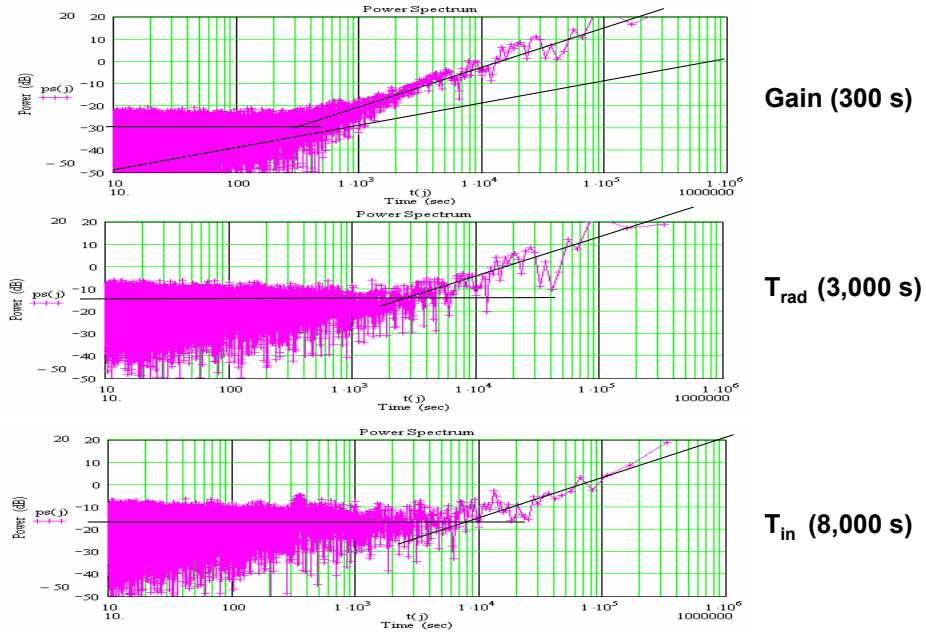

Figure 4-12. Power spectra for the Gain, T_r, and T_a plotted versus 1/f (sec) for the cold load with radiometer at the ambient laboratory temperature for 4.8 days. The "1/f" points where the power increases for lower frequencies are noted on the right. The black lines through the low frequency values all increase faster than 1/f.

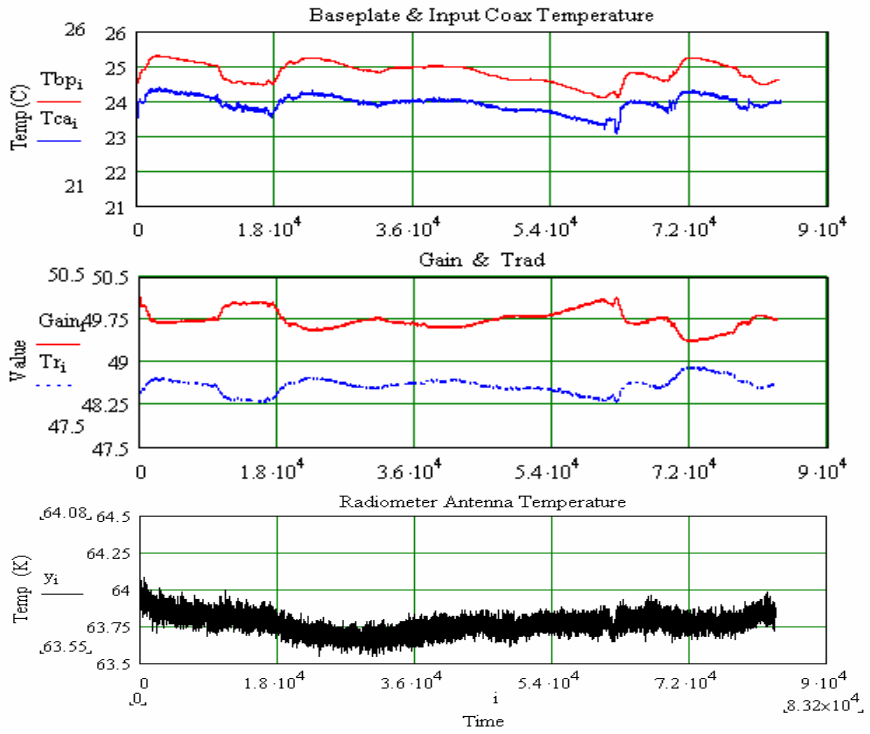

Figure 4-13. 5-second sample data from the 4.8-day test with the cold load with radiometer at the ambient laboratory temperature. The RMS of the baseplate temperature (top red) was 0.3°C. The gain average (lower red) is 75 seconds and was offset by 30. The T_r average is 1275 seconds. The RMS of the radiometer antenna temperature is 0.06 K.

A summary of the measured RMS values for the laboratory testbed compared to the model are shown in Table 4-2 for a range of N_g and N_r. Also included is a column of the structure function, which is the RMS of the first difference of the data. The structure function is representative of the RMS or NEDT of the radiometer and is in close agreement with the model. There is also good agreement between the model and the measured data; however, the measured data has a slightly larger RMS than the model. This can be explained by the fact that there are variations in the hot and cold calibration sources, and the corrections for the input coax temperatures will add small errors.

Another detailed analysis of the testbed power spectra data is included in Appendix 5 (14 Dec 2005 memo by Alan Tanner). This spectral analysis also shows how the running-average technique improves the antenna temperature estimates.

Table 4-2. Measured RMS for T_a in Laboratory Testbed Compared to Model

Test Condition τ = 5 sec, τ_i = 3 sec	N_g sec	N_r sec	ΔT Structure (K)	ΔT Measured (K)	ΔT Model (K)
LNA Cold Load T_i = 150 K	5	5	0.15	0.15	0.13
	35	500	0.02	0.04	0.03
	75*	1275*	0.02	0.05	0.03
Hot Load T_i = 450 K	5	5	0.12	0.13	0.12
	35	500	0.06	0.08	0.07
	75*	1275*	0.06	0.08	0.07

* Represents long term data runs (5-8 days) presented in this section.

5.0 Summary

This ultra stable radiometer research project has addressed the problem of how to design and build a low-noise microwave radiometer to achieve the calibration stability of <0.1 K over 8 days. The key result has been that precise temperature control of all the radiometer components is required to meet this requirement. This result was then demonstrated with the testbed radiometers. In addition, we have demonstrated that with a stable temperature environment, using long-term running averages of the radiometer gain (G) and the noise temperature (T_r) results in the lowest noise performance with the required stability. An analytical noise modes to optimize the switching sequence for the lowest noise, based on the power spectra of the gain and T_r, was also developed. Other stability issues that were addressed in this research were component characterization as a function of temperature, a procedure for measurement and correction for radiometer system non-linearity, noise diode calibration, low noise amplifier performance over voltage, and temperature control requirements to achieve the required stability.

The practical result of this research was the incorporation of these results into the design of the Aquarius radiometers. For example, one of the key elements in the Aquarius design is to mount all the radiometer front-end components near the antenna feed on the ortho-mode transducer in a temperature controlled and thermally isolated location. This research has also helped to define the temperature control requirements for this area. In addition, the Aquarius team will perform thermal testing on all components to ensure their stability and to characterize their performance, e.g., the noise diode. Incorporating the two noise diodes in the system was also a direct result of this research to provide the comparison for this calibration technique.

The other main area of benefit to Aquarius was in the radiometer operation and data analysis using an optimum radiometer switching method with the long-term averaging of the gain and radiometer noise to obtain the lowest noise performance. In the proposed Aquarius switching sequence, about 58% of the time will be spent observing the input signal, and with the running averages of gain and T_r, this will result in a ΔT noise of ~0.05 K, for a 6-second integration time. This result is based on our model calculations and shows that this radiometer will easily meet the system requirements.

There is the question as to what limits the long-term calibration stability of the radiometer. The answer is that the calibration depends on the stability of all the front-end components. Most of these components are passive, and if their temperature is controlled, they are expected to be stable. The two active components, which may change over long time periods, are the noise diode output power and the PIN diode Dicke switch loss. Based on our experience with the spaceborne noise diodes and PIN diode switches in the Topex/Poseidon and Jason missions, these changes are very small and only detectable after months of time.

In the Aquarius mission, it is planned to observe stable Earth-based targets, e.g., the Dome Sea in Antarctica and large numbers of ocean buoys, to monitor and then correct for any long term drifts. Given that we are doing everything we know how to do to build a stable radiometer, based to a large extent on this research, the Aquarius mission will provide an excellent example of a stable microwave radiometer.

6.0 Publications

1. William J. Wilson, Alan Tanner, and Fernando Pellerano, "Ultra Stable Microwave Radiometers for Future Sea Surface Salinity Missions," Earth Science Technology Conference, Pasadena, CA, 11-13 June 2002.

2. William J. Wilson, Alan Tanner, and Fernando Pellerano, "Ultra Stable Microwave Radiometers for Future Sea Surface Salinity Missions," 2nd Inter Microwave Radiometer Calibration Workshop, Barcelona, Spain, 9-11 October 2002.

3. Alan B. Tanner, William J. Wilson, and Fernando A. Pellerano, "Development of a high stability L-band radiometer for ocean salinity measurements," IEEE 2003 International Geoscience and Remote Sensing Symposium, Toulouse, France, 21-25 July 2003.

4. William J. Wilson, Alan Tanner, and Fernando A. Pellerano, "Development of a high stability L-band radiometer for ocean salinity measurements," Earth Science Technology Conference, Palo Alto, CA, 23-25 June 2004.

5. Fernando A Pellerano, William J Wilson, and Alan B Tanner, "Development of a high stability Microstrip-based L-band radiometer for ocean salinity measurements," IEEE 2004 International Geoscience and Remote Sensing Symposium, Anchorage AK, 20-24 September 2004.

Appendix 1 Ultra Stable Radiometer Testbed

JET PROPULSION LABORATORY INTEROFFICE MEMORANDUM

TO: USR team
FROM: Alan Tanner
SUBJECT: noise diode thermal tests
DATE: 2/19/2003

SUMMARY

An updated description of the USR testbed is provided and measurements collected in November and December of 2002 reported. The focus of these tests is to establish thermal requirements for the 'ultra stable' or Aquarius radiometers. Following a hardware overview in Section 1, the test results and analysis are presented in two parts: Section 2 presents measured thermal sensitivities of noise diodes, couplers, pads, and coaxial cables; and Section 3 examines the stability of the radiometer system using a long (300 hour) run of uninterrupted data collected in December.

The thermal sensitivity tests of Section 2 reveal noise diode temperature coefficients of 400 to 1100 parts per million of output power per degree Celsius (ppm/C) within a few degrees of 23 C. The directional couplers exhibit sensitivities of about 400 to 600 ppm/C in the coupled power versus temperature near 23 C. Combined, the net sensitivity is about 900 to 1700 ppm/C, depending on part selection. Both of these devices- noise diode and coupler- are found to be highly nonlinear outside of a narrow range of just a few degrees from 23 C. Inside of this range the thermal sensitivities are repeatable to about 100 ppm/C under a variety of test conditions with different length coaxial cables. This repeatability indicates that the thermal coefficients are not strongly affected by changes to the standing waves or port impedances as the coaxial cables are modified. Adjustments to the bias current do not change the sensitivities of the noise diodes either. The other devices tested, including pads and cable, showed much lower sensitivities- well below 100 ppm/C. In the context of a salinity mission, a 100 ppm uncertainty in gain translates to 0.02K uncertainty in brightness temperature given an ocean brightness of 100K and a reference temperature of 300K (0.02 K = 200 K delta * 100 ppm gain uncertainty due to noise diode errors).

The long-term tests of Section 3 demonstrate that the above temperature sensitivities can be applied in a meaningful way to correct the noise diodes (and hence the gain of the radiometer) to the 100 ppm level provided that the system is held within a degree or two from the setpoint of 23 C and that the thermistors used to measure temperature are thermally well coupled to the noise diodes. Temperature gradients within the system will limit the accuracy of the correction. Subsequent analysis of offset errors (as opposed to 'gain' errors) in Section 3 demonstrates that the radiometric temperatures were also very sensitive to gradients near the RF loads attached to the antenna and reference ports of the Dicke switch. Errors caused by such gradients are examined, and results show that linear combinations of multiple thermistors can reduce the radiometric errors associated with these loads by a factor between about 2 and 5.

The results of these tests- which do not yet include major components of the OMT or the diplexer of Aquarius- is that a radiometric stability requirement of 0.02K translates to: (1) absolute temperature control of the radiometer electronics to within +/- 1 K; (2) gradients within the RF electronics within +/- 0.1K; and (3) thermistor precision- including errors caused by gradients between the thermistor and RF components- of +/- 0.01 K.

1. SYSTEM OVERVIEW

1.1- Thermal control system:

Our primary temperature controller is the large (about 15 x 20 inch) thermoelectric cooler (TEC) plate that we purchased from TECA Inc. The RF components are screwed down to this plate, and insulating foam is packed around and above the RF components to minimize coupling to the room air temperature. The controlling electronics consists of a thermocouple sensor and a commercial controller that communicates with the rest of our data system

via and RS422 serial port. The computer can program the set point temperature of the controller via this port. The observed stability of the temperature controller is about +/- 0.2 C.

In addition to the primary TEC, we have added three more TEC and controller sub-systems: one is identical to the primary TEC, and two are small (about 1 x 1 x 0.1 inch thick) TEC elements that can be applied to individual components within either of the two larger plates. All are capable of heating and cooling. The idea behind the small elements is to control individual components without reconfiguring RF cables within the radiometer. The larger secondary TEC plate sits about six inches away from the primary TEC and can be used to control larger assemblies. The controllers in all cases are identical to that of the primary TEC, and each can be programmed independently from the main data system to heat or cool individual components or assemblies as required. Software has been developed to sweep or step the various TEC's through a programmed sequence of temperatures at controlled rates.

Temperature sensing in the testbed is accomplished with an independent set of sixteen thermistors that can be placed anywhere in the bench top system. The calibration is accurate to within +/- 0.3 C, based on the data sheet supplied with the thermistors and the accuracy of our resistance measurement. When all sixteen thermistors are tied together thermally and allowed to settle to room temperature the measured variations between these sensors are less than +/- 0.1 C. The observed sensitivity and stability of these sensors is better than +/- 0.01 C.

1.2- RF & data System:

The electrical configuration of the bench top system is shown in Figure 1. For all tests described in this report the noise diodes, Dicke switch, and null switch were switched according to the sequence of Table 1. In the present case, the "antenna" is actually a matched load with temperature T_A, as in Figure 1. Each measurement lasts 10 milliseconds, and the complete sequence takes 0.1 seconds. Note that this timing is suitable for bench top tests of the noise diodes, and has not been optimized for any radiometric application (where we'd want more antenna duty cycle, for example).

time (ms)	Dicke mode	noise diode	null switch
0	antenna		
10	antenna	A	
20	antenna	B	
30	antenna	C	
40	antenna		X
50	reference		
60	reference	A	
70	reference	B	
80	reference	C	
90	reference		X

Table 1: Testbed timing

Data are acquired via the two detector-V/F converters shown in Figure 1. This redundant configuration is left over from previous experiments, but it continues to be useful for constraining a variety of back-end errors during analysis. One of the digitizers uses an Analog Devices AD650 voltage to frequency converter (V/F) and the other uses an AD652 synchronous V/F. The detector and video amplifiers are also configured differently: the detector for the AD650 operates at an RF power level of about -35 dBm, which is 4 dB lower than that of the AD652; and the detector output is loaded with 100 ohms versus 2k ohms in the AD652. The frequencies from the V/F converters are counted by the data system over the 10 ms gates, and the resulting counts are binned according to measurement mode, averaged over a user specified integration interval (usually ten seconds), and then recorded to disk along with thermistor measurements.

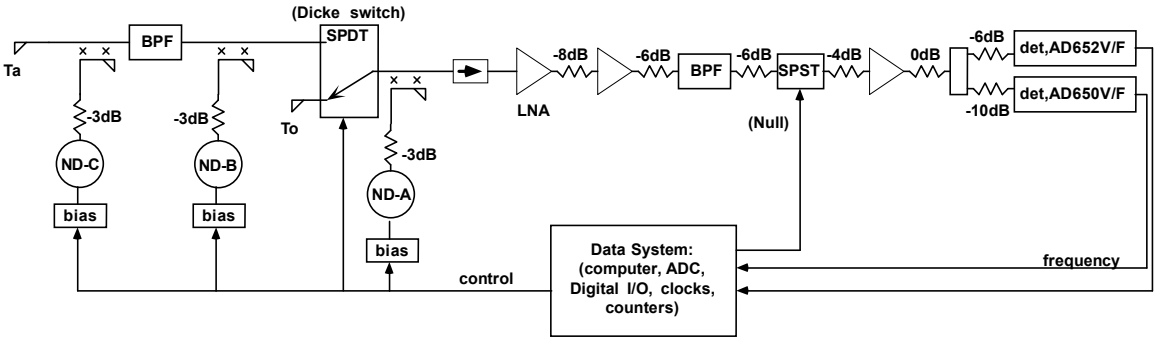

Figure 1: Initial configuration of testbed.

2. NOISE DIODE TESTS

Measurements of noise diode output power versus temperature were made in November. These tests were generally made by sweeping the temperature of one or two noise diodes while holding at least one noise diode constant in temperature. The constant temperature diode provided the needed standard to judge changes in the other noise diodes. Several different heating/cooling strategies were tested.

2.1- First attempt, using TEC elements:

In the first set of tests the small TEC elements were used to heat and cool a given noise diode and directional coupler together. This was the easiest test since the TEC element could be placed between the noise diode/coupler assembly and the base plate without modifying the thermal enclosure and without changing the interconnecting RF cables.

Figures 2a, 2b, and 2c provide an example of the noise diode temperature versus time, noise diode output versus time, and noise diode output versus the temperature, respectively, for one such test. In this case the temperature of noise diode-C was slowly scanned between 10 and 50 C, as shown in Figure 2a. Figure 2a also shows the temperatures of the directional coupler (which is attached to noise diode C via a 3dB pad and a male-to-male SMA connection), the current regulator (which is mounted to the top of the coupler), the "plate" as measured by nine thermistors at various points around the primary TEC plate, and "room air" as measured by four thermistors that were sitting together outside of the thermal enclosure. Note that the four room air temperatures are nearly equal (so they appear as a single trace on the scale of Figure 2a), but that the plate temperatures span about 2 degrees due to temperature gradients throughout the testbed. Also note that there are large gradients between the noise diode, coupler, and regulator temperatures. These gradients were difficult to suppress given the short coaxial cable lengths and close proximity to the constant-temperature components within the testbed.

Output power variations of noise diode-C relative to noise diode-A were computed from the noise diode deflection ratio:

$$D_{C/A} = \frac{V_{ANC} - V_A}{V_{ANA} - V_A}, \tag{1}$$

where V_A represent the measured response to the antenna, V_{ANC} is antenna plus noise diode-C, and V_{ANA} is antenna plus noise diode-A. In Figures 2b and 2c this deflection ratio has also been normalized by dividing the ratio of equation 1 by the mean value indicated in the vertical axis is the figure.

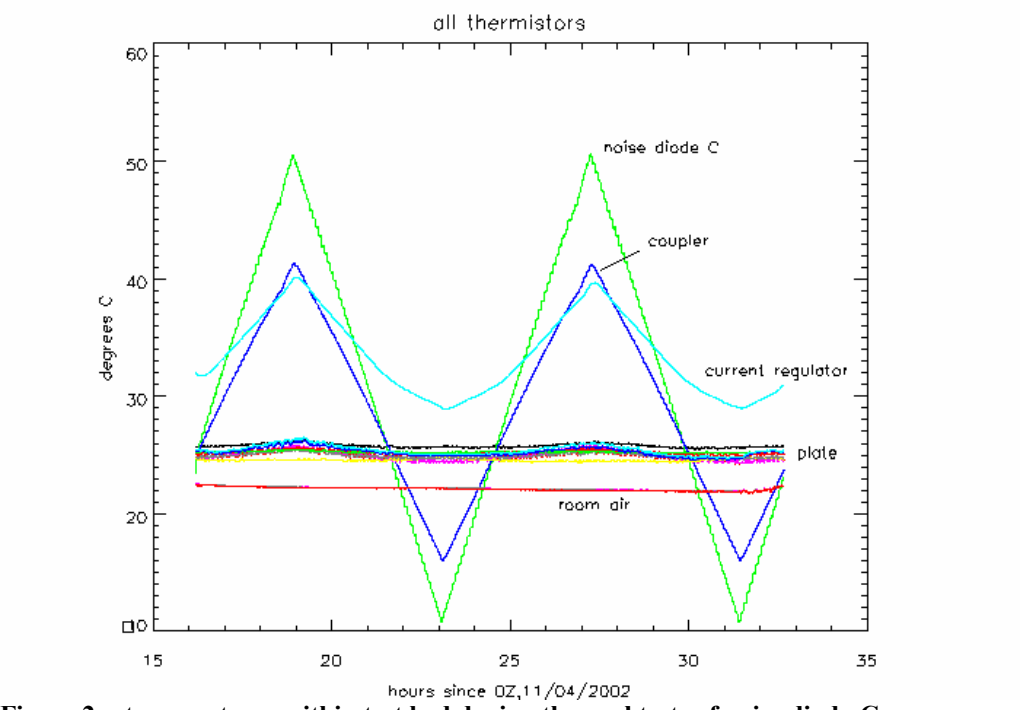

Figure 2a: temperatures within test bed during thermal tests of noise diode-C

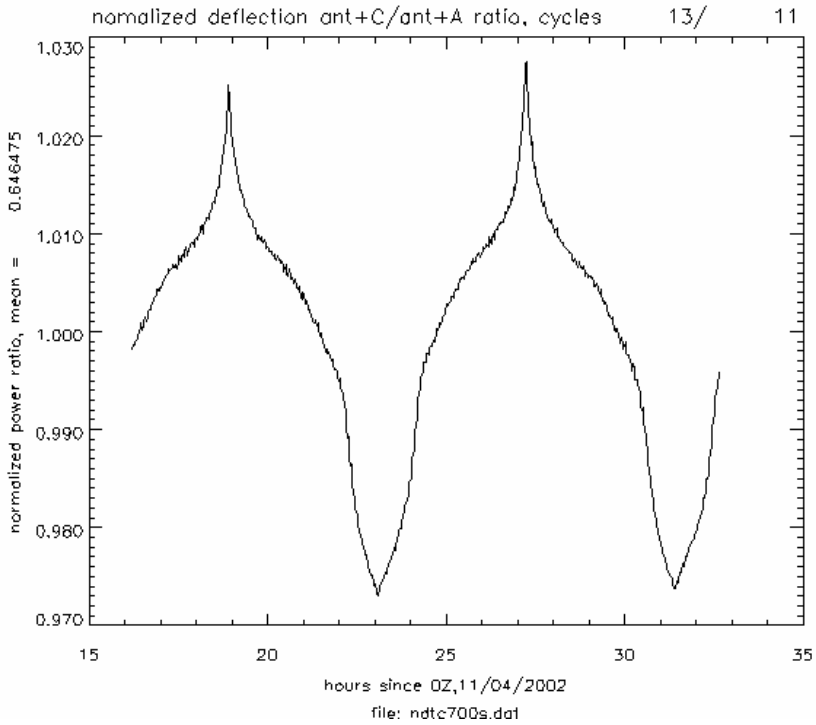

Figure 2b: Noise diode-C output during temperature sweeps of coupler/noise diode assembly

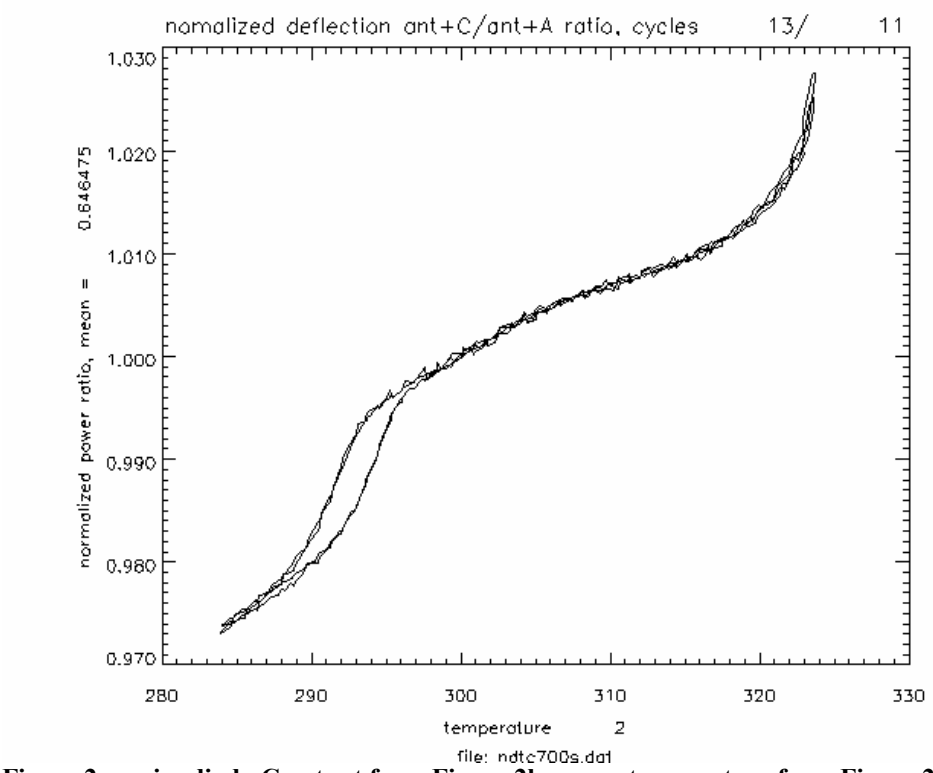

Figure 2c: noise diode-C output from Figure 2b versus temperature from Figure 2a.

As can be seen in Figure 2c, there are significant nonlinearities and an apparent hysteresis in the noise diode power versus temperature curve. At 300 K the slope of this curve is 780 parts per million per degree C (ppm/C), but at other temperatures the slope can be much worse- in excess of 4000 ppm/C.

Figure 3a shows a similar result for noise diode-B which again shows a jump around 295K, but without the hysteresis. The slope of Figure 3a at 300 K is about 1960 ppm/C. No measurements of noise diode-A were made using the TEC elements due to difficulties fitting the TEC between the Dicke switch and the LNA.

2.2- Noise diode stability versus bias current:

To test a possibility that the thermal sensitivity of a noise diode might be 'tuned out' by adjusting the bias current, Figures 3a, 3b, and 3c show the results of thermal cycling in which the bias current to noise diode B has been adjusted to 4.00, 6.00, and 8.00 milliamps (mA), respectively. The respective slopes at 300 K are 1960, 1720, and 1840 ppm/C. These data indicate that the thermal sensitivity of these noise diodes can not be tuned out with bias current.

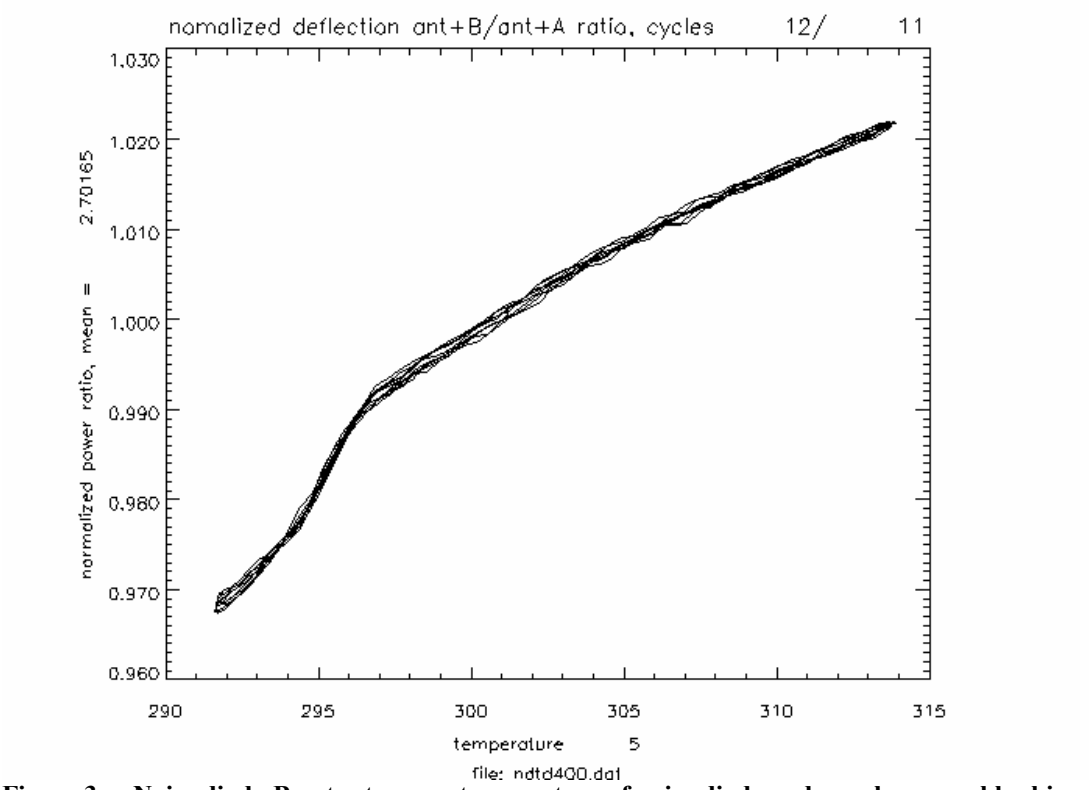

Figure 3a: Noise diode-B output versus temperature of noise diode and coupler assembly; bias current= 4.00 mA; slope = 1960 ppm/C @300 K

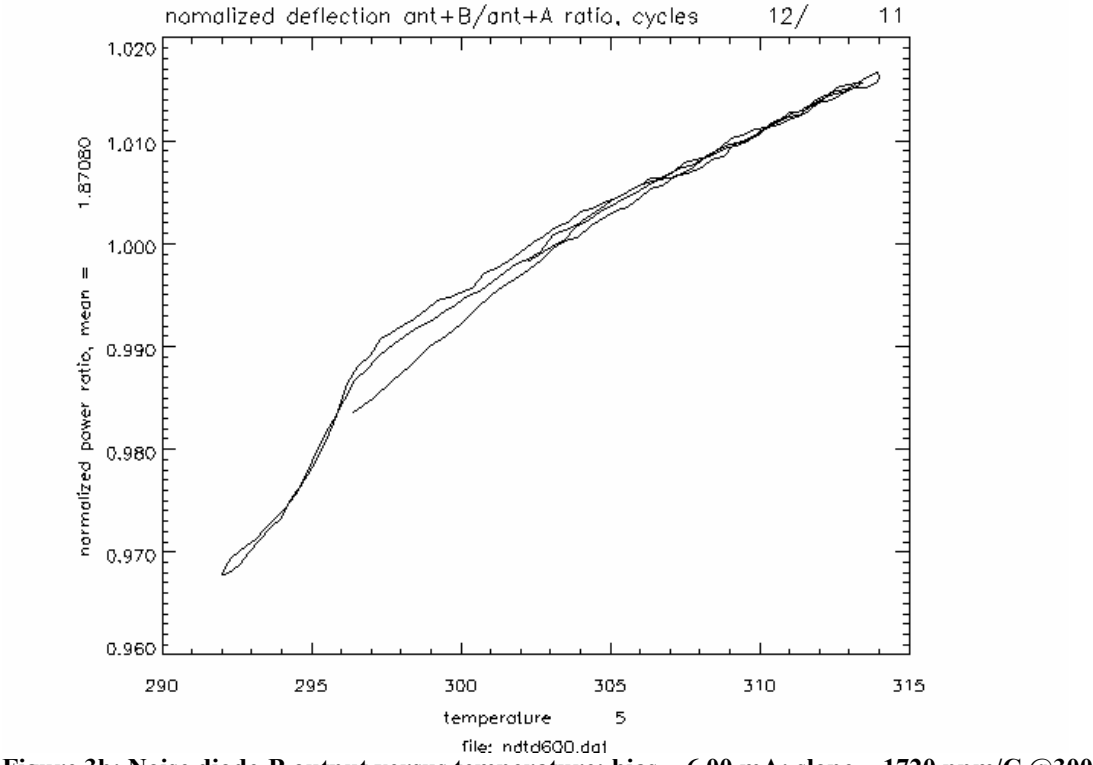

Figure 3b: Noise diode-B output versus temperature; bias = 6.00 mA; slope = 1720 ppm/C @300 K

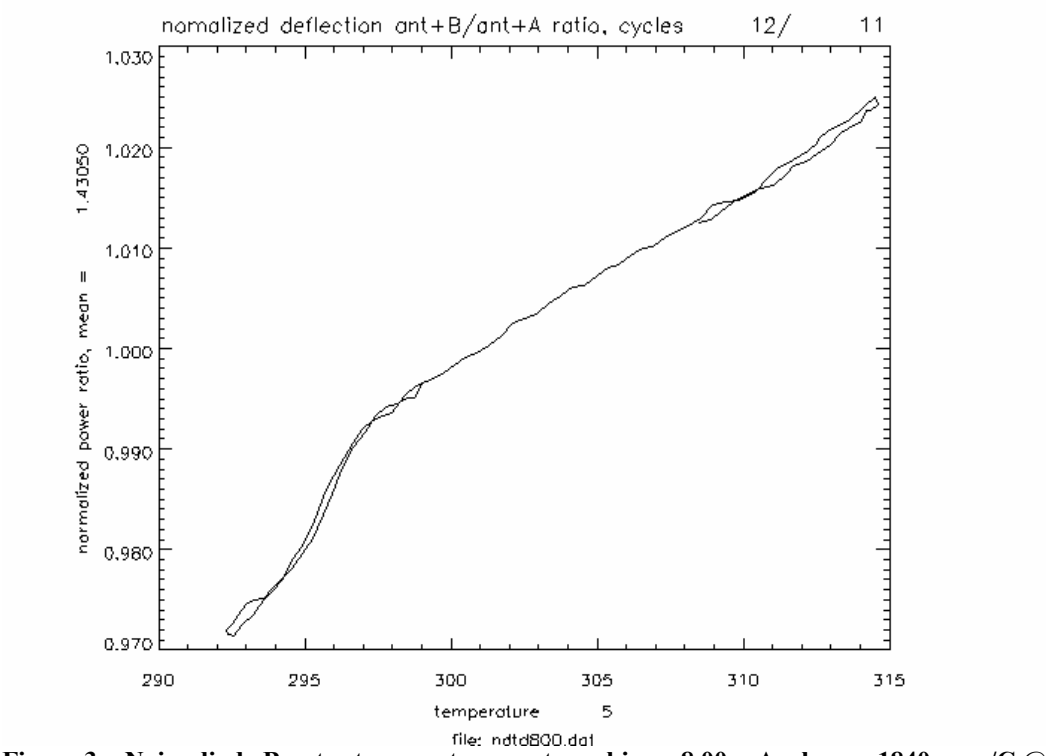

Figure 3c: Noise diode B output versus temperature; bias = 8.00 mA; slope = 1840 ppm/C @300 K

2.3- Second attempt- using the heat-gun/freeze-mist technique to isolate component sensitivities:

To isolate the thermal coefficients of the noise diodes, pads, and directional couplers several tests were attempted using the TEC elements in various configurations to vary the temperature of the coupler, pad, or noise diode while holding the other components stable. Unfortunately, these test produced inconsistent results due to difficulties in isolating the temperatures of the components. One problem was that the coaxial cables leading to and from the device under test- which were kept as short as possible in the interest of good RF practice- were also good heat conductors. This made it difficult to adequately decouple the device temperatures. Gradients throughout a device also created uncertainty in the temperature sensing since results depended on where the thermistor was attached to the device.

To reduce these errors, the coaxial cables needed to be lengthened so that device temperatures could be isolated. To expedite the measurements we also switched to a less controlled- but effective- heat-gun/ freeze-mist method for changing the device temperature. This method involved running about six inches of coaxial cable away from the primary TEC plate through the insulation so that the device under test could be heated and cooled in isolation from the rest of the testbed. The device temperatures were measured with thermistors that were attached with heat conducting putty and tape. Figures 4a and b shows how the temperature of noise diode-B was varied, and how the output of noise diode-B varied using this technique. Transient data due to abrupt heating and cooling have been removed from Figure 4b. As can be seen, the sensitivity to temperature is considerably less (940 ppm/C at 300 K) than the noise diode/ coupler assembly (compare to 1960 ppm/C, from figure 3a). Figure 4c and 4d show the responses of noise diode-C and noise diode-A when they were tested in the same manner; these exhibit sensitivities at 300 K of about 400 ppm/C and 1000 ppm/C, respectively.

Figures 5a thru 5e provide a detailed breakdown of thermal sensitivities for the remaining components measured with the heat-gun freeze-mist technique. Of all these tests only the coupled port of the directional coupler showed a significant sensitivity, as can be seen in Figure 5a. Figure 5a also shows the jump at 295 K that was seen in previous tests. The thru-arm of the same coupler was largely unaffected by temperature, as evident in Figure 5b (measured

using noise diode-C of Figure 1). Figure 5c shows that the 3 dB pad[1] was stable, at about -66 ppm/C. Figure 5d shows that the coaxial cables used for these tests- with a total length of about twelve inches (six up and six back down to the TEC plate), were also stable at about -54 ppm/C. And Figure 5e shows that the noise diode current regulator was stable to within +/- 20 ppm/C.

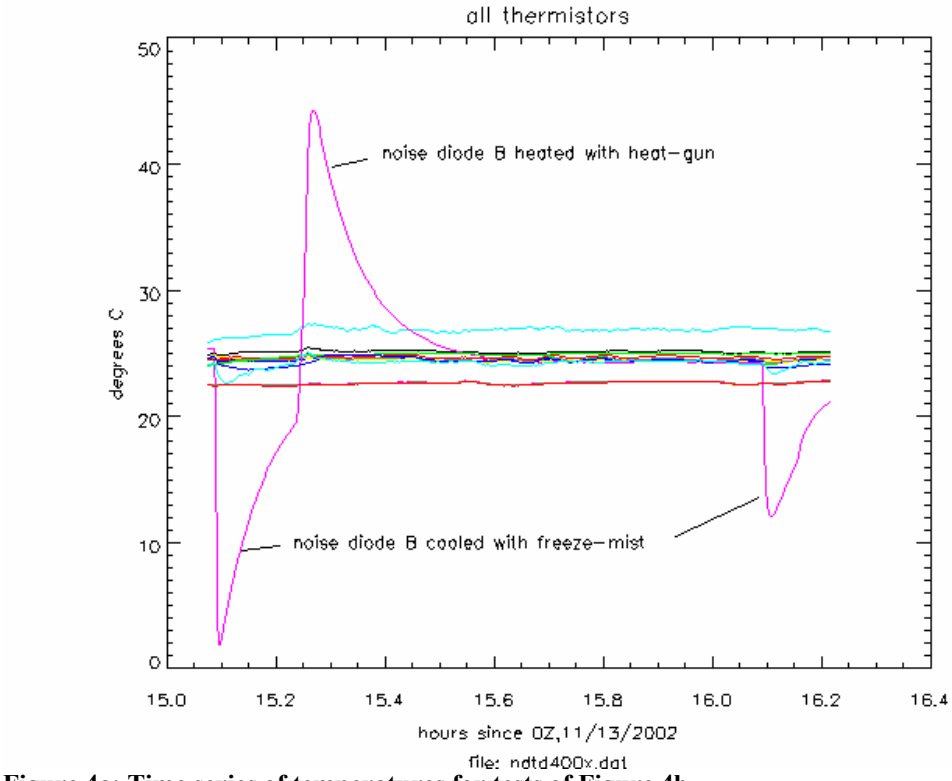

Figure 4a: Time series of temperatures for tests of Figure 4b.

[1] The test of Figure 5c was for a Mini-Circuits pad (model MCLBW-S3W3). We also tested a Narda (model 4779-3) 3dB pad and measured a coefficient of -27 ppm/C, and a Midwest Microwave pad (model ATT-263F-03-SMA-02) which had a sensitivity of -50 ppm/C.

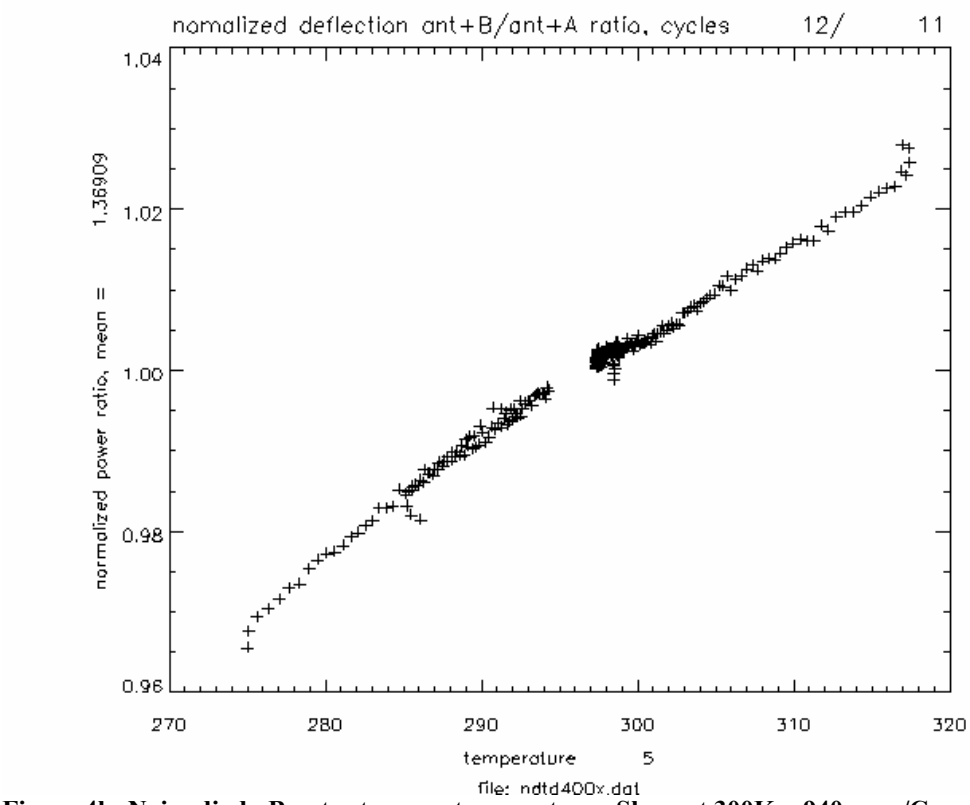

Figure 4b: Noise diode-B output versus temperature. Slope at 300K = 940 ppm/C.

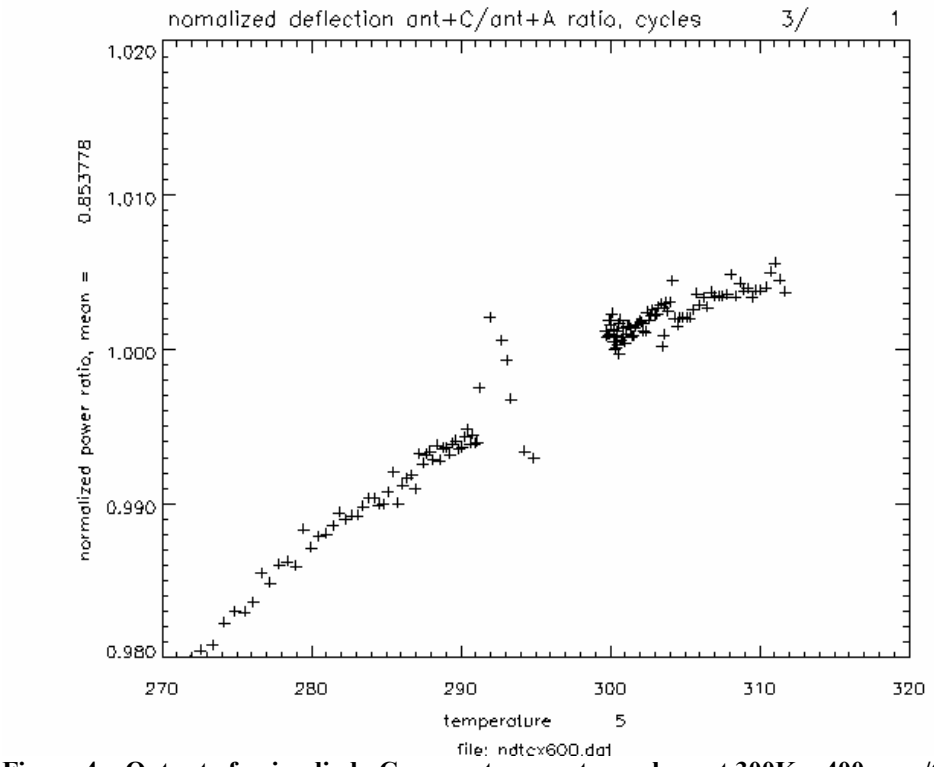

Figure 4c: Output of noise diode-C versus temperature; slope at 300K = 400 ppm/C.

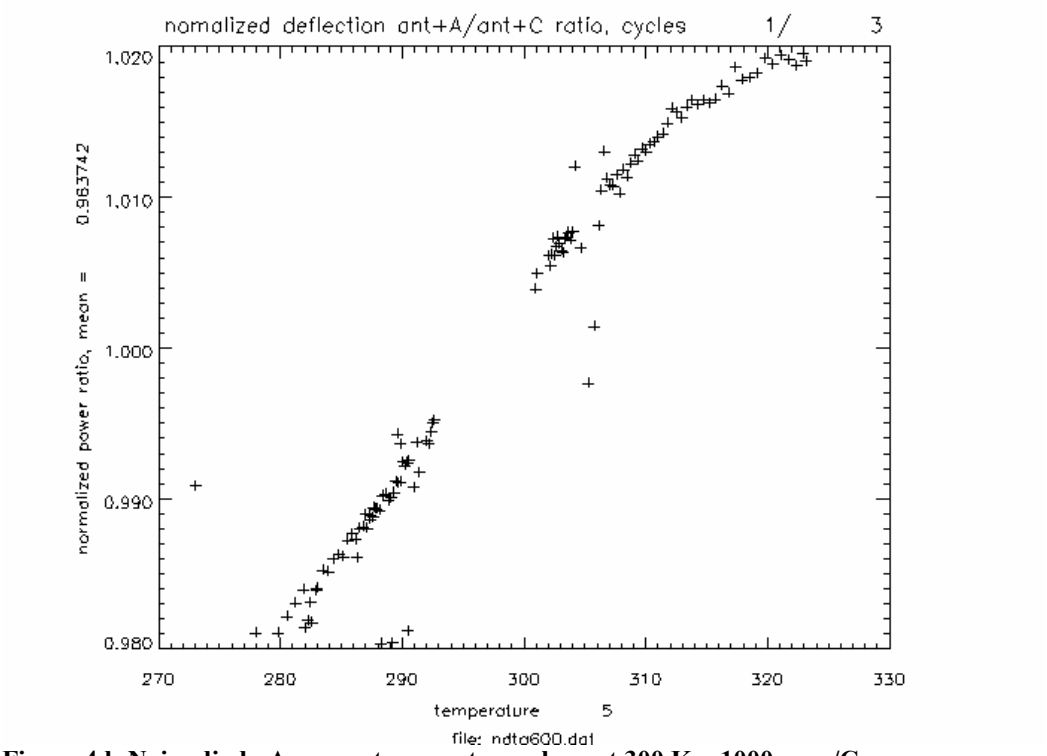

Figure 4d: Noise diode-A versus temperature; slope at 300 K = 1000 ppm/C.

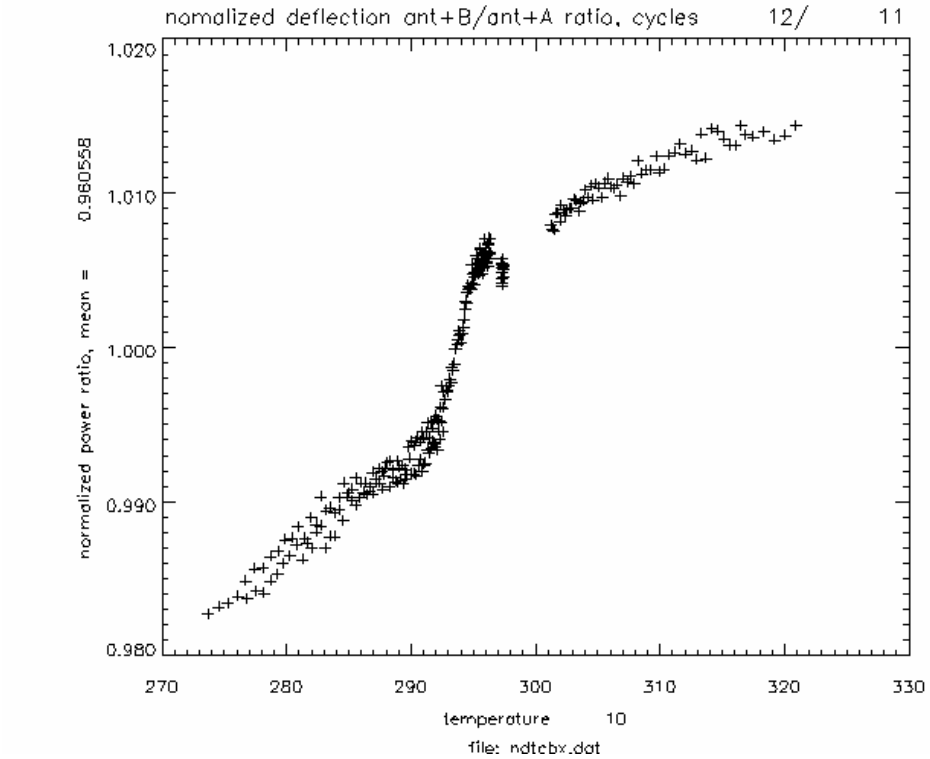

Figure 5a: coupler sensitivity; slope at 300 K = 430 ppm/C

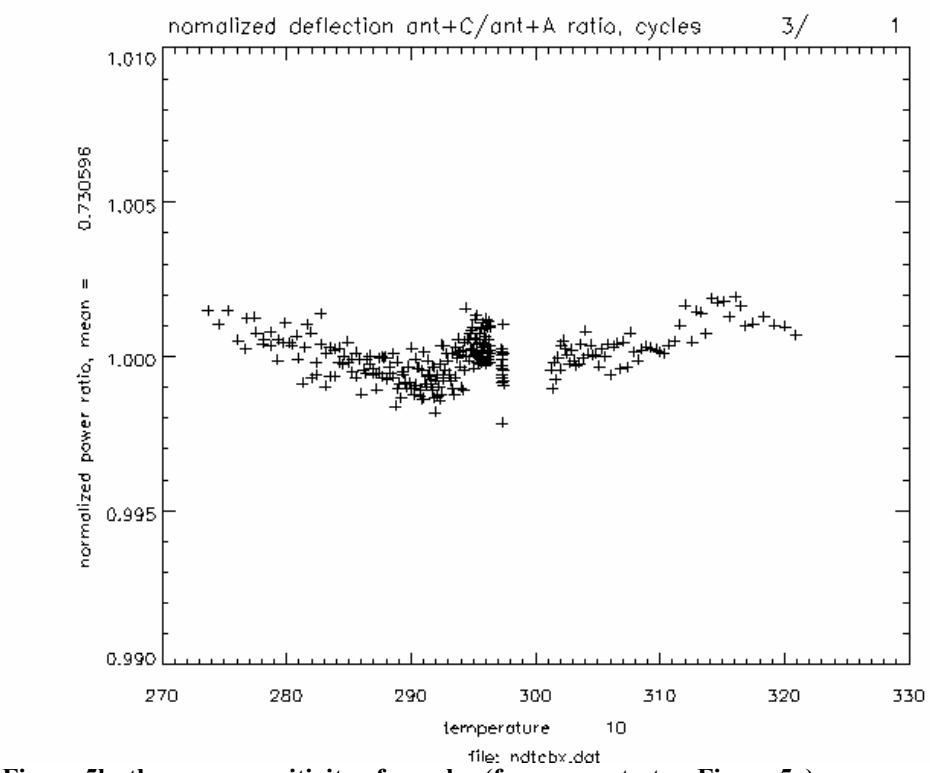

Figure 5b: thru-arm sensitivity of coupler (from same test as Figure 5a)

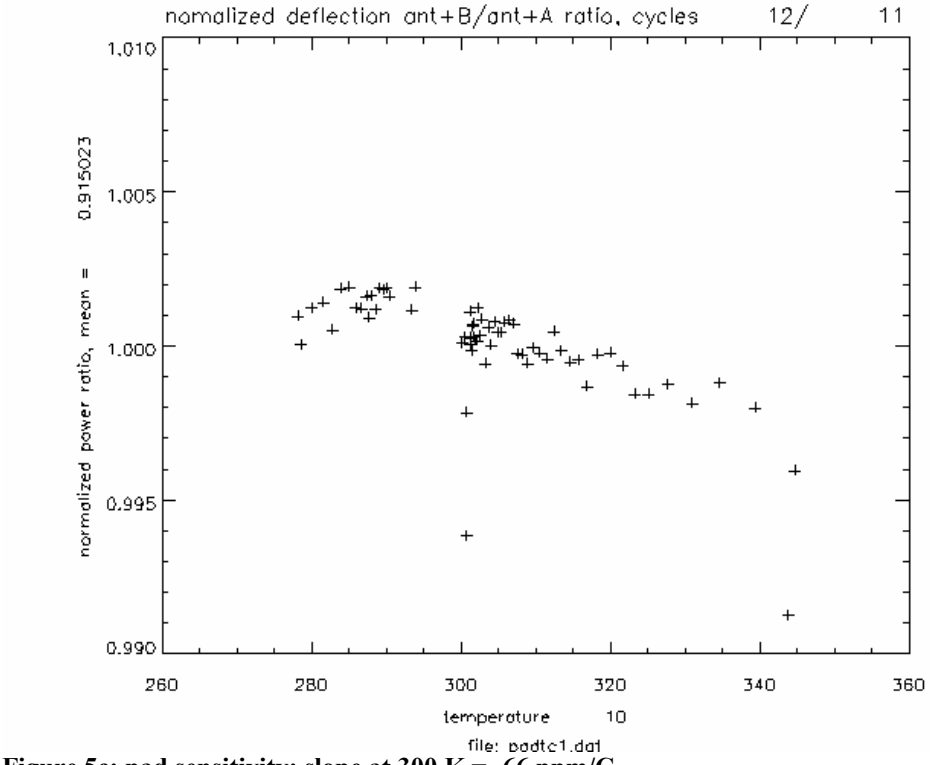

Figure 5c: pad sensitivity; slope at 300 K = -66 ppm/C

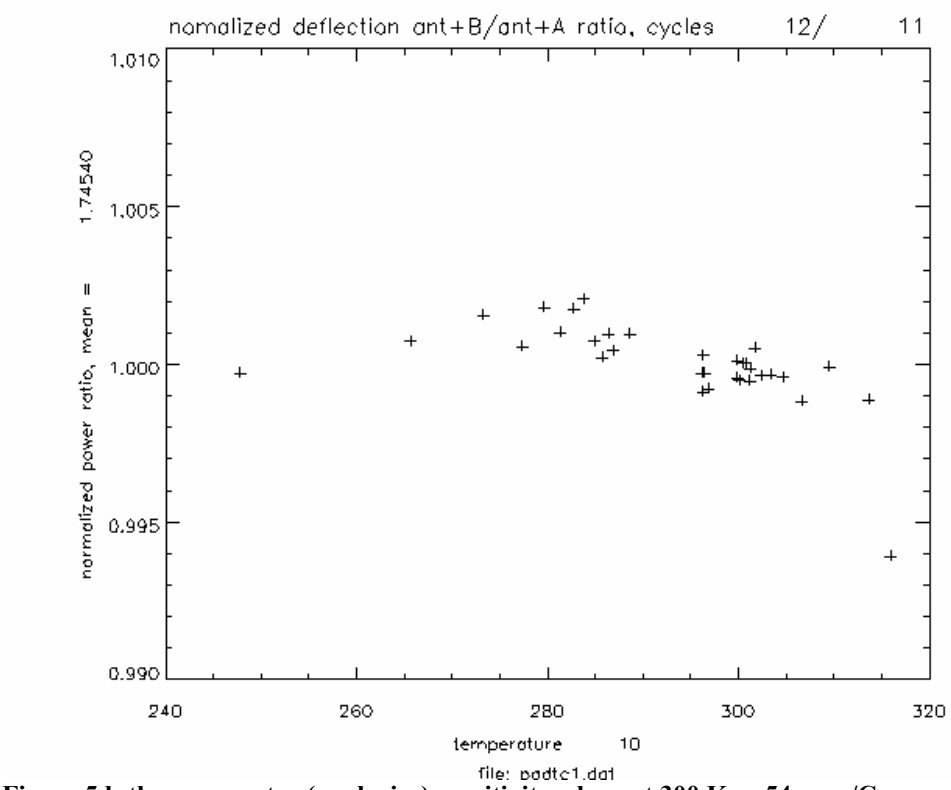

Figure 5d: thru-connector (no device) sensitivity; slope at 300 K = -54 ppm/C

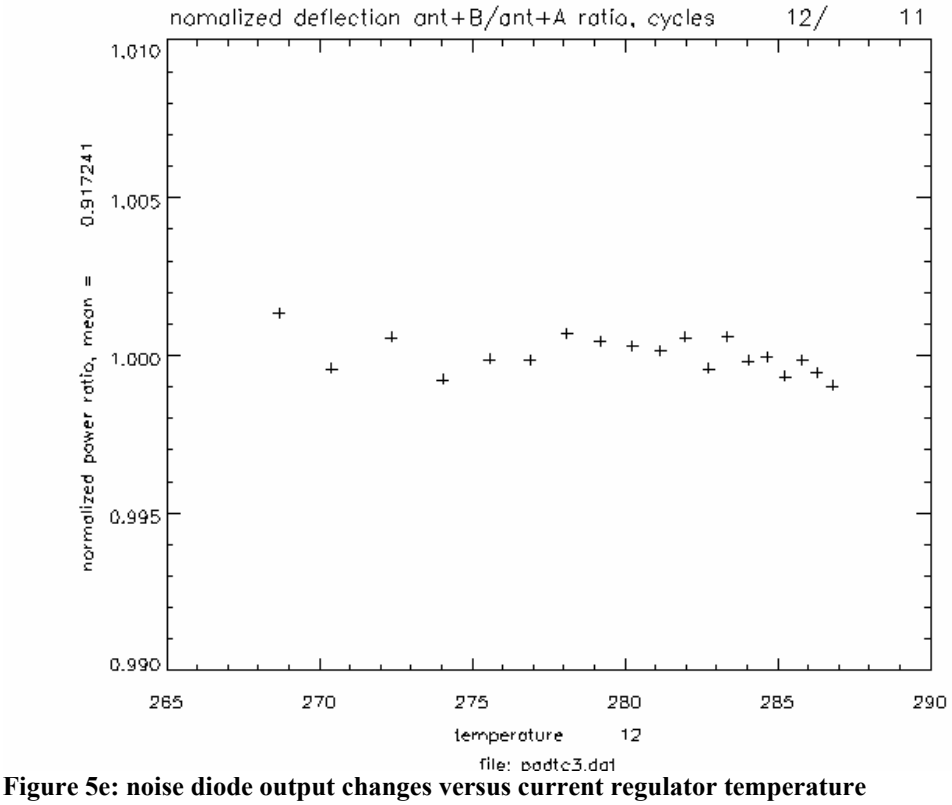

Figure 5e: noise diode output changes versus current regulator temperature

2.4- Third attempt- the dual-plate method:

The sum of noise diode and directional coupler thermal coefficients for noise diode-B from Figures 4 and 5 is (430 + 940 ppm/C =) 1370 ppm/C at 300K, which does not add up to the 1960 ppm/C observed for the assembly in Figure 3a. This discrepancy could be caused by a variety of factors, including differences in the RF circuitry after adding the longer coaxial cables. Another suspected error is inaccurate temperature measurements due to thermal gradients within the assemblies. As noted above, we had difficulty with gradients when the devices were heated and cooled in close proximity to the constant temperature plate. This caused ambiguity in the temperature measurements. For example, the sensitivity of the noise diode-C/ coupler assembly from Figure 2 can be interpreted as either 780 ppm/C (as Figure 2c) or 1300 ppm/C by choosing either the noise diode or the coupler temperatures, respectively, from Figure 2a.

To reduce the error caused by gradients, noise diode-C and its coupler were moved to the secondary TEC plate. About 12 inches of coaxial cable connects the RF signal between the two plates. With the new configuration we could vary the soak temperature of either noise diode-C and its coupler, or the rest of the testbed on the primary TEC without suffering from thermal gradients between closely spaced components. Figure 6 shows a sample of the temperatures measured as the primary TEC was ramped through a test sequence. As can be seen in Figure 6, thermal gradients occurred primarily along the coaxial transmission line between the two plates. The disadvantage of this configuration is that one can't separate the temperature coefficients of components within each plate. We therefore need to be mindful of the stability of other interconnecting components such as the bandpass filter of Figure 1 and the coaxial cables. For the following tests the bandpass filter of Figure 1 was removed. Coaxial cable losses were measured, and will be discussed later.

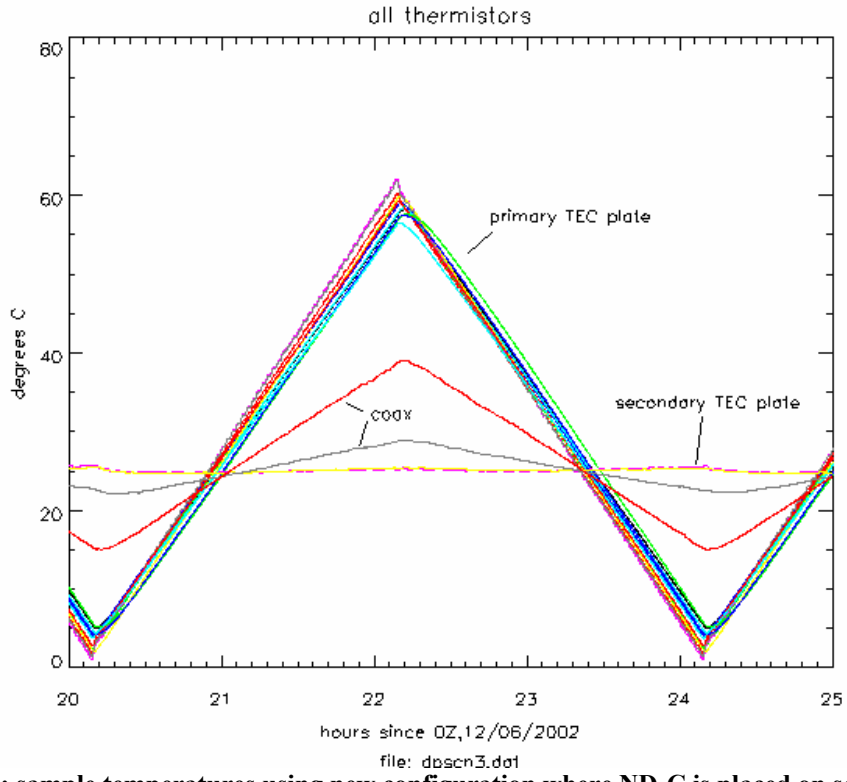

Figure 6: sample temperatures using new configuration where ND-C is placed on secondary plate.

With the new test setup we were able to make more consistent tests of the noise diode/coupler assemblies. Figures 7a-c give the revised curves for all three noise diodes. Noise diode-B, from Figure 7b, now exhibits 1430 ppm/C which is more consistent with the sum of the noise diode and coupler sensitivities from Figures 4b and 5a. In all three cases we see that the couplers have the same troublesome jump near 295 K. Figure 7d shows the measured sensitivity after removing the coupler and replacing it with a 20 dB pad; again we see that the coupler is responsible for a large part of the sensitivity of the assembly.

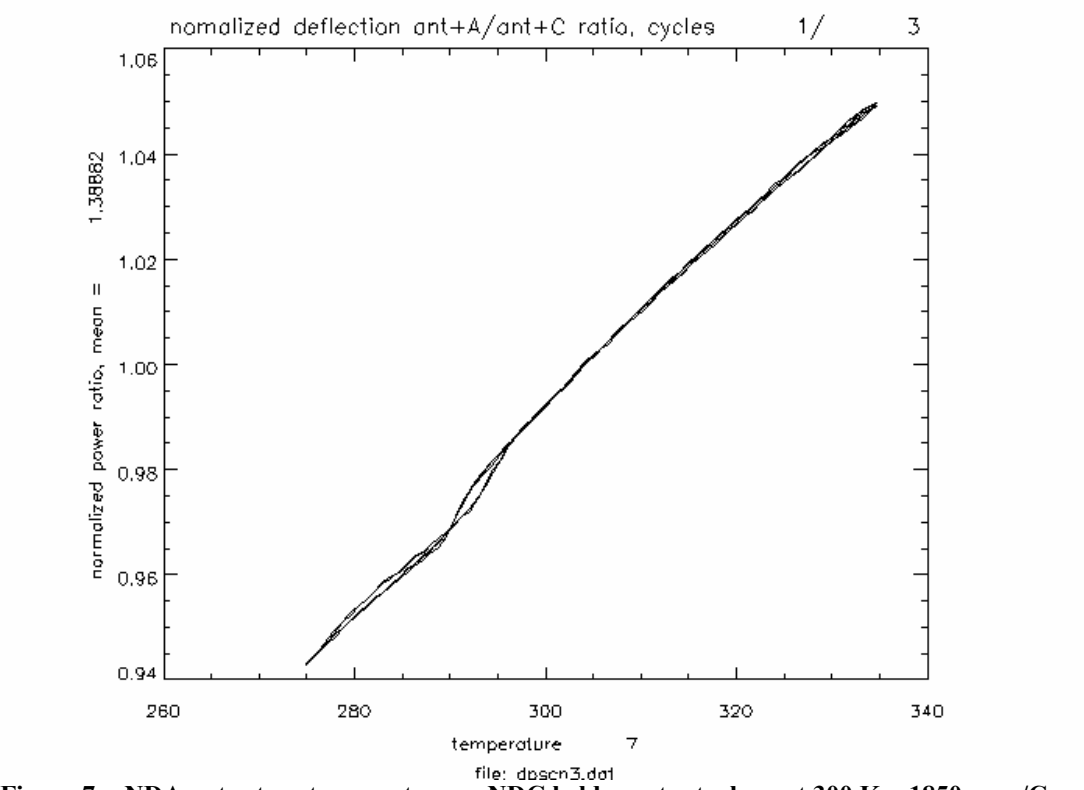

Figure 7a: NDA output vs. temperature as NDC held constant; slope at 300 K = 1850 ppm/C

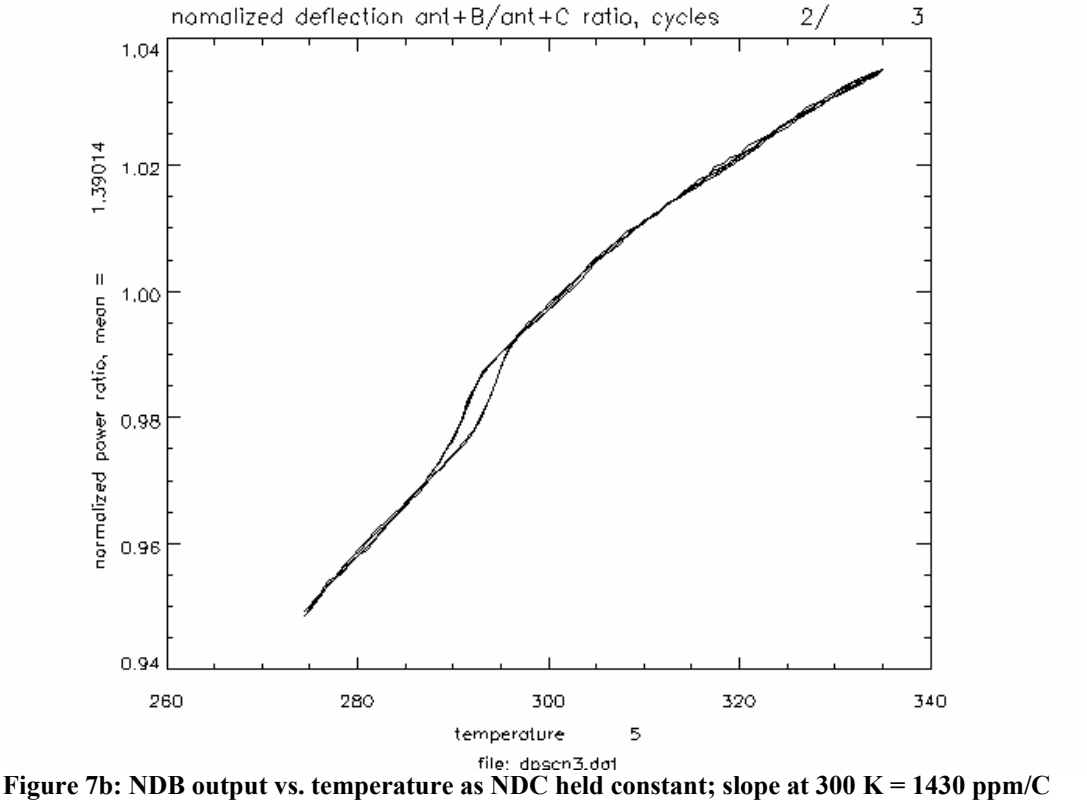

Figure 7b: NDB output vs. temperature as NDC held constant; slope at 300 K = 1430 ppm/C

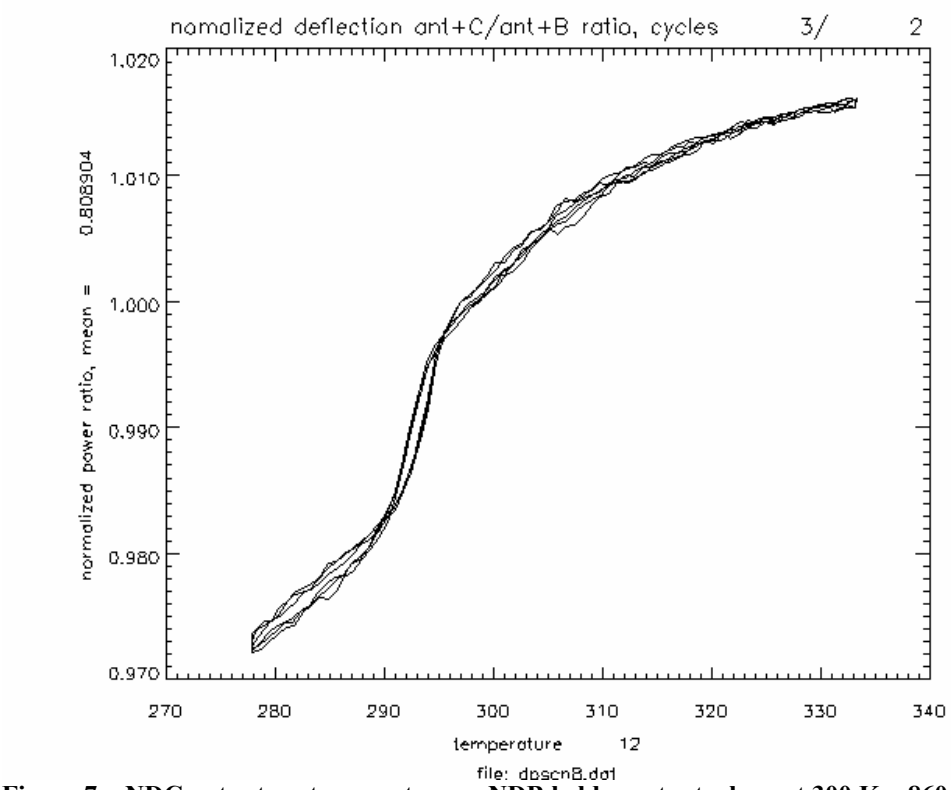

Figure 7c: NDC output vs. temperature as NDB held constant; slope at 300 K = 860 ppm/C

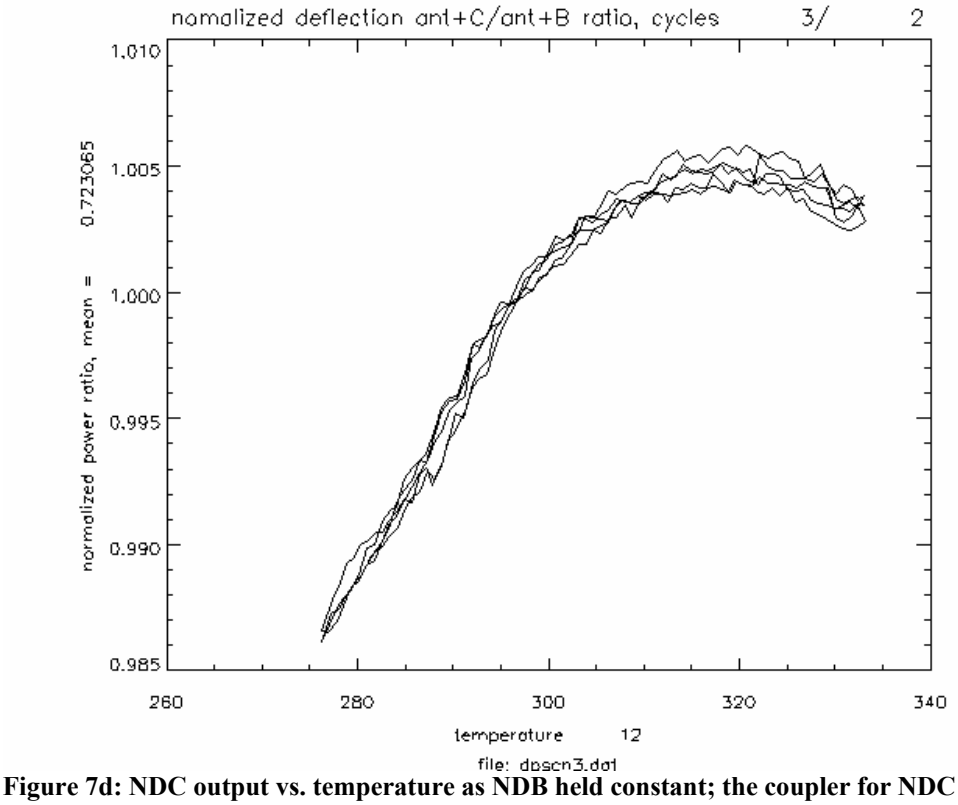

Figure 7d: NDC output vs. temperature as NDB held constant; the coupler for NDC has been replaced with a 20dB pad; slope at 300 K = 300 ppm/C

2.5- Coaxial cable tests:

The above results depend on the assumption that the coaxial cables used in the tests were stable. So far the only evidence for this was Figure 5d, which showed a slightly negative temperature coefficient. To better characterize the cable, the dual-TEC plate configuration was used to measure the insertion loss of coaxial cables versus temperature. For these tests we moved noise diode-C back to the primary TEC and ran it's output through a 1 foot length of coax to the secondary TEC plate. This signal was then connected to the device under test (coax) and returned to the primary plate via another foot of coax. This configuration placed the device under test between noise diodes C and B, in place of the bandpass filter of Figure 1. The noise diode-C/ noise diode-B deflection ratio was used to measure insertion loss changes with temperature. Two tests were made: one of a thru-connector (SMA 'bullet') to calibrate the two one-foot test cables and one with the one-meter length of coaxial cable which was coiled up, secured to the secondary plate, and connected between the two test cables. In both cases the secondary plate was swept through a range of temperature while the primary plate was held constant. All cables were RG405 (0.085 inch diameter) semi-rigid copper. Both of the tests showed a negative slope in the transmission coefficient[2] versus temperature of the coaxial cable, as summarized in Table 2. Note that the coefficient of -158 ppm/C is for the test cables with just the ends tied to the secondary plate, so this figure does not represent the insertion loss versus soak temperature.

thru-connector with 12" test cables	-158 ppm/C
add 1 meter cable	-427 ppm/C
1 meter RG405 cable alone	-269 ppm/C

Table 2: Temperature coefficients derived from coaxial cable tests (negative coefficients indicate decreasing output power with higher temperature).

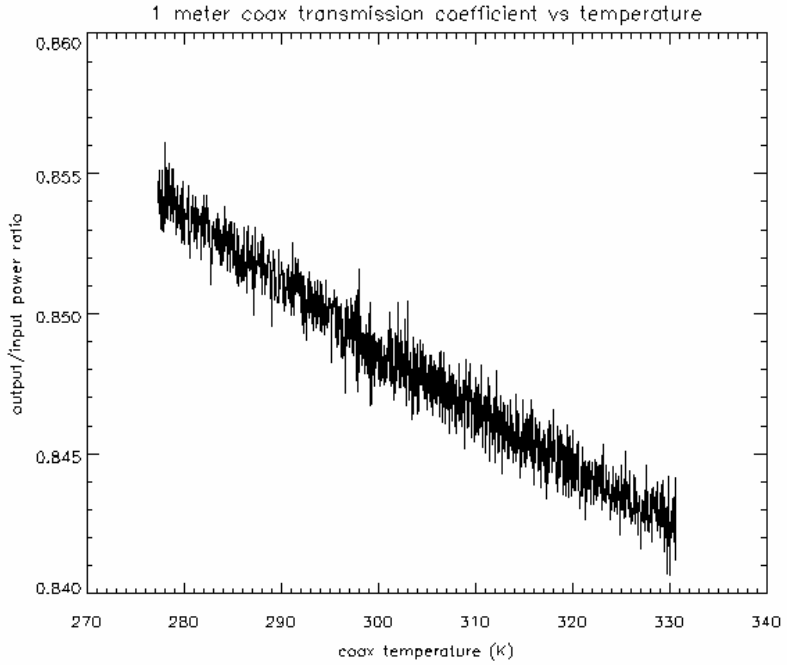

Figure 8: transmission coefficient versus temperature for a 1 meter length of semi-rigid cable; slope= -269 ppm/C.

[2] To be consistent I want to plot everything versus output power, so I've used the term "transmission coefficient" to refer to the output/input power ratio. I don't know of any better term: "loss" or "insertion loss" increase with decreasing power, and the term "gain" would be confusing in the present context. The term "efficiency" could also be used here.

Figure 8 shows the transmission coefficient versus temperature which has been calculated by dividing the 1 meter coax power measurements by the thru-connector measurements. In Figure 8 the transmission coefficient of the 1 m coax at 300K is about 0.85, or 0.7 dB of insertion loss. This agrees with the losses specified by the vendor: we used RG405 (0.085" semi-rigid copper cable), which has a specified loss of 22 dB/ 100 ft, or 0.72 dB/ meter [Pasternack Inc. catalog #2002, pp187]. These losses also agree with theoretical series resistance losses for copper that can be calculated with the parameters and equations presented in Table 3: these calculations predict a loss, L, of 15.8 %, or a transmission coefficient of 0.842.

From Table 3 we also note that series losses change in proportion to the square root of the bulk copper resistance. The bulk resistivity of copper is 1.7e-8 ohm-m at 20 C, and changes by about 3900 ppm/C near room temperature [Jordan, 1988]. We can therefore anticipate that the RF losses of coaxial cable will exhibit a sensitivity of 1950 ppm/C (= 3900 / 2). For the 1 meter length of coax with 15.8 % loss, the thermal sensitivity in the transmission coefficient should therefore be about -366 ppm/C (= 1950 ppm/C * 0.15/0.85), which is about 100 ppm/C higher than the measured coefficient of -269 ppm/C.

We should note that none of these tests take into account standing waves which undoubtedly exist in the test cables. These will change the insertion loss of the cables as the cables expand or contract with temperature. At this time I believe that these effects are below the 100 ppm/C level. One data point for this error estimate is the 100 ppm/C difference between the theoretical and measured coefficients. Also, from Table 2, the -158 ppm/C figure is about 70 ppm/C higher than expected: if -269 ppm/C the correct coefficient for the 1 meter cable, then we would have expected 0.61 * 0.5 * -269 = -82 ppm/C for the test cables, where 0.61 is the total length of the test cables in meters and 0.5 is an approximate weighting to account for the fact that only one end of each cable changes in temperature.

frequency	f: 1.4 GHz
copper bulk resistivity at 20C	R_o: 1.7 x 10^{-8} ohm-m
skin depth	δ: $\sqrt{\frac{R_o}{\pi f \mu_o}}$
surface resistivity	R_m: R_o/δ ohm-square
RG405 center conductor diameter	a: 255 um
RG405 shield inner diameter	b: 825 um
coaxial series resistance	R: $\frac{R_m}{2\pi}\left(\frac{2}{a}+\frac{2}{b}\right)$
characteristic impedance	Z_c: 50 ohm
power loss per unit length	L: R/Z_c

Table 3: equations and parameters used to calculate coaxial losses (neglecting dielectric loss) [from Collin, 1966].

2.6- Summary of noise diode test results:

Table 4 provides a summary and revised estimates of the noise diode and coupler sensitivities which combines the coaxial data with the noise diode data from the previous sections. Details of the coaxial cable corrections are provided in the Table, and sensitivities have been adjusted either upwards or downwards depending on whether the noise diode under test or the reference noise diode, respectively, were affected by variable coaxial losses. Table 4 also includes some additional 'heat-gun' measurements of noise diode-B at bias currents of 6 and 8 mA which were not reported in the previous section.

Noise diode-A:	ND+ coupler (ppm/C)	coupler (ppm/C)	ND alone (ppm/C)
Dual-plate test from Fig.7a; subtracted 180 ppm/C for reference noise diode (-60 ppm for 12" coax between plates, -120 ppm for approximately 12" total length coax on primary TEC):			
Heat-gun test from Fig.4d; added 30ppm/C for 6" coax:	1670		1030
Noise diode B:			
TEC element test of Fig.3a; negligible coax loss; 4mA:	1960		
TEC element test of Fig.3b; negligible coax loss; 6mA:	1720		
TEC element test of Fig.3c; negligible coax loss; 8mA:	1840		
Heat-gun test of Fig.4b; +30 ppm/C for 6"coax; 4mA:			970
Heat-gun test; +30 ppm/C for 6"coax; 6mA:			960
Heat-gun test; +30 ppm/C for 6"coax; 8mA:			1000
Heat gun test of Fig 5a; +60 ppm for 2x 6" coax:		490	
Dual plate test of Fig.7b; -60ppm/C for 12" coax; 6mA:	1370		
Noise Diode C:			
TEC element test of Fig.2c; added 60 ppm for 12" coax following coupler:	820		
Heat-gun test of Fig.4c; added 30 ppm/C for 6" coax:			430
Dual plate test of Fig. 7c; added 60 ppm/C for 12" coax:	920		
Dual plate test of Fig. 7d; added 60 ppm/C for 12" coax:			360
Difference of Figs 7c and 7d (identical test conditions):		560	

Table 4: Summary and revised estimates of noise diode and coupler thermal sensitivity tests; all sensitivity are with respect to noise diode output power near an ambient temperature of 296 K.

3. RADIOMETRIC TESTS

The two-plate configuration was used in December to test the system's radiometric performance. For these tests noise diode-C was placed on the secondary TEC plate together with a 20 dB pad. The pad replaced the 20 dB coupler and antenna load of Figure 1. Following some initial debugging- which included hardware modifications to shield the pin diode Dicke switch from radio interference- the testbed was run continuously for two weeks. Through these two weeks, a variety of thermal tests were programmed into the two TEC's for the purpose of calibrating the noise diodes and determining the stability of the system. The time history of the temperatures are plotted in Figure 9a. The tests of Figure 9a include: slow sweeps of the primary TEC (from 18 to 30 hours on the time scale of Figure 9a- also see Figure 6 for expanded time scale), sweeps of the secondary TEC (30 to 42 hours), abrupt 5 degree steps of the TEC's for examining time dependant gradients (65 to 90 hours- also see Figure 9b); a long period where the secondary plate was held at 70 C (110 to 250 hours); and several periods in which both plates were held at a constant 23 C.

The performance of the primary TEC controller is illustrated in Figures 9b through 9e. These figures plot the temperatures within the primary TEC measured by thermistors which were all within about 6 inches of the plate center. Figure 9b expands the scale from Figure 9a during the temperature 'steps', and shows how the various components respond faster or slower than others. Figure 9c illustrates the magnitude of gradients induced by the temperature steps by plotting the difference between the temperatures of Figure 9b and the reference load of the Dicke switch. These represent the worst case gradients during these tests. Figure 9d and 9e show the 'best case' stability of the temperatures and of the gradients, respectively, during a period when the TEC was programmed to hold a 'constant' 23 C. As shown, the primary TEC is only stable to about 0.5 C peak to peak, and gradients are nearly as large- varying by up to 0.3 C peak to peak.

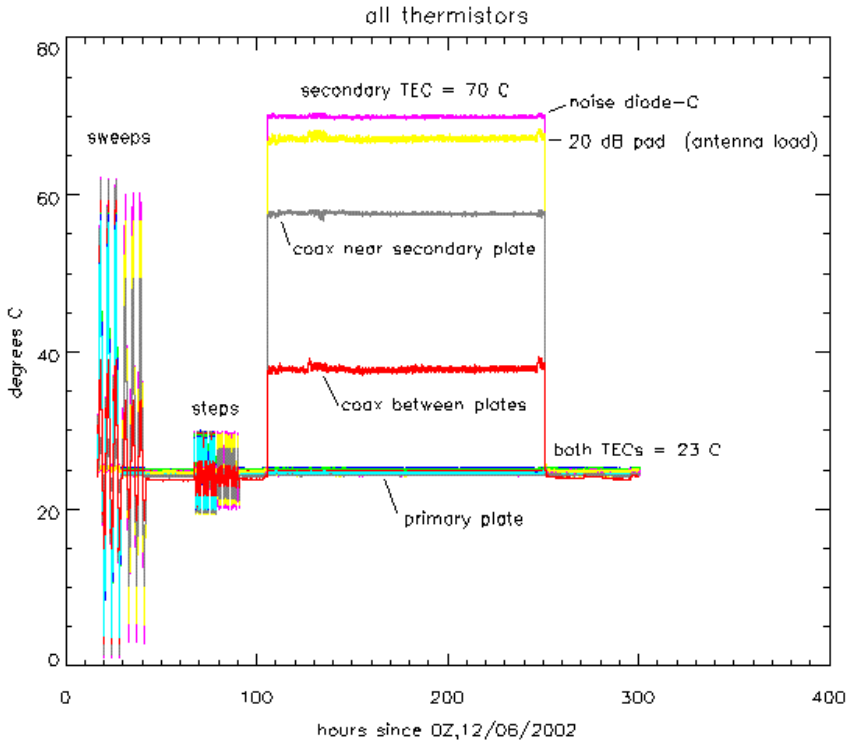

Figure 9a: Temperature record for recent tests lasting two weeks

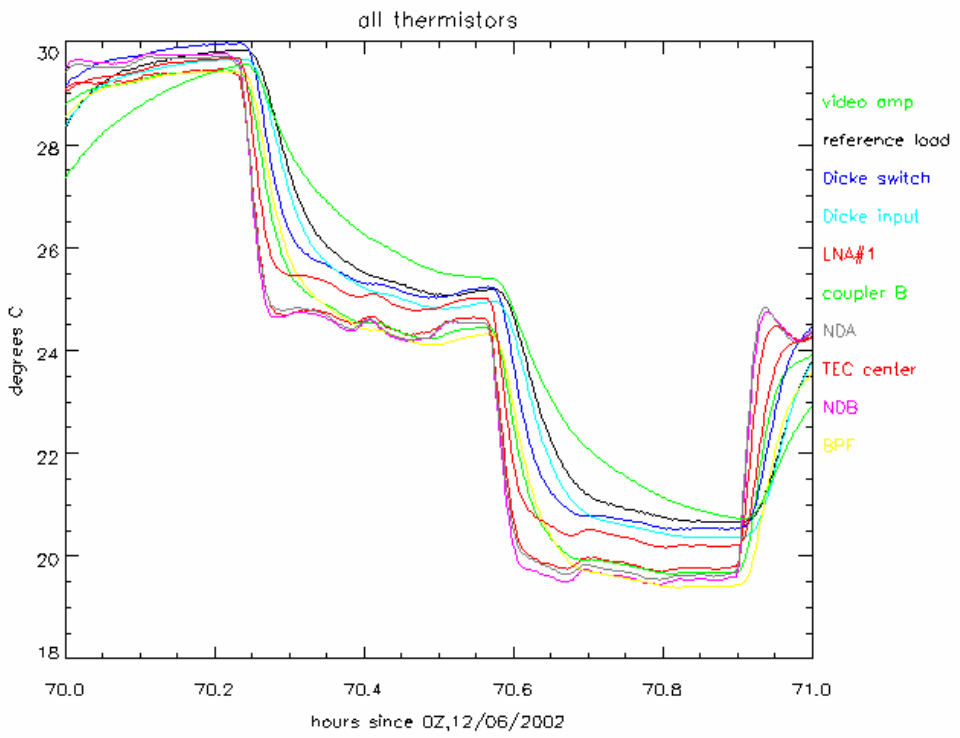

Figure 9b: Expanded scale during temperature 'steps' of the primary TEC.

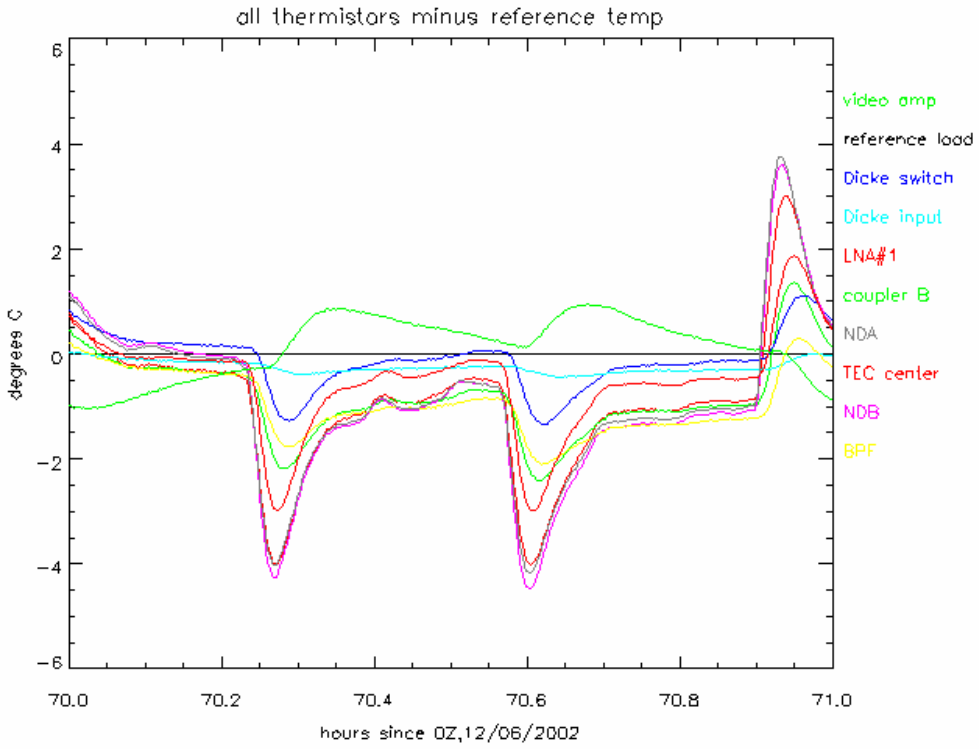

Figure 9c: Differences between reference load and other temperatures from Figure 9b.

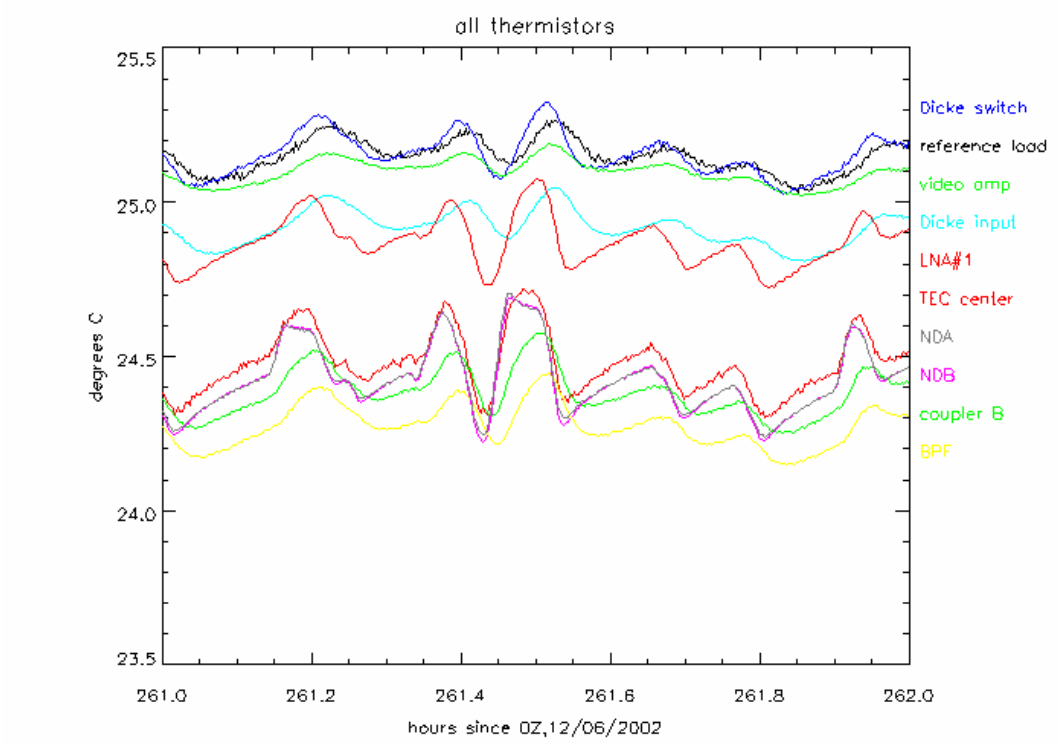

Figure 9d: expanded scale of primary TEC temperatures while holding 'constant' 23C.

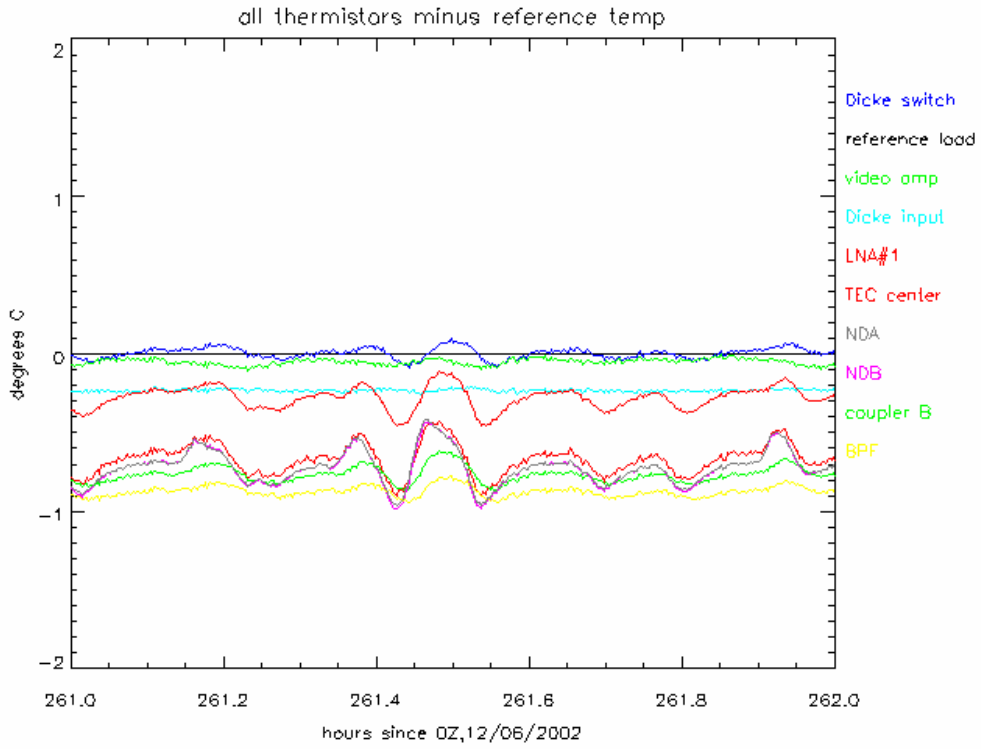

Figure 9e- Differences between reference temperature and temperatures from Figure 9d.

3.1- Null offset measurements:

Data from both the AD650 and AD652 V/F converters were collected in all 10 measurement modes of Table 1. These include null offset measurements which have been plotted in Figure 10a thru 10c. Figures 10a plots the null offset signal which has been scaled to degrees Kelvin of brightness temperature using a preliminary calibration. 10-second boxcar averages apply, and the mean offsets have been subtracted. In both cases the null offset noise of Figure 10a are significant at about the 0.1 to 0.5 K level when the temperature of the system is stable. Evidently, the stability is much worse when the physical temperature of the video amplifiers fluctuate (near 20 and 70 hours).

Figure 10b compares the spectra of the AD650 data from Figure 10a with the theoretical 1/f noise of the OP-37 video amplifiers. The theoretical noise has been extrapolated from a specified voltage spectral density of 5 nV/root(Hz) at 1 Hz. Figure 10b shows that the noise is consistent with the theoretical limits of the amplifier. Similar results can be shown for the AD652 detector/digitizer[3].

The testbed system collects null offset measurements in both the antenna mode and the reference mode (as in Table 1). Figure 10c plots the difference between the antenna-mode and reference mode null offset measurements for each of the detector/digitizers. The null offset will be subtracted from all other measurement cycles in the same manner, so these differences reflect the effective detector/digitizer noise performance for the system. Neither of the traces in Figure 10c are identically zero because: (1) there is a slight leakage of the RF signal through the null switch of Figure 1 (the switch isolation is 34dB, which accounts for the 0.02K steps at 100 and 250 hours when the antenna noise temperature was changed from 23 C to 70 C and back again); (2) there is quantization noise (which accounts for the high frequency noise- the AD650 is better than the AD652 because of the way the frequencies are measured); and (3) there is back-end RFI leakage from the data system into the video amplifiers which changes synchronously with the TTL control signal of the Dicke switch (this accounts for the DC offsets of about +/- 0.02K in the two traces of Figure 10c). Overall, the data of Figures 10c indicate that, after subtracting the null offset, the AD650 digitized data are reliable to about 0.02K over a wide temperature range.

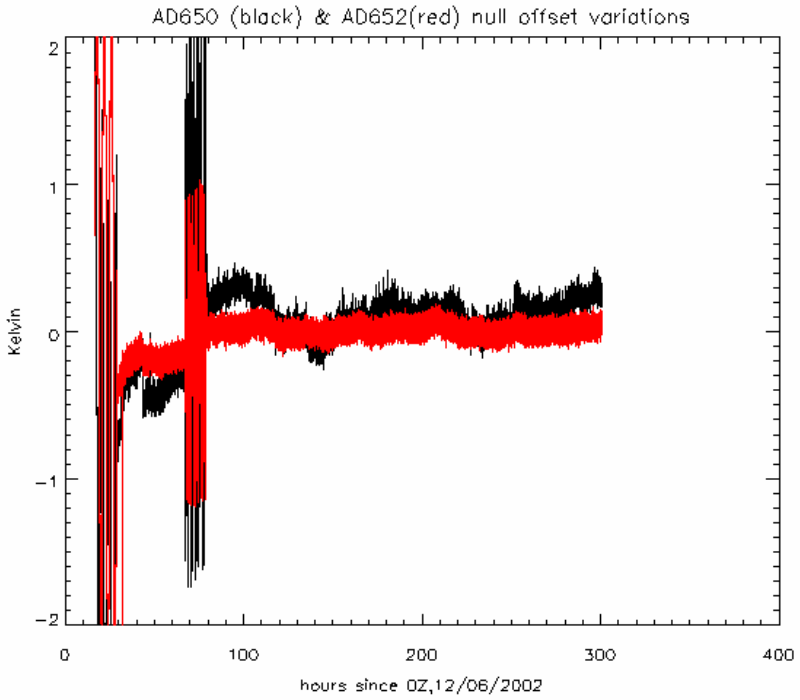

Figure 10a: Null offset fluctuations for the two detector/digitizer circuits.

[3] The Kelvin scale of Figure 10a were scaled to detector voltages for Figure 10b with the following factors: 0.36 μv/K (AD650) and 1.1 μv/K (AD652). These factors differ for two reasons: (1) the AD650 detector is operated at an RF power level 4 dB lower (0.4 times lower) than the AD652, and (2) the AD650 circuit loads the detector with 100 ohms, versus 2000 ohms for the AD652 circuit.

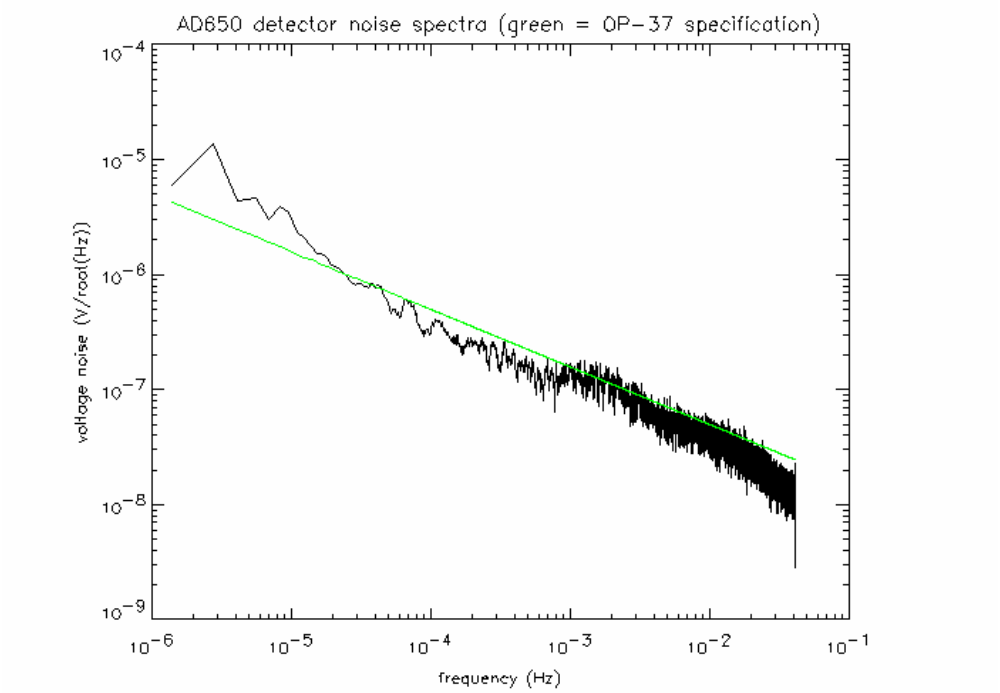

Figure 10b: Spectra from Figure 10a (excluding 0-100 hours) compared to OP-37 specification.

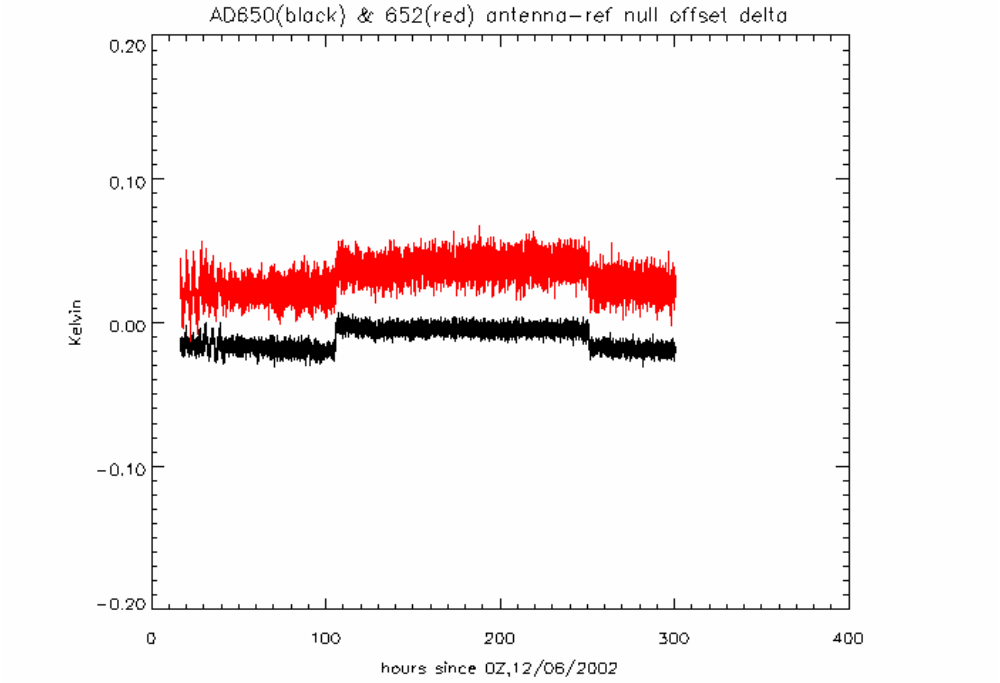

Figure 10c: Difference between antenna and reference mode null offset measurements.

3.2- Gain measurements:

The pre-calibrated normalized gain of the testbed system versus baseplate temperature is plotted in Figure 11a. The gain variations of Figure 11 were measured using diode-C on the secondary plate as the primary TEC was varied in temperature. Data were normalized by the mean value of the deflections according to

$$g_{normal} = \frac{V_{ANC} - V_A}{\langle V_{ANC} - V_A \rangle}. \quad (2)$$

where V_{ANC} is the response to noise diode-C in the antenna mode of the Dicke switch, V_A is the response to the antenna lode without the noise diode, and <> is the expectation operator. As can be seen, the gain of the system versus baseplate temperature is well correlated, with a slope of -7250 ppm/C. This slope is dominated by the RF amplifier sensitivities, which are known to have a large negative gain versus temperature slope.

Figure 11b plots the spectral density of normalized gain fluctuations based on data collected between 260 hours and 300 hours of Figure 9a when both TEC's where programmed for a constant 23 C. Several spectra are plotted: the black trace is based on the gain measurements provided by noise diodes (as in Equation 2, and averaged over all noise diodes); the blue trace was derived from the measured baseplate temperature using the gain versus temperature sensitivity of Figure 11a, as in

$$g = 1 - 0.00725 * (T_{baseplate} - < T_{baseplate} >); \quad (3)$$

and the green trace of Figure 11b is the spectrum of the ratio of the noise diode and temperature-fit gain estimates (i.e. divide Equation 2 by Equation 3). The red line is a reference level corresponding to a spectral density of $10^{-9}/f$. As can be seen, the gain predicted by a fit to the baseplate temperature matches the noise diode deflections very well- particularly near 2 millihertz (mHz). The TEC controllers are known to oscillate with an amplitude of about 0.3K over a period of about 500 seconds, which accounts for the spectral peak near 2 mHz. Above 10 mHz the noise diode deflection measurements exhibit a higher noise than the thermistor-fit data due to the 30 MHz detection bandwidth. If the noise diodes are perfect, and if the temperature fit is perfect, then the green trace below 10 mHz represents the 1/f noise of the radiometer's receiver chain (including RF amplifiers and the detector). This spectrum fits a trend of about $\sqrt{2x10^{-9}/f}$ (gain/$\sqrt{Hz}$) near 1 millihertz. For reference, the gain of the AWVR radiometers- which operate near 30 GHz and have a much more precise temperature control- have a 1/f spectrum of $\sqrt{0.8x10^{-9}/f}$ (gain/$\sqrt{Hz}$). These numbers are important because they will determine the optimum timing and duty cycles for the radiometer.

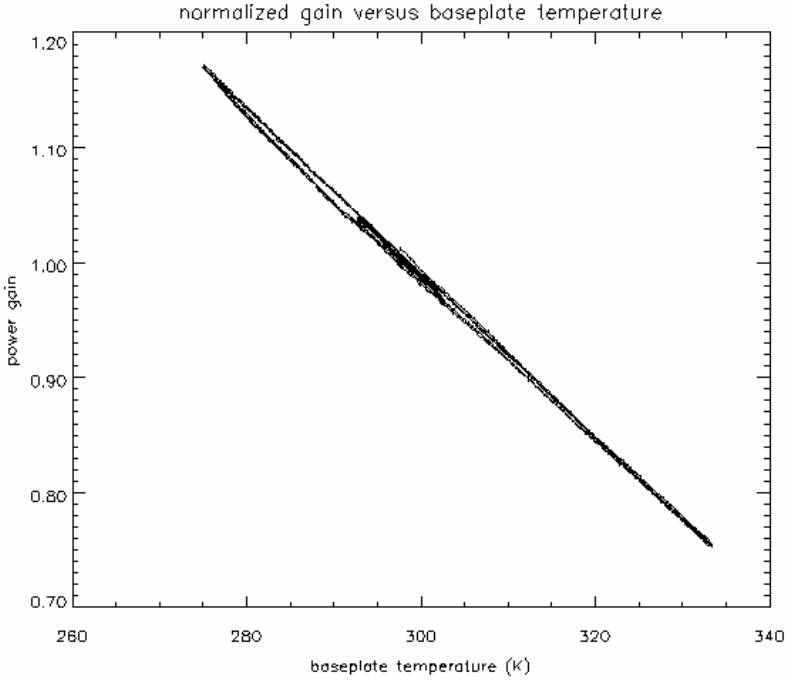

Figure 11a: pre-calibrated gain versus baseplate temperature; slope: -7250 ppm/C.

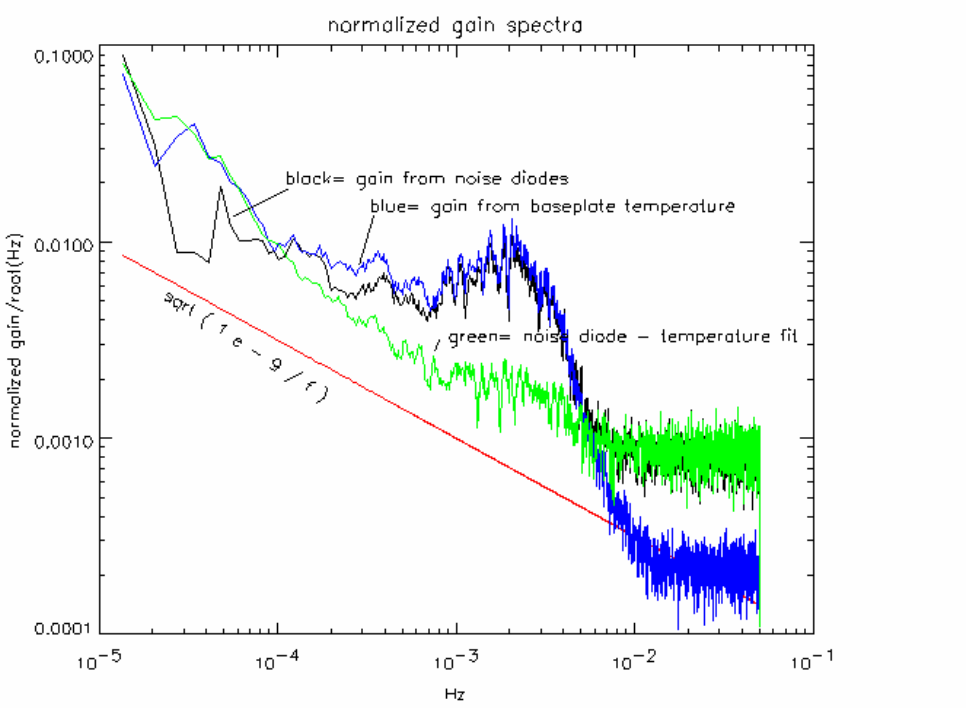

Figure 11b: Spectra of pre-calibrated gain as the system is held at a 'constant' 23C.

Figure 11c plots several estimates of the post-calibration normalized gain errors. These represent the stability of the system after calibrating the gain with the noise diode deflections. These errors have been estimated by three methods: (1) the noise diode-A versus noise diode-B deflection ratio, as in Equation 1; (2) the noise diode-B temperature coefficient of 1600 ppm/C from Table 4, which was applied to the noise diode temperature to produce an error estimate in the same manner as Equation 3; and (3) the normalized ratio of noise diode versus reference-load gain estimates computed from

$$D_{N/R} = \frac{g_{noisediode}}{g_{referenceload}} \Bigg/ \left\langle \frac{g_{noisediode}}{g_{referenceload}} \right\rangle \tag{4}$$

where $g_{noisediode}$ is the gain measured by the noise diode deflections- as in Equation 2, but averaged over all available noise diode deflections- and $g_{referenceload}$ is the gain estimated from the reference load response, V_o, and an estimate of the system noise temperature according to

$$g_{referenceload} = \frac{V_o}{T_o + T_r} \tag{5}$$

where T_o is the reference-load temperature as measured with a thermistor, and T_r is an apriori estimate of the receiver noise temperature. As discussed below, the receiver noise of the system is about 225 K. Also, as stated in the previous section, it is implicit that the detector's null offset has been subtracted from the reference measurement.

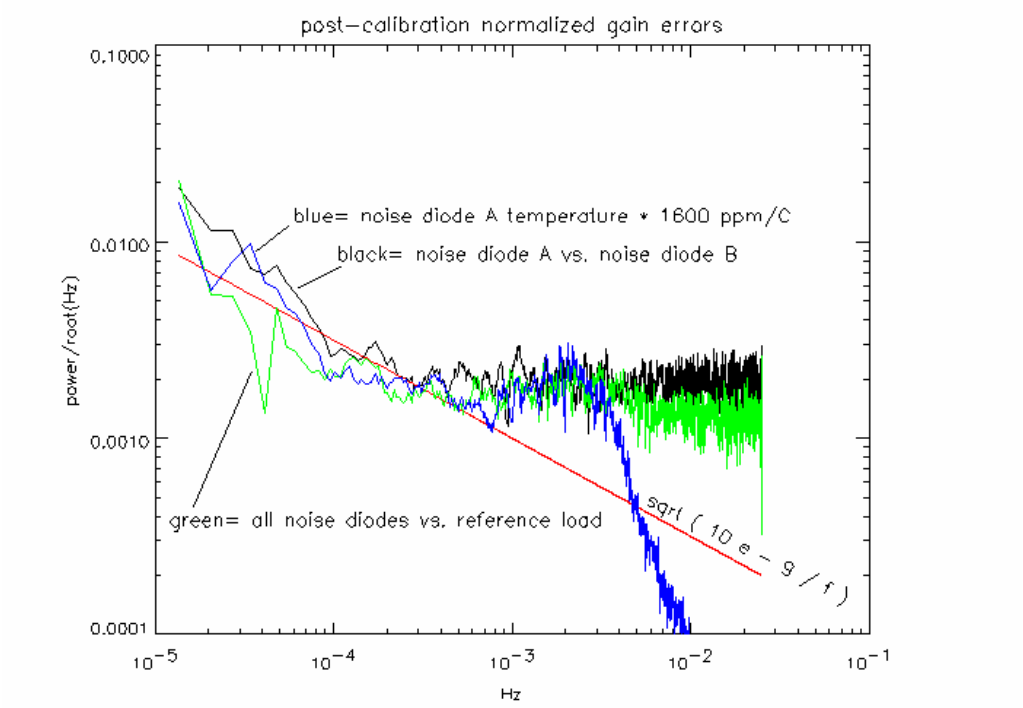

Figure 11c: Spectra of post-calibration gain errors estimated by various means.

In Figure 11c it is interesting to see that the errors estimated by comparing the noise diodes with the system noise temperature are in good agreement with the error estimates for the noise diodes. These data indicate that the system noise is about as stable- if not more stable- than the noise diodes. Note, however, that the noise diode performance indicated in Figure 11c is quite poor: at about $\sqrt{1\text{x}10^{-9}/\text{f}}$ (gain/$\sqrt{\text{Hz}}$), the 1/f noise is only about 2 times better than the uncalibrated receiver of Figure 11b. AWVR system noise 1/f spectrum, for reference, is near $\sqrt{3\text{x}10^{-11}/\text{f}}$ (normalized $T_s/\sqrt{\text{Hz}}$), so the these testbed gain data are at least 6 times less stable than the levels we hope to attain (so that we can apply long running averages to estimate T_r to reduce the NEDT of Aquarius, for example).

We should also note that the error estimates provided by the noise diode deflection ratio in Figure 11c may mask common-mode errors that we can expect if both noise diodes change in temperature together. In such a case we would expect to see that the errors derived from the 1600 ppm/C should be worse than errors observed in the deflection ratio. The fact that these two error estimates are about equal in Figure 11c suggests either that the noise diode temperature errors are not common-mode, or that other error sources- such as instability in the Dicke switch- may be raising the noise diode deflection errors. I have examined the first of these possibilities by computing a regression fit of the individual noise diode temperatures to their deflection ratios, and have found that the noise diode temperatures account for some of the deflection ratio errors. Another significant component of the noise diode deflection errors is drift.

Figure 12 plots an example of the noise diode deflection ratio deviations- in this case noise diode C/A- versus time along with a regression fit to the temperatures of the noise diodes and interconnecting components, and a single-term linear drift coefficient. A 3000 second boxcar average has been applied to Figure 12. In Figure 12 the 'fit' evidently matches the deflection ratio data quite well, and the residual errors (green) look like white noise. The fit coefficients- computed by linear regression of the 'stable' temperature data between 260 and 300 hours- are summarized in Table 5 for all three noise diode deflection ratio combinations.

The noise diode temperature coefficients associated with the C/A or C/B deflection ratios of Table 5 are in good agreement with the sensitivities of Table 4. The coefficients derived from the noise diode A/B deflection ratio, on the other hand, are suspect because their temperatures are tightly coupled (noise diodes A and B happen to be

mounted very close together on the primary TEC plate). In Table 5 we also see that the temperature coefficients associated with the Dicke switch are reasonably consistent between the noise diode B/A and C/A fits; both are roughly -250 ppm/C, which indicates that the Dicke switch loss increases slightly with temperature. The Dicke switch temperature can also be associated with the coaxial cables that connect between the couplers for noise diodes A and B; with a total length of about 1 foot, and based on the tests of the previous section, these cables may contribute about -120 ppm/C to the -250 ppm/C coefficient attributed to the Dicke switch. The temperature coefficients in Table 5 listed for the coaxial cable refer to the 1-foot cable that connects noise diode-C on the secondary TEC plate to the coupler of noise diode-B on the primary plate. These coefficients are inconsistent between the C/A and C/B fit, but they are also quite small, and they are insignificant contributors to the errors of Figure 12.

Figure 13 and Table 6 present similar results to those of Figure 12 and Table 5 for data collected during the stepped temperature experiments near 80 hours in Figure 9a. In Figure 13, from 64 to 78 hours the primary TEC plate was stepped up and down in 5 degree increment, as in Figure 9b, in order to produce the maximum possible gradients, as in Figure 9c. From 78 to 80 hours the secondary plate was stepped in the same manner. The effects on the noise diode C/A deflection ratio in Figure 13 are apparent. In Figure 13 we also see that the fit has greatly reduced the transient errors. Furthermore, the fit coefficients of Table 6 are in good agreement with those of Table 5. Inconsistencies between Table 5 and 6 include the drift coefficients- which have evidently been thrown off in Figure 13 by an unexplained change between the deflection ratios before and after the stepping experiments (black trace). Also, the coaxial cable coefficients of Table 6 have become somewhat larger- and now have opposite signs from those of Table 5.

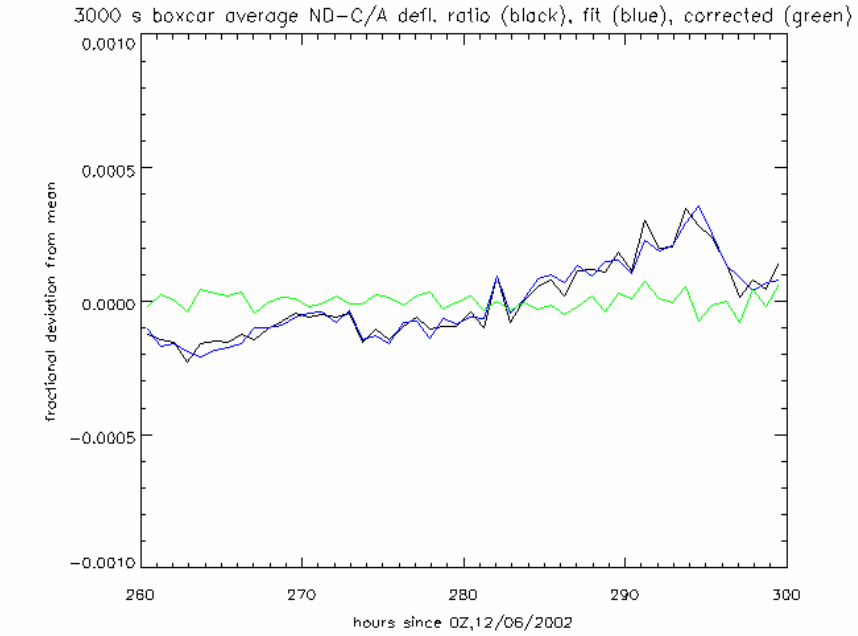

Figure 12: Deflection ratio and fit using coefficients from Table 5 for 'constant' 23C data.

```
NDC/B deflection ratio:
                    NDC, NDB temperatures(ppm/C):  353  -1483
                             drift rate (ppm/hr):  17.0
                         coax temperature (ppm/C):  47

NDC/A deflection ratio:
                     NDC, NDA temperatures (ppm/C):  400  -1752
                             drift rate (ppm/hr):  9.6
          coax, Dicke switch temperatures(ppm/C):  86   -249

NDB/A deflection ratio:
                   NDB, NDA temperatures  (ppm/C): 1057  -1397
                             drift rate (ppm/hr): -7.5
                Dicke switch temperature (ppm/C): -278
```

Table 5: Temperature coefficients and drift rates derived from 'constant' 23C deflection ratios between 260 and 300 hours of Figure 9a. These coefficients were computed by linear regressions of the noise diode deflection ratios to the above temperatures and to time; no constraints were applied, and in the case of the noise diode B/A deflection ratio, the temperatures were too well correlated to isolate the correct noise diode temperature coefficients.

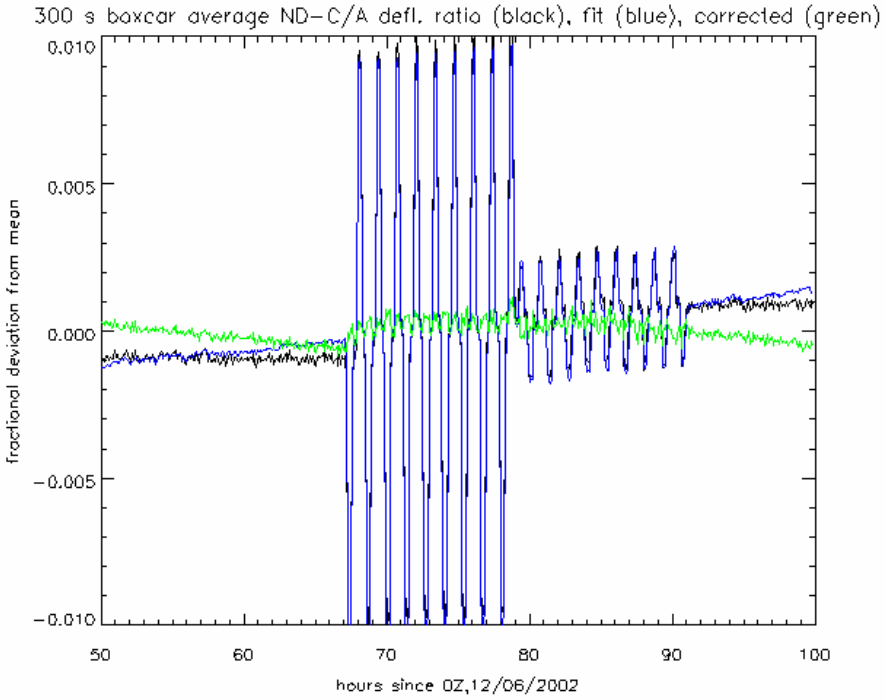

Figure 13: Noise diode C/A Deflection ratio and temperature fit during 'steps'

```
NDC/B deflection ratio:
                    NDC, NDB temperatures(ppm/C): 447 -1506
                             drift rate (ppm/hr):  15
                         coax temperature (ppm/C): -175

NDC/A deflection ratio:
                     NDC, NDA temperatures (ppm/C): 333 -1677
                             drift rate (ppm/hr):  54
          coax, Dicke switch temperatures(ppm/C): 349  -459

NDB/A deflection ratio:
                   NDB, NDA temperatures  (ppm/C): -2086 1976
                             drift rate (ppm/hr):  40
                Dicke switch temperature (ppm/C): -226
```

Table 6: Temperature coefficients and drift rates derived from 'stepped' temperatures between 50 and 100 hours of Figure 9a (also see Figures 9b and 9c and 13).

The consistency of the above results over a variety of test conditions indicate that a noise diode temperature correction can be applied to improve post-calibration gain stability. Figure 14 presents a revised set of gain stability estimates based on linearly de-trended and temperature corrected noise diode deflections. The spectra of the three noise diode deflection ratios (i.e. C/A, C/B, and B/A) are plotted in green in Figure 14, and the temperature correction formula which apply are presented in Table 7. Figure 14 also presents a revised spectrum of the difference of noise diode and reference load gain measurements after a similar de-trending and a temperature fit to the low noise amplifier (LNA) and Dicke switch temperatures. The last equation in Table 7 provides the regression formula for system noise temperature. In each equation of Table 7 the choice of thermistor temperatures has been reduced to a minimum significant set based on the consistency of results presented earlier. Note that the Dicke switch temperature coefficient of 250 ppm/C has been included with formula for the noise diode-A to negate variable losses in the Dicke switch. The coaxial cable temperature, on the other hand, has been neglected due to the inconsistencies noted earlier. The Dicke switch coefficient of 290 ppm/C appears in the regression fit for system noise temperature, and agrees nicely with the 250 ppm/C coefficient estimated above. The remaining coefficient of 1930 ppm/C assigned to the LNA temperature, and the method by which the absolute noise temperatures were calibrated, will be discussed below.

From Figure 14 we see that the 1/f noise associated with the corrected noise diode deflections is not detectable compared to the white noise. The minimum detectable 1/f noise is about $\sqrt{1\text{x}10^{-10}/\text{f}}$, and evidently the noise diode estimated gain errors are below this level. The system noise temperature error is just barely detectable at low frequencies, and is roughly equal to the $\sqrt{1\text{x}10^{-10}/\text{f}}$ level (neglecting the lowest frequency data point- which is statistically insignificant). This is an encouraging result since it shows that we are near to the performance of the AWVR.

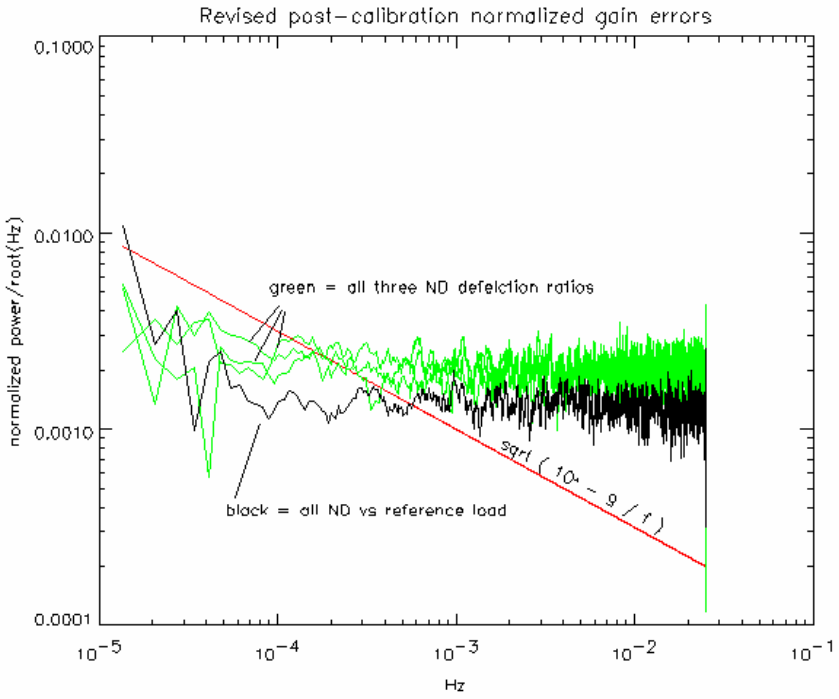

Figure 14: revised gain error estimates after applying coefficients of Table 7.

Corrected Noise Diode-A Deflection:

$$d_{ANA} = (V_{ANA} - V_A)[1 - 1.7\times10^{-3} (T_{NA} - 298) - 0.25\times10^{-3} (T_{Dicke} - 298)]$$

Corrected Noise Diode-B Deflection:

$$d_{ANB} = (V_{ANB} - V_A)[1 - 1.55\times10^{-3} (T_{NB} - 298)]$$

Corrected Noise Diode-C Deflection:

$$d_{ANC} = (V_{ANC} - V_A)[1 - 0.4\times10^{-3} (T_{NC} - 298)]$$

System noise temperature (Dicke switch in reference mode):

$$T_{sys} = (225. + T_o)[1 + 1.98\times10^{-3} (T_{LNA} - 298) + 0.29\times10^{-3} (T_{Dicke} - 298)]$$

Table 7: temperature coefficients and equation used to revise the post-calibration gain errors of Figure 14; V_{ANA}, V_{ANB}, V_{ANC}, are the detected responses to noise diodes in the antenna mode of the Dicke switch; V_A is the response to the antenna with no noise diodes; T_{sys}, is referenced to the antenna port of the radiometer; T_{NA}, T_{NB}, T_{NC}, T_o, T_{LNA}, and T_{Dicke}, are thermistor temperatures (in Kelvin); and a nominal baseplate temperature of 298 K is subtracted from each thermistor.

3.3- Receiver noise temperature measurements:

Receiver noise is measured in the reference mode of the Dicke switch with

$$T_R = \frac{V_o}{g_{noisediode}} - T_o \tag{7}$$

or in the antenna mode with

$$T_R = \frac{V_A}{g_{noisediode}} - T_A \tag{8}$$

where $g_{noisediode}$ is the gain of the system as calibrated with the noise diodes. When the primary TEC is stable, noise diodes A and B are used to compute gain according to

$$g_{noisediode} = \frac{d_{ANA} + d_{ANB} + d_{oNA}}{T_{ANA} + T_{ANB} + T_{oNA}} \tag{9}$$

where d_{yNx} is the corrected noise diode deflection, from Table 7, for noise diode 'x' (= A, B, or C) in the 'y' mode of the Dicke switch (y=A for antenna or y=o for reference), and T_{yNx} is a corresponding estimate of the effective noise diode noise temperature. Noise diode-A is used twice since it is injected after the Dicke switch. Noise diode-C is used to estimate gain in cases where the primary TEC changes in temperature and the secondary TEC is constant 23 C, as in

$$g_{noisediode} = \frac{d_{ANC}}{T_{ANC}}. \tag{10}$$

The noise diode noise temperatures, T_{yNx}, of the testbed is calibrated by linear regression against the antenna load temperature, as discussed in the next section.

Figure 15a plots the receiver noise measured in both modes of the Dicke switch during the tests of Figure 9a using Equations 7 and 8. As can be seen in Figure 15a, the receiver noise changes when the primary TEC changes. Figure 15b plots the receiver noise versus LNA temperature to show these changes. Figure 15a also shows a small jump in the receiver noise at 90 hours that is probably related to the same discontinuity observed in Figure 13. There is also a small and unexplained offset between the antenna and reference mode noise temperatures.

Figure 15b indicates that the receiver noise temperature is tightly coupled to the temperature of the LNA. Similar scatter plots versus other temperatures in the testbed can be produced, but none show such a good correlation as Figure 15b. A variety of multi-temperature linear regressions have been tested, and results indicate that minor improvements can be made when the LNA temperature is combined with the Dicke switch temperature. A regression over the entire 300 hour data set of Figure 15a results in the following Equation:

$$T_R = 223.984 + 0.0043t + 0.129(T_{Dicke} - 298) + 1.264(T_{LNA} - 298) \tag{11}$$

where t is time in hours from Figure 15a, and T_{Dicke} and T_{LNA} are the Dicke switch and LNA temperatures in Kelvin. Figure 15c plots the residual errors which remain after subtracting the predicted receiver noise of Equation 11 from the measured receiver noise of Figure 15a. Errors are plotted versus LNA temperature, and on this scale we see a significant nonlinearity with temperature. We also see that the offset between antenna and reference mode data increases at lower temperatures; this error can be traced to noise diode calibration errors, as discussed in the next section. Figure 15c also shows a 'spike' in the antenna-mode data (green) near 298 K which is caused by those segments of the data set in which the secondary TEC was scanned.

Equation 11 is largely redundant with the system noise temperature expression that was provided in Table 7. The only differences are the choice of units and the fact that Equation 11 was derived from a larger data set than Table 7. Table 7 was based on the last 40 hours as the TEC's were held relatively constant. If we neglect the drift coefficient and scale the coefficients of Table 7 (ppm/C of system temperature) to those of Equation 11 (K/K), we get

$$T_R = 225 + 0.15(T_{Dicke} - 298) + 1.03(T_{LNA} - 298) \tag{12}$$

Equation 12 is in good agreement with Equation 11, and actually results in a better temperature correction by removing the slope near T_{LNA}=298 K in Figure 15c.

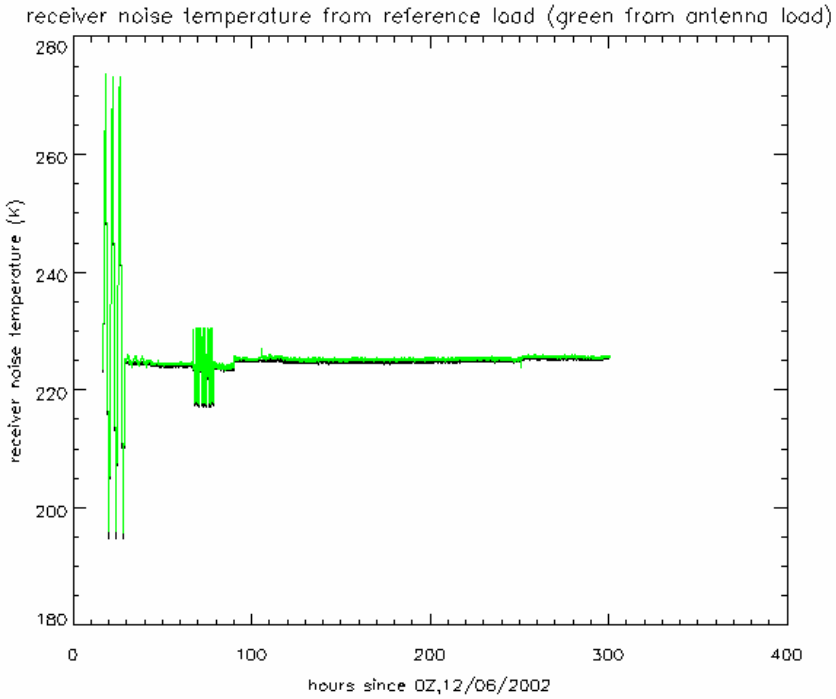

Figure 15a: Receiver noise temperature.

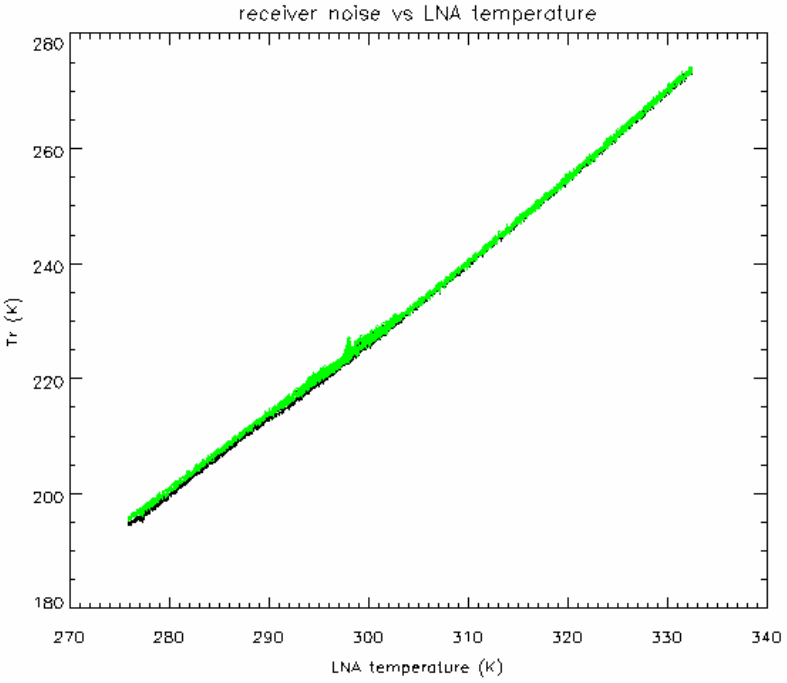

Figure 15b: Receiver noise temperature versus temperature of LNA; slope=1.4 K/K.

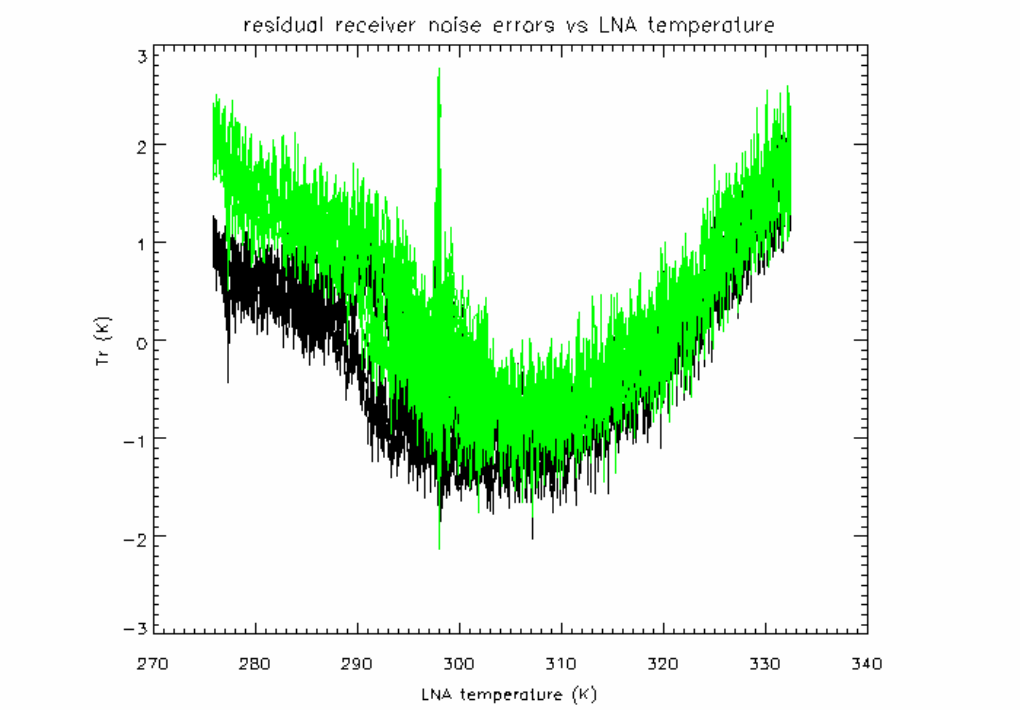

Figure 15c: Residual errors after subtracting the fit of Equation 11.

3.4- Calibrated brightness temperatures:

In the simplest mode of operation the brightness temperatures are calculated with the following equation:

$$T_B = T_o - \frac{V_o - V_A}{g_{noisediode}} \tag{13}$$

where T_o is the reference load temperature of the Dicke switch as measured with a thermistor, V_o is the detected response to the reference load, V_A, is the response to the 'antenna' (in this case the load on the secondary plate), and $g_{noisediode}$ is the gain derived from noise diode deflections according to equations 9 and 10. The effective noise temperatures of the noise diodes in Equations 9 and 10 is calculated by linear regression of the brightness temperature of Equation 13 with the thermistor sensed antenna load temperature. The antenna load consists of a 20 dB pad located on the secondary TEC plate. This pad is connected between noise diode-C and the 12 inch coaxial cable that leads to the thru-arm of the noise diode-B coupler located on the primary TEC plate (as mentioned above, the bandpass filter of Figure 1 was not included in these tests). Table 8 summarizes the noise diode noise temperatures estimated from regressions fits to the antenna temperatures for several selected time spans. Each of the selected time spans correspond to segments in Figure 9a with a sufficient range of antenna load temperatures to perform the regression: the first segment from 10 to 65 hours uses data where the antenna temperature was swept repeatedly between 0 and 60 C, whereas the two subsequent segments, of 90-120 hours and 200-300 hours, use temperatures that stepped between 23 and 70 C. The last column of Table 8 is based on a regression against all 300 hours of data. In all cases the linear regressions simultaneously compute noise diode temperatures and a constant offset between the radiometric temperature and the thermistor temperature, which are included in Table 8.

Variations in Table 8 between the different time intervals reflect the reliability of the noise diode temperature calibrations. The largest anomaly in Table 8 is the approximate 1 % increase in all three noise diode temperatures that occurs between the first two columns; these errors may be related to dynamic differences associated with the continuously swept antenna temperature versus a single step from 23 C to 70 C. The differences between the second and third column, both of which are based on a step between 23 C and 70 C, are not as large, but they are also not as consistent among the three noise diodes: note that noise diodes A and B increase by about 0.3 % while noise diode-C decreases by 0.2 %. Some of these changes can be traced to a long term drift in the system that that may be

caused by a slow change in the 12 inch coaxial cable that connects the two TEC plates. Evidence for this drift will be will be presented below.

In all the regressions of Table 8 the offsets indicates that the radiometric temperature was persistently about 0.35 C higher than the thermistor sensed temperature. As discussed below, I expect that a combination of measurement errors related to temperature gradients near the matched loads, thermistor calibration errors, and possibly errors in the balance of the Dicke switch can account for these offsets. I have examined and eliminated one other possibility, which is that residual noise passed from noise diode-C through the 20 dB pad may be biasing the antenna temperature upwards. If noise diode-C were to produce an off-mode noise temperature 35 K above ambient, this would account for the 0.35 K bias when the 20 dB pad is installed. To test this I removed the 20 dB pad and connected noise diode-C directly to the antenna port. This resulted in an increase of less than 0.1 K in the antenna brightness temperature above the ambient temperature of the noise diode, and thus rules out this potential error.

Time segment (hours):	10 - 65	90 - 120	200 - 300	10 - 300
T_{ANA}(K):	735.731	743.726	746.253	745.752
T_{ANB}(K):	741.005	750.096	752.481	751.976
T_{ANC}(K):	534.960	541.824	540.553	540.190
Thermistor-T_B offset(K):	-0.415	-0.359	-0.330	-0.361

Table 8: Noise diode noise temperatures based on calibrations from different intervals of Figure 9a.

Figure 16a plots the thermistor sensed 'antenna' temperature together with the radiometric measurements of Equation 13 using noise diode temperatures from the last column of Table 8 (which is the average of the entire data set). Figure 16b plots the difference between the thermistor and radiometric data of Figure 16a. The integration time used in these plots is 100 seconds. As can be seen, the worst errors occur when either of the two TEC's change in temperature. Upon close examination one can also see that the magnitude of the errors depend more on the rate of change, and less on the magnitude of change, of the TEC temperatures. Note that the errors near 20 hours and the errors near 70 hours have roughly the same magnitude of about 1 K peak to peak even though the magnitude of TEC modulation in Figure 9a differs greatly. The time scales for these intervals were expanded in Figures 6 and 9b, respectively, and one can see that both modulation schemes (sweeps and steps) resulted in comparable time-variable gradients of a few (about 2 ~ 4 C) degrees among the thermistors distributed around the primary TEC plate. These gradient-dependant errors can also be seen in Figure 16c, which expands the time scale of the radiometric errors to match the thermistor measurements of Figure 9b.

Fluctuations in the noise diode calibrated gain errors can not account for the brightness temperature errors observed in Figure 16b near 70 hours. From Figure 13 the corrected peak-to-peak gain modulation errors during the stepping experiments is about 0.1 %. When multiplied by the maximum difference between the antenna and reference load temperatures of 5 K, the gain modulation errors can only account for 0.005 K of brightness temperature modulation error in Figure 16c. Temperature dependant gain errors will only be significant when the antenna and reference load temperature difference is much larger. From Figure 10c we can also eliminate the possibility of back-end errors. This leads us to examine 'offset' errors that affect the radiative balance of the Dicke switch. Such errors include emission from lossy components with uneven temperatures, and temperature gradients near the reference and antenna loads that affect the thermistor measurements.

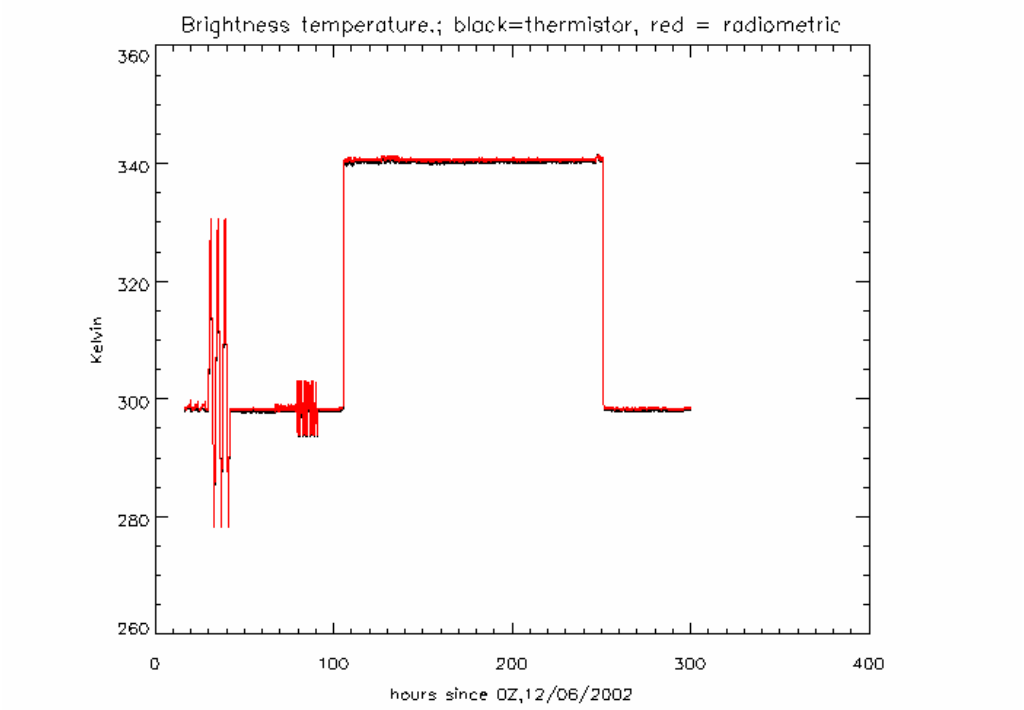

Figure 16a: Brightness temperatures as measured by the thermistor and the radiometer.

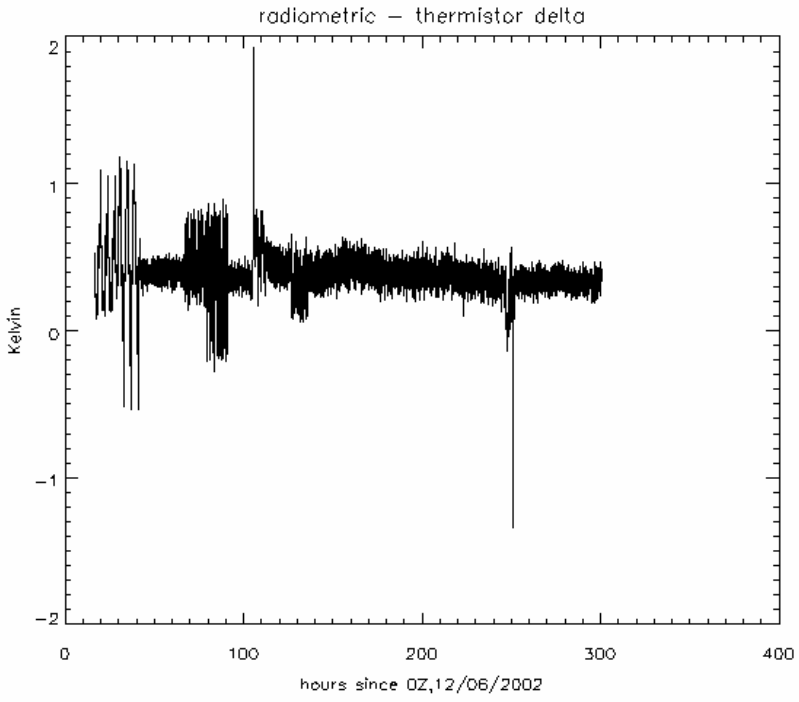

Figure 16b: Difference of radiometric and thermistor-sensed temperatures; 100 s integrations apply.

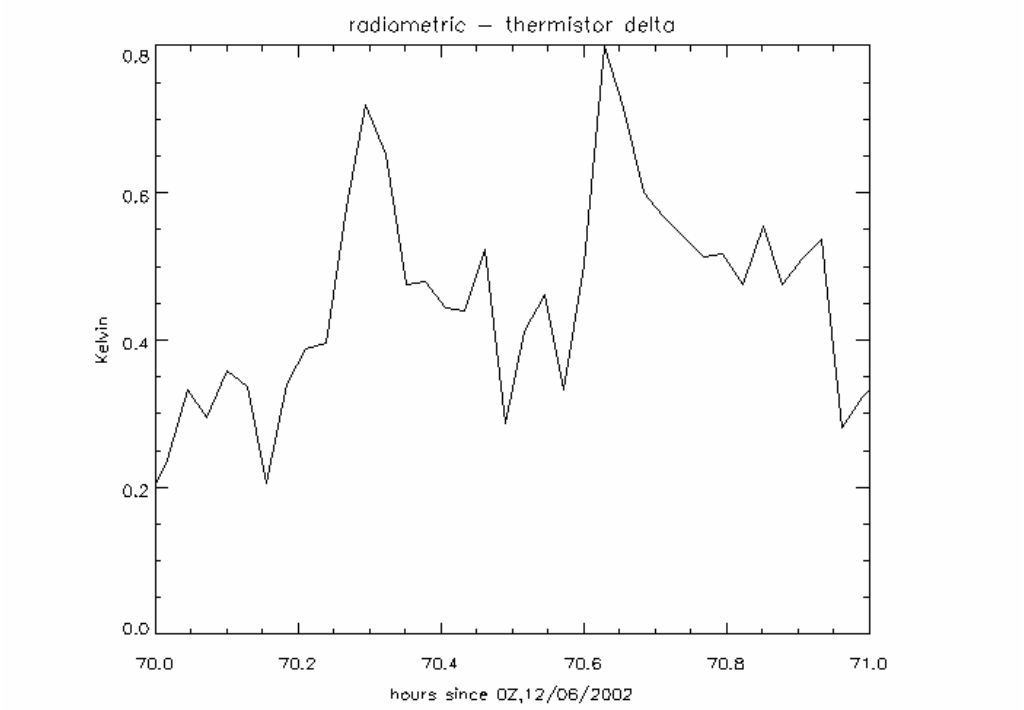

Figure 16c: expanded time scale of Figure 16b for comparison with Figure 9b.

Errors associated with temperature gradients among the lossy front-end components can be examined by performing linear regression of the radiometric errors in Figure 16b against the temperatures of Figure 9a. This analysis is motivated by the radiative transfer equation, which for small temperature perturbations can be reduced to:

$$T_E \equiv T_B - T_A \cong c_0 + \sum_{i=1}^{N} c_i T_i \qquad (14)$$

where T_E is the brightness temperature error of Figure 16b, computed from the difference of radiometric (T_B) and thermistor sensed (T_A) temperatures, c_0 is a fixed offset, and c_i is a coefficient to be applied to the respective thermistor temperature, T_i. Under ideal circumstances- if all the thermistors were accurate and if they completely described the radiometric errors- we would be able to further constrain Equation 14 by forcing c_0 to zero, and the sum of all c_i to zero so that radiative balance is achieved when all temperatures are equal to the reference load temperature. However, we will not enforce this constraint in order to accommodate a variety of factors, including thermistor calibration errors and gradients between the thermistors and the RF circuits. Equation 14 also neglects the fact that some of the losses are temperature dependant (the coaxial cable, for example). If we were to derive a detailed radiative transfer equation we would need to express losses as a function of temperature, and then compound these terms by the temperatures of the lossy components to estimate the emission and extinction of radiation throughout the front-end circuits. Such an equation would involve nonlinear terms which are not expressed in Equation 14. We do not yet have adequate knowledge of how losses change with temperature, so it is impractical to formulate such an expression. We can, however, reasonably assume that such nonlinear terms can be approximated by Equation 14 for small perturbations of temperature about a setpoint.

I have spent a lot of time fitting the data set of Figures 9a and 16b using Equation 14. Much of this work has been to discern which thermistors are significant and which are not. Many of the thermistors of the testbed are correlated, and it is necessary to isolate those thermistors which have a significant bearing on the radiometric errors. The following procedure was developed to prioritize the 'significance' of a given thermistor by a process of elimination: (1) perform a linear regression of T_E against a set of N candidate thermistors using Equation 14; (2) repeat the regression after removing one thermistor from the set, then repeat this for each thermistor; (3) compare the residual errors from step (2) with that of step (1) to determine which thermistor can be removed with the least increase in the residual errors; (4) remove that thermistor from the set, decrement N, and return to step (1) until N=0. The order of elimination provides the prioritized list of thermistors, as sorted from least to most significant.

I have applied the above algorithm to various segments of data from Figures 9a and 16b. Some of the segments tested correspond to periods when the temperatures were being stepped and/or swept, and others were during steady conditions with the antenna load at either 23 C or 70 C. The two large temperature steps from 23 C to 70 C, and back down to 23 C, were also analyzed. Computer printouts generated by this analysis are supplied in Appendix-A.

The analysis of Appendix-A show that the antenna load and noise diode-C temperatures are consistently among the most significant temperatures when applied to Equation 14. Depending the test conditions, the regressions produce weighting coefficients which add 20% to 50% of the noise diode-C temperature, while simultaneously subtracting a corresponding amount of the antenna load (20 dB pad) temperature. As described earlier, noise diode-C is attached directly to the 20 dB pad that we use as the antenna load. Yet from Figure 9a we see that there are large gradients between the thermistor measurements of noise diode-C, the 20 dB pad, and the coaxial cable near the pad- especially when the secondary TEC is heated above ambient temperature. All three of these thermistors are within about two inches of one another, so we see that there are large temperature gradients near and probably within the pad. The analysis of Appendix-A shows that these gradients are indeed problematic. The thermistor attached to the 20 dB pad evidently does a poor job of measuring the noise temperature of the pad.

The above results suggest that the noise temperature of the antenna load might be better estimated by a weighted sum of thermistor measurements. When considering such a scheme we should note that the noise diode calibration of our testbed depends on the reference and antenna load thermistor measurements. Different weightings will affect the noise diode calibration, so the question arises as to what the proper reference points are for the calibration. If we had a real antenna we would have a well defined point- namely the antenna aperture- to establish the calibration. In the testbed we might choose either end of the coaxial cable that connects the antenna load to the rest of the radiometer, and in theory this choice would modify the noise diode temperature by the 5% losses of the coaxial cable. But we don't have a good model for these losses and in the end we'd still be dealing with unknown gradients and electrical losses near the antenna load. For the present study we have chosen, instead, to ignore these losses and simply calibrate the noise diodes with respect to the thermistor attached to the antenna load. This turns out to be our best choice even if we don't know exactly where along the transmission line- if anywhere- this thermistor temperature applies. For the analysis of Equation 14 we can show that we don't need to precisely define such a point: by combining Equations 13 and 14, one can regroup the antenna and reference load temperatures together with the thermistor temperatures in the summation, as in,

$$\frac{V_o - V_A}{d_N} T_N \cong c_0 + \sum_{i=1}^{N} c_i T_i \ , \qquad (15)$$

where d_N and T_N refer to any of the noise diode deflections and temperatures, as in Equations 9 or 10. Equation 15 shows that a change in the noise diode temperature amounts only to a change of scale between the radiometric and thermistor measurements. The residual errors that remain after fitting the data to Equation 15 are identical to those of Equation 14, and we see that these errors will scale directly by the noise diode temperature estimate. For the purpose of this error analysis we only need the noise diode temperature to be approximately correct. The accuracy of the thermistors attached to the antenna and reference loads is sufficient for such analysis, so we will continue to use them as our reference points for the calibration.

Returning to the results of Equation 14 and the analysis of Appendix-A: Upon studying the results of Appendix-A, and after some trial and error, I have found that the radiometric errors are reduced for every test case by replacing the antenna load temperature estimate with the coefficients from case #4 of Appendix-A, or

$$T_A = 0.1374\, T_{coax\_near\_TEC\#2} + 0.4962\, T_{antenna\_load} + 0.3720\, T_{noise\_diode\text{-}C} - 1.2641\,K \ . \qquad (16)$$

The three temperatures here correspond to the thermistors located closest to the antenna load. Upon applying Equation 16 to the testbed data and repeating the analysis- as presented in Appendix-B- we find that a similar result applies to the estimate of the reference load temperature, and that nearly all errors are further reduced by replacing the reference load temperature with the coefficients from case #0 of Appendix-B, or

$$T_o = 0.1413\, T_{LNA\_isolator} - 0.2545\, T_{reference\_load} + 1.1222\, T_{coax\_at\_Dicke\_input} - 2.3646\,K \ . \qquad (17)$$

Here, $T_{LNA\_isolator}$ is the temperature of the isolator that immediately follows the Dicke switch, $T_{reference\_load}$ is the temperature which was previously used for T_o, and $T_{coax\_at\_Dicke\_input}$ is the temperature of the coaxial cable where the antenna signal enters the Dicke switch. This thermistor is also about an inch away from the reference load, and is tightly coupled to the temperature of the pin diode Dicke switch. Surprisingly, the fit coefficients of Equation 17

indicate that the reference load temperature is better measured by this thermistor than by the thermistor attached to the reference load. This result, I have since found, may be related to a poor thermal connection between the thermistor and the reference load: I recently ran some test in which I added a second thermistor to the reference load and found that time variable gradients between the two reference load measurements were comparable to gradients between the reference load and the Dicke switch input.
Table 9 summarizes the reduction of residual errors as Equations 16 and 17 are applied to the various test cases of the Appendix. Figure 17 plots the corresponding errors for comparison with Figure 16b. The results of Table 9 show very good performance during the latter half of the experiment, with radiometric errors in cases 3 and 4 of 0.017 K, and case 2 of 0.0141K. This is very close to the theoretical delta-T, which in the special case of $T_o = T_A$ is

$$\Delta T \cong \frac{\sqrt{2}T_{sys}}{\sqrt{B\tau d}} = \frac{\sqrt{2}(225K + 296K)}{\sqrt{30MHz * 1000s * 0.1}} = 0.0135K \quad (18)$$

where d is duty cycle from Table 1. Subtracting the theoretical delta-T in quadrature from the errors of Table 9 leaves about 0.004 to 0.010 K of residual error in cases 2, 3, and 4- which is about 3 to 5 times lower than the uncorrected errors. Errors during the first half of the experiment (cases 1 and 6) aren't as good due to at least two factors: (1) the noise diode calibrations changed during the first 100 hours, as evident in Table 8; and (2) the temperatures of the TEC plates were deliberately being changed to produce the maximum error. To evaluate the magnitude of the noise diode drift problem, the second to last column of Table 9 provides errors after adjusting the noise diode calibration to minimize the local errors. As can be seen, the improvements are minor- as are the changes to the noise diode temperatures (given in parenthesis). The last column of Table 9 provides the most optimistic scenario after recalculating the fit coefficients to minimize errors within each test case. These fit coefficients have been provided in Appendix-C. With the exception of case 1, these residual error show a little improvement over the two previous cases. Overall, these results show that the selection of thermistors and the regression fits of Equations 16 and 17 work well for most cases, but they work better for steady temperature cases (improvement factor of 3 to 5) than the perturbed temperature cases (improvement factor of about 2).

Table 10 presents standard deviations of various temperatures and of temperature differences for the same test cases using the same 1000 second boxcar integrations as Table 9. The correlation between Tables 10 and 9 isn't perfect, but the general pattern confirms that uncorrected radiometric stability is approximately equal to the stability of temperature gradients within the radiometer, and not to the stability of the soak temperature.

Finally, Figure 18 provides the spectra of the steady 23 and 70 C errors of Figure 17, which show that residual errors are essentially white down to 10 micro-hertz.

Radiometric vs. thermistor residual errors. All errors in K, with 1000s boxcar integrations.	T_A=#13 T_o=#0	T_A=Eq16 T_o=#0	T_A=Eq16 T_o=Eq17	T_A=Eq16 T_o=Eq17 adjusted T_{ND} (T_{ND}%)	local fits from Apx.-C
CASE#0 0-300 hours (all data)	0.1300	0.1089	**0.0664**	0.0664 (-0.01%)	0.0574
CASE#1 0-100 hours (steps and sweeps)	0.1982	0.1973	0.1152	0.1037 (-0.58%)	0.0584
CASE#2 260-300 hours (steady 23C)	0.0212	0.0146	0.0141	0.0141 (0.00%)	0.0144
CASE#3 140-240 hours (steady 70C)	0.0382	0.0177	0.0178	0.0178 (0.00%)	0.0175
CASE#4 140-300 hours (70C & 23C)	0.0581	**0.0173**	0.0173	0.0173 (0.00%)	0.0172
CASE#5 90-130 hours (70C & 23C)	0.1332	0.0412	0.0400	0.0376 (-0.07%)	0.0279
CASE#6 65-95 hours (+/- 5K steps)	0.1148	0.0966	0.0697	0.0580 (-1.76%)	0.0421

Table 9: Reduction of residual errors in Figure 16b as antenna (#13) and reference load (#0) thermistors are replaced by Equation 16 and 17; the second to last column recalculates the errors after adjusting the noise diode noise temperatures (by a percentage given in parenthesis) ; the last column represent a best-case scenario in which the fit coefficients are recalculated for each case (these fit coefficients are provided in Appendix-C). The errors highlighted (bold) correspond to the cases from which the regression fits were derived, so these will naturally show the greatest error reduction compared to a previous column.

	primary TEC		secondary TEC	
thermistors:	#0	#0-#10	#13	#13-#12
CASE#0:	3.509	0.130	21.143	0.289
CASE#1:	6.440	0.239	6.166	0.395
CASE#2:	0.067	0.017	0.061	0.037
CASE#3:	0.025	0.004	0.091	0.063
CASE#4:	0.046	0.013	19.505	0.111
CASE#5:	0.065	0.020	20.613	0.376
CASE#6:	1.688	0.122	1.650	0.304

all units: Kelvin
Thermistor #0= Reference load
Thermistor #10= Isolator
Thermistor #13= Antenna load
Thermistor #12= Noise diode-C

Table 10: standard deviations of various thermistor temperatures and of their differences for comparison with the radiometric errors of Table 9; 1000 second boxcar integrations have been applied. The temperature differences are representative of thermal gradients.

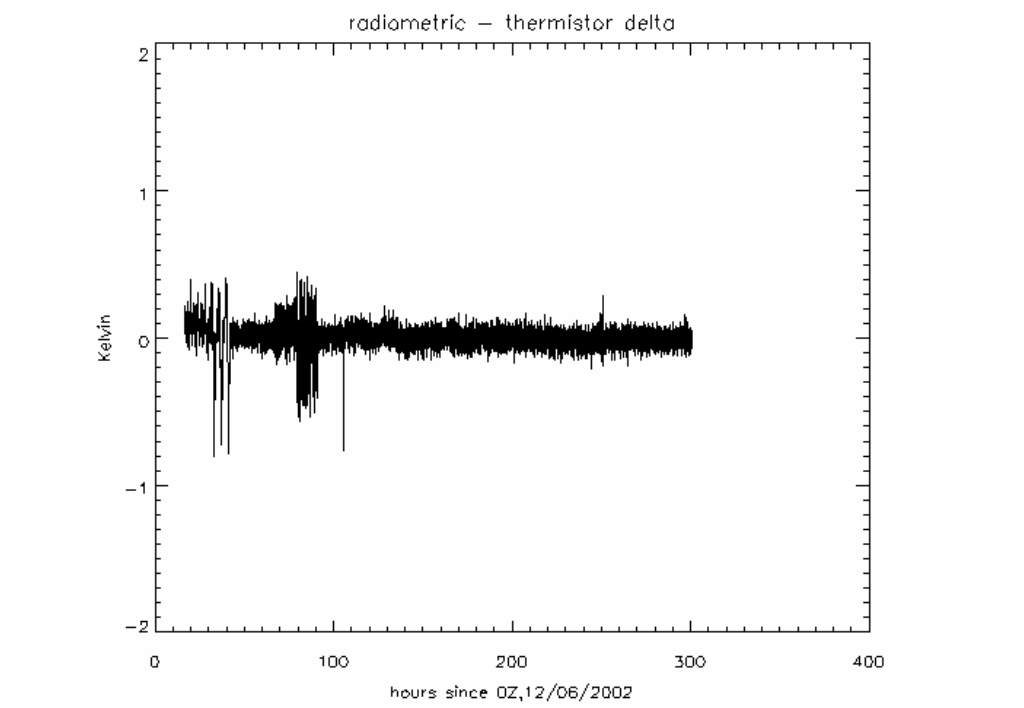

Figure 17: Brightness temperature errors after applying temperature corrections of Equations 16 and 17; 100 second boxcar integrations apply.

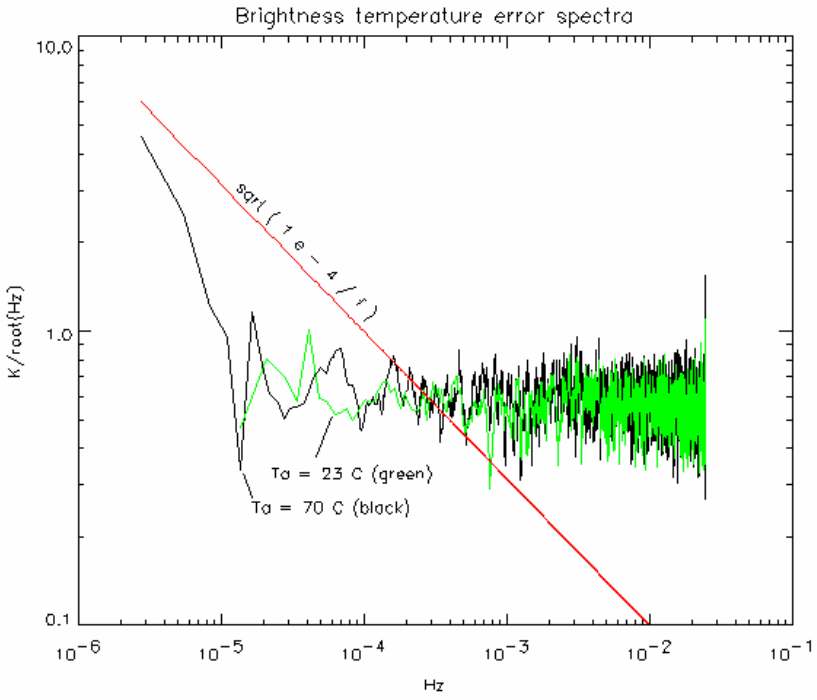

Figure 16d: error spectra for segments of Figure 15b: 70 C data from 140 to 240 hours (black), and 23C data from 260-300 hours (green).

3.4- NEDT:

Table 11 presents some noise equivalent delta-T (NEDT) estimates for a salinity mission using the stability results of the testbed. The relevant stability parameters from the above tests are the 1/f spectral coefficients b_g and b_r which quantify the stability of amplifier gain and receiver noise. The gain coefficient, b_g, has been estimated from the temperature corrected curve of Figure 11b. The receiver noise 1/f coefficient, b_r, has been estimated from Figure 14 from the "all noise diodes vs. reference load" spectrum. I have applied the analysis of my 5/10/02 memo, titled "delta-T and duty cycle optimizations," to compute the duty cycles for the reference load (do) and noise diode (d_n) which minimize the NEDT of the antenna brightness temperature using a calibration formula that applies separate running averages of gain and receiver noise. The integration times associated with the antenna brightness temperature, receiver noise, and gain are provided with each case in Table 11 as t_A, t_r, and t_g, respectively. The different test cases of Table 11 apply different limits and constraints as follows: the first case optimizes all four parameters, t_r, t_g, d_o, and d_n; the second case assumes that d_o and d_n are equal; the four remaining cases limit t_r to 5000 or 1000 seconds with and without the d_o=d_n constraint. The "/TP" figure represents the relative performance compared to a 'perfect' total power radiometer with 100 % antenna duty cycle. As can be seen, the optimizations can accommodate a wide range of tr without significant changes to the NEDT (provided $t_r >> t_g >> t_A$). Overall, at 0.04K, the NEDT is not as low as the 0.02K goal of the USR, but it comes close. The only means to reach the 0.02K goal within the 12 second available integration time will be to improve the gain stability (the AWVRs have a gain stability of b_g=7x10^{-10} versus 2x10^{-9} in the testbed), lower the noise figure, and increase the bandwidth.

```
NEDT simulation parameters:
Tr=255.        ; receiver noise temp (K)
To=295.        ; reference temp (K)
Ta=100.        ; antenna brightness temperature (K)
BW=20e+6       ; bandwidth (Hz)
taua=12.       ; observation time (s)
Tnd=500.       ; noise diode deflection (K)
br=1e-10       ; 1/f spectra coefficient of normalized Tr (/Hz)
bg=2e-9        ; normalized gain 1/f spectra coefficient (/Hz)

optimized NEDT results:
                    integration times (s)      duty cycles
   NEDT(K)   /TP      tA       tr       tg      do      dn
   0.0375    1.64   12.0   555630.    96.2    0.24    0.02
   0.0376    1.64   12.0   157812.    96.2    0.13    0.13
   0.0381    1.66   12.0     5000.    86.2    0.19    0.10
   0.0382    1.67   12.0     5000.    89.3    0.14    0.14
   0.0401    1.75   12.0     1000.    71.4    0.23    0.12
   0.0403    1.76   12.0     1000.    69.4    0.18    0.18
```

Table 11: calculated NEDT and optimized duty cycles given gain and receiver noise stability of the testbed data; the spectra coefficients b_g and b_r have been estimated from Figures 11b and 14, respectively.

We should also qualify the results of Table 11 by noting that these NEDT calculations do not account for noise diode instability. Figures 17a and 17b plot two of the noise diode deflection ratios for the tests of Figure 9a. Ignoring the transients and steps during the large temperature swings, the C/A deflection ratio show drifts on the order of -0.5% between 100 and 250 hours while noise diode C was heated to 70 C. This drift is almost certainly caused by slow changes in the coaxial cables, and not in the noise diodes. Note that the B/A deflection ratio of Figure 17b shows much less drift than the C/A ratio, indicating that the drift occurs between noise diode-C and the rest of the system. Yet Table 8 indicates that both noise diodes A and B drifted upward, based on the antenna load temperature calibration. These fact indicate that the losses increased between the antenna and the radiometer. Based on past experience, this drift is probably caused by residual bending stresses between the center conductor and the Teflon insulator within the 12 inch coaxial cable that connects the antenna load to the rest of the system. This is a known problem that can be fixed with better cable bending and assembly procedures- and with better cable- so we can expect to reduce such errors in the future.

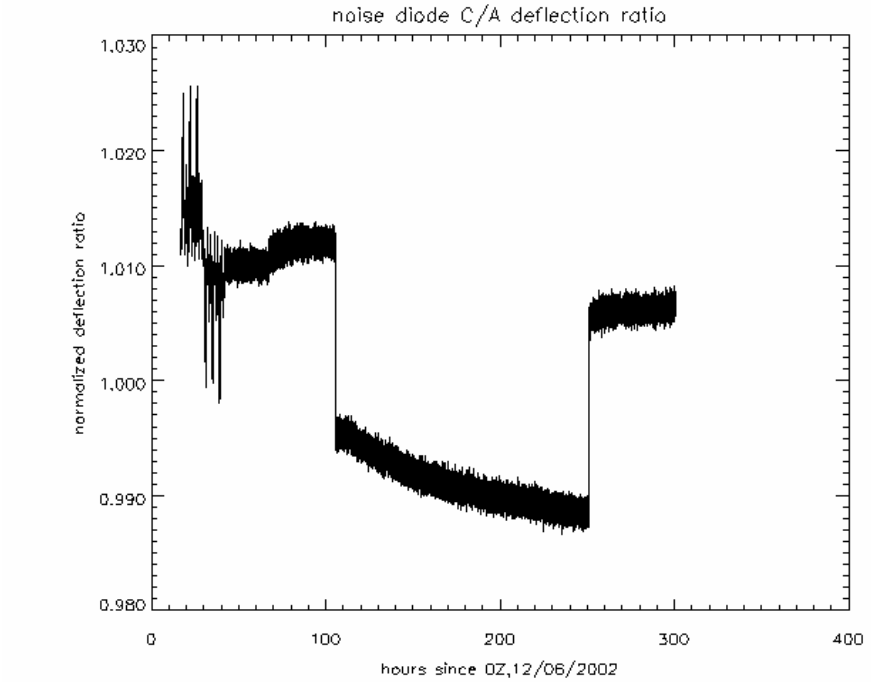

Figure 17a: noise diode C/A deflection ratio; noise diode-C was heated to 70 C between 100 and 260 hours, and a substantial drift of about 0.5% is evident during this period.

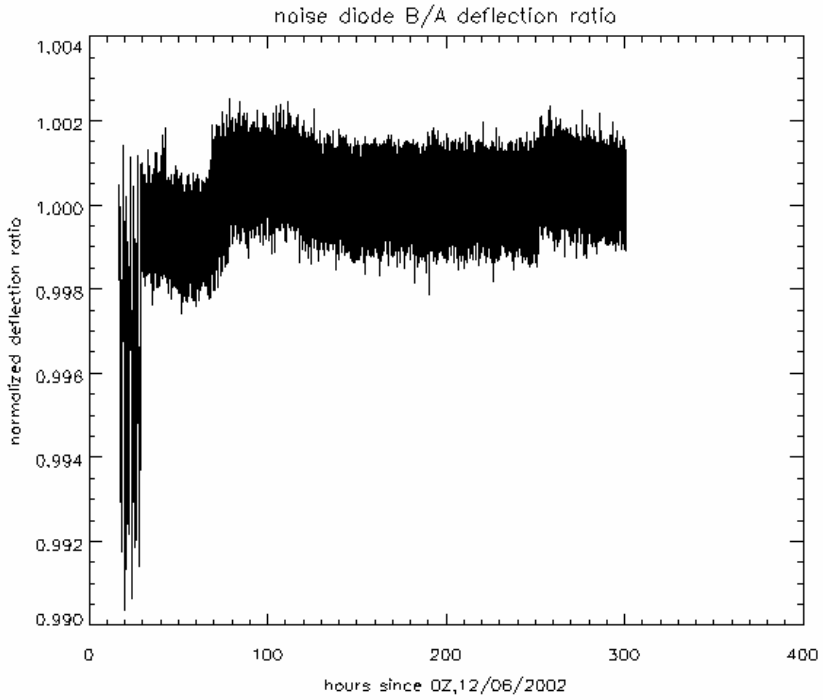

Figure 17b: noise diode B/A deflection ratio; both noise diodes are on the same plate.

4. Conclusion

These preliminary testbed results are encouraging in that they demonstrate that it will be possible to attain 0.04 K of NEDT in a salinity mission with modest thermal control. Gain errors versus temperature were characterized and

corrected to about 100 ppm/C, which translates to approximately 0.02 K of radiometric error per 1K of instrument temperature change given the 200 K contrast between the ocean brightness temperature and the reference temperature of the instrument. Time variable offset errors were found to be dominated by temperature gradients between components and between components and the thermistors used to measure temperatures. The offset errors could be reduced to about 1/2 to 1/4 of the gradient errors observed between neighboring components, but it is clear that gradients between a thermistor and a reference load will produce comparable radiometric errors. Taken together, these results indicate that the thermal requirements for the Aquarius radiometer will need to be broken down to several levels to distinguish between soak temperature errors, and gradient errors at two or more spatial scales. In round numbers, I would say that that a 0.04 K NEDT requirement will demand absolute temperature control to keep the instrument within +/- 1K, and sufficient insulation around the instrument- and heat conduction within the instrument- to keep time variable gradients between components below +/- 0.1K, and time variable gradients within components (especially within the Dicke switch) below +/- 0.01 K. These specifications apply, of course, only to the radiometer electronics. The antenna feedhorn and OMT are another matter, and we will need to test their thermal characteristics before we can define their control requirements.

REFERENCES:

E.C.Jordan, editor, “Refernce data for Engineers: Radio, Electronics, Computer, and Communications”, seventh edition, 1988, Howard W. Sams & Co..

R.E Collin, “Foundations for Microwave Engineering”, 1966, McGraw Hill, Inc..

Appendix A: Computer printouts to accompany regression analysis following Equation 14

Each of the following test cases correspond to a different time spans from Figure 9a. As presented, each case starts with the prioritized list of thermistors and associated RMS residual errors. A selection of the most significant thermistors is then applied, and the retrieved weighting coefficients, c_i of Equation 14, are tabulated. This tabulation also includes a sum of the weighting coefficients, which is of interest since we expect their sum in Equation 14 to be close to zero. Following this Tabulation the same weighting coefficients are applied to a 'standard' test case, using data between 140 and 300 hours, to test whether the coefficients derived from one segment in time improve the performance at another segment of time. These errors can also be compared to the uncorrected errors presented in the following header along with other relevant data:

```
Analysis uses noise diode temperatures:
TndA=      745.654
TndB=      751.877
TndC=      540.119

Antenna temperature = thermistor #12
Dicke Reference load temperature= thermistor #0

Uncorrected Tb errors for "standard" test cases
(1000 s boxcar integrations apply):

  0.0212  K for points > 260 hours (steady 23 C)
  0.0382  K for points 140 to 240 hours (steady 70 C)
  0.0592  K for points > 140 (70 and 23 C)
-------------------------------------------------------
(test cases start on next page)
```

Appendix A (cont)

```
CASE#0:  regressions based on all 16.9 to 300.5 hours

Tb residual errors as least significant thermistors are removed:
(100 second boxcar integrations apply)
  0.0617 (K) with all 15 thermistors
  0.0616 (K) without  1 radiometer (TEC#1) plate center
  0.0616 (K) without  4 coax at dicke switch input
  0.0618 (K) without 14 coax near antenna (TEC#2)
  0.0620 (K) without  8 low noise amplifier
  0.0620 (K) without  3 dicke switch body
  0.0623 (K) without  9 video amp
  0.0632 (K) without  5 noise diode-B
  0.0637 (K) without  7 noise diode-A
  0.0660 (K) without 10 isolator at LNA input
  0.0696 (K) without 13 antenna load
  0.0779 (K) without  2 coax near radiometer (TEC#1)
  0.0941 (K) without  6 unused bandpass filter
  0.1435 (K) without  0 reference load
  0.1488 (K) without 15 coax between TECs #1 and #2
  0.1497 (K) without 12 noise diode-C or any thermistors
proceeding with thermistor channels:      13       2       6       0
      15      12

Fit coefficients using "significant" thermistors:
 -0.1447 (K/K) * T_antenna load
  0.6513 (K/K) * T_coax near radiometer (TEC#1)
 -1.0795 (K/K) * T_unused bandpass filter
  0.6021 (K/K) * T_reference load
 -0.2887 (K/K) * T_coax between TECs #1 and #2
  0.2239 (K/K) * T_noise diode-C
 -0.0356 (K/K) sum of temperature coefficients
 10.1965 (K) offset
corresponding Tb errors for "standard" test cases
(1000 s boxcar integrations apply):
  0.0220 K for points > 260 hours (23 C)
  0.0200 K for points 140 to 240 hours (70 C)
  0.0220 K for points > 140 (70 and 23 C)
```

Appendix A (cont)

```
CASE#1:  regressions based on  16.9 to 100.0 hours (sweeps and steps)

Tb residual errors as least significant thermistors are removed:
(100 second boxcar integrations apply)
  0.0599 (K) with all 15 thermistors
  0.0599 (K) without  5 noise diode-B
  0.0599 (K) without  2 coax near radiometer (TEC#1)
  0.0600 (K) without  1 radiometer (TEC#1) plate center
  0.0599 (K) without  8 low noise amplifier
  0.0601 (K) without  6 unused bandpass filter
  0.0613 (K) without 14 coax near antenna (TEC#2)
  0.0627 (K) without  3 dicke switch body
  0.0698 (K) without 13 antenna load
  0.0755 (K) without  4 coax at dicke switch input
  0.0838 (K) without  7 noise diode-A
  0.1001 (K) without  0 reference load
  0.1008 (K) without 10 isolator at LNA input
  0.1697 (K) without  9 video amp
  0.1773 (K) without 15 coax between TECs #1 and #2
  0.2174 (K) without 12 noise diode-C or any thermistors
proceeding with thermistor channels:      13       4       7       0
      10       9      15      12

Fit coefficients using "significant" thermistors:
 -0.1349 (K/K) * T_antenna load
 -1.1490 (K/K) * T_coax at dicke switch input
  0.1015 (K/K) * T_noise diode-A
  1.4280 (K/K) * T_reference load
 -0.6698 (K/K) * T_isolator at LNA input
  0.4039 (K/K) * T_video amp
 -0.2398 (K/K) * T_coax between TECs #1 and #2
  0.2082 (K/K) * T_noise diode-C
 -0.0518 (K/K) sum of temperature coefficients
 15.0234 (K) offset
corresponding Tb errors for "standard" test cases
(1000 s boxcar integrations apply):
  0.0296 K for points > 260 hours (23 C)
  0.0195 K for points 140 to 240 hours (70 C)
  0.1540 K for points > 140 (70 and 23 C)
```

Appendix A (cont)

```
CASE#2:  regressions based on 260.0 to 300.5 hours (steady 23C)

Tb residual errors as least significant thermistors are removed:
(100 second boxcar integrations apply)
  0.0454 (K) with all 15 thermistors
  0.0454 (K) without  6 unused bandpass filter
  0.0454 (K) without  1 radiometer (TEC#1) plate center
  0.0454 (K) without  3 dicke switch body
  0.0454 (K) without  8 low noise amplifier
  0.0455 (K) without  2 coax near radiometer (TEC#1)
  0.0455 (K) without  9 video amp
  0.0455 (K) without  7 noise diode-A
  0.0455 (K) without  5 noise diode-B
  0.0456 (K) without 10 isolator at LNA input
  0.0458 (K) without  0 reference load
  0.0458 (K) without  4 coax at dicke switch input
  0.0463 (K) without 15 coax between TECs #1 and #2
  0.0479 (K) without 14 coax near antenna (TEC#2)
  0.0495 (K) without 13 antenna load
  0.0499 (K) without 12 noise diode-C or any thermistors
proceeding with thermistor channels:      14      13      12

Fit coefficients using "significant" thermistors:
  0.1630 (K/K) * T_coax near antenna (TEC#2)
 -0.4077 (K/K) * T_antenna load
  0.2334 (K/K) * T_noise diode-C
 -0.0112 (K/K) sum of temperature coefficients
  3.7739 (K) offset
corresponding Tb errors for "standard" test cases
(1000 s boxcar integrations apply):
  0.0151 K for points > 260 hours (23 C)
  0.0202 K for points 140 to 240 hours (70 C)
  0.6160 K for points > 140 (70 and 23 C)
```

Appendix A (cont)

```
CASE#3:  regressions based on 140.0 to 240.0 hours (steady 70 C)

Tb residual errors as least significant thermistors are removed:
(100 second boxcar integrations apply)
  0.0490 (K) with all 15 thermistors
  0.0490 (K) without  1 radiometer (TEC#1) plate center
  0.0490 (K) without  9 video amp
  0.0490 (K) without  8 low noise amplifier
  0.0490 (K) without  3 dicke switch body
  0.0490 (K) without 10 isolator at LNA input
  0.0490 (K) without  6 unused bandpass filter
  0.0490 (K) without  0 reference load
  0.0491 (K) without  4 coax at dicke switch input
  0.0491 (K) without 15 coax between TECs #1 and #2
  0.0492 (K) without  5 noise diode-B
  0.0492 (K) without  7 noise diode-A
  0.0493 (K) without  2 coax near radiometer (TEC#1)
  0.0496 (K) without 14 coax near antenna (TEC#2)
  0.0531 (K) without 12 noise diode-C
  0.0697 (K) without 13 antenna load or any thermistors
proceeding with thermistor channels:      14      12      13

Fit coefficients using "significant" thermistors:
  0.0716 (K/K) * T_coax near antenna (TEC#2)
  0.3664 (K/K) * T_noise diode-C
 -0.5235 (K/K) * T_antenna load
 -0.0856 (K/K) sum of temperature coefficients
 29.1690 (K) offset
corresponding Tb errors for "standard" test cases
(1000 s boxcar integrations apply):
  0.0178 K for points > 260 hours (23 C)
  0.0176 K for points 140 to 240 hours (70 C)
  1.5122 K for points > 140 (70 and 23 C)
```

Appendix A (cont)

```
CASE#4:  regressions based on 140.0 to 300.5 hours (70 C & 23 C data)

Tb residual errors as least significant thermistors are removed:
(100 second boxcar integrations apply)
  0.0482 (K) with all 15 thermistors
  0.0482 (K) without  1 radiometer (TEC#1) plate center
  0.0482 (K) without  9 video amp
  0.0483 (K) without 15 coax between TECs #1 and #2
  0.0483 (K) without  8 low noise amplifier
  0.0483 (K) without  3 dicke switch body
  0.0483 (K) without 10 isolator at LNA input
  0.0483 (K) without  6 unused bandpass filter
  0.0483 (K) without  2 coax near radiometer (TEC#1)
  0.0484 (K) without  7 noise diode-A
  0.0484 (K) without  5 noise diode-B
  0.0486 (K) without  0 reference load
  0.0486 (K) without  4 coax at dicke switch input
  0.0501 (K) without 14 coax near antenna (TEC#2)
  0.0805 (K) without 13 antenna load
  0.0826 (K) without 12 noise diode-C or any thermistors
proceeding with thermistor channels:      14      13      12

Fit coefficients using "significant" thermistors:
  0.1374 (K/K) * T_coax near antenna (TEC#2)
 -0.5038 (K/K) * T_antenna load
  0.3720 (K/K) * T_noise diode-C
  0.0056 (K/K) sum of temperature coefficients
 -1.2641 (K) offset
corresponding Tb errors for "standard" test cases
(1000 s boxcar integrations apply):
  0.0146 K for points > 260 hours (23 C)
  0.0177 K for points 140 to 240 hours (70 C)
  0.0173 K for points > 140 (70 and 23 C)
```

Appendix A (cont)

```
CASE#5:  regressions based on  90.0 to 130.0 hours (23C and 70 C data)

Tb residual errors as least significant thermistors are removed:
(100 second boxcar integrations apply)
  0.0533 (K) with all 15 thermistors
  0.0532 (K) without  7 noise diode-A
  0.0532 (K) without  4 coax at dicke switch input
  0.0532 (K) without  3 dicke switch body
  0.0533 (K) without 14 coax near antenna (TEC#2)
  0.0537 (K) without  0 reference load
  0.0543 (K) without  9 video amp
  0.0545 (K) without  8 low noise amplifier
  0.0550 (K) without  1 radiometer (TEC#1) plate center
  0.0567 (K) without  5 noise diode-B
  0.0577 (K) without 10 isolator at LNA input
  0.0587 (K) without  2 coax near radiometer (TEC#1)
  0.0588 (K) without  6 unused bandpass filter
  0.0611 (K) without 15 coax between TECs #1 and #2
  0.1520 (K) without 13 antenna load
  0.1613 (K) without 12 noise diode-C or any thermistors
proceeding with thermistor channels:       2       6      15      13
      12

Fit coefficients using "significant" thermistors:
  0.6520 (K/K) * T_coax near radiometer (TEC#1)
 -0.7136 (K/K) * T_unused bandpass filter
 -0.1182 (K/K) * T_coax between TECs #1 and #2
 -0.2358 (K/K) * T_antenna load
  0.2581 (K/K) * T_noise diode-C
 -0.1575 (K/K) sum of temperature coefficients
 47.0625 (K) offset
corresponding Tb errors for "standard" test cases
(1000 s boxcar integrations apply):
  0.0245 K for points > 260 hours (23 C)
  0.0198 K for points 140 to 240 hours (70 C)
  0.0405 K for points > 140 (70 and 23 C)
```

Appendix A (cont)

```
CASE#6:  regressions based on  65.0 to  95.0 hours (stepped +/- 5 C)

Tb residual errors as least significant thermistors are removed:
(100 second boxcar integrations apply)
  0.0508 (K) with all 15 thermistors
  0.0507 (K) without  0 reference load
  0.0507 (K) without 10 isolator at LNA input
  0.0508 (K) without  8 low noise amplifier
  0.0512 (K) without  6 unused bandpass filter
  0.0516 (K) without  4 coax at dicke switch input
  0.0530 (K) without  7 noise diode-A
  0.0545 (K) without 14 coax near antenna (TEC#2)
  0.0559 (K) without 15 coax between TECs #1 and #2
  0.0590 (K) without  2 coax near radiometer (TEC#1)
  0.0623 (K) without  3 dicke switch body
  0.0758 (K) without  5 noise diode-B
  0.0818 (K) without  9 video amp
  0.0982 (K) without  1 radiometer (TEC#1) plate center
  0.1536 (K) without 13 antenna load
  0.1702 (K) without 12 noise diode-C or any thermistors
proceeding with thermistor channels:      15       2       3       5
       9       1      13      12

Fit coefficients using "significant" thermistors:
 -0.1171 (K/K) * T_coax between TECs #1 and #2
  0.2203 (K/K) * T_coax near radiometer (TEC#1)
 -0.2329 (K/K) * T_dicke switch body
  0.2192 (K/K) * T_noise diode-B
  0.1471 (K/K) * T_video amp
 -0.3200 (K/K) * T_radiometer (TEC#1) plate center
 -0.1803 (K/K) * T_antenna load
  0.2169 (K/K) * T_noise diode-C
 -0.0467 (K/K) sum of temperature coefficients
 14.2622 (K) offset
corresponding Tb errors for "standard" test cases (1000 s boxcar integrations
apply):
  0.0267 K for points > 260 hours (23 C)
  0.0208 K for points 140 to 240 hours (70 C)
  0.2592 K for points > 140 (70 and 23 C)
```

Appendix-B

Repeat of analysis with antenna temperature fit from case #4 of Appendix-A.

```
   TNDA: 745.662 K
   TNDB: 751.886 K
   TNDC: 540.760 K

Antenna temperature = .1374*T_coax + .4962*T_A + .3720*T_NDC - 1.2641 K
Dicke Reference load temperature= thermistor #0

Uncorrected Tb errors for "standard" test cases
(1000 s boxcar integrations apply):
  0.0146  K for points > 260 hours (23 C)
  0.0177  K for points 140 to 240 hours (70 C)
  0.0173  K for points > 140 (70 and 23 C)
-----------------------------------------------------------

CASE#0:  regressions based on   0.0 to 300.5 hours (all data)

Tb residual errors as least significant thermistors are removed:
(100 second boxcar integrations apply)
  0.0815 (K) with all 11 thermistors
  0.0815 (K) without  3 dicke switch body
  0.0816 (K) without  5 noise diode-B
  0.0819 (K) without  2 coax near radiometer (TEC#1)
  0.0819 (K) without  6 unused bandpass filter
  0.0824 (K) without  8 low noise amplifier
  0.0837 (K) without 15 coax between TECs #1 and #2
  0.0856 (K) without  9 video amp
  0.0868 (K) without  1 radiometer (TEC#1) plate center
  0.0880 (K) without 10 isolator at LNA input
  0.0968 (K) without  0 reference load
  0.1239 (K) without  4 coax at dicke switch input or any thermistors
proceeding with thermistor channels:      10       0       4

Fit coefficients using "significant" thermistors:
 -0.1413 (K/K) * T_isolator at LNA input
  1.2545 (K/K) * T_reference load
 -1.1222 (K/K) * T_coax at dicke switch input
 -0.0090 (K/K) sum of temperature coefficients
  2.3646 (K) offset
corresponding Tb errors for "standard" test cases
(1000 s boxcar integrations apply):
  0.0141 K for points > 260 hours (23 C)
  0.0178 K for points 140 to 240 hours (70 C)
  0.0182 K for points > 140 (70 and 23 C)
```

Appendix B (cont)

```
CASE#1:  regressions based on   0.0 to 100.0 hours (steps and sweeps)

Tb residual errors as least significant thermistors are removed:
(100 second boxcar integrations apply)
  0.0969 (K) with all 11 thermistors
  0.0970 (K) without  3 dicke switch body
  0.0971 (K) without  5 noise diode-B
  0.0986 (K) without  2 coax near radiometer (TEC#1)
  0.0993 (K) without  6 unused bandpass filter
  0.1002 (K) without  8 low noise amplifier
  0.1054 (K) without  9 video amp
  0.1099 (K) without  1 radiometer (TEC#1) plate center
  0.1132 (K) without 10 isolator at LNA input
  0.1334 (K) without  0 reference load
  0.1561 (K) without 15 coax between TECs #1 and #2
  0.2123 (K) without  4 coax at dicke switch input or any thermistors
proceeding with thermistor channels:       1      10       0      15
       4

Fit coefficients using "significant" thermistors:
  0.0817 (K/K) * T_radiometer (TEC#1) plate center
 -0.2447 (K/K) * T_isolator at LNA input
  2.1190 (K/K) * T_reference load
  0.0429 (K/K) * T_coax between TECs #1 and #2
 -1.9793 (K/K) * T_coax at dicke switch input
  0.0196 (K/K) sum of temperature coefficients
 -6.3156 (K) offset
corresponding Tb errors for "standard" test cases
(1000 s boxcar integrations apply):
  0.0156 K for points > 260 hours (23 C)
  0.0191 K for points 140 to 240 hours (70 C)
  0.2632 K for points > 140 (70 and 23 C)
```

Appendix B (cont)

```
CASE#2:  regressions based on 260.0 to 300.5 hours (steady 23C)

Tb residual errors as least significant thermistors are removed:
(100 second boxcar integrations apply)
  0.0462 (K) with all 11 thermistors
  0.0462 (K) without  8 low noise amplifier
  0.0462 (K) without  3 dicke switch body
  0.0462 (K) without  1 radiometer (TEC#1) plate center
  0.0462 (K) without  2 coax near radiometer (TEC#1)
  0.0462 (K) without  5 noise diode-B
  0.0462 (K) without  9 video amp
  0.0462 (K) without 15 coax between TECs #1 and #2
  0.0463 (K) without  6 unused bandpass filter
  0.0464 (K) without 10 isolator at LNA input
  0.0467 (K) without  4 coax at dicke switch input
  0.0467 (K) without  0 reference load or any thermistors
proceeding with thermistor channels:      10       4       0

Fit coefficients using "significant" thermistors:
 -0.1538 (K/K) * T_isolator at LNA input
 -1.1920 (K/K) * T_coax at dicke switch input
  1.3215 (K/K) * T_reference load
 -0.0243 (K/K) sum of temperature coefficients
  6.9058 (K) offset
corresponding Tb errors for "standard" test cases
(1000 s boxcar integrations apply):
  0.0141 K for points > 260 hours (23 C)
  0.0178 K for points 140 to 240 hours (70 C)
  0.0182 K for points > 140 (70 and 23 C)
```

Appendix B (cont)

```
CASE#3:  regressions based on 140.0 to 240.0 hours (steady 70C)

Tb residual errors as least significant thermistors are removed:
(100 second boxcar integrations apply)
  0.0492 (K) with all 11 thermistors
  0.0492 (K) without 15 coax between TECs #1 and #2
  0.0492 (K) without  1 radiometer (TEC#1) plate center
  0.0492 (K) without  8 low noise amplifier
  0.0492 (K) without  9 video amp
  0.0492 (K) without 10 isolator at LNA input
  0.0492 (K) without  5 noise diode-B
  0.0492 (K) without  2 coax near radiometer (TEC#1)
  0.0493 (K) without  6 unused bandpass filter
  0.0493 (K) without  0 reference load
  0.0493 (K) without  4 coax at dicke switch input
  0.0495 (K) without  3 dicke switch body or any thermistors
proceeding with thermistor channels:       0       4       3

Fit coefficients using "significant" thermistors:
  0.6558 (K/K) * T_reference load
 -0.6110 (K/K) * T_coax at dicke switch input
 -0.1060 (K/K) * T_dicke switch body
 -0.0613 (K/K) sum of temperature coefficients
 18.1557 (K) offset
corresponding Tb errors for "standard" test cases
(1000 s boxcar integrations apply):
  0.0147 K for points > 260 hours (23 C)
  0.0176 K for points 140 to 240 hours (70 C)
  0.0176 K for points > 140 (70 and 23 C)
```

Appendix B (cont)

```
CASE#4:  regressions based on 140.0 to 300.5 hours (70C & 23C)

Tb residual errors as least significant thermistors are removed:
(100 second boxcar integrations apply)
  0.0483 (K) with all 11 thermistors
  0.0483 (K) without  1 radiometer (TEC#1) plate center
  0.0483 (K) without  8 low noise amplifier
  0.0483 (K) without  3 dicke switch body
  0.0483 (K) without  6 unused bandpass filter
  0.0483 (K) without  2 coax near radiometer (TEC#1)
  0.0483 (K) without  9 video amp
  0.0483 (K) without  5 noise diode-B
  0.0484 (K) without 10 isolator at LNA input
  0.0485 (K) without 15 coax between TECs #1 and #2
  0.0486 (K) without  0 reference load
  0.0486 (K) without  4 coax at dicke switch input or any thermistors
proceeding with thermistor channels:      15       0       4

Fit coefficients using "significant" thermistors:
  0.0006 (K/K) * T_coax between TECs #1 and #2
  0.8810 (K/K) * T_reference load
 -0.8964 (K/K) * T_coax at dicke switch input
 -0.0147 (K/K) sum of temperature coefficients
  4.1990 (K) offset
corresponding Tb errors for "standard" test cases
(1000 s boxcar integrations apply):
  0.0142 K for points > 260 hours (23 C)
  0.0178 K for points 140 to 240 hours (70 C)
  0.0172 K for points > 140 (70 and 23 C)
```

Appendix B (cont)

```
CASE#5:  regressions based on  90.0 to 130.0 hours (70C & 23C)

Tb residual errors as least significant thermistors are removed:
(100 second boxcar integrations apply)
  0.0667 (K) with all 11 thermistors
  0.0667 (K) without 15 coax between TECs #1 and #2
  0.0668 (K) without  9 video amp
  0.0668 (K) without 10 isolator at LNA input
  0.0668 (K) without  8 low noise amplifier
  0.0671 (K) without  6 unused bandpass filter
  0.0671 (K) without  4 coax at dicke switch input
  0.0672 (K) without  5 noise diode-B
  0.0672 (K) without  1 radiometer (TEC#1) plate center
  0.0675 (K) without  0 reference load
  0.0684 (K) without  3 dicke switch body
  0.0698 (K) without  2 coax near radiometer (TEC#1) or any thermistors
proceeding with thermistor channels:       0       3       2

Fit coefficients using "significant" thermistors:
  0.2886 (K/K) * T_reference load
 -0.5278 (K/K) * T_dicke switch body
  0.2251 (K/K) * T_coax near radiometer (TEC#1)
 -0.0141 (K/K) sum of temperature coefficients
  4.3802 (K) offset
corresponding Tb errors for "standard" test cases
(1000 s boxcar integrations apply):
  0.0147 K for points > 260 hours (23 C)
  0.0176 K for points 140 to 240 hours (70 C)
  0.0232 K for points > 140 (70 and 23 C)
```

Appendix B (cont)

```
CASE#6:  regressions based on  65.0 to  95.0 hours (+/- 5K steps)

Tb residual errors as least significant thermistors are removed:
(100 second boxcar integrations apply)
  0.0859 (K) with all 11 thermistors
  0.0859 (K) without  0 reference load
  0.0861 (K) without  2 coax near radiometer (TEC#1)
  0.0863 (K) without 10 isolator at LNA input
  0.0867 (K) without  8 low noise amplifier
  0.0872 (K) without  3 dicke switch body
  0.0895 (K) without  6 unused bandpass filter
  0.0948 (K) without  4 coax at dicke switch input
  0.0954 (K) without  9 video amp
  0.1054 (K) without  5 noise diode-B
  0.1152 (K) without 15 coax between TECs #1 and #2
  0.1417 (K) without  1 radiometer (TEC#1) plate center or any thermistors
proceeding with thermistor channels:       4       9       5      15
       1

Fit coefficients using "significant" thermistors:
 -0.1248 (K/K) * T_coax at dicke switch input
  0.1004 (K/K) * T_video amp
  0.3066 (K/K) * T_noise diode-B
  0.1053 (K/K) * T_coax between TECs #1 and #2
 -0.3698 (K/K) * T_radiometer (TEC#1) plate center
  0.0177 (K/K) sum of temperature coefficients
 -5.1797 (K) offset
corresponding Tb errors for "standard" test cases
(1000 s boxcar integrations apply):
  0.0154 K for points > 260 hours (23 C)
  0.0207 K for points 140 to 240 hours (70 C)
  0.6770 K for points > 140 (70 and 23 C)
```

Appendix-C

Recalculated fit coefficients based on the six thermistors selected in Equations 16 and 17. Associated errors are provided in Table 9.

```
CASE#0:  regressions based on   0.0 to 300.5 hours (all data)
 -0.1374 (K/K) * T_isolator at LNA input
  1.3583 (K/K) * T_reference load
 -1.2069 (K/K) * T_coax at dicke switch input
  0.3223 (K/K) * T_noise diode-C
 -0.3116 (K/K) * T_antenna load
 -0.0396 (K/K) * T_coax near antenna (TEC#2)
 -0.0148 (K/K) sum of temperature coefficients
  4.4029 (K) offset

CASE#1:  regressions based on   0.0 to 100.0 hours (steps and sweeps)
 -0.1515 (K/K) * T_isolator at LNA input
  1.5092 (K/K) * T_reference load
 -1.3263 (K/K) * T_coax at dicke switch input
  0.2538 (K/K) * T_noise diode-C
 -0.1243 (K/K) * T_antenna load
 -0.1744 (K/K) * T_coax near antenna (TEC#2)
 -0.0134 (K/K) sum of temperature coefficients
  3.8957 (K) offset

CASE#2:  regressions based on 260.0 to 300.5 hours (steady 23C)
 -0.0974 (K/K) * T_isolator at LNA input
  1.3205 (K/K) * T_reference load
 -1.2784 (K/K) * T_coax at dicke switch input
  0.2231 (K/K) * T_noise diode-C
 -0.3900 (K/K) * T_antenna load
  0.1624 (K/K) * T_coax near antenna (TEC#2)
 -0.0598 (K/K) sum of temperature coefficients
 17.9003 (K) offset

CASE#3:  regressions based on 140.0 to 240.0 hours (steady 70C)
 -0.0952 (K/K) * T_isolator at LNA input
  0.7569 (K/K) * T_reference load
 -0.7299 (K/K) * T_coax at dicke switch input
  0.3887 (K/K) * T_noise diode-C
 -0.5438 (K/K) * T_antenna load
  0.0942 (K/K) * T_coax near antenna (TEC#2)
 -0.1291 (K/K) sum of temperature coefficients
 41.0454 (K) offset

CASE#4:  regressions based on 140.0 to 300.5 hours (70C & 23C)
 -0.1349 (K/K) * T_isolator at LNA input
  0.9134 (K/K) * T_reference load
 -0.8269 (K/K) * T_coax at dicke switch input
  0.3766 (K/K) * T_noise diode-C
 -0.5172 (K/K) * T_antenna load
  0.1482 (K/K) * T_coax near antenna (TEC#2)
 -0.0407 (K/K) sum of temperature coefficients
 12.3082 (K) offset
```

Appendix-C (cont.)

```
CASE#5:  regressions based on  90.0 to 130.0 hours (70C & 23C)
 -0.1269 (K/K) * T_isolator at LNA input
  1.2814 (K/K) * T_reference load
 -1.2061 (K/K) * T_coax at dicke switch input
  0.3037 (K/K) * T_noise diode-C
 -0.4293 (K/K) * T_antenna load
  0.1363 (K/K) * T_coax near antenna (TEC#2)
 -0.0408 (K/K) sum of temperature coefficients
 12.2545 (K) offset
CASE#6:  regressions based on  65.0 to  95.0 hours (+/- 5K steps)
  0.0170 (K/K) * T_isolator at LNA input
  0.9159 (K/K) * T_reference load
 -0.9226 (K/K) * T_coax at dicke switch input
  0.2458 (K/K) * T_noise diode-C
 -0.1564 (K/K) * T_antenna load
 -0.1223 (K/K) * T_coax near antenna (TEC#2)
 -0.0225 (K/K) sum of temperature coefficients
  6.7948 (K) offset
```

Appendix 2 Component Temperature Sensitivity

JET PROPULSION LABORATORY INTEROFFICE MEMORANDUM

FROM: Alan Tanner
TO: USR team
DATE: 7/11/3
SUBJECT: loss and excess noise analysis of various components

This memo reports data collected by the USR testbed at JPL between April and June of 2003. Measurements of the insertion loss and of the excess noise versus device temperature are reported for the Peregrine SPDT and SPST FET switches, the PIN diode switch, waveguide/coax adaptors, coaxial isolator, diplexer, and the Goddard-built noise diode / coupler assemblies.

The analysis presented below follows that of my previous memo of 2/19/03, "noise diode thermal tests," and adds some better modeling which accounts for standing waves between the radiometer and the devices being tested.

1. Testbed Configuration

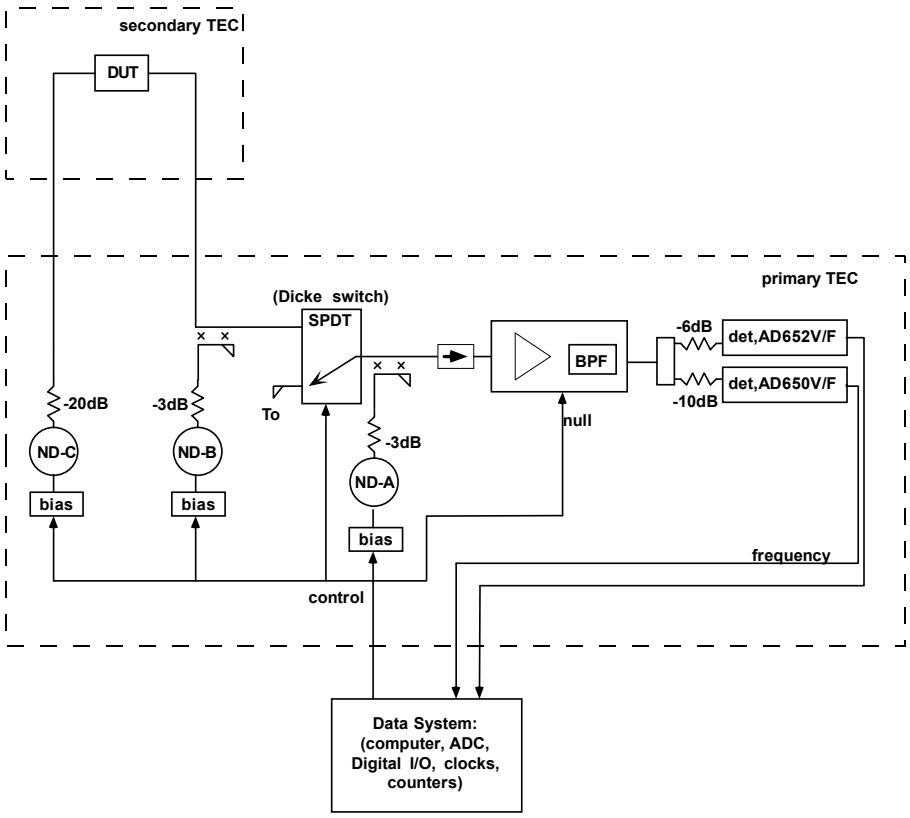

Figure 1: testbed layout

The configuration of the testbed is given in Figure 1. As described previously (see my 2/19/03 IOM, "noise diode thermal tests") the testbed consisted of a primary TEC plate which supported most of the radiometer, and a secondary TEC plate which cooled or heated the device under test (DUT). The DUT and radiometer were well insulated from the room air temperature with foam, and the temperatures of the two plates could be set anywhere between about 0 and 80 C under the control of a computer. In all tests presented below the radiometer was held at a constant 23 C and the DUT temperature was ramped up and down at a rate of +/- 2 degrees / 5 minutes repeatedly

between 0 and 60 C. The standard test sequence involved 12 hours of such ramps, or about five ramp cycles between 0 and 60 C, followed by 12 hours at a steady temperature of 23 C.

Some hardware upgrades since February include better test cables, and better heat sink techniques. The test cables used to connect the DUT to the radiometer where upgraded from the 0.085 inch semi rigid to a pair of flexible low-loss Storm coaxial cables. Each cable was two feet in length, and had an insertion loss of -0.3 dB which was very stable with cable flex. Heat sinking was improved by thermally shunting the ends of these test cables to the TEC plate with some specially fabricated clamps. These clamps greatly reduced thermal gradients within the DUT and thereby improved confidence in the measured device temperature.

The focus of the April-June tests were to measure the insertion loss and the excess noise temperature of various devices over a range of physical temperature. Insertion loss was measured as before with the noise diode-C versus noise diode-A deflection ratio. The "excess" noise, T_E, was estimated by comparing the radiometrically measured brightness temperature, T_B, to a thermistor measurement of the "antenna" load, T_A, according to

$$T_E = T_B - T_A . \tag{1}$$

In most of the tests the 20dB pad connected to noise diode-C in Figure 1 served as the antenna load. The physical temperature of this pad was assumed to equal the noise temperature at its output when noise diode-C was turned off. There was some concern that residual noise from the noise diode may have been significant, so the above assumption was tested by comparison with a matched load. These tests confirmed that there was no such problem: there was no discernable difference between the pad and the load at the 0.1K level, and direct measurements of the noise diode without a pad revealed less than 1 K excess noise from residual diode heat (or less than 0.01K after the 20 dB pad).

2. Calibration

Brightness temperature, T_B, was computed from the reference and noise diode-A response according to

$$T_B = T_o - \frac{V_o - V_A}{V_{oNDA} - V_o} T_{NDA} , \tag{2}$$

where T_o is the Dicke switch reference temperature, as measured with a thermistor, V_o is the radiometer response to the reference, V_A is the "antenna" response (i.e. looking towards the DUT), V_{oNDA} is the reference-plus-noise-diode-A response, and T_{NDA} is the calibrated noise diode-A noise temperature.

Note that only noise diode-A was used in Equation 2 to measure system gain. Also note that noise diode-A was only used when the Dicke switch was in the reference mode. The Dicke switch and noise diode was used in this manner to isolate the measurements from source impedance of the DUT, which changed from device to device. These impedance mismatches otherwise interacted with leakage of the noise diode signals to create standing waves which significantly degraded the noise diode-B and the antenna-mode-noise-diode-A reliability. These mismatches also interacted with the input impedance of the radiometer to create other standing wave problems- to be discussed shortly.

Calibration data were collected in two tests: one test with a matched load as the DUT, and one test with a short 2 inch length of semi-rigid cable as the DUT. The matched load data was used to calibrate noise diode A by regression of brightness temperature versus load temperature. The second test was used to calibrate noise diode C with respect to A, and to measure insertion loss of the test cables versus cable temperature. Insertion loss, L, was measured with the noise diode-C / noise diode-A deflection ratio as

$$g \equiv \frac{1}{L} = \frac{V_{ANDC} - V_A}{V_{oNDA} - V_o} \frac{T_{NDA}}{T_{NDC}} \tag{3}$$

where g is defined here as the inverse of insertion loss (which is proportional to gain), V_{ANDC} is the response to noise diode-C, T_{NDC} is the noise diode-C temperature, and the other terms are from Equation 2. Initially, the 2-inch thru-cable test was used to calibrate T_{NDC} by assuming that mismatches and standing waves were small, and applying the following radiative transfer model:

$$T_B \cong gT_A + (1-g)T_D \tag{4}$$

where T_D is the device temperature. By this model, T_{NDC} was adjusted until the excess noise predicted by Equations 3, 4, and 1 matched the measured data of Equations 1 and 2. This approach worked well for devices that were well

matched, but it proved inadequate for devices that were poorly matched. Specifically, the Peregrine FET switches had some mismatch problems, and the radiometer itself had a bad mismatch at its input due to a poorly matched Dicke switch (a PIN diode switch). The standing wave between the DUT and the radiometer in these tests made it difficult to determine whether the excess noise of the FET switch was caused by passive losses, or active bias current noise (e.g. due to gate leakage).

To resolve the standing wave issues, a network analyzer was borrowed to measure the complex port impedances of the various devices. As depicted in Figure 2, the port impedances were measured looking into the device (Z_D) and into the radiometer (Z_r) at the connection to the radiometer. These impedances were then used to estimate the reflection coefficient, Γ, which was needed to separate reactive losses from ohmic losses. The reactive losses account for noise which originates in the radiometer and reflects off of the DUT. In Figure 2, the noise emitted by the radiometer towards the DUT was approximated by the radiometer's reference temperature, T_o, since the radiometer's input included a ferrite isolator of the same temperature. This isolator is also critical to the following model since it isolates LNA noise- which might otherwise interfere with itself. The net temperature reaching the radiometer, T_B, was thus modeled as a sum of terms involving the 'antenna' temperature, T_A, the device temperature, T_D, and the reflected temperature, T_o, according to the following radiative transfer equation:

$$T_B \cong T_A g_\Omega g_\Gamma + T_D g_\Gamma (1 - g_\Omega) + T_o (1 - g_\Gamma) \tag{5}$$

where g_Ω is the inverse of ohmic insertion loss, and g_Γ is the inverse of reactive loss. The reactive losses were calculated from

$$g_\Gamma = 1 - |\Gamma|^2 = 1 - \left| \frac{Z_D - Z_r}{Z_D + Z_r} \right|^2 . \tag{6}$$

Note that Equation 6 only depends on the port impedances, and not on the transmission line impedance, so these losses do not necessarily equal the losses one would measure into 50 ohm devices (e.g. as would be the standard of a scattering matrix).

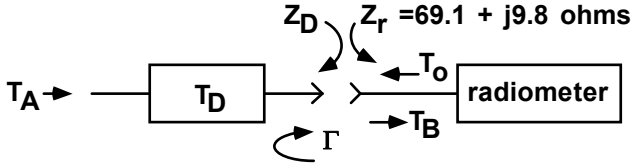

Figure 2: model used to account for reflected device losses. The port impedances, Z_D and Z_r, were measured with a network analyzer at the point where the test cable could be disconnected from the radiometer input.

To properly apply Equations 5 and 6, it was also necessary to revise the calibrations of the noise diode temperatures, T_{NDA} and T_{NDC}. Using the matched load data, T_{NDA} was revised by regression of the measured noise temperature of Equation 2 to that predicted by Equation 5 with g_Ω set to unity and g_Γ calculated from Equation 6 with the measured impedances. The reactive gain term, g_Γ, was about 0.96 in this case, and the result of this new calibration was to deliberately lower the sensitivity of T_B to changes in T_A. This is illustrated in Figure 3, which plots the excess noise of Equation 1 as the matched load temperature was varied. Figure 3 also compares the radiometric data (black) to the noise temperature predicted by Equation 5 (green)- to which the radiometer was calibrated. The slope of these curves would be zero only if the radiometer were matched to the load (if $g_\Gamma = 1$).

Similarly, noise diode-C was calibrated from the 2-inch coaxial test by matching the excess noise of Equation 1 to the noise predicted by Equations 5 and 6, given the measured impedances, and the measured loss computed from Equation 3 and

$$g_\Omega = g / g_\Gamma . \tag{7}$$

Figure 4 illustrates the theoretical and measured excess noise curves after this calibration. In this case T_A was the temperature of the 20 dB pad of Figure 1, which was held at a constant temperature, and ohmic losses in the test cables resulted in an excess noise which increased slightly as the ends of the test cables were heated. The slope of both curves of Figure 4 would only be zero if there were no ohmic losses (if $g_\Omega = 1$). The ohmic losses were measured with Equations 3 and 7, and these also varied slightly with temperature- as shown in Figure 5. Nominally, these data indicate there is approximately 5% loss in the test cables, or 0.2 dB, which can be associated with the temperature variations applied to the ends of the test cables as devices are tested. Most of the cable was relatively stable in temperature, so this loss was only a fraction of the net cable loss. Between the 20 dB pad of Figure 1 and

the radiometer, the net insertion loss of the test cables was 0.7 dB, as measured with the network analyzer. For the present analysis, the 0.2dB loss has been treated as a lumped element loss of temperature T_D.

To date, none of the tested devices- including the load and the test cables- have shown any sensitivity in the reactive loss to the device temperature which could be detected by the network analyzer. The sensitivity and stability of the network analyzer was about 1% (.05dB in the reflection coefficient), and the process of sweeping the temperature while recording port impedances has not been automated. So not all devices were tested. But spot checks of the Peregrine switches, the matched load, and the test cables revealed no significant correlation between port impedance, Z_D, and device temperature, T_D. Such correlations undoubtedly exist- and might easily be significant in larger systems or at higher frequencies- but they couldn't be detected with the network analyzer in these tests. Also note that the curve of Figure 5 indicates only 0.3% change over the full temperature range, which would be difficult to measure with the network analyzer.

Another point of interest in Figure 5 is the red curve, which is a fit of the measured losses to the following form:

$$g_\Omega = 1 - b\sqrt{T_D} \tag{8}$$

where b is a fit coefficient. This formula is based on an educated guess as to the nature of the ohmic losses. In my previous memo of 2/19/3, the copper losses of coaxial cable were found to agree well with theory, and these losses changed as the square root of the bulk electrical conductivity. Measurements also agreed with published temperature coefficient for copper bulk resistivity of 3900 ppm/K near 290 K, which suggests that resistivity is linear with temperature since a linear extrapolation of 3900 ppm/K nearly intersects zero resistance at zero Kelvin. Thus we might expect electrical loss to change as the square root of temperature. In Figure 5, the curve of Equation 8 is in reasonable agreement with the measured loss of the test cables, so these data suggest that variations in ohmic losses are indeed the primary variable with temperature, and that reactive losses are relatively stable.

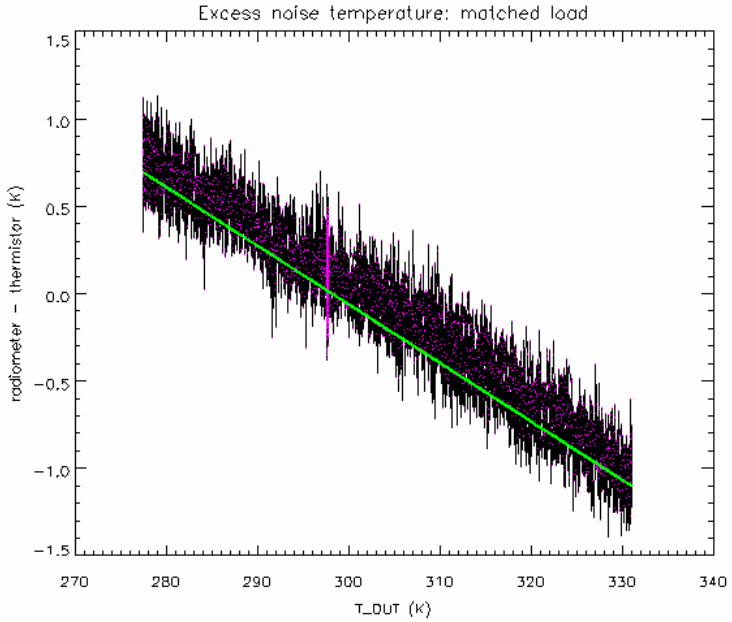

Figure 3: Comparison of radiometric and thermistor temperatures for the matched load calibration. The green line is the excess noise predicted by Equation 5, given the impedance mismatches of the system. The black data points are the calibrated radiometric response of Equation 2. Both curves are plotted as excess noise according to Equation 1.

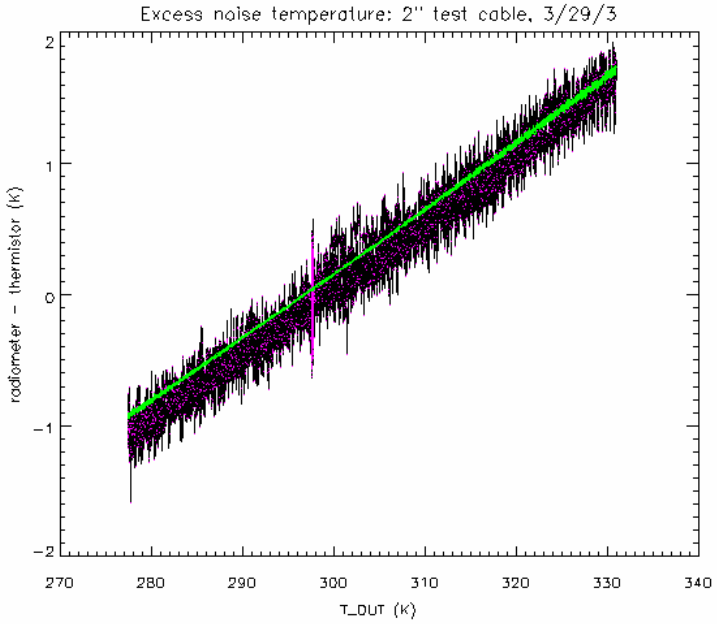

Figure 4: Excess noise produced by the test cables, as measured using a short length of coaxial cable in place of the DUT. The green curve is the noise predicted by Equations 5 and 6 given the measured impedances and the measured ohmic loss of Figure 5.

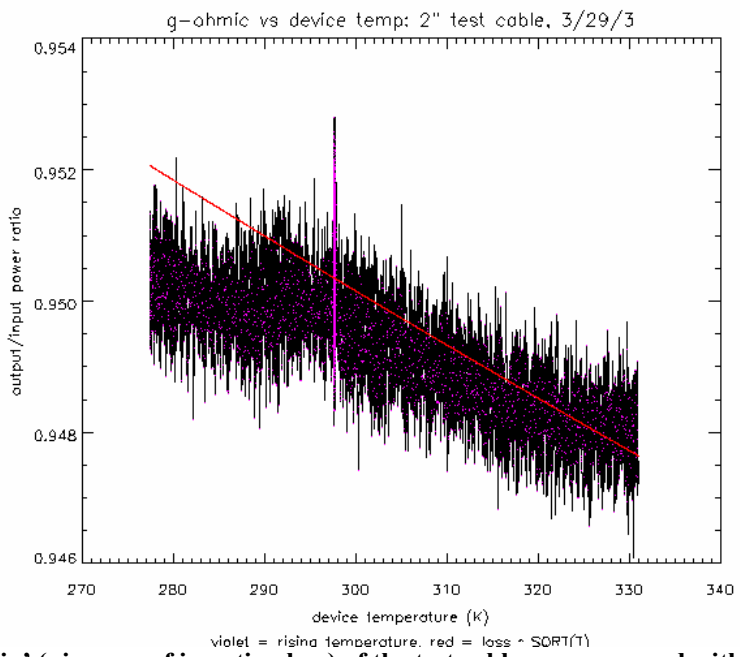

Figure 5: ohmic 'gain' (=inverse of insertion loss) of the test cables, as measured with the noise diode C/A deflection ratio of Equation 3, and scaled to ohmic losses with Equation 7. The red curve represents a fit to Equation 8- in which ohmic losses follow a SQRT(T) trend- which is believed to be a reasonable model for copper electrical loss.

Regression fits of Figures 4 and 5 yields the following

$$\begin{aligned} g_{\Omega-\text{thru}} &= 0.981 - 0.00182 * \sqrt{T_D} \\ T_{E-\text{thru}} &= -14.60 + 0.0487 * T_D \end{aligned} \tag{9}$$

These fits have been applied as corrections to the gain and excess noise measurements presented in the next section according to

$$\begin{aligned} g_{\Omega-\text{corrected}} &= \frac{g_\Omega}{g_{\Omega-\text{thru}}} \\ T_{E-\text{corrected}} &= T_E - T_{E-\text{thru}} \end{aligned} \quad . \tag{10}$$

No such corrections were applied to tests of components of high isolation, such as switches that were in the 'off' mode.

3. Test Results

a) Peregrine FET switches

The two FET switches that were tested were the Peregrine model PE4246 (SPDT) and PE4220 (SPST). The SPST switch had an internal load so that the switch was matched in the high isolation state (off). The SPDT switch was terminated externally on the second input port for these tests. These devices are sold as surface mount integrated circuits, but we procured them pre-mounted on fiberglass 'development' boards with SMA connectors. To avoid stray radio noise in the laboratory, we also mounted these circuit boards in metal boxes.

These switches were meant to operate from a specified supply voltage of 3 volts, but we found that they produced a large excess noise signal at that voltage. We also found that the noise decreased rapidly when the supply voltage was lowered. Figure 6 plots the excess noise of the SPDT switch as the supply voltage varied, and Figures 7 and 8 show the excess noise as temperature was varied in the 'on' and 'off' states, respectively, while holding the supply voltage at 3 volts. Clearly, these switches will unacceptable as Dicke switches; the excess noise is too large- too sensitive to supply voltage- very asymmetric in the two switch positions- and highly nonlinear with temperature. However, based on Figure 6, and other data which showed that the switch loss and isolation did not degrade

significantly through a range of 1 to 3 volts, the thermal tests were repeated at 1.5 volts. These test results are provided in Figures 9 and 10, which show that the excess noise is in good agreement with the noise predicted by the radiative transfer calculation of Equation 5. An example of the insertion loss for the SPST switch is plotted in Figure 11 for the 3 volt supply, and Figure 12 for the 1.5 volt supply, and these show a slight degradation with the lower voltage (0.8 vs. 1.1 dB ohmic insertion loss at 25 C). The SPDT switch exhibited better loss characteristics, as shown in Figure 13 (about 0.5 dB ohmic insertion loss). Overall, however, the SPST and SPDT both exhibited large reactive losses, as summarized in Table 1 at the end of this section. One suspected problem with these switches was that they were mounted on development boards which were not built from proper microwave materials: they were built on multi-layer glass-epoxy boards common for digital electronics, and it is not known how well these materials perform at microwave frequencies.

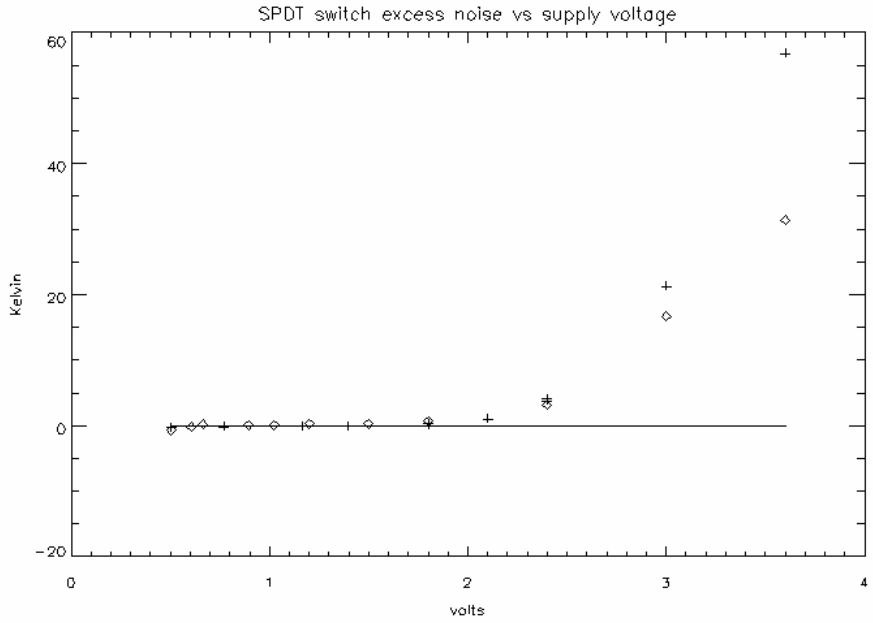

Figure 6: SPDT excess noise as a function of supply voltage in the 'on' state (+) and 'off' state (o).

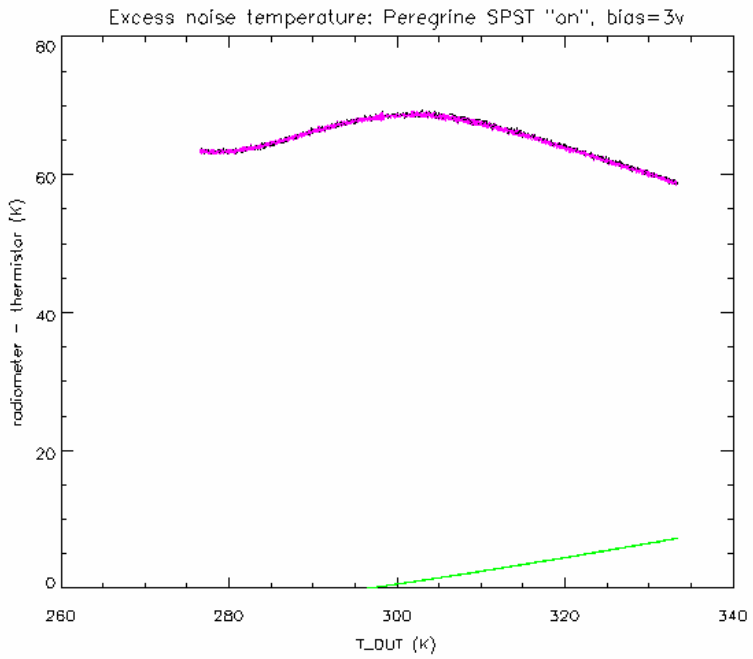

Figure 7: Excess noise of the SPST switch in the 'on' mode (low isolation). As in all such plots, violet data points are an overlay of the measured noise as the device temperature was increasing. The green line is the calculated excess noise derived from the radiative transfer equation (5) using the measured reactive and ohmic losses, and the physical temperature of the device.

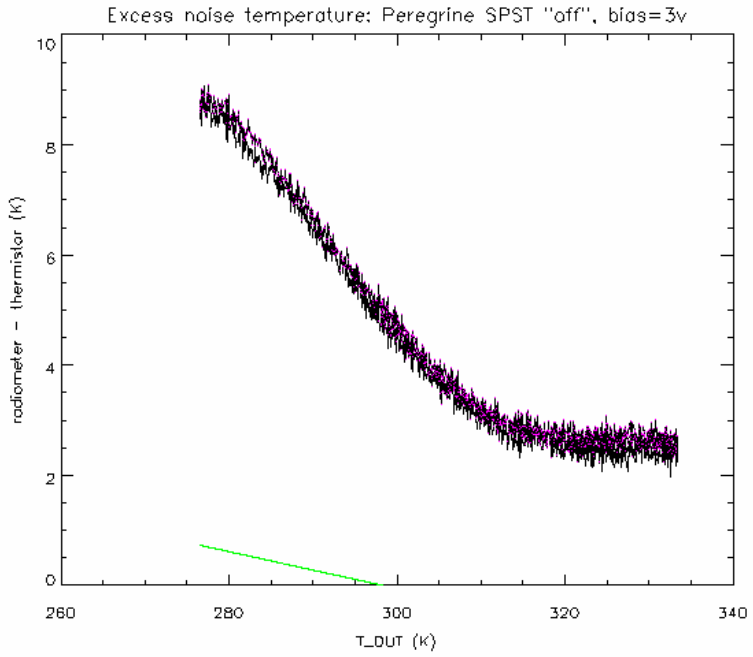

Figure 8: Excess noise of the SPST switch in the 'off' mode (high isolation). In this case, T_A was measured by a thermistor attached to the switch integrated circuit.

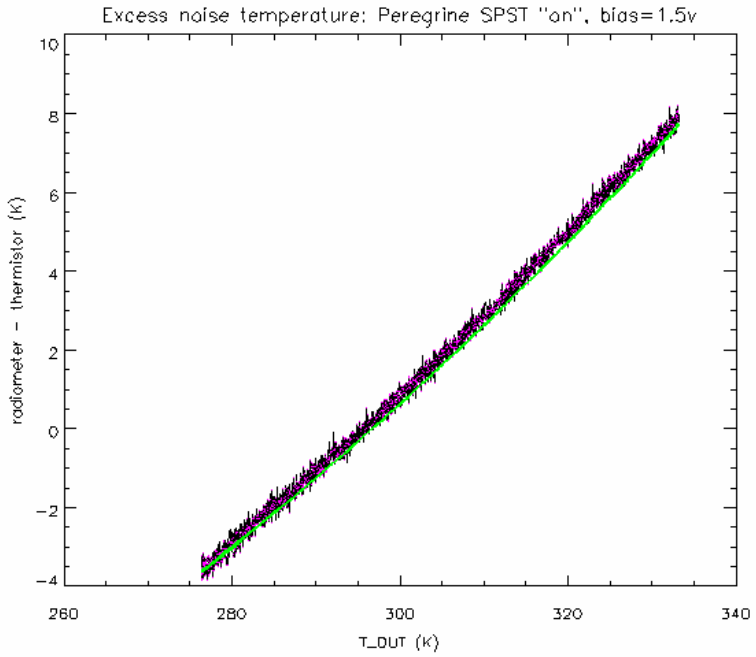

Figure 9: same as Figure 7, but with lower supply voltage.

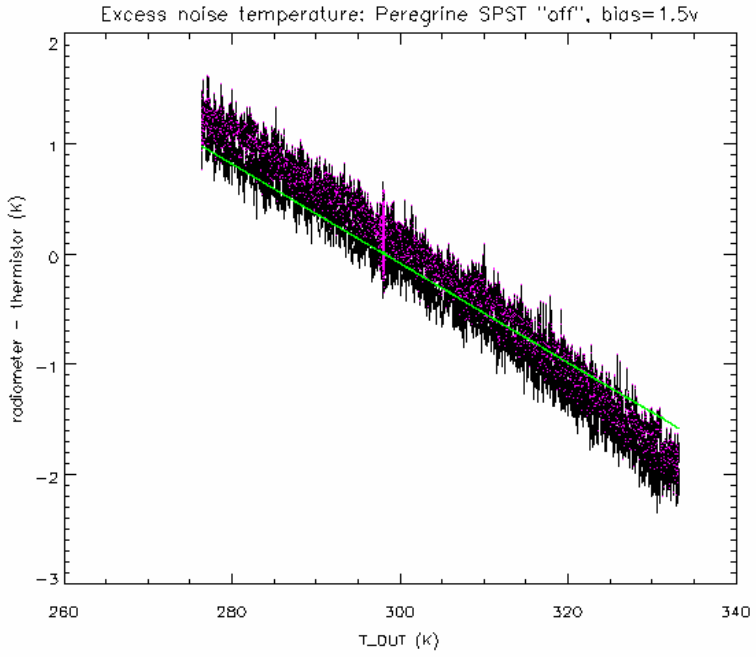

Figure 10: same as Figure 8, but with lower supply voltage.

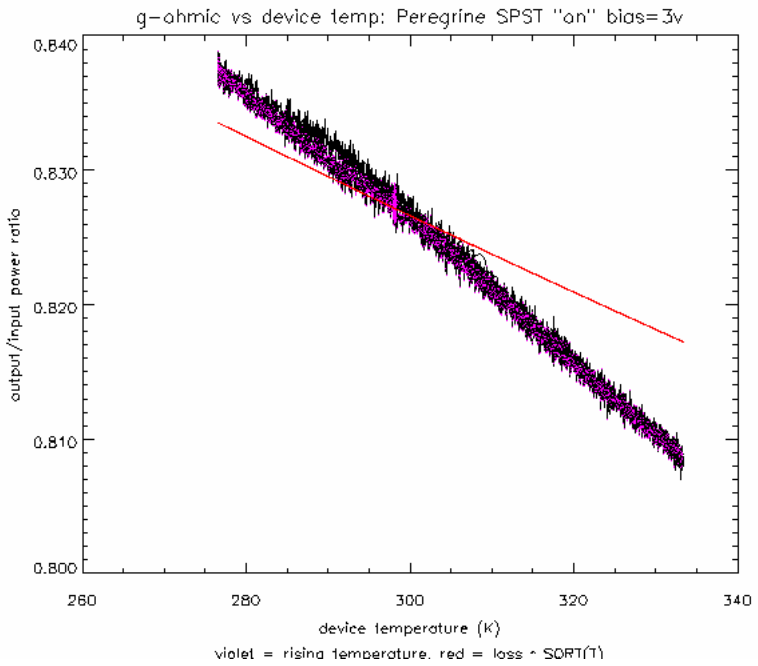

Figure 11: g_Ω (inverse of ohmic insertion loss) of the SPST switch at 3 volts, associated with Figure 7. The red curve is a fit to Equation 8.

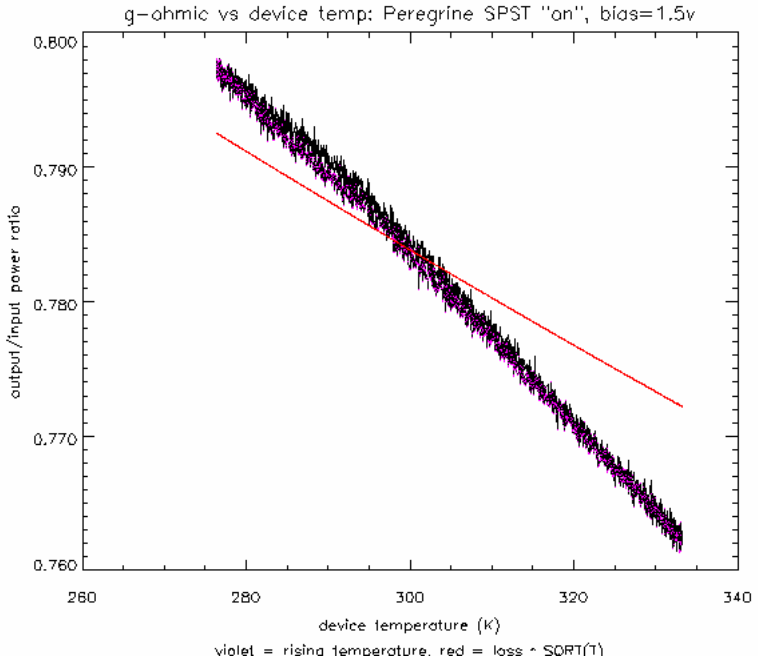

Figure 12: g_Ω of the SPST switch at 1.5 volts, associated with Figure 9. At this lower voltage, g_Ω decreased slightly.

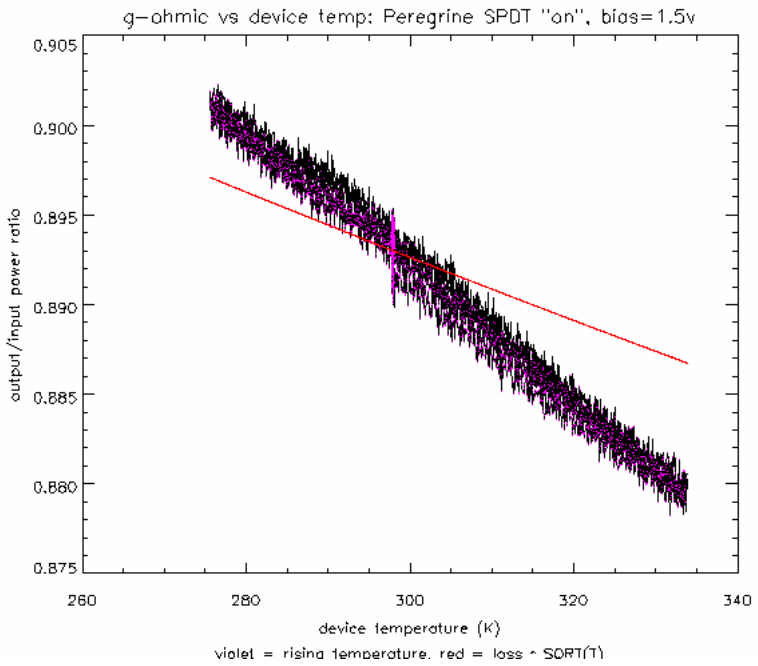

Figure 13: g_Ω of the SPDT switch at 1.5 volts

b) PIN diode switch

Only one PIN diode SPDT switch has been tested so far, and this switch was the same one used as the Dicke switch. The switch needed to be removed from the radiometer and placed on the secondary TEC plate for this test, so there was no Dicke switch and the excess noise was not measured. The excess noise of this switch is at least known to be balanced, however, based on other data. Only the insertion loss could be measured as a function of switch temperature, and these data are presented in Figure 14. As can be seen, the loss of this switch again matched the SQRT(T) trend, which suggests that much of the switches loss may be attributed to copper losses within the device.

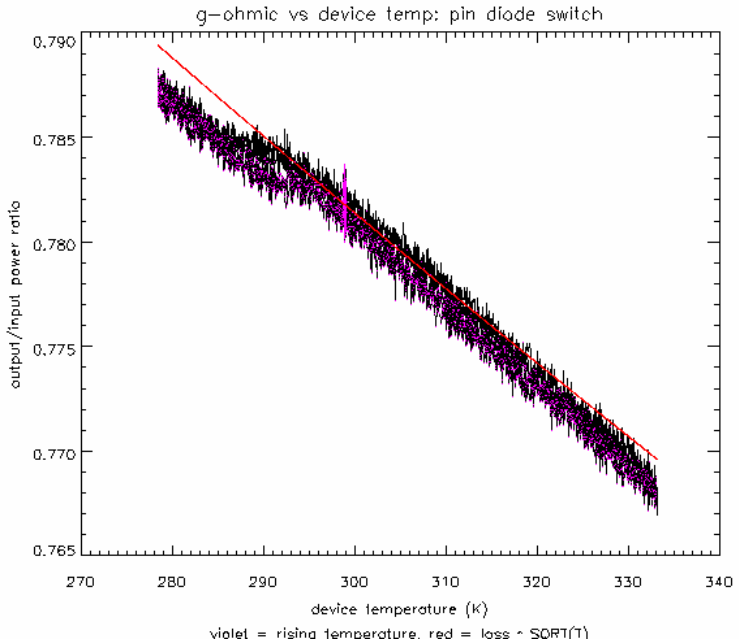

Figure 14: g_Ω of the PIN diode switch. This is the same switch that was used for the Dicke switch of Figure 1, so it needed to be removed from the radiometer to be tested on the secondary TEC plate.

b) Waveguide/coax adapters

Two waveguide/coaxial adapters were tested. The waveguide flanges were connected back to back, and N-type connectors on both ends needed to be adapted to SMA to connect the test cables. Also, since these devices were quite large, it was not possible to heat sink the test cables to the TEC in the same manner as the other test. There were also thermal gradients throughout the waveguide due to the bulk of these components and difficulties insulating the assembly from room temperature. Nonetheless, it was possible to confirm that these adapters exhibited very low loss, as shown in Figure 15.

c) Isolator

Test results of a coaxial isolator are plotted in Figures 16 and 17. The loss data of Figure 17 show a sort of hysteresis at the colder temperature range that is as yet unexplained. The violet overlay identifies the part of the curve in which the temperature was increasing.

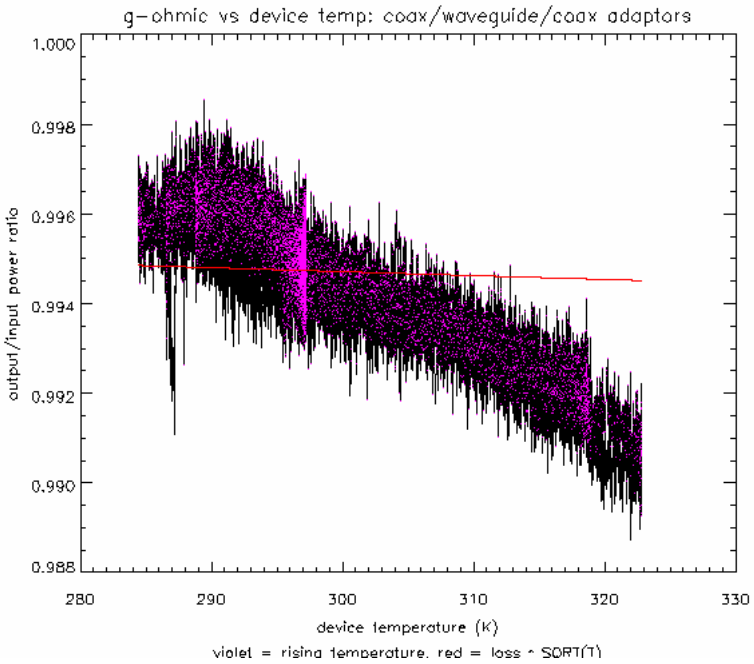

Figure 15: g_Ω of the waveguide adapters

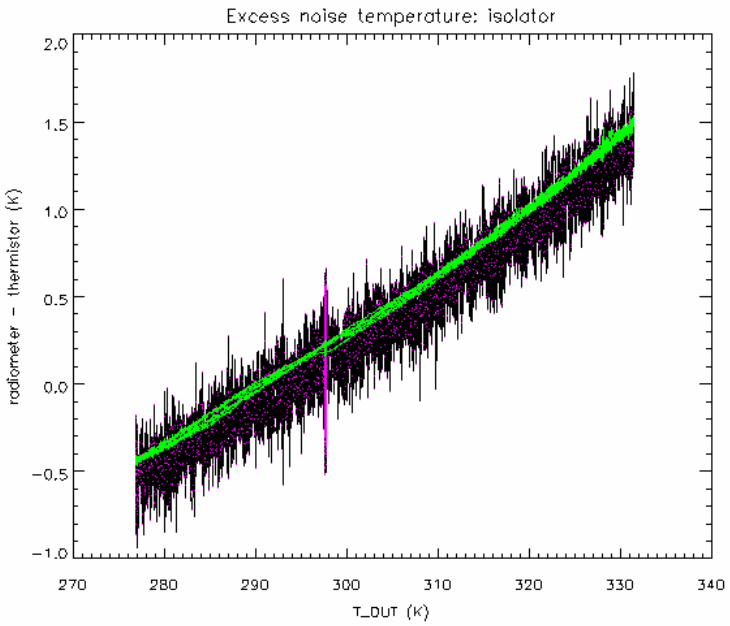

Figure 16: excess noise of the isolator

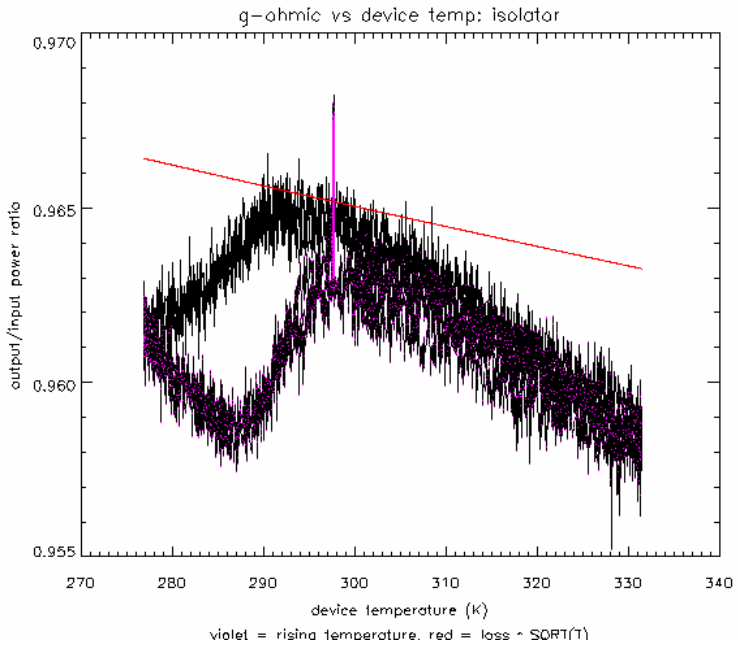

Figure 17: g_Ω of the isolator

d) Diplexer

The diplexer had some intermittence problem, as shown in Figures 18 and 19. Measurements of the input impedance and of the insertion loss on the network analyzer confirm that this device has some bad internal connection which changes as the device is shaken.

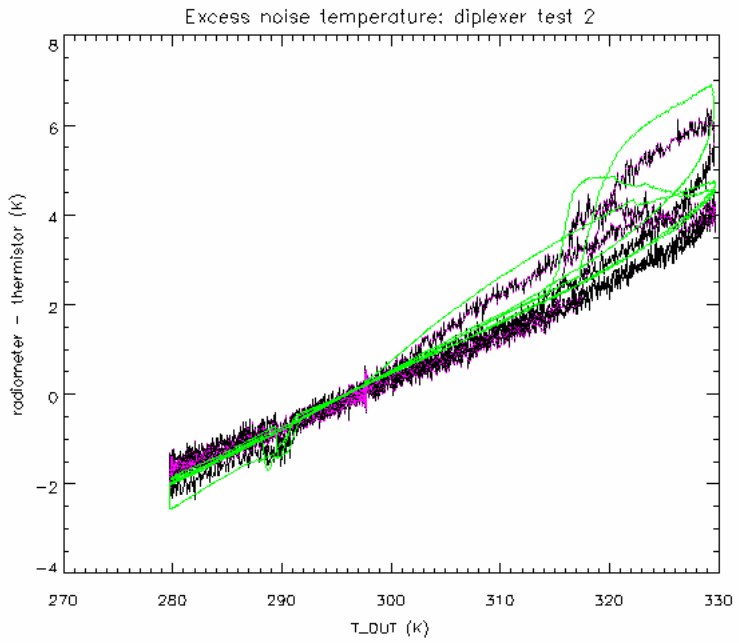

Figure 18: Excess noise of the diplexer.

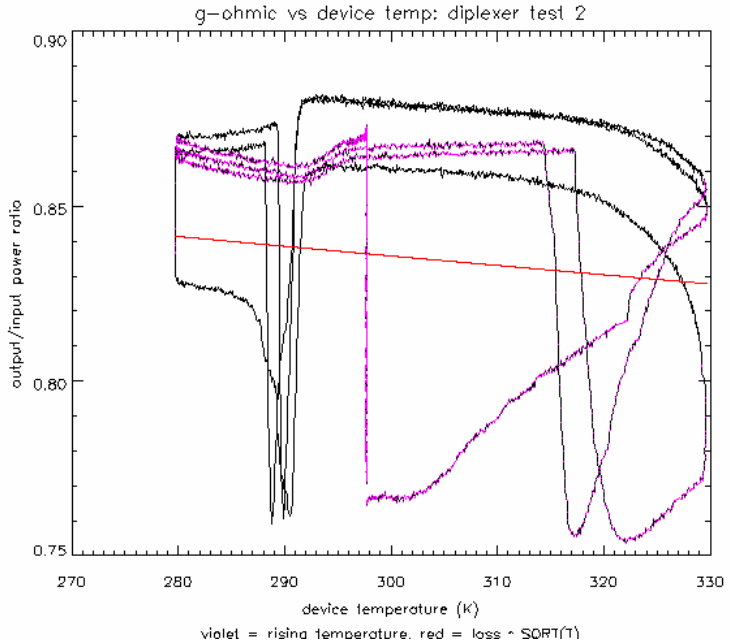

Figure 19: g_Ω of the diplexer. The port impedance of the diplexer also changed with the insertion loss, so the losses plotted here may not be entirely ohmic.

e) Goddard noise diode & coupler assemblies.

Test results for the four noise diode assemblies built at Goddard are presented in Figures 20 to 25. These assemblies consisted of a single directional coupler with a noise diode and an isolator attached to the forward coupled port, and a termination on the reverse coupled port. The thru-arm of the couplers of these assemblies were connected to the test cables of Figure 1 such that the noise diode coupled towards the radiometer.

Tests revealed that the thru-arm insertion loss and excess noise of all of these assemblies were very well matched, low loss, and were very stable. Figures 20 and 21 provide one such example. However, tests of the noise diodes revealed some problems. The noise diodes were tested with the regulated 6 mA source that normally biases noise diode-B in Figure 1, and the stability of the diode versus temperature was measured with the same noise diode deflection ratio that we have used in the past. Figures 22 thru 25 plot these ratios, and we see that only the serial number 8611 diode was well behaved. The 8614 assembly had a random 4% jump between two states, and the jumps did not travel in a consistent direction as the temperature rose or fell. The 8608 diode also had some small irregularities at the 0.5% level, and the 8607 diode showed a 1% higher output as the temperature was increasing. All four noise diode exhibited a consistent 4% rise over the 55 degree temperature range of the test, or about 700 ppm/K- which is encouraging since this is an improvement over any diode that we have tested to date. Aslo, the stable insertion loss of the couplers is an improvement over past results. But we will need to investigate the noise diode problems.

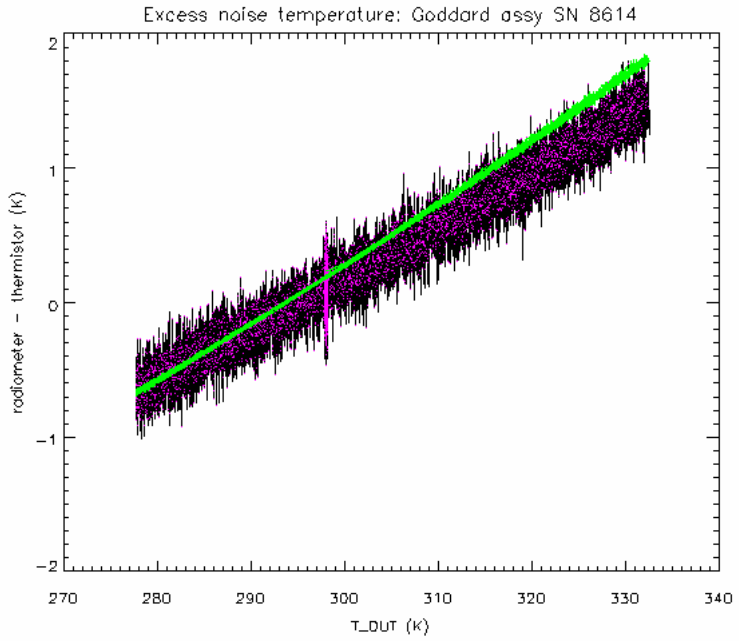

Figure 20: g_Ω of one of the Goddard built noise diode and coupler assemblies; all four assemblies exhibited a similar curve.

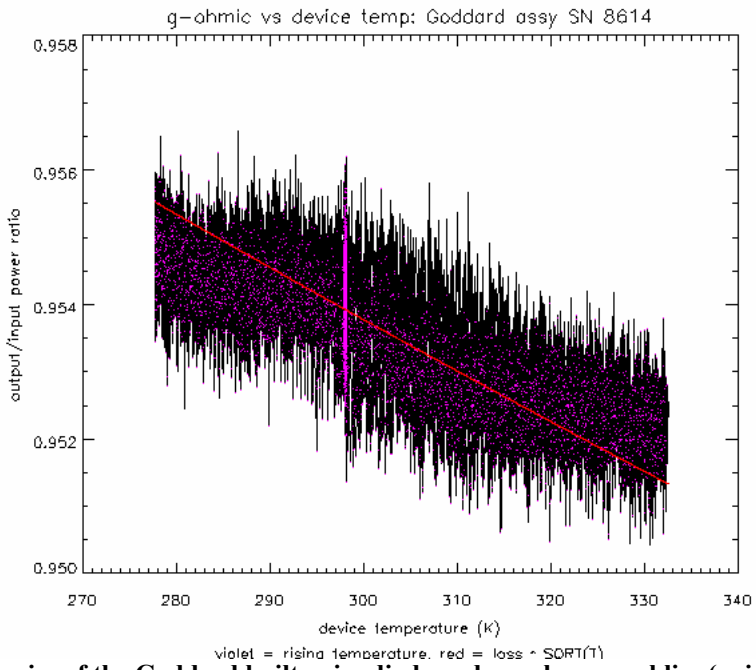

Figure 21: Excess noise of the Goddard built noise diode and coupler assemblies (noise diode switched off); all four assemblies exhibited a similar curve.

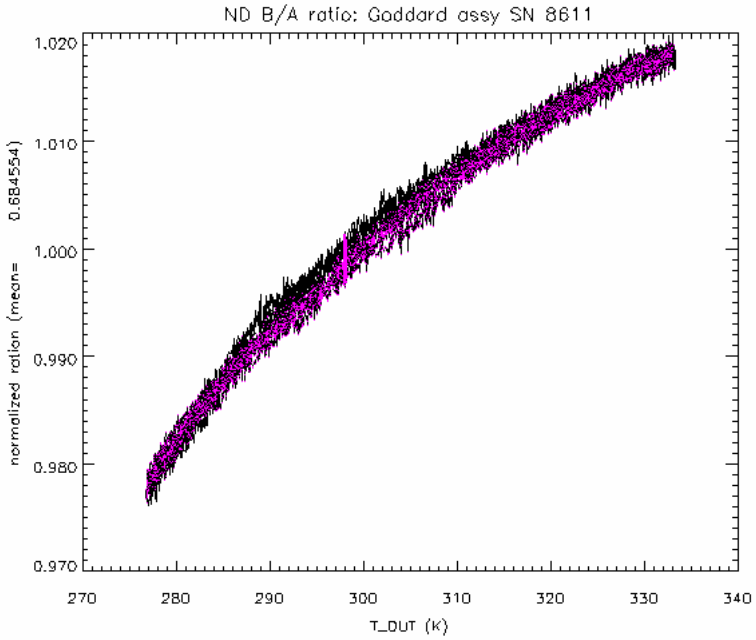

Figure 22: Noise diode deflection ratio for the S/N 8611 Goddard assembly, where noise diode-B is the noise diode within the assembly. The bias current was 6 mA. This was the most stable of the four noise diodes tested.

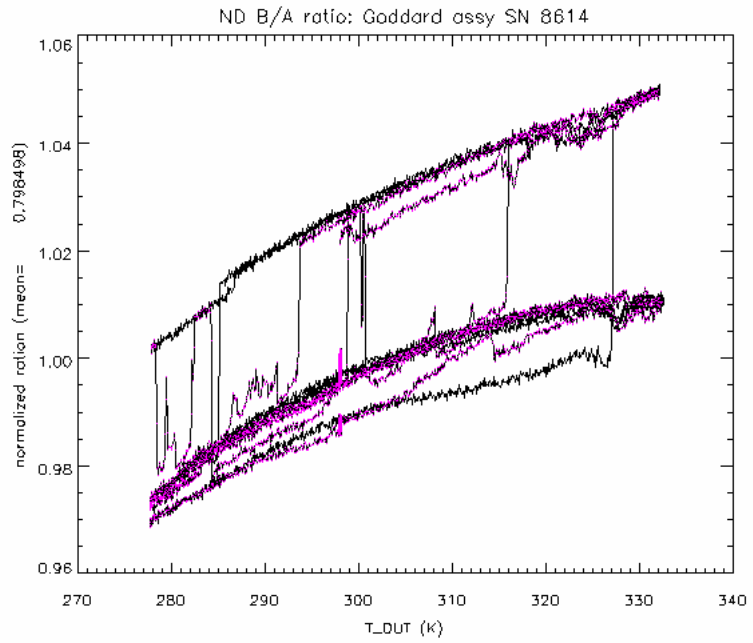

Figure 23: Noise diode deflection ratio for the S/N 8614 assembly. This device was tested twice with similar results. The source of the apparent intermittence is not yet known. Also see Figures 20 and 21, which show no corresponding intermittence in the thru-arm of the coupler.

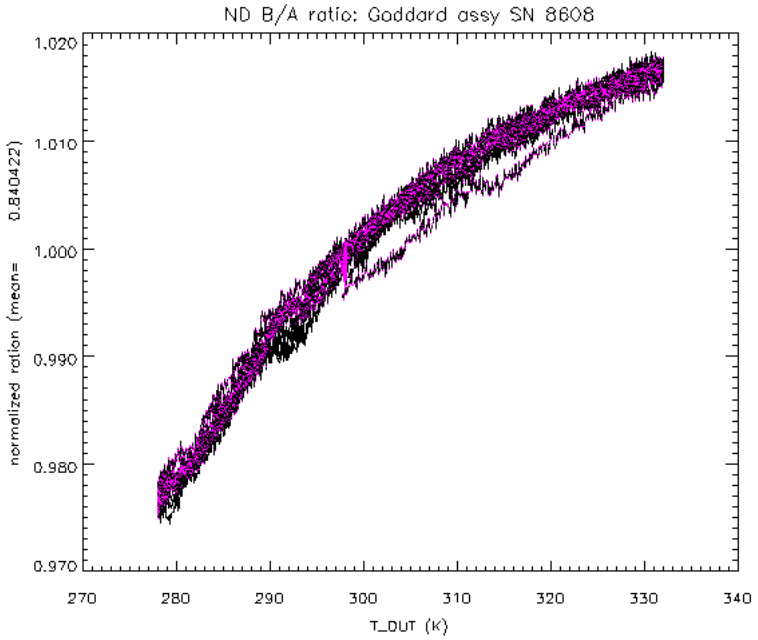

Figure 24: Noise diode deflection ratio for the S/N 8608 assembly.

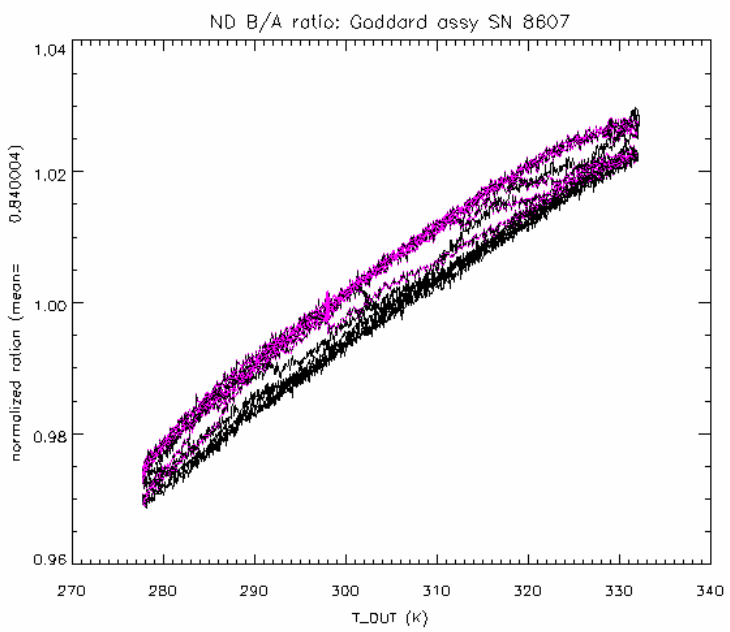

Figure 25: Noise diode deflection ratio for the S/N 8607 assembly.

no.	DUT	Z_D real ohms	Z_D imag. ohms	g_Γ react-ive	g_Ω ohmic at 25C	$\frac{\partial g_\Omega}{\partial T_D}$ ppm/K	1-g (fract-ional loss)	$\frac{\partial T_E}{\partial T_D}$ predicted	$\frac{\partial T_E}{\partial T_D}$ measured
0	Peregrine SPDT "on" bias=1.5v	35.73	3.70	0.897	0.893	-384.	0.199	0.093	0.079
1	Peregrine SPDT"off" bias=1.5v	35.30	4.60	0.895				-0.104	-0.130
2	2" test cable 3/29/3	48.50	2.50	0.966	1.001	-16.	0.034	0.001	0.003
3	Peregrine SPST "on" bias=1.5v	43.95	-2.41	0.939	0.785	-623.	0.263	0.199	0.202
4	Peregrine SPST "off" bias=1.5v	48.59	-4.50	0.955				-0.045	-0.056
5	Peregrine SPST "off" bias=3v	48.59	-4.50	0.955				-0.045	-0.114
6	Peregrine SPST "on" bias=3v	43.95	-2.41	0.939	0.827	-515.	0.223	0.161	-0.087
7	matched load	48.80	2.20	0.967				-0.033	-0.034
8	pin diode switch				0.782	-370.			
9	coax/waveguide/coax adaptors	49.37	2.57	0.969	0.995	-142.	0.036	0.007	-0.010
10	2" test cable 4/12/3	48.50	2.50	0.966	1.005	-1.	0.029	-0.004	0.002
11	Peregrine SPDT "on" bias=1.5v	35.73	3.70	0.897	0.896	-398.	0.196	0.091	0.091
12	isolator	43.00	2.60	0.942	0.965	-124.	0.091	0.036	0.036
13	diplexer test 1	48.80	2.20	0.967	0.857	-672.	0.172	0.152	0.130
14	diplexer test 2	48.80	2.20	0.967	0.836	-160.	0.192	0.145	0.129
15	Goddard assy SN 8611	50.85	5.73	0.976	0.953	-38.	0.070	0.046	0.036
16	Goddard assy SN 8614	53.40	4.96	0.982	0.954	-54.	0.063	0.046	0.039
17	Goddard assy SN 8608	48.80	2.20	0.967	0.973	-31.	0.060	0.027	0.035
18	Goddard assy SN 8607	52.63	5.60	0.981	0.954	-34.	0.064	0.045	0.037
19	repeat SN 8614	53.40	4.96	0.982	0.954	-59.	0.063	0.046	0.040
20	2" test cable 6/13/3	48.50	2.50	0.966	1.000	-0.	0.034	0.001	-0.000
21	load 7/9/3	48.80	2.20	0.967				-0.034	-0.051

Table 1: summary of test results, sorted chronologically. The complex input impedance of each device is given, along with the reactive and ohmic 'gains' (inverse of insertion loss). All ohmic gains were measured at 25 C and normalized to that of the 2 inch coaxial cable of test #20 with Equation 10. Ohmic gain is meaningless for the matched load and switches in the 'off' state, and has been omitted from the table in those cases. The variation of gain versus temperature near 25C is given in parts-per-million per Kelvin. The last three columns compare the fractional loss, computed as 1 - g, where $g=g_\Omega g_\Gamma$ from Equation 7, with the slope of T_E versus device temperature as predicted with Equation 5, and as measured.

4. Summary/ Conclusions

With this latest round of tests we have improved our modeling of component loss, and have been able to precisely predict the noise temperature seen through components with a combination of reactive and ohmic losses. In previous tests, we ignored the reactive component, and this undoubtedly lead to errors in our estimation of component loss since our testbed radiometer was not well matched to 50 ohms. Table 1 summarizes these test results, and in the last three columns provides a comparison of excess noise versus device temperature sensitivities predicted by (1) the net measured component loss (if we ignored the reactive component); (2) Equation 5; and (3) as measured. In all cases- particularly the Peregrine switches- the sensitivity estimates where greatly improved by including the reactive component. I expect that we will find more applications for such modeling in future work- especially in cases where one needs to predict the radiative transfer between major assemblies which are thermally decoupled.

The component test data revealed quite a large number of problems: The FET switches produce a lot of noise unless they are operated at about half of their rated voltage (this probably rules them out for a flight system unless much more extensive analysis and testing can be done to understand the problem); the frequency diplexer has a bad intermittent problem which needs to be fixed; the ferrite isolator had a strange hysteresis in the temperature curve that should be examined; and three of the four new noise diodes had different sorts of stability problems. These results really underscore the need for rigorous testing of flight hardware. Each of these would be a real problem for the Aquarius radiometers if they went undetected before flight.

Appendix 3 Non-Linear Correction

TO: USR team
FROM: Alan Tanner
SUBJECT: Herotek DT1020 detector linearity
DATE: 10/4/2

MEASUREMENTS:
The linearity of the Herotek DT1020 detectors have been measured using the USR testbed. The measurements were made by monitoring noise diode deflections as the antenna noise temperature was varied. Noise diode deflections are the difference in detector voltage between on and off states of the injected noise diode. The noise diode injection adds power to the antenna noise temperature, so the deflections should be constant with antenna temperature. Deviations from a constant reveal nonlinearities in the slope of the input power versus output voltage.

Two tests were conducted at two power levels. For the first, I left the gain settings of the V/F and the RF pads of the testbed as-is, per Bill Wilson's measurements of September 19. In this configuration the reference load (about 295 Kelvin) results in -34.1dBm of power at the detectors, and the measured detector voltages (for both the AD650 and Ad652 V/F's) are 0.24 mV, corresponding to a sensitivity of 0.61 mV/microwatt[4]. During the noise diode injection cycle the voltage increases to 0.58mV (which scales to -30.2dBm input power, or 0.95 microwatts). In the second test I lowered the gain of the AD650 V/F by a factor of six so that tests could be made at higher power levels. I then decreased the attenuator before the detector from -10dB to -3dB to raise the detector power without affecting amplifier power levels upstream of the detector. Between these two tests the linearity was measured in the range of -30dBm to -18dBm. The variable noise source that was introduced at the antenna port consisted of a noise diode and a variable attenuator.

Figure 1 shows how the ratio of noise diode deflections changed as the antenna noise temperature was adjusted (by switching the attenuator in 2dB increments). The ratio plotted in Figure 1 was computed from:

$$R = \frac{V_{aNDA} - V_a}{V_{oNDA} - V_o} \tag{1}$$

where V_{aNDA} is the measured voltage response to the antenna plus noise diode "A" (we also have noise diodes "B" and "C" in our testbed- which weren't used for these tests), V_a is the antenna-only measurement, V_{oNDA} is corresponds to the reference mode of the Dicke switch while noise diode "A" was on, and V_o is the reference-only measurement. Note that noise diode "A" is the only noise diode in the testbed that is injected after the Dicke switch. Equation 1 utilizes the reference mode noise diode deflections to normalize the measurements.

As can be seen in Figure 1, the noise diode deflection ratio is significantly affected by the power level.

Figure 2 provides the same data of Figure 1 in the form of a scatter plot against detector voltage. As can be seen in these figures, the detector sensitivity is about 4 to 5 % higher than the expected unity ratio when the detected voltage is 1.6mV- which corresponds to -25.8 dBm.

Figure 3 plots the results for the second test, in which the detector power maximum was increased to about -17.9 dBm. As can be seen, the non-linearity of the detector in this case is very significant, at about 30%. Taken togethr, Figures 2 and 3 show a systematic tendency for the detector to overestimate power at the higher power levels. I have, in the past, observed the very same pattern in AWVR data.

[4] According to the manufacturer, the open-circuit sensitivity of these detectors is supposed to be 1mV for -30dBm, which scales to 0.39mV at -34.1dBm. So our measured sensitivity is a little lower than specifications. Some of this discrepancy may be due to the fact that we load the diodes with 2k resistors. In any case, we are in the ballpark.

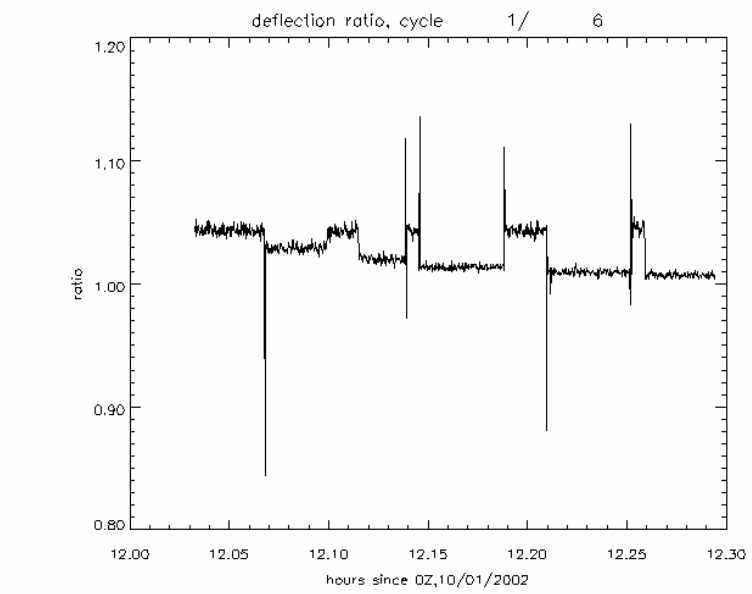

Figure 1: Time series of the noise diode deflection ratio as the antenna noise power was stepped through the attenuator sequence: 0,-2,0,-4,0,-6,0,-8,0,-10 dB. At 0 dB of attenuation the noise power reaching the detector was approximately -25.8 dBm. Transients are evident as the attenuator was switched, and these data can be ignored.

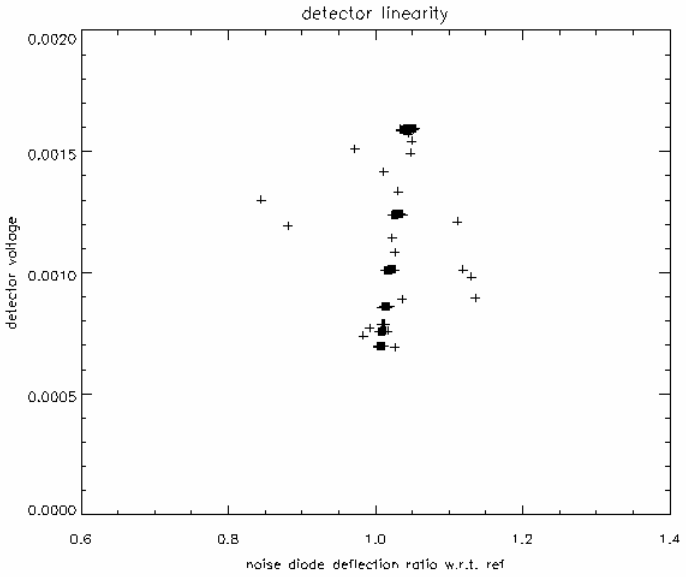

Figure 2: same data as Figure 1, except the deflection ratio is plotted on the horizontal axis and the vertical axis is the detected voltage during the antenna plus noise diode measurement.

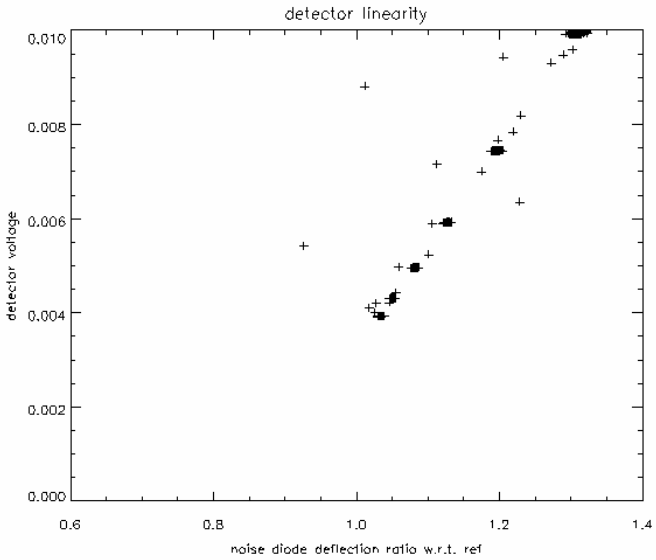

Figure 3: Noise diode deflection ratios for the second test. The maximum detected voltage of 10mV corresponds to a maximum input power of about -17.9dBm.

ANALYSIS:
The above data are differential measurements which compare the sensitivity of the detector at two points along the curve of the input power versus output voltage. In principle we ought to be able to reconstruct the input/output curve by integrating the differential measurements. However, our sensitivity isn't very good, and the integral solution will be complicated by the fact that it takes a fairly substantial noise diode deflection to see the nonlinearity. An alternate approach is to simply guess at a formula to 'linearize' the detector, then solve for one or more coefficients until the data of Figures 2 and 3 fall on a vertical line (i.e. to a unity deflection ratio).

I have in the past experimented with many ad-hoc linearizing formula, including power law relations and polynomial corrections, but I never found any that satisfactorily worked over a wide range of power levels. Recently, however, I tried the following form:

$$V_{linearized} = C \ln\left[\left(V_{detected} + C\right)/C\right]. \qquad (2)$$

where $V_{detected}$ is the measured detector voltage and $V_{linearized}$ is the corrected voltage. The C coefficient is simply adjusted until the deflection ratios such as Figures 2 and 3 are desensitized to the offset power. This form was motivated by the familiar diode formula where current is proportional to exp(qV/kT)-1. Equation 2 is simply an inversion of the diode formula where I have substituted current with $V_{detected}$ and power with $V_{linearized}$. I have not yet justified this form rigorously. I can only say that this form fits the data very well.

Figures 4 and 5 present the results of Equation 2 when applied to the data of Figures 2 and 3, respectively. In both cases the same coefficient of C=0.02 volts was applied. I have also tested this formula against data that was simultaneously collected in the AD652 detector/digitizer and found it to work equally well.

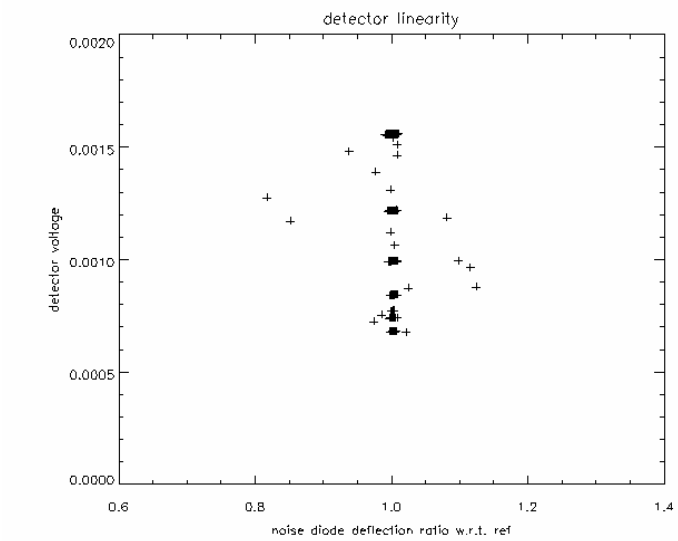

Figure 4: noise diode deflection ratios for the same data of Figure 2 after correcting the detector voltages by Equation 2 with C=0.02 volts.

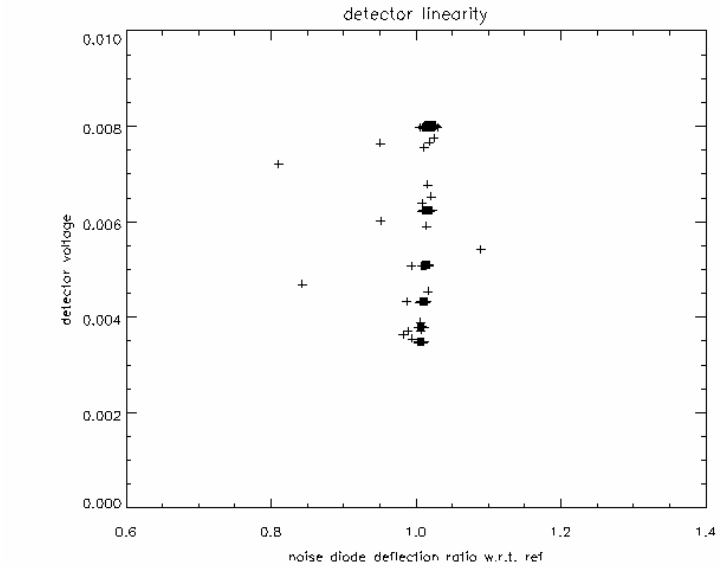

Figure 5: noise diode deflection ratios for the same data of Figure 3 after correcting the detector voltages by Equation 2 with C=0.02 volts.

Figure 6 summarizes the net fractional error of our detectors using the above formula.

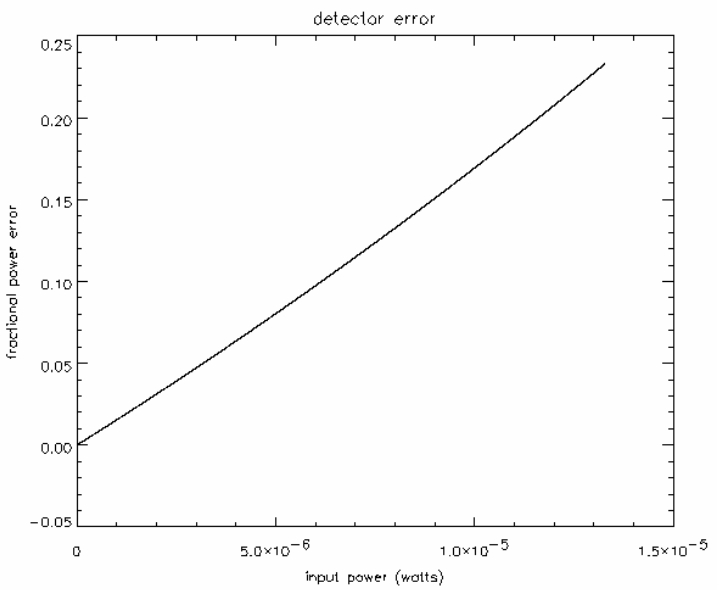

Figure 6: Estimated detector errors computed as $(V_{detected} - V_{linearized})/V_{linearized}$ using Equation 2 with C=0.02 volts and a sensitivity of 0.610mV/microwatt.

JET PROPULSION LABORATORY INTEROFFICE MEMORANDUM

TO: USR team
FROM: Alan Tanner
SUBJECT: Herotek DT1020 detector linearity- continued
DATE: 10/24/2

Introduction

Since my last memo of 10/4/2 I have extended the detector linearity measurements to include: (1) wider power range, (2) a range of detector load resistors, and (3) a temperature range from about 5 to 45 C. I also repeated the RF power measurements. This memo summarizes the new results. I have also spent some time attempting to model these results with the diode equation, but these efforts have been unsuccessful. I was tempted to derive such a model when I found that the linearity of the diode seemed to match the form of the standard diode current equation. I soon found out that detector diodes are more complex than that, and I have since made measurements which don't fit the simple model. I'll report these results below.

Bill Wilson also gave me a number of articles [1,2] that describe some more established methods for measuring detector nonlinearity on the bench. One is the 'two tone' method by which higher order terms in a polynomial expansion of the detector response are derived from intermodulation products measured on a spectrum analyzer. Another method described in literature is the 'constant ratio' method by which a fixed RF attenuator is switched in and out of the receiver repeatedly as the input signal power is varied. The attenuator represents a constant ratio that should correspond to the ratio of detected voltages. Changes in this ratio versus signal strength reflect nonlinearity in the detector. Both of these methods ought to work fine for our testbed, and I will be interested to try them and compare the result with those that I report here. One problem with both of these tests, however, is that they can't be performed on the radiometer as a complete system. The constant ratio method won't work if the attenuator generates an appreciable thermal signal- which it will if it's applied at the radiometer front-end. The two-tone method uses CW signals applied directly to the detector, and there are a fair number of assumptions needed to relate the measurements to the radiometric (Gaussian noise) response.

The method which I have applied here would have to be called the 'constant deflection' method. By this approach, detector nonlinearity is observed in deviations of the noise diode deflection as the antenna noise temperature changes. Unlike the two-tone or constant ratio methods, the deflection method can be applied to the complete radiometer system. In fact, this method can often be applied without any special accommodations or tests since the routine data from any noise adding (e.g.- with noise diode injection) radiometer may be sufficient to characterize the linearity of the system. For example, I know that Steve Keihm has used this technique to correct linearity problems in water vapor radiometers by simply watching the noise diode deflections versus brightness temperature. I've used this technique in the AWVR's as well, and I think it would be a useful tool for validating the linearity of a spaceborne system.

Incidentally, the power measurements that I made are 1.7dB lower than Bill's measurements of September 18. I think this discrepancy was caused by a bad calibration of the power meter. When I first got the meter I used the 50MHz, 0dBm calibration reference provided on front of the meter and found that the meter initially read 1.7dB high. So I recalibrated the meter. I didn't think much of it until I found that my testbed measurements were the same 1.7 dB lower than Bill's. I think that a previous user must have left a bad calibration in the memory of the meter. In any case, the new measurements explain why the detector sensitivity seemed too low in the last data set. The new data indicates a low-level sensitivity of 0.905 mv/uw into 2 k ohm, which is closer to the specified 1 mv/uw.

Measurements

Figure 1 depicts the laboratory configuration of the deflection test using the testbed (1.4 GHz radiometer, 25MHz bandwidth). The antenna in this case was replaced with a noise source that could be adjusted between 300K and 1500K. Also, the noise diode was injected after the Dicke switch so that the deflection can be measured in both the

'antenna' and 'reference' modes of the switch. With both of these measurements we can normalize the antenna deflections and examine the linearity with the deflection ratio

$$D = \frac{V_{AN} - V_A}{V_{ON} - V_O}, \tag{1}$$

where the four voltages represent the response to the antenna, antenna plus noise diode, ambient temperature reference, and reference plus noise diode, as in Figure 1. If the injection were on the antenna side of the Dicke switch one could still make the linearity measurements, but we'd have to be careful to ensure that the gain and noise diode output were stable during the measurements.

In a 'perfect' system- i.e. a linear system with no mismatches- D should always be unity. If the system is not linear then D will change as the antenna noise temperature changes. D can also deviate from unity if the injected noise diode signal leaks backwards towards mismatches in the Dicke switch, but this error should remain constant provided that the mismatches are constant. The isolator was placed before the antenna port to ensure this consistency.

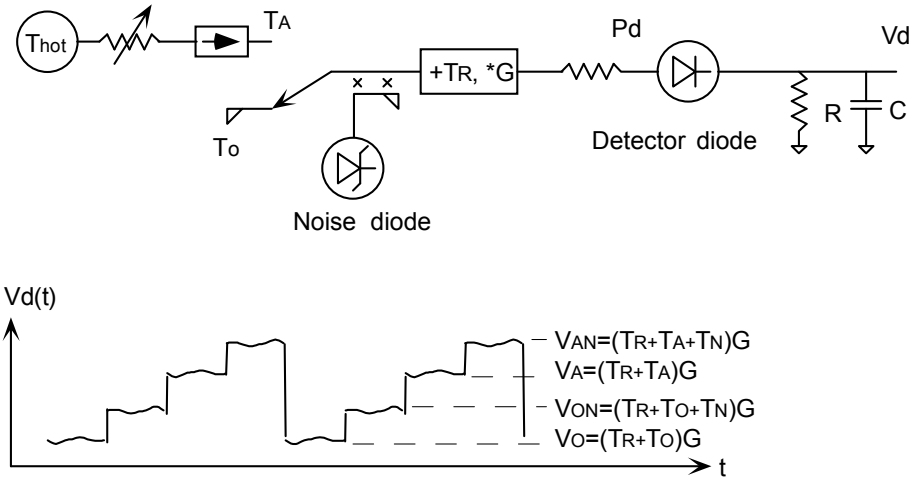

Figure 1: Basic layout of the detector linearity test, and the measurement sequence. The Dicke Switch and noise diode injection modes are switched on 10 ms measurement intervals.

The effective noise temperature of the injected noise diode was about 800K. This is a fairly hot signal for a radiometer, but it is helpful to have a large deflection when the antenna temperature is hot.

The detector voltage was amplified with an OP-37 video amplifier, then integrated and digitized in 10 ms gate intervals using an Analog Devices AD650 V/F converter. A PC averaged and recorded the data as a dedicated digital controller sequenced the testbed through the different measurements of Figure 1. Several modifications to the video amplifier were made in order to test the detector over a wide range of power and detector loads. RF power was tested over several ranges by changing the video gain with a feedback resistor and by changing RF attenuators at the detector input. The load resistor, R in Figure 1, was also changed.

The RF power reaching the detector was measured with a laboratory power meter. Power was measured prior to a number of tests involving different attenuator settings, and the measurements have been included in the graphs presented below. These data were also used to establish the low-level sensitivity of the detectors. The sensitivity depended on the load resistor, R of Figure 1, and there were three load resistors tested: with R= 2kohm the low-level sensitivity was 0.905 mv/uw; with R=237 ohms the sensitivity was 0.655 mv/uw; and with R=50 ohms the low level sensitivity was 0.321 mv/uw. If the diode is modeled as a voltage source with a series resistor, these voltage sensitivities indicate an internal resistance of about 100 ohms.

Figure 2 presents some data collected from the linearity tests. In this case the detector was loaded with R=237 ohms (the graph text indicates 200 ohms- which is incorrect). Data were collected in three separate tests covering three power ranges that were set by adjusting attenuators prior to the RF detector. In each of the three cases Equation 1

has been applied to graph the changes in the noise diode deflection ratio, D, versus power. The power associated with each deflection measurement was estimated from the detector voltage measured during the 'antenna plus noise diode' mode, or V_{AN} of Equation 1, using the low level sensitivity of the detector. The power meter measurements are plotted with horizontal dashed lines. Power measurements were made at the highest and lowest power for each of the three tests included in Figure 2. Each test was conducted by stepping the variable attenuator of Figure 1 in 2dB steps between 0 and 10 dB, and then to an 'off' mode, at which point the antenna noise temperature equals to the ambient temperature. Approximately ten one-second data points were collected at each attenuator setting. Note, in Figure 2, in each of the three cases, that D is close to unity for the lowest power in the range. This is expected from Equation 1 since the antenna and reference levels are equal. In all three tests, however, D increases as the antenna noise increases, indicating that the detector sensitivity is increasing with power. Also note that the data points at the highest power level are well above the dashed line. This also indicates that the detector voltage is exceeding the linear response.

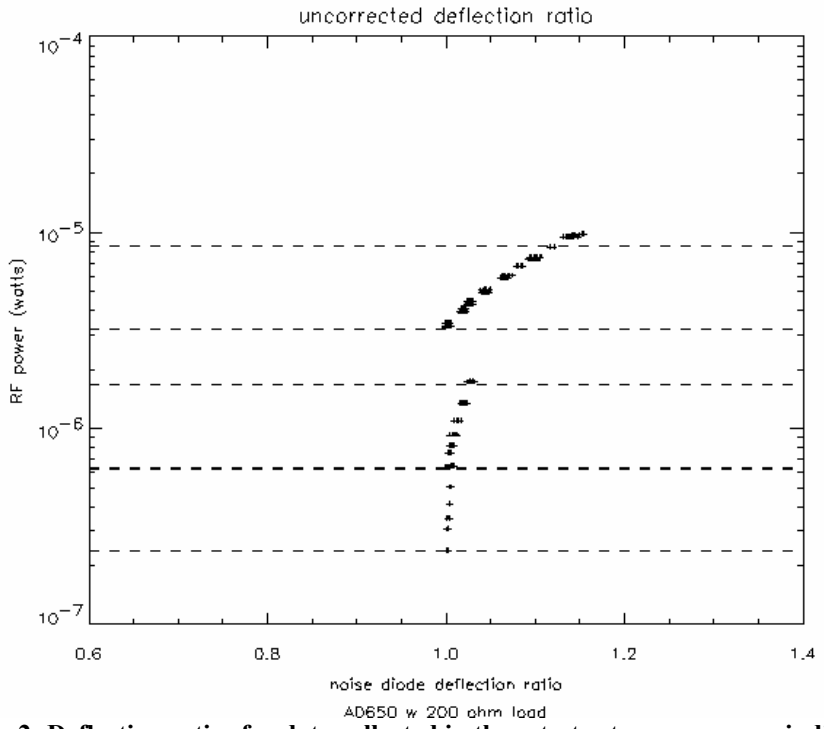

Figure 2: Deflection ratios for data collected in three tests at power ranges indicated with the horizontal dashed lines (0.23uw~0.64uw, 0.63uw~1.7uw, and 3.1~8.6uw). The horizontal dashed lines represent independent measurements of the detector RF power which were made by substituting a power meter for the detector and measuring the high and low levels prior to each test. Each test was conducted by stepping the variable attenuator at the antenna port between 0dB, -2, -4, -6, -8 -10dB, and 'off' modes. The power ranges were changed between tests by changing the RF pads before the detector and the video gain before the V/F converter; the two highest ranges correspond to 3 and 10 dB pads at the detector; the lowest range added 4dB more padding prior to the last RF amplifier.

Figure 3 presents the same data of Figure 2 after applying a 'linearizing' formula. Two sets of deflection measurements are plotted: 'raw' data ("+") and 'linearized' data ("x"). The 'linearized' data was computed from Equation 1 after applying the following formula to the detector voltage:

$$V_{linearized} = C \ln\left[\left(V_{detected} + C\right)/C\right] \quad (2)$$

where $V_{detected}$ is the measured voltage, V_{linear} is the corrected voltage, and C is a fit coefficient. In this case C=0.025 volts, as indicated in the figure. The 'raw' data points of Figure 2 use the linearizing formula to estimate the power for the vertical scale and to estimate an equivalent low level reference deflection in the denominator of Equation 1. Only the numerator of Equation 1 is based on the uncorrected data. By plotting the 'raw' data in this way one can more clearly see the continuity of the response between the three power ranges. Also note that the power estimated from the linearized detector voltage is more closely aligned with the power meter measurements (dashed lines). This further confirms that the linearizing formula works. The motivation behind Equation 2 will be discussed shortly.

Figures 4 and 5 show the available linearity data for detector loads of R=2k and R=50 ohms, respectively. Again, independent power measurements are plotted as horizontal dashed lines. Equation 2 has been applied to both of these cases, and the fit coefficients are indicated at the top of the figures. Note that although the scales of all these plots are the same, that the data sets span different ranges of power. The highest power tested was about 20 microwatts when the detector was loaded with 50 ohms. At such a high power level the linearization of Equation 2 clearly fails to fit the data. The uncorrected linearity of the detector, however, apparently improves with the lower impedance. For example, at 1 microwatt (-30dBm), using Equation 2 with the fit coefficients from the figures and the low level sensitivities noted above, the detected voltage overshoots the linear voltage by 2.5% when loaded with 2k-ohm, 1.3% with 237 ohms, and 0.4% when loaded with 50 ohms.

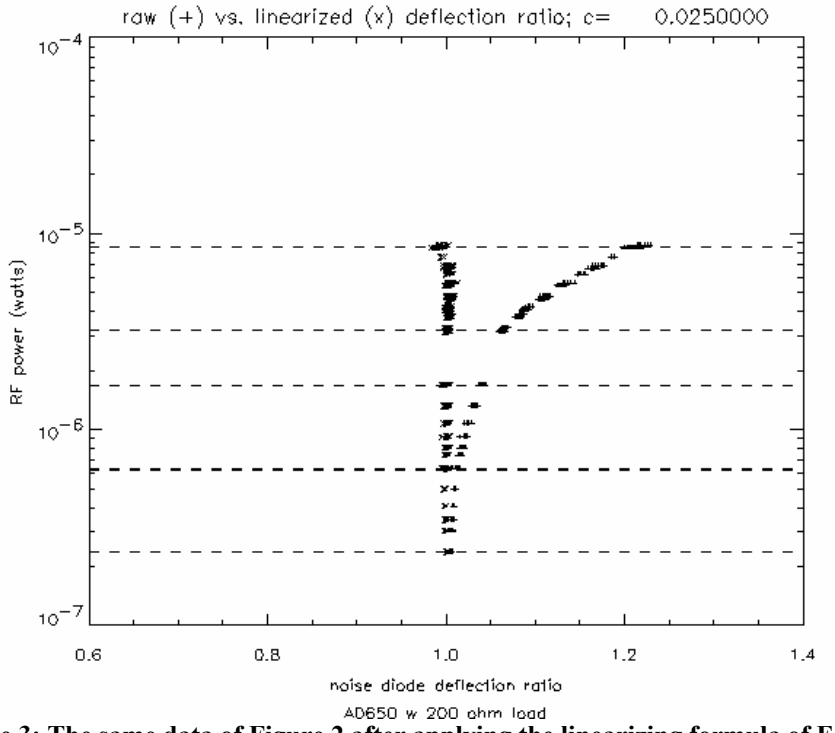

Figure 3: The same data of Figure 2 after applying the linearizing formula of Equation 2. Data that follow the vertical axis have been linearized. Data that curve to the right were computed from the ratio of uncorrected deflections over linearized reference deflections.

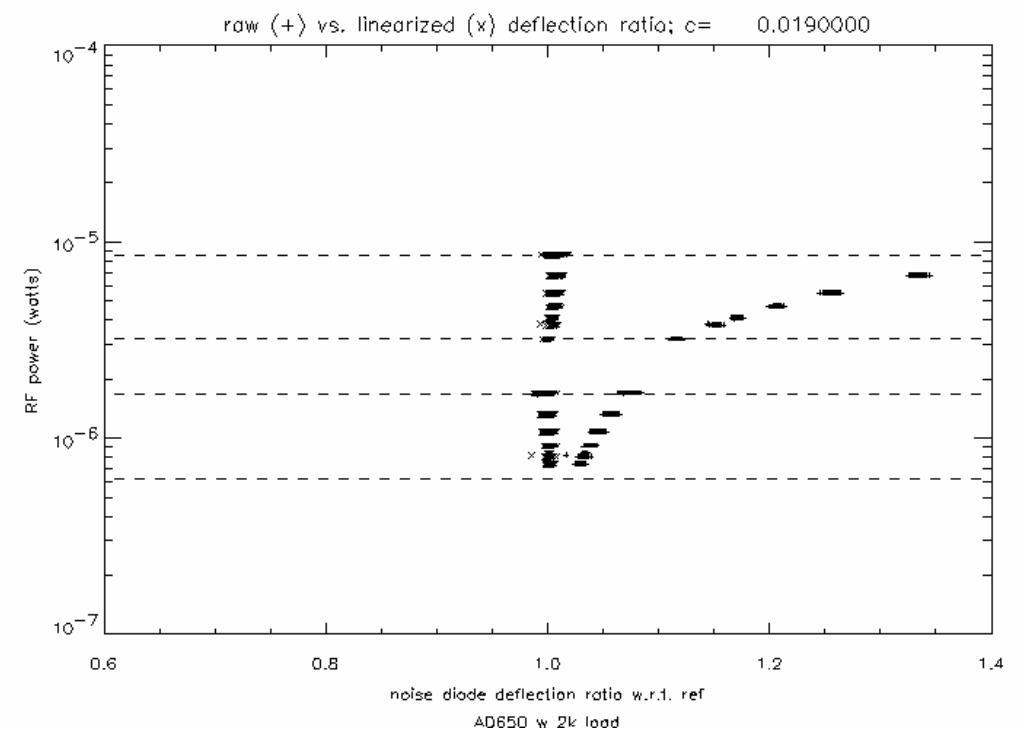

Figure 4: Linearity data for a 2000 ohm load impedance (data points near 0.6uw are missing, due to operator error)

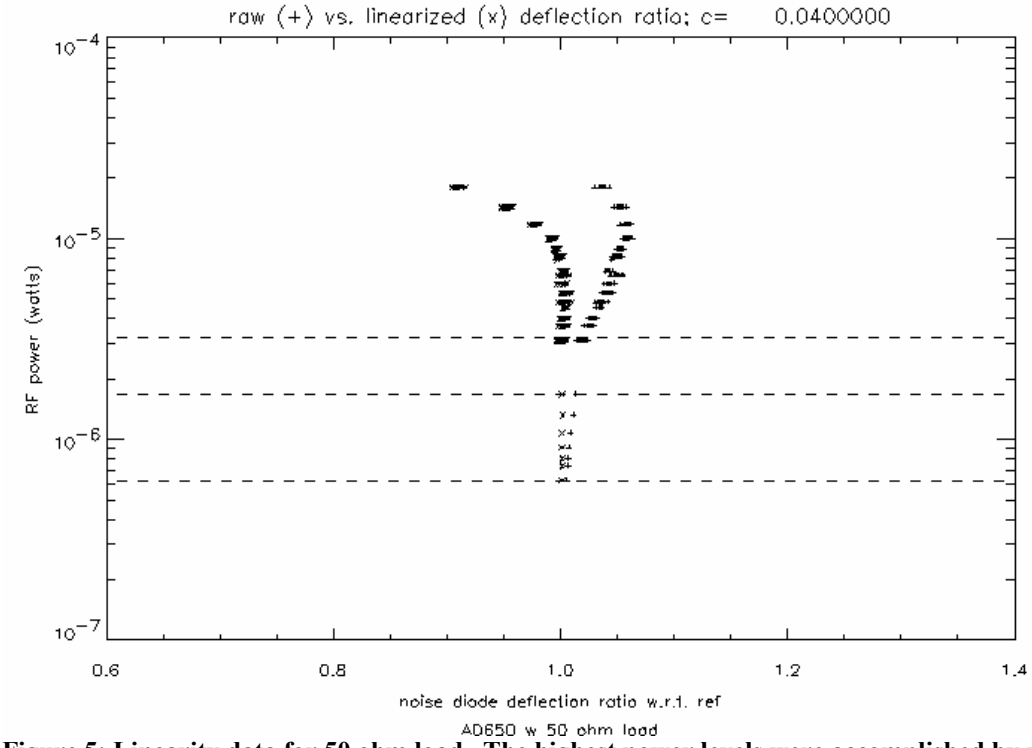

Figure 5: Linearity data for 50 ohm load. The highest power levels were accomplished by removing the power splitter just before the detector.

Discussion of the 'linearization':

The specific form of an equation to characterize the non-linearity of a detector is open to debate. Equation 2 was applied only because it seems to fit the widest range of data. Other investigators may find better forms to fit different detector diodes. In the end the only thing that matters is that the linearized noise diode deflections should be made constant throughout the dynamic range of the radiometer. This should be a sufficient condition to ensure linearity of the system. In essence, the deflections measure the derivative of the voltage versus power curve; if we can show that the derivative is constant, then it follows that the system is linear. The only potential pitfall to this approach occurs when one tries to extrapolate from the measurements. For example, one could run into trouble trying to estimate the receiver noise temperature by extrapolating from warmer data and assuming that the linearized data are valid all the way to zero volts. To minimize this error, one can appropriately constrain the problem by only considering forms where the power versus voltage response converges to the low-level sensitivity of the detector as the voltage approaches zero. The above data, particularly Figure 3 which spans a large dynamic range, supports this constraint. Such a constraint, for example, rules out power-law fits such as $V_{linear}=V^{n}_{detected}$ where n is the fit coefficient. Such a form can linearize the data over a narrow range, but it doesn't work with the data of Figure 3. I can't explain why the specific formula of Equation 2 works. I merely stumbled into it and found that it worked better than a variety of power law and polynomial fits that I'd previously tried. Equation 2 was initially inspired by the diode equation where current is proportional to exp(qV/kT)-1. Equation 2 is the inverse of

$$V_{detected} = C\left[\exp\left(V_{linear}/C\right)-1\right]. \tag{3}$$

Now it just happens that kT/q equals 0.025 volts at room temperature, which matches the coefficient, C, that fit the data so nicely in Figure 3. It is very tempting to read some physical meaning into this coincidence. However, I've tried and I haven't been able to make any such connection. I can only report a few observations that I made along the way.

Pursuing the notion that the fit coefficient, C, of Equation 2 might be related to the thermal voltage, kT/q, of the diode equation, I measured the linearity of the detector over a range of temperature to see if the data could be improved by making the fit coefficient proportional to temperature. Figures 6 and 7 plot the results of that test. In these plots the data are color-coded according to temperature such that red=45 Celsius, black=25 C, and blue=5 C. These data were collected when the detector was loaded with R=2k ohms. In both of these plots the blue data points are shifted upwards and the red points are shifted down: this is related to an increase in RF gain when the RF amplifiers are cooled.

In Figure 6 a fixed fit coefficient of 0.019 was applied, and in Figure 7 the fit coefficient was adjusted in proportion to temperature as C=0.019 T / 296, where T is the diode temperature in Kelvin. It is a little difficult to make a final conclusion from these figures, but it does appear that the fixed coefficient fit the data better than the proportional coefficient. Note that the linearized points fall closer to the vertical line at D=1 in Figure 6. These result tend to contradict the notion that the fit coefficient, C, might be related to the thermal voltage of the diode equation.

Some other formula worth mentioning are

$$V_{detected} = V_{linear} + \frac{1}{2C}V_{linear}^{2}, \tag{4}$$

which is the Taylor expansion of Equation 3 truncated to two terms, and has the inverse (using the quadratic equation)

$$V_{linear} = C\sqrt{1+\frac{2V_{detected}}{C}} - C, \tag{5}$$

and

$$V_{linear} = V_{detected} - \frac{1}{2C}V_{detected}^{2} \tag{6}$$

which approximates both Equation 5 and Equation 2 at low voltages. Equation 4 is consistent with models that appear in literature [1,2], where the nonlinearity is dominated by intermodulation in the V^4 term of the polynomial expansion of the detector transfer function.

Figures 8, 9, and 10 present the same linearity data as Figures 3, 4, and 5, respectively, after replacing the linearizing function of Equation 3 with Equation 5. Comparing these figures we see that Equations 3 and 5 work equally well

at low levels, but that Equation 5 seems to have an advantage- particularly with the higher load resistance- as the power increases. Both models fail, however, at the highest power levels shown in Figures 5 and 10. Finally, Figure 11 shows the results of Equation 6 for comparison with Figure 3. Again the model does an effective job of linearizing the data at low levels, but the performance is significantly worse at higher levels.

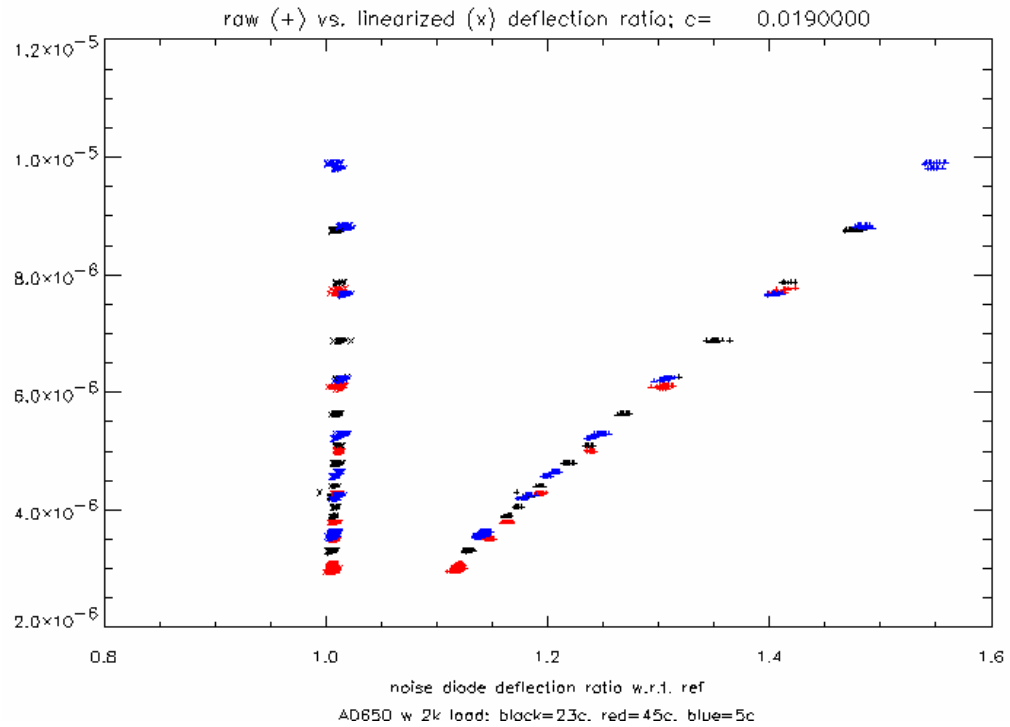

Figure 6: Linearity measurements using a fixed fit coefficient of C=0.019

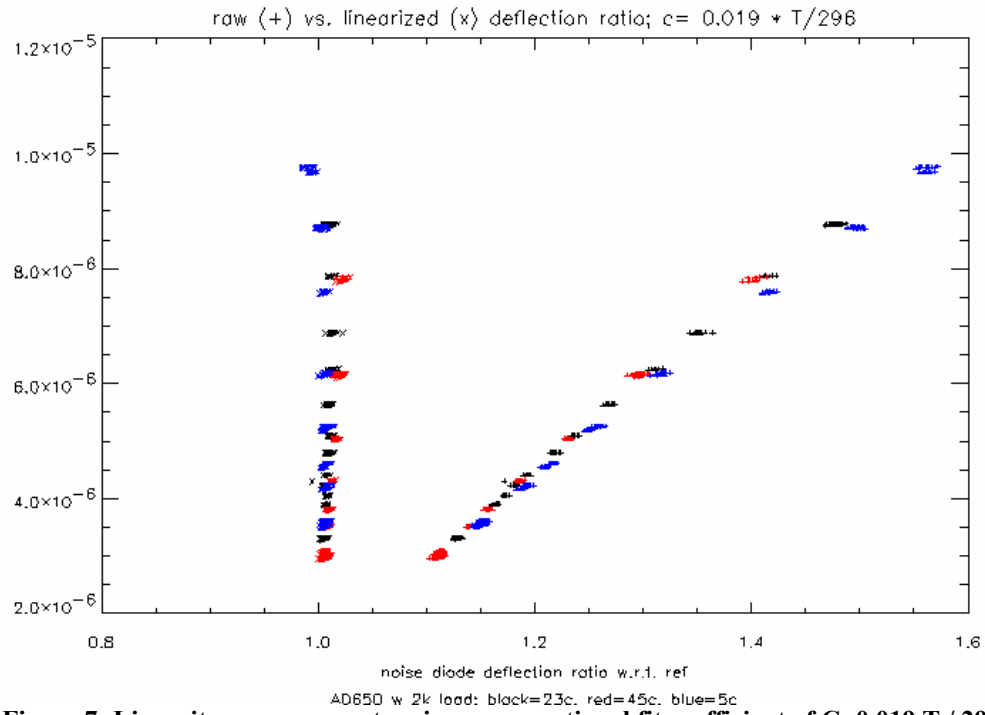

Figure 7: Linearity measurements using a proportional fit coefficient of C=0.019 T / 296

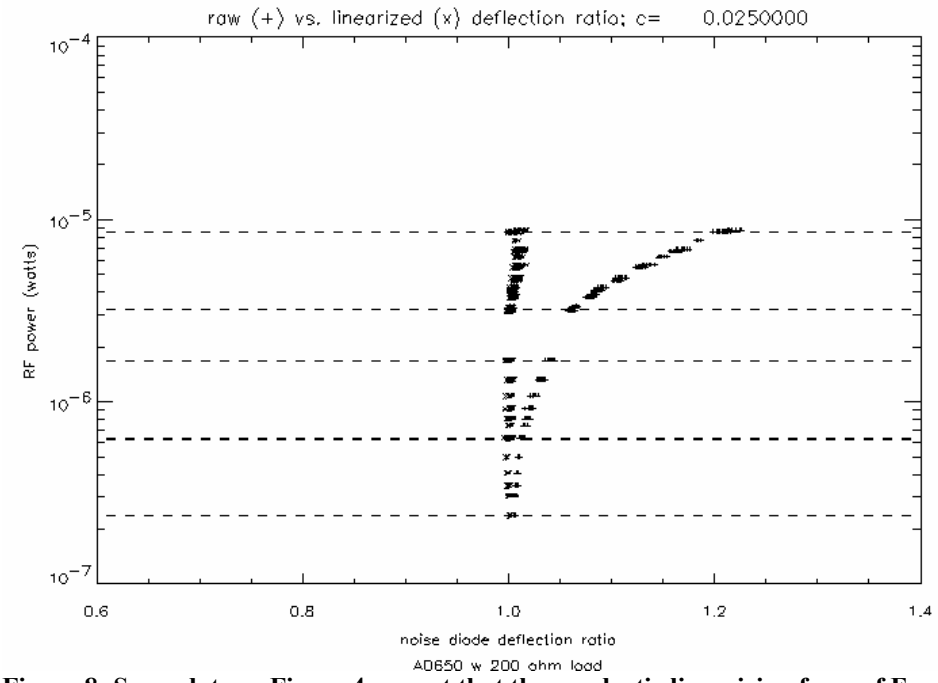

Figure 8: Same data as Figure 4, except that the quadratic linearizing form of Equation 5 has been applied.

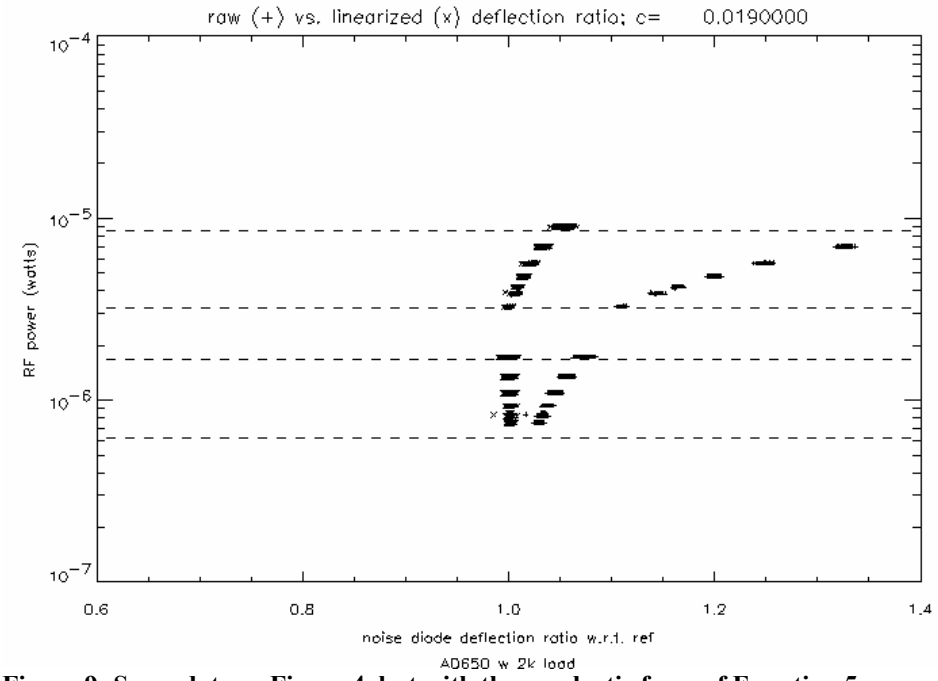

Figure 9: Same data as Figure 4, but with the quadratic form of Equation 5.

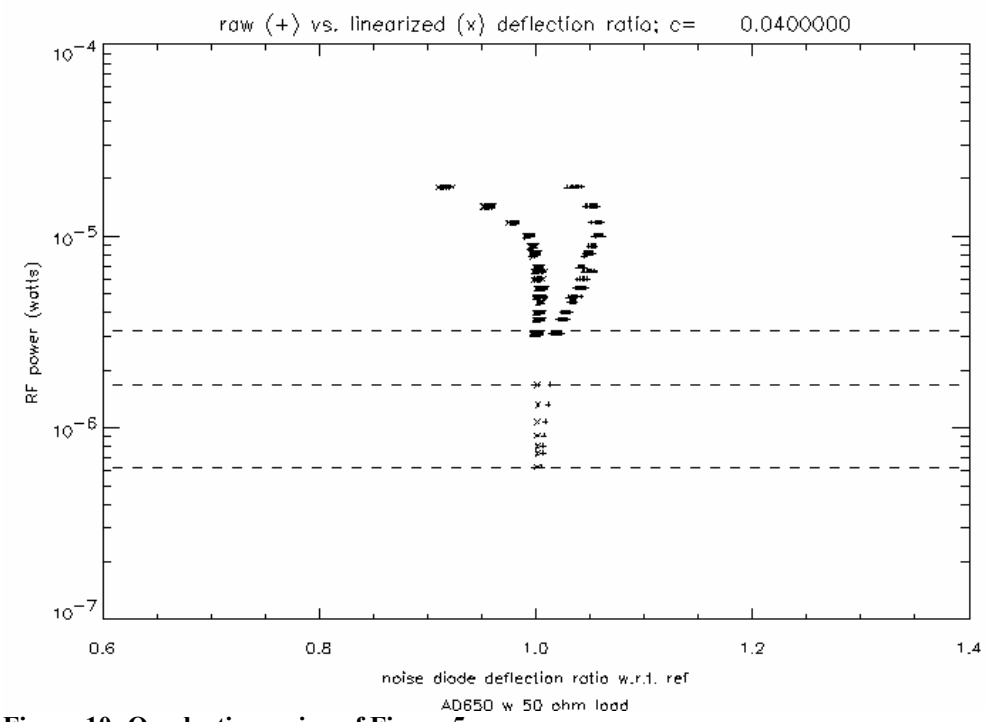

Figure 10: Quadratic version of Figure 5.

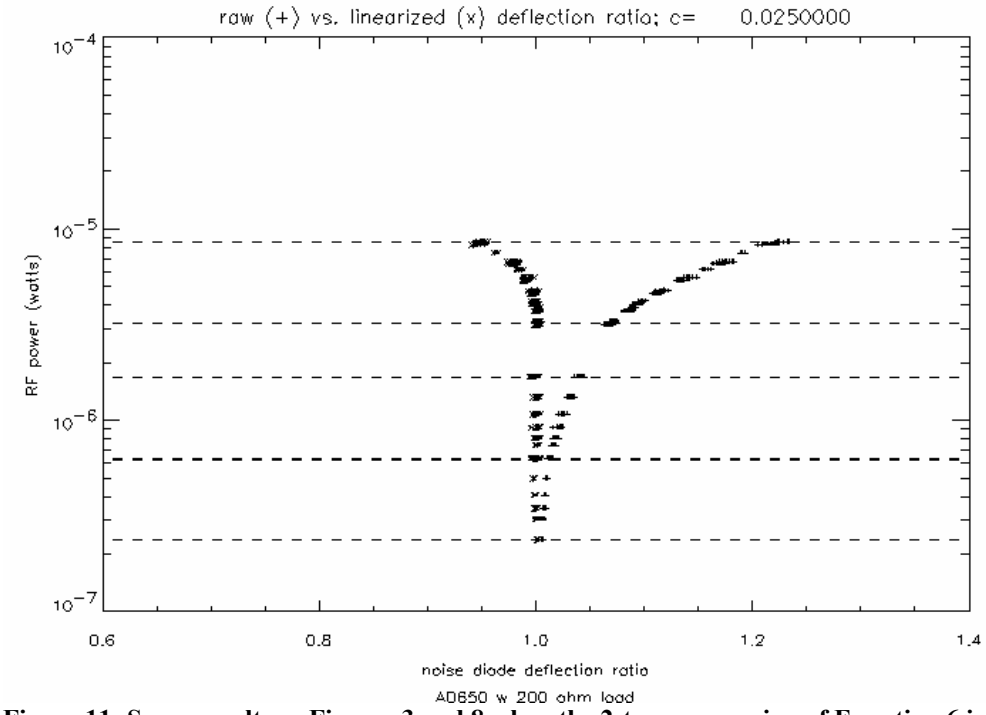

Figure 11: Same results as Figures 3 and 8 when the 2-term expansion of Equation 6 is applied.

Conclusion:

The data presented above indicate that at low levels the nonlinearity of the power versus voltage curve of a detector can be well characterized with a single coefficient using a variety of models. For the DT1020 detectors all of these models converge to Equation 6 at levels of about -25dBm or less. At higher levels some of the models worked better than others, but none of the models worked well at the highest detector power levels. The behavior of

detectors, evidently, gets more complicated as the RF power increases. We also found that nonlinearity of the detector is insensitive to temperature.

The linearity measurement technique that we have applied will lend itself well to in-situ validation of a detector's linearity using the natural variations of the brightness temperature scene. This capability ought to be considered in the system design. If we stay below the poorly characterized region above -25dBm, we should be able to fix linearity problems on-orbit.

At power levels below -25 dBm we also found that the linearity of the DT1020 detector improves as the load impedance decreases. Given an internal resistance of 100 ohms, these data indicates that 2k ohms load resistance presently used in the testbed is unnecessarily high, and that we should lower the load impedance. A lower load impedance will also lower the amplifier current noise slightly. An OP-37 amplifier has about 3.5 nV/root(Hz) and 1.7 pA/root(Hz) input noise at 10 Hz, so the current and voltage noise are about equal at 2k ohms, and could be lower by a factor of root(2) with lower impedance.

The linearity versus load impedance is reflected in the fit coefficients presented above: C=19 mV at 2,000 ohms, 25 mV at 237 ohms, and 40 mV at 50 ohms. Using Equation 4, we can calculate that the detected voltage corresponding to, say, a 1% nonlinearity is 1% of 2C, or 0.38mV at 2,000 ohms, 0.5mV at 237 ohms, and 0.8mV at 50 ohms. These voltages correspond to power levels of -33.7 dBm, -31.2 dBm, and -26.0 dBm, respectively. If RF power is not an issue, then these data indicate a slight advantage to running at the lowest impedance. -26dBm is a little too close to the poorly modeled region above -25 dBm, so I'd back off a bit from 50 ohms and say that 100 ohms, and roughly -29dBm, and 0.6 mv are about the best operating conditions for the DT1020.

References:

[1] Victor S. Reinhardt, Yi Chi Shih, Paul A. Toth, Samuel C. Renolds, Arnold L. Berman, "Methods for Measuring the Power Linearity of Microwave Detectors for Radiometric Applications," IEEE Trans. MTT, vol 43, no 4, pp715-720, April 1995.

[2] T. Narhi, "Nonlinearity characterization of microwave detectors for radiometric applications," Electronics Letters, vol 32, no 3, pp 224-225, February 1, 1996.

JET PROPULSION LABORATORY INTEROFFICE MEMORANDUM

TO: USR files
FROM: Alan Tanner, Bill Wilson
DATE: 8/17/04
SUBJECT: Detector linearity correction for remaining USR tests

Here is a summary of the linearity test done on 13 August 2004, including correction algorithms and their implications for estimated receiver noise.

The linearization formula is: $V_{linear} = V_c * \ln[V_{nonlinear} / V_c + 1]$, where $V_{nonlinear}$ is the detected voltage, and V_c is the correction factor. Note that a larger V_c corresponds to less correction since it would imply that the detector goes nonlinear at a higher voltage.

The two detector digitizers of the USR are setup as follows:

The AD652 detector/digitizer assembly loads the Herotek detector with a 2K-ohm load, and then amplifies the voltage by a factor of 5005 before the V/F converter (VFC). At 1.0 volt, the VFC frequency is 50 kHz. Therefore, if we set V_c = alpha * 5005*50000 we can use the detected VFC counts in the above linearization formula. The parameter alpha is the system nonlinearity factor in volts. Also, the sensitivity of the detector into a 2K load resistor is ~1030 volts/watt- if you wish to calculate the RF power.

The AD650 detector/digitizer assembly loads the Herotek detector with a 100-ohm load, and then amplifies the voltage by a factor of 5505 before the VFC. At 1 volt, the VFC frequency is 9.45 kHz. Therefore, if we set V_c = alpha * 5505*9450 we can use the detected VFC counts in the above linearization formula. The sensitivity of this detector with a 100 ohms load is ~580 volts/watt.

From today's data, we estimate that the system linearity correction voltage is 0.023 volts for the AD650 detector/digitizer assembly, and 0.025 volts for the AD652 detector/digitizer assembly.

The following plots summarize how well these corrections work. The test involved measuring noise diode-A deflections as the input noise temperature was varied between roughly the 40 K of the 'LNA-load' (i.e. the LNA which has been turned backwards to make a cold load), and roughly 500 K as noise was coupled in via a stepped attenuator. Figure 1 plots the noise diode-A antenna/reference deflection ratios of the AD652 before (black) and after (red) the nonlinearity correction was applied. Figure 2 plots the same for the AD650. In both cases, the linearized deflections cross over the nonlinear deflections when the antenna noise equals the reference temperature of the Dicke switch.

In Figures 3 and 4 are additional plots of this type of data, with additional measurement runs and also the ratio of noise diode-B antenna / noise diode-A reference, showing that the non-linearity correction voltages are consistent for both noise diodes.

The above corrections have a pronounced effect on the receiver noise temperature estimates. Figure 5 is the estimate without the correction and Figure 6 is the estimate with the correction. These are not accurately calibrated (I used only the rough approximation that TNDA= 300 K), but that doesn't matter for these illustrations since I only want to see of the two digitizers agree. As can be seen, the linearity corrections shift both receiver noise temperature estimates upwards by 7-8 K. The corrections make the two digitizers agree much better.

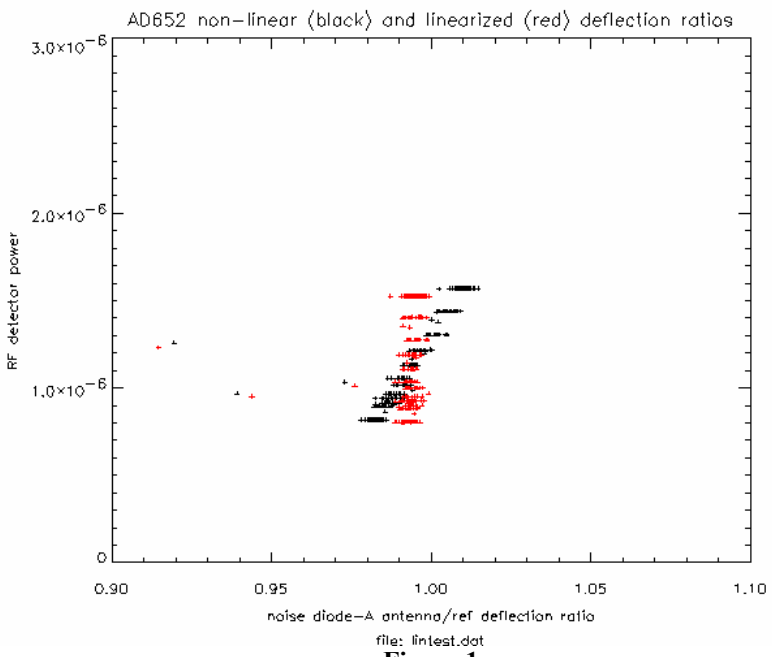

Figure 1

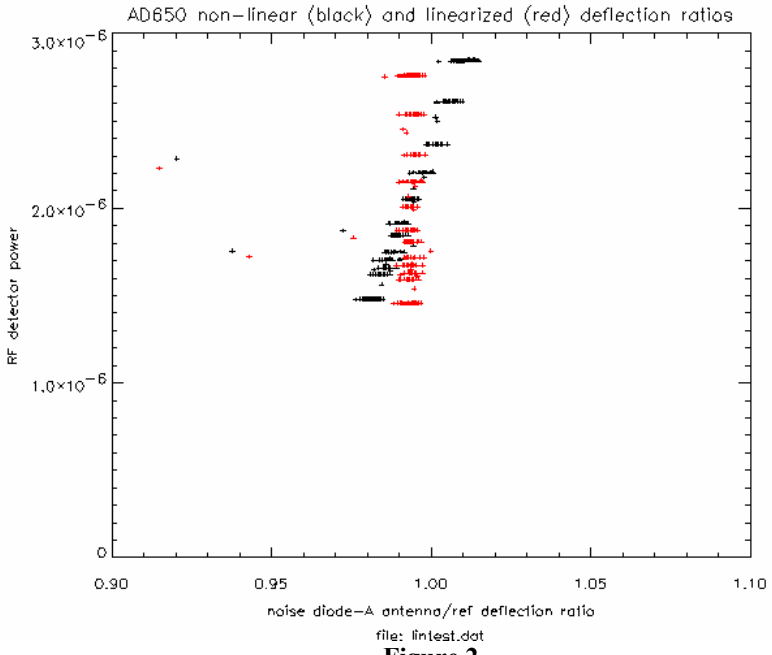

Figure 2

Figure 3

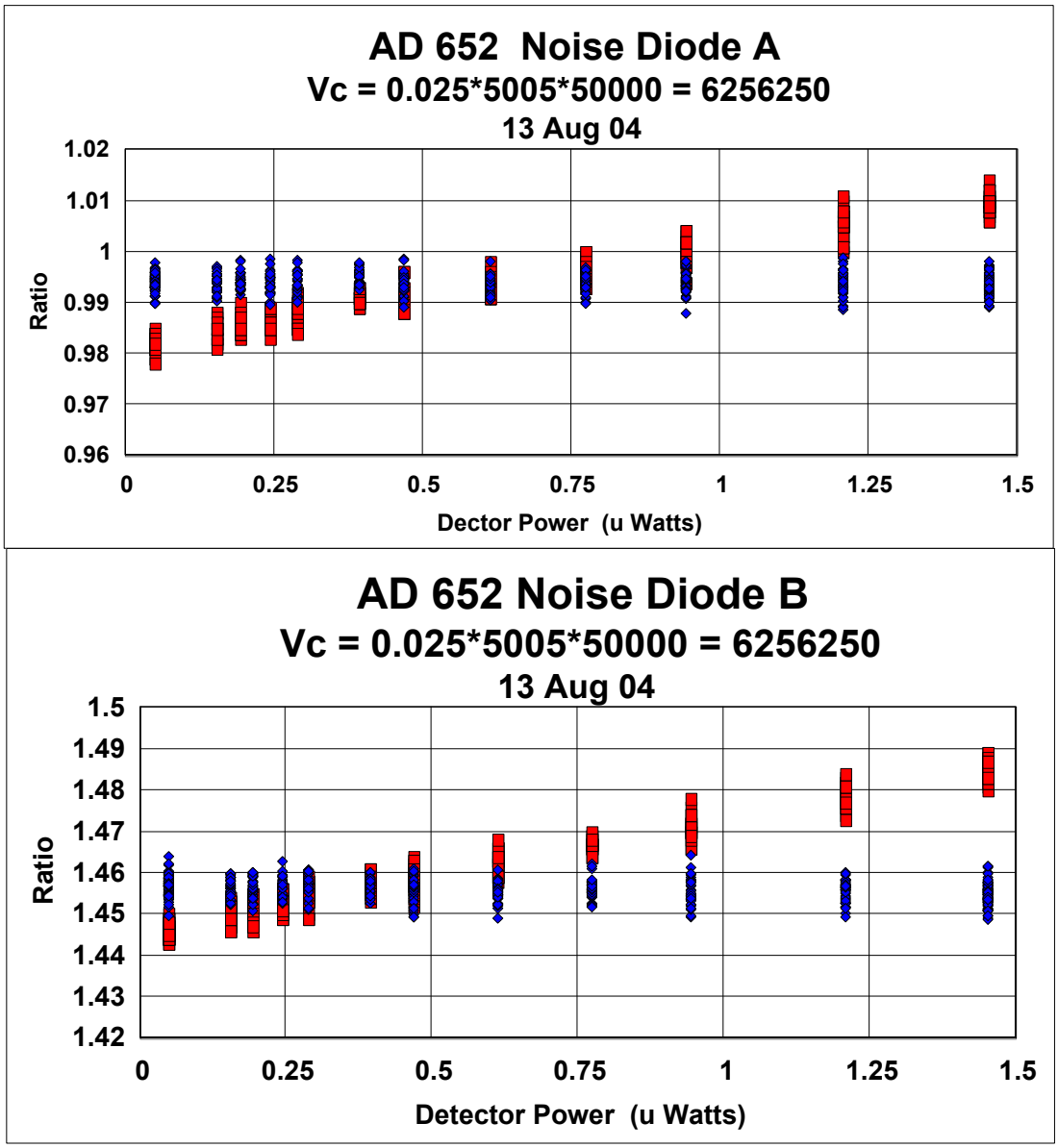
AD 652 Noise Diode A
Vc = 0.025*5005*50000 = 6256250
13 Aug 04
Ratio
1.02
1.01
1
0.99
0.98
0.97
0.96
0
0.25
0.5
0.75
1
1.25
1.5
Dector Power (u Watts)
AD 652 Noise Diode B
Vc = 0.025*5005*50000 = 6256250
13 Aug 04
Ratio
1.5
1.49
1.48
1.47
1.46
1.45
1.44
1.43
1.42
0
0.25
0.5
0.75
1
1.25
1.5
Detector Power (u Watts)

Figure 4

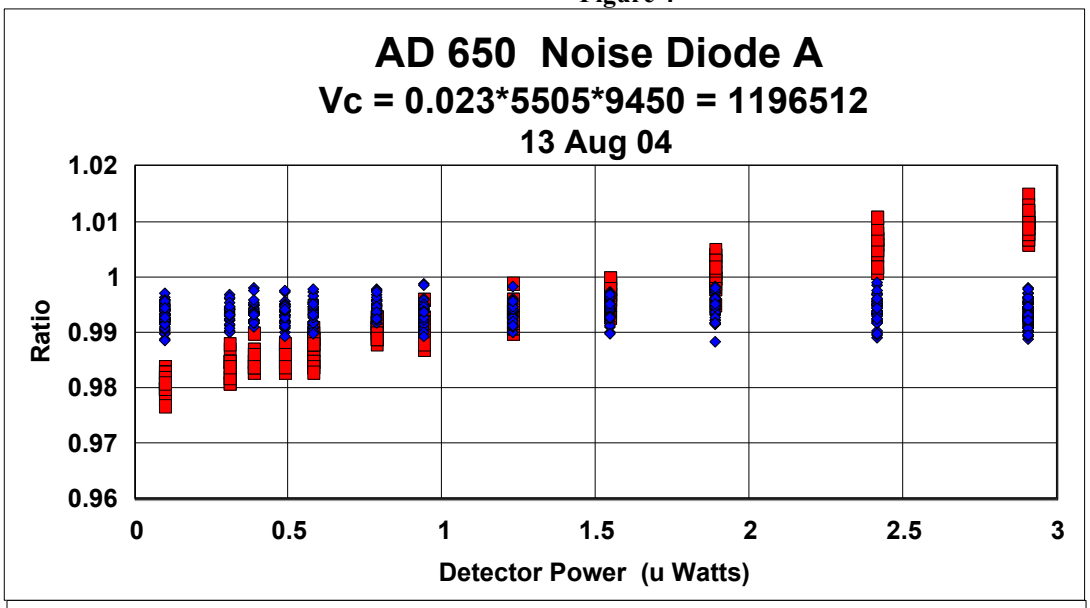
AD 650 Noise Diode A
Vc = 0.023*5505*9450 = 1196512
13 Aug 04
Ratio
1.02
1.01
1
0.99
0.98
0.97
0.96
0
0.5
1
1.5
2
2.5
3
Detector Power (u Watts)

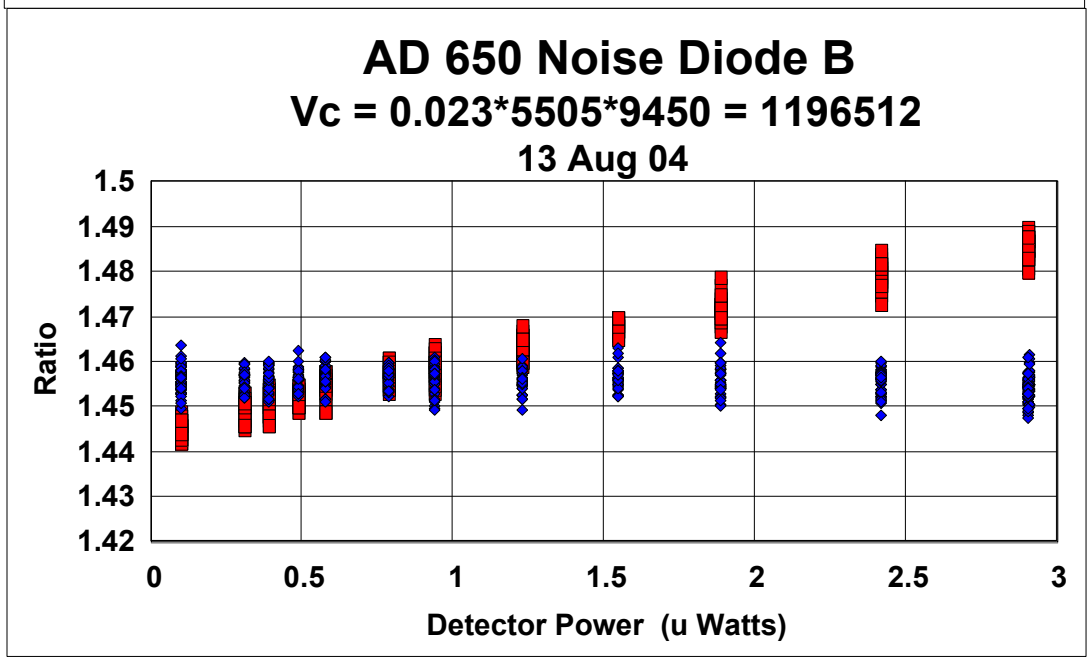
AD 650 Noise Diode B
Vc = 0.023*5505*9450 = 1196512
13 Aug 04
Ratio
1.5
1.49
1.48
1.47
1.46
1.45
1.44
1.43
1.42
0
0.5
1
1.5
2
2.5
3
Detector Power (u Watts)

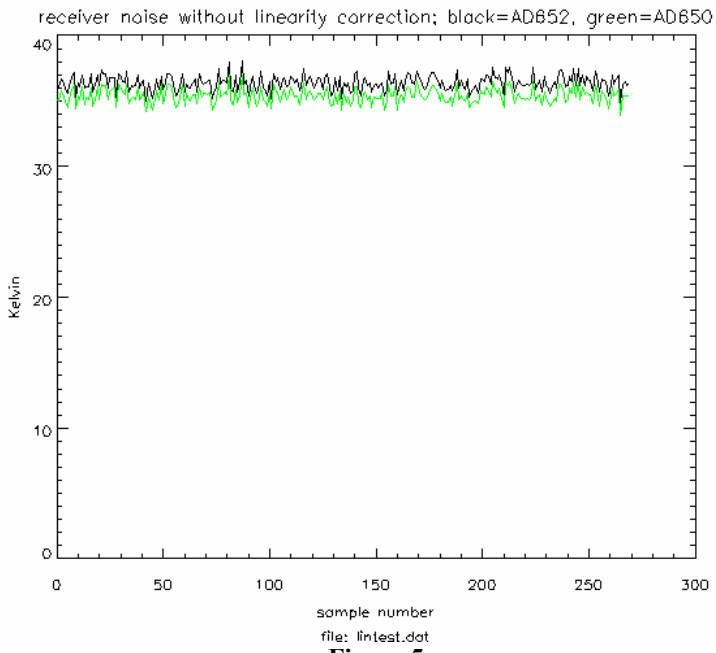

Figure 5

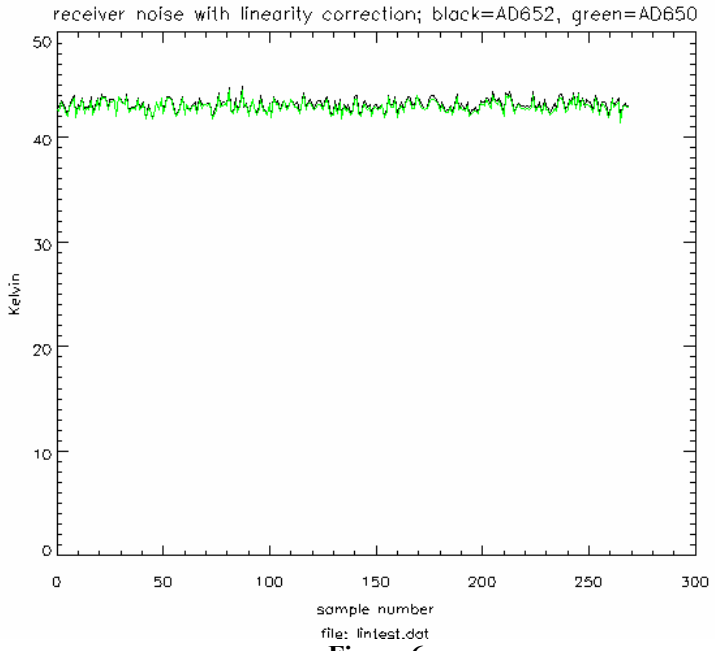

Figure 6

Appendix 4 Running Average Delta-T Optimization

JET PROPULSION LABORATORY INTEROFFICE MEMORANDUM

TO: USR/IIP team
FROM: Alan Tanner
DATE: 5/10/2
SUBJECT: delta-T and duty cycle optimizations

I've been using data from the AWVR to quantify the delta-T we might achieve in the Aquarius radiometer. Specifically, I've examined how to use running-average estimates of receiver noise and gain to decrease the delta-T and to increase the antenna duty cycle. Such a scheme would take advantage of the fact that the time scales associated with gain and receiver noise temperature fluctuations will probably be longer than the on-orbit per-pixel observing time.

1. Optimization of integration time

The baseline design for the Aquarius radiometer includes a Dicke switch and noise diode injection circuits. In the simplest mode of operation these circuits provide an instantaneous estimate of gain and offset so that antenna brightness temperature, T_A, would be calculated from

$$T_A = T_o - (C_o - C_A)\frac{T_{ND}}{C_{ND}}. \quad (1.1)$$

Here, T_o is the temperature of the reference load (of the Dicke switch), T_{ND} is the noise diode equivalent temperature (which is established by tip-curve calibration, in the case of the AWVR), C_{ND} is the difference of "counts" measured between the on and off states of the noise diode[5], and C_o and C_A are the respective measurements of the reference load and the antenna. We use the term "counts" here to imply an integration of the detector voltage over a sample interval, τ (i.e. by counting pulses from a V/F converter).

In equation 1.1 we make no assumptions about the stability of the receiver gain or the receiver noise temperature; we only assume that these factors are common to all of the measurements. If, on the other hand, we know that the receiver noise temperature is relatively stable over the observation time of interest we can reformulate the calibration as follows:

Assuming a low detector null offset[6], we have

$$C_o = G(T_r + T_o), \quad (1.2)$$

where G is the receiver gain (in counts/K) and T_r is the receiver noise temperature. Likewise,

$$C_A = G(T_r + T_A). \quad (1.3)$$

If we have T_r and T_o we can estimate the antenna brightness temperature from

$$T_A = (T_o + T_r)\frac{C_A}{C_o} - T_r \quad (1.4)$$

Here, we've used the reference load of the Dicke switch to estimate the instantaneous gain. Equation 1.4 has a delta-T advantage over Equation 1.1 in that gain has been calculated from a single-ended total-power measurement whereas the gain estimate of Equation 1.1 is calculated from the difference between on-off states of the noise diode.

[5] In the case of the AWVR, C_{ND} and T_{ND} are actually a composite measurement of three separate noise diodes measured in both modes of the Dicke switch (six deflection measurements in all). For the present discussion we will treat them as one noise diode.

[6] Equation 2 implies that the measured counts should be zero for a zero system noise temperature. A null offset in the detector or integrator circuits will otherwise need to be removed. The AWVR's operate at a sufficiently high detected power level that a null correction is not required.

For example, with the nominal parameters for the AWVR of T_r=500, T_o=300, T_{ND}=500, one can show[7] that the noise in the estimate of gain by equation 1.1 will be 3.1 times higher than the gain estimated in the total power mode.

Estimates of receiver noise can be computed from the reference load and injected noise diode data according to:

$$T_r = C_o \frac{T_{ND}}{C_{ND}} - T_o \,. \tag{1.5}$$

Figure 1.1 shows 14-days of receiver noise temperature deviation from a mean value for the AWVR using Equation 1.5 and after applying a 223 second boxcar average. Three RF channels (22.2GHz, 23.8GHz, and 31.4GHz) are plotted with three colors, and a small diurnal oscillation is evident in each.

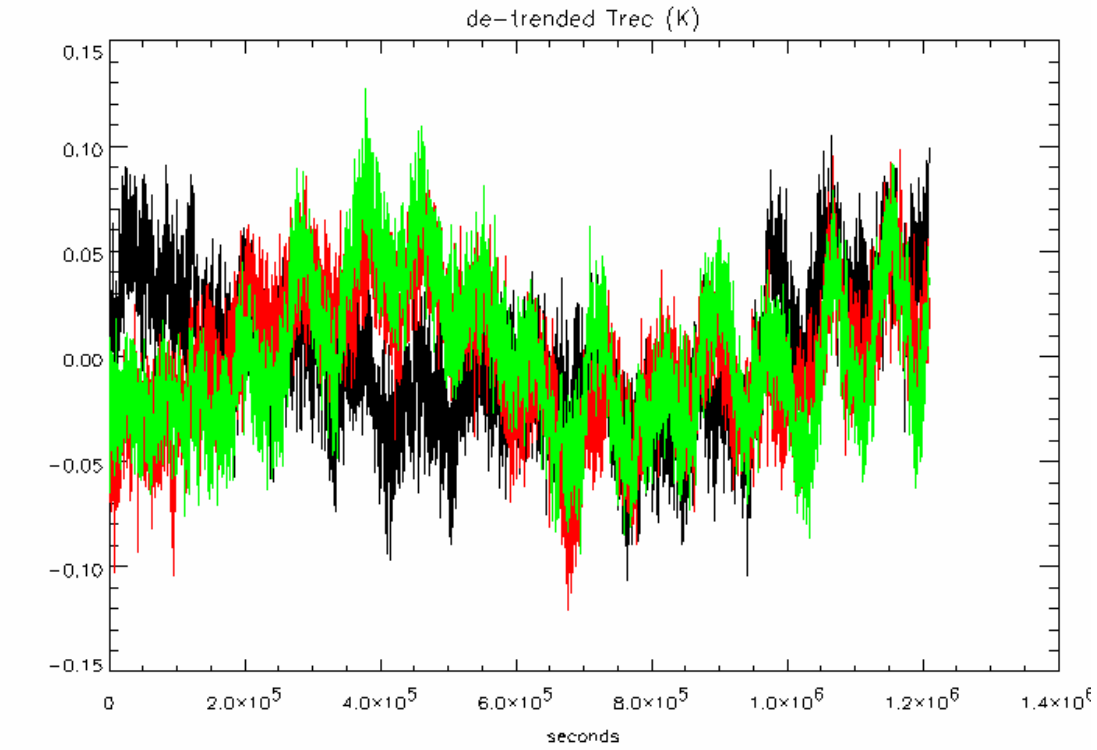

Figure 1.1: Time series of A-1 Tr for 14 days starting 3/14/02 after removing the mean value of each of three channels (approximately 500K in all cases). 223s boxcar integrations apply. Black, red, and green traces correspond to 31.4, 22.2, and 23.8 GHz channels, respectively. Nominal receiver noise temperatures are 540.9 (31.4GHz), 449.7 (22.2GHz), 436.9K (23.8GHz).

To quantify the stability of T_r, Figure 1.2 plots the root of power spectrum of the receiver noise of Figure 1.1. These spectra show that low frequency instability exceeds the short-term white noise at frequencies well below 1 mHz. Figure 1.2 also plots an overlay of a 1/f (sloped and dashed lines) fit to the spectra, and a white noise (horizontal dashed) fit. The form of this fit is

$$S(f) = a + b / f \,. \tag{1.6}$$

The fit coefficients are tabulated under Figure 1.2. This model will be used to determine a time constant with which to form a running average of receiver noise.

[7] C_{ND} is computed from the difference of the reference counts and the counts measured with the noise diode turned on. With equal integration times for reference and noise diode measurements, the gain errors will increase over the error of any single measurement by the weighted root-sum-square of reference and noise diode errors normalized by the relative magnitude of the noise diode temperature according to root$[(T_r+T_o+T_{ND})^2+(T_r+T_o)^2]/T_{ND}$ (=3.1 above).

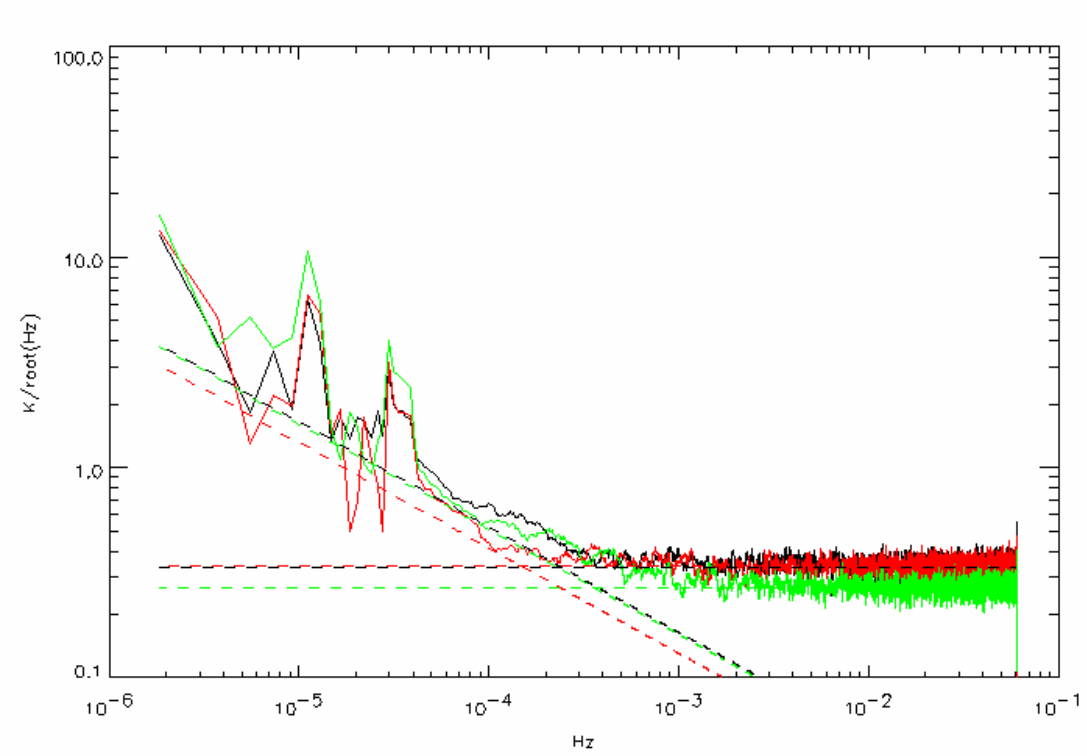

Figure 1.2: Tr spectra for same channels of Figure 1. Dashed overlays are approximate 1/f and white noise fits as follows:

```
f0 (black) S(f)= 0.11 + 2.7e-5/f (K^2/Hz), fknee=  0.00024
f1  (red)  S(f)= 0.11 + 1.7e-5/f (K^2/Hz), fknee=  0.00015
f2 (green) S(f)= 0.07 + 2.6e-5/f (K^2/Hz), fknee=  0.00035
```

A running average of receiver noise will be computed from a time series of receiver noise temperature measurements according to

$$T_{rmi} = \frac{1}{2m+1}\sum_{j=i-m}^{i+m} T_{rj} \tag{1.7}$$

where T_{rj} is computed with Equation 1.5 from counts measured at time t= j*τ, and τ is the sample interval. To optimize the quantity m, we will decompose the noise associated with T_{ri} into white noise, which we hope to reduce by increasing m, and the 1/f noise which we want to preserve by keeping m small. The increase in 1/f noise with m will be calculated from

$$\sigma^2(m) = \left\langle (T_{rmi} - T_{ri})^2 \right\rangle \tag{1.8}$$

where <.> is the expectation operator. Equation 1.8 expands to

$$\sigma^2(m) = \left(\frac{1}{2m+1}\right)^2 \sum_{j=i-m}^{i+m}\sum_{k=i-m}^{i+m} \left\langle T_{ri}T_{ri}\right\rangle - \left\langle T_{ri}T_{rk}\right\rangle - \left\langle T_{ri}T_{rj}\right\rangle + \left\langle T_{rj}T_{rk}\right\rangle \tag{1.9}$$

where the four terms can be identified with the autocorrelation function. A suitable expression for the autocorrelation will be derived from Structure Functions, which are provided by Janssen [1] for the spectra of Equation 1.6:

$$F(j-k) \equiv \frac{1}{2}\left\langle (T_{rj} - T_{rk})^2 \right\rangle = \left\langle T_{ri}T_{ri}\right\rangle - \left\langle T_{rj}T_{rk}\right\rangle = \frac{b}{2}\phi(j-k) - \frac{a}{2\tau}. \tag{1.10}$$

where τ is the boxcar integration time- which is equal to the sample interval- and

$$\phi(n) = (n-1)^2\ln(n-1) - 2n^2\ln(n) + (n+1)^2\ln(n+1). \tag{1.11}$$

Figure 1.3 compares the theoretical (dashed) and measured (solid) structure functions derived from the present data set according to Equation 1.10. As can be seen in Figure 1.3, the model is suitable for time scales of up to about

10,000 seconds. Diurnal errors which are not modeled are evident in the local maximum at 1/2 day (43,200 seconds) and minimum at 1 day (86,400 seconds).

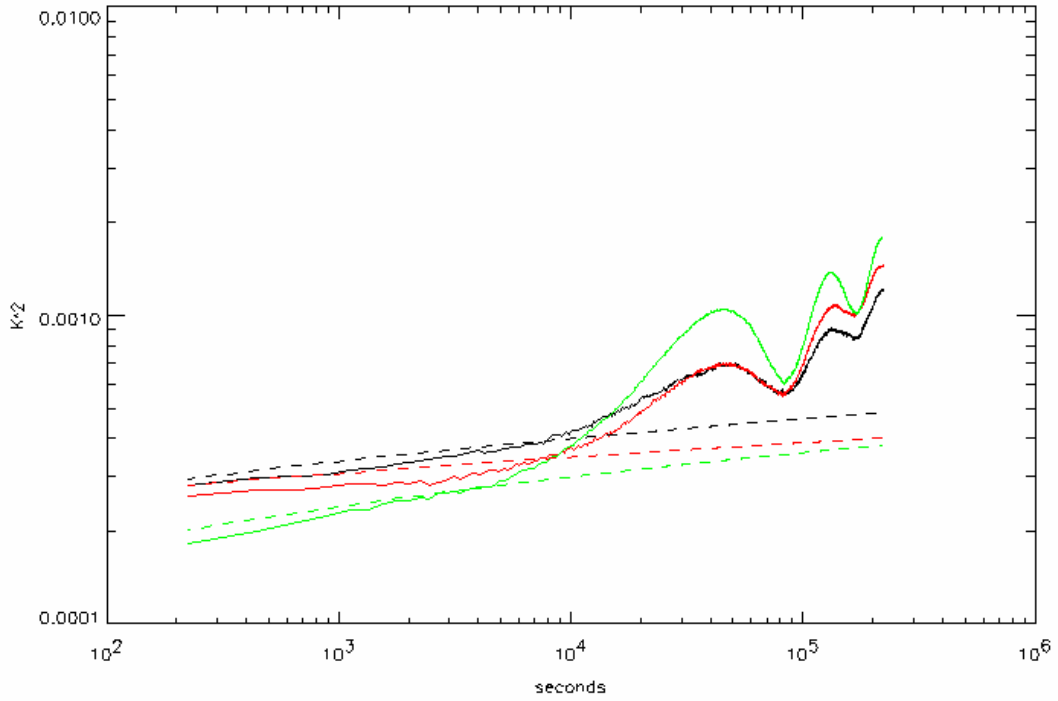

Figure 1.3: Comparison of structure functions by theory (dashed) and data (solid) using equation 9, the data of Figure 1, and the fit to the data from the spectra of Figure 2. A 223 second boxcar integration interval applies.

Rearranging the terms of Equation 1.10, we have

$$\left\langle T_{rj} T_{rk} \right\rangle = \left\langle T_{ri} T_{ri} \right\rangle - \frac{b}{2}\phi(j-k) - \frac{a}{2\tau} \tag{1.12}$$

Applying the 1/f term of Equation 1.12 to Equation 1.9 eventually[8] leads to

$$\sigma_{1/f}{}^2(m) = b\theta(m), \tag{1.13}$$

where

$$\theta(m) \equiv \frac{2(m+1)^2}{2m+1}\ln(m+1) - \frac{2m^2}{2m+1}\ln(m) - \ln(2m+1) \tag{1.14}$$

Equation 1.13 is the increasing 1/f noise which is to be balanced against the decreasing white noise with increasing m. The white noise will contribute $\frac{a}{2\tau(2m+1)}$ to the sample variance of Equation 1.7, given the spectra of Equation 1.6. The net error in the estimate of T_r as a function of m is therefore

$$\sigma^2_{T_r}(m) = b\theta(m) + \frac{a}{2\tau}\frac{1}{2m+1} \tag{1.15}$$

Which has a minimum in the root of the equation

$$\left(m^2 + m\right)\ln\left(1 + \frac{1}{m}\right) = \frac{a}{4b\tau}. \tag{1.16}$$

[8] Getting from Equation 1.9 to Equation 1.13 involves an expansion and some series identities. Start by reducing 1.9 with 1.12 to get summations involving only $\phi(j)$, $\phi(k)$, and $\phi(j-k)$; finish by applying 1.11and expanding the summations until the series identities are evident.

The left side of Equation 1.16 is well approximated by m+0.5 for m>1, so that the optimum integration time, τ_r, that minimizes error in the estimate of T_r is

$$\tau_r = (2m+1)\tau = \frac{a}{2b} \qquad \text{for } \tau_r >> \tau \,, \tag{1.17}$$

or

$$m = \frac{a}{4b\tau} - \frac{1}{2} \,. \tag{1.18}$$

Applying Equation 1.17 to the spectral fits of Figure 2 yields an optimum integration time of about 2000 seconds which, by Figure 1.3, is within the valid range of the model.

Figure 1.4 illustrates the relative magnitude of white noise, 1/f noise, and their sum from Equation 1.15 for various observation intervals, τ. Note that the minimum total error only deviates from the solution of Equation 1.17 when τ approaches τ_r. Also note that in all other cases the 1/f noise is greater than the white noise contribution.

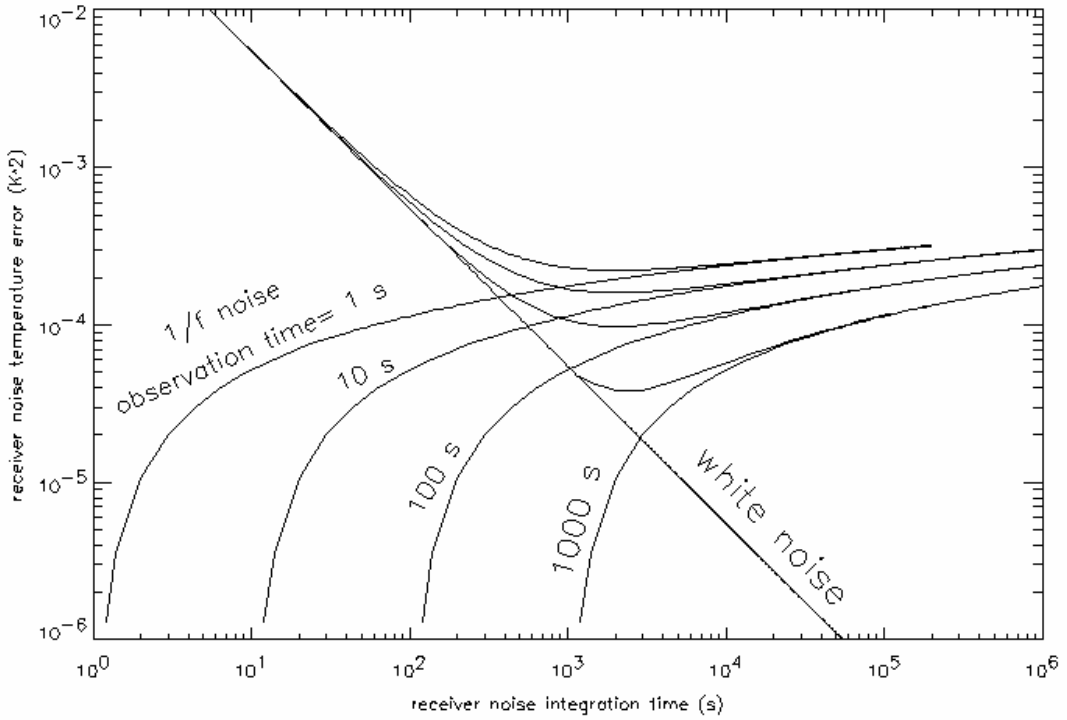

Figure 1.4: decomposition of 1/f and white noise components from Equation 1.15 for various observation intervals. The spectra of Equation 1.6 applies with a=0.11 K^2/Hz, b=2.7e-5 K^2/Hz from Figure 1.2.

The same analysis can be applied to form a running average of the receiver gain. Figures 1.5 and 1.6 plot the measured AWVR gain time series and power spectra, respectively. Gain in this case has been calculated from the reference counts, as in Equation 1.4.

Using the spectral fits of Figure 1.6, in which the knee frequency is about 0.06 Hz, and applying Equation 1.17, produces an optimum integration time of about 8 seconds.

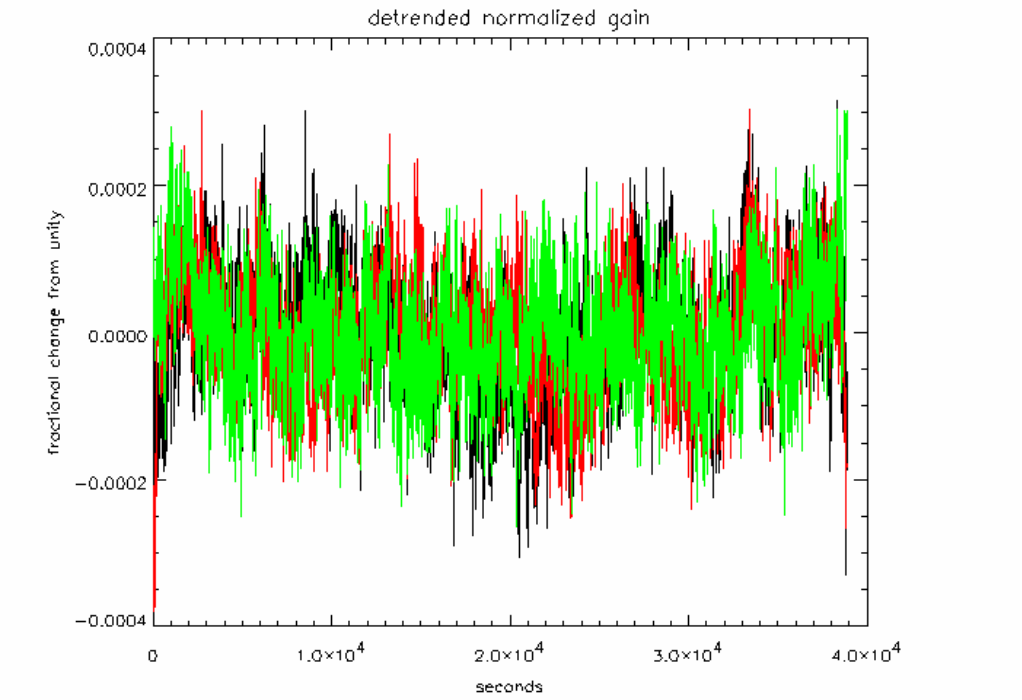

Figure 1.5: 10 hours of gain. A running average of Tr was applied, and gain was estimated from reference load data. Integration time= 19*.413s = 7.8s.

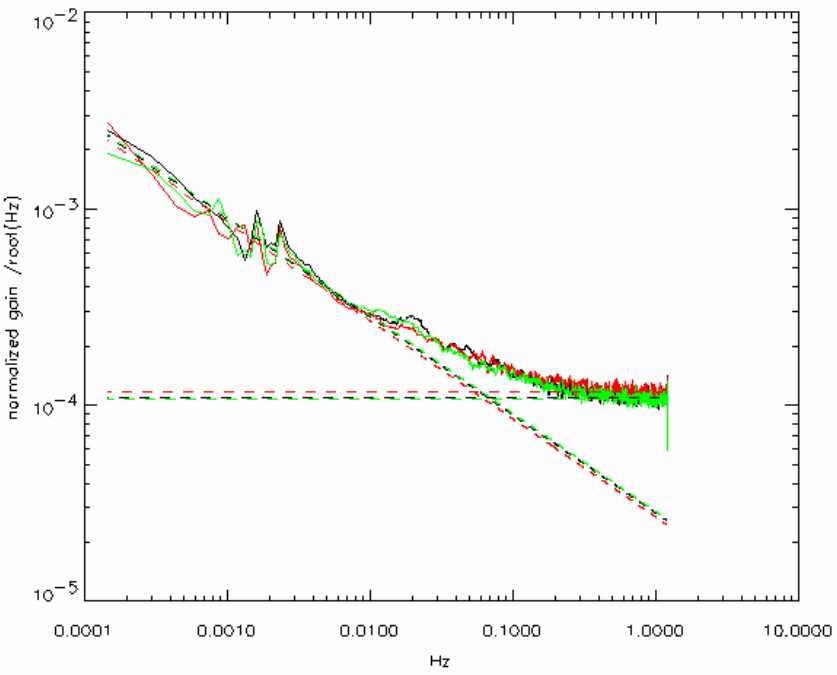

Figure 1.6: Power spectra of gain from Figure 5 (reference estimated gain- without boxcar averages beyond 0.413s). Fit coefficients follow:

```
f0 S(f)= 1.20e-008+ 8.1e-010/f (gain^2), fknee=    0.067
f1 S(f)= 1.35e-008+ 7.3e-010/f (gain^2), fknee=    0.054
f2 S(f)= 1.16e-008+ 8.3e-010/f (gain^2), fknee=    0.072
```

Figure 1.7 shows the spectra of gain when gain is calculated from the noise diode deflections, as in Equation 1.1. Note that the 1/f spectra are unchanged from Figure 1.6, but that the white noise components are about 10x higher (about 3.1 in the square root). This result demonstrates the improved gain estimate. The comparison of Figures 1.6 and 1.7 will also be useful in the next section.

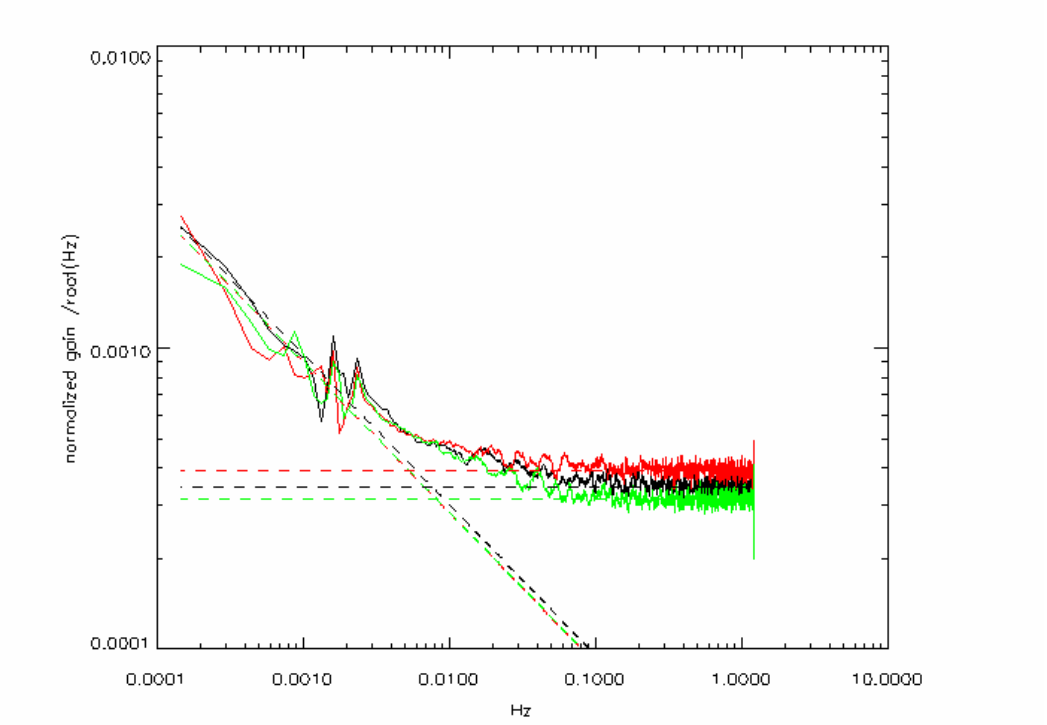

Figure 1.7: Spectra of gain when gain is estimated by noise diode deflections (no Tr estimate). Fit coefficients are:

```
f0 S(f)= 1.2e-007+ 9.2e-010/f (K^2), fknee=    0.0076
f1 S(f)= 1.5e-007+ 8.1e-010/f (K^2), fknee=    0.0053
f2 S(f)= 1.0e-008+ 8.2e-010/f (K^2), fknee=    0.0083
```

2. Optimization of duty cycles

The above results can be used to adjust the duty cycles of the radiometers noise diode, antenna, and reference measurements. Based on Equation 1.4, we start with the following formula for the brightness temperature estimate:

$$T_A = gC_A - T_r \tag{2.1}$$

where the lower case "g" represents the inverse of gain (G^{-1}), C_A is the measured response to the antenna brightness, and T_r is the estimate of receiver noise temperature. Each of these quantities includes an error, which we express as

$$T_A = < T_A > (1+\delta_T) = < g > (1+\delta_g) < C_A > (1+\delta_A) - < T_r > (1+\delta_r) \tag{2.2}$$

where <.> denotes the expectation operator, and each δ term represents a normalized (or fractional) measurement error. By subtracting the identity, $<T_A>=<g><C_A>-<T_r>$, and by assuming small delta terms (i.e. $\delta << 1$) we get

$$< T_A > \delta_T \cong (< T_A > + < T_r >)\delta_g + (< T_A > + < T_r >)\delta_A - < T_r > \delta_r . \tag{2.3}$$

Equation 2.3 relates brightness temperature error to fractional errors in the three terms of Equation 2.1. To expand each of these errors in terms of specific measurement errors, we will use the radiometer timing model of Figure 2.1. Figure 2.1 depicts a scheme in which the reference load of the Dicke switch is measured with a duty cycle of d_o, the noise diode plus reference is measured with a duty cycle of d_N, and the antenna is measured with a duty cycle of $1-d_N-d_o$. For the present discussion we will exclude the possible measurement of antenna plus noise diode. Three integration times are also depicted: antenna brightness temperature will be computed from boxcar integrations lasting τ_A seconds; gain from integrations lasting τ_o seconds; and receiver noise temperature from τ_r second integrations. We assume that the radiometers hardware and data system can measure and accumulate the data with a sufficiently short interval, τ, so that noise diode, antenna, and reference measurements are effectively concurrent. The following analysis assumes that $\tau < \tau_A < \tau_o << \tau_r$.

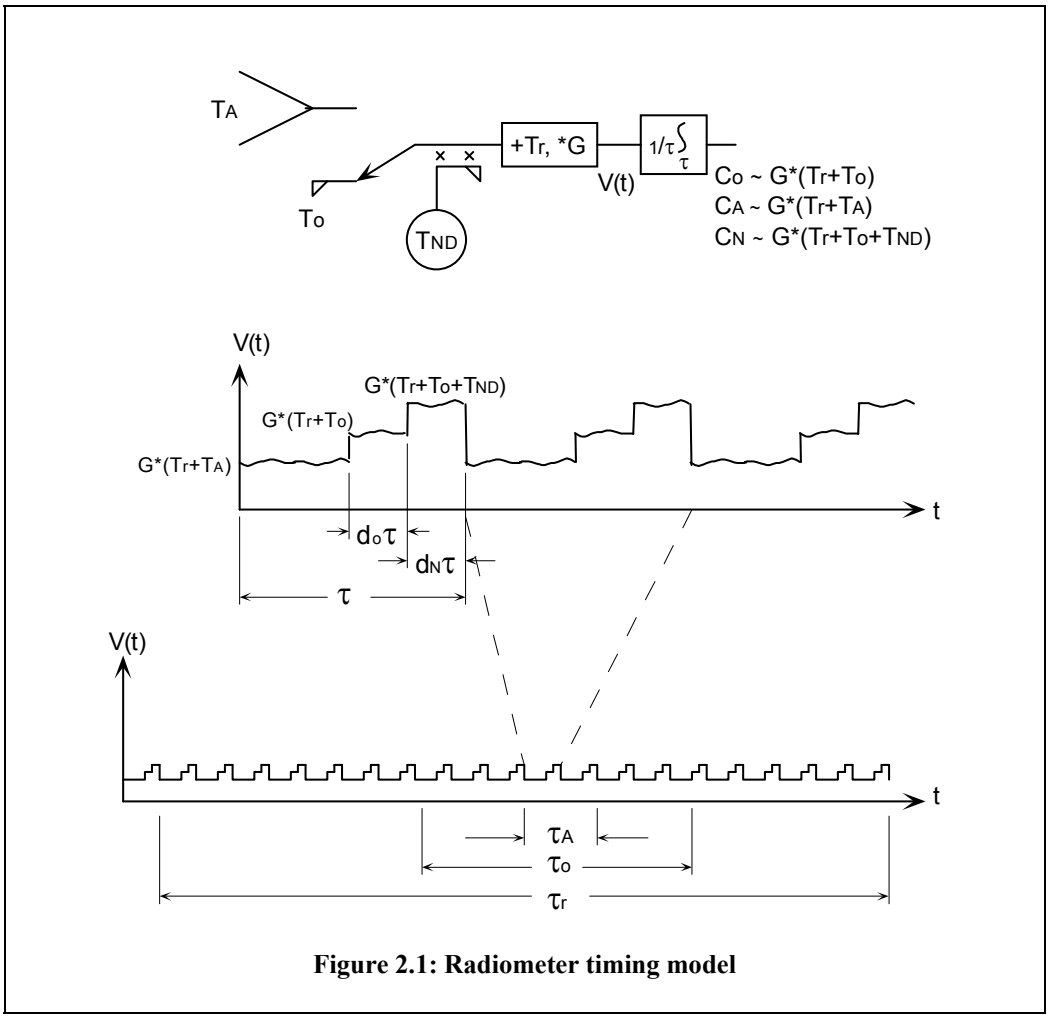

Figure 2.1: Radiometer timing model

The receiver noise temperature will be estimated from Equation 1.5, which expands to

$$T_r = <T_r>(1+\delta_r) = <C_o>(1+\delta_{or})\frac{T_{ND}}{<C_N>(1+\delta_{Nr}) - <C_o>(1+\delta_{or})} - T_o \tag{2.4}$$

$$= g(T_o + <T_r>)(1+\delta_{or})\frac{T_{ND}}{g(T_{ND}+T_o+<T_r>)(1+\delta_{Nr}) - g(T_o+<T_r>)(1+\delta_{or})} - T_o$$

where δ_{Nr} and δ_{or} are the fractional errors associated with C_N and C_o for an integration time of τ_r seconds. When these errors are small with respect to unity, Equation 2.4 leads to

$$\delta_r \cong \frac{(T_{ND}+T_o+<T_r>)(T_o+<T_r>)}{<T_r>T_{ND}}(\delta_{or}-\delta_{Nr}). \tag{2.5}$$

With Equation 2.5 and the bandwidth, duty cycles, and integration time of Figure 2.1, the white noise component of T_r is

$$<\delta_{rw}{}^2> = \left[\frac{(T_{ND}+T_o+<T_r>)(T_o+<T_r>)}{<T_r>T_{ND}}\right]^2 (<\delta_{or}{}^2> + <\delta_{Nr}{}^2>). \tag{2.6}$$

$$= \left[\frac{(T_{ND}+T_o+<T_r>)(T_o+<T_r>)}{<T_r>T_{ND}}\right]^2 \left(\frac{1}{B\tau_r d_o} + \frac{1}{B\tau_r d_N}\right)$$

where B is the detection bandwidth of the radiometer, and we have applied the standard radiometer noise formula and the assumption that δ_{Nr} and δ_{or} are zero-mean and uncorrelated. The "w" subscript has been added to δ_{rw} to distinguish between the white noise and the 1/f noise. Equation 2.6 predicts the "a" term of Equation 1.6 through the equation

$$a = 2\tau_r <T_r>^2 <\delta_{rw}{}^2> \tag{2.7}$$

where a has units K^2/Hz. By applying Equations 2.6 and 2.7 along with the measured 1/f coefficient "b" to Equation 1.17 we can estimate the optimum τ_r for a given duty cycle. We can then calculate the variance of the net receiver noise temperature error applicable to the observation time $\tau=\tau_A$ with Equation 1.15.

Gain in Equation 2.1 will be estimated with

$$g = \left(d_o\frac{T_o+T_r}{C_o} + d_N\frac{T_{ND}+T_o+T_r}{C_N}\right)\frac{1}{d_o+d_N}. \tag{2.8}$$

In this case we've formed a weighted average of the gain estimates provided by reference counts, C_o, and noise diode counts, C_N. This is a more general expression than the form implied in Equation 1.4, and has the effect of increasing the effective duty cycle to d_o+d_N. By expanding each of the measurements in Equation 2.8 in terms of fractional errors (as in Equations 2.2 or 2.4), we have

$$\delta_g = \frac{1}{d_o+d_N}\left[-d_o\delta_{oo} - d_N\delta_{No} + \delta_{ro}<T_r>\left(\frac{d_o}{<T_r>+T_o} + \frac{d_N}{<T_r>+T_{ND}+T_o}\right)\right] \tag{2.9}$$

where δ_{oo} and δ_{No} are the fractional errors associated with the reference and noise diode counts given an integration time of τ_o seconds. The "o" subscript has also been added to δ_{ro} to distinguish it from δ_r in Equation 2.3 (the distinction will be explained shortly).

To evaluate the optimum gain integration time, τ_o, we will assume that $\tau_r >> \tau_o$ so that the white noise in Equation 2.9 is dominated by δ_{oo} and δ_{No}. We will also assume that the 1/f component of the gain is much greater than that of the receiver noise- based on Figures 1.2, 1.6, and 1.7. With these assumptions we can evaluate the gain integration time with

$$\delta_{g'} \equiv \frac{-d_o\delta_{oo} - d_N\delta_{No}}{d_o+d_N} \tag{2.10}$$

which predicts the gain white noise spectra (as in Equation 2.5, 2.6, and 2.7) according to

$$a_g = \frac{2}{B(d_o+d_N)}, \tag{2.11}$$

where a_g has units of normalized gain squared per Hz, and sets the optimum gain integration time in Equation 1.17 for a given 1/f coefficient, b_g (from Figures 1.6 or Figure 1.7).

The net delta-T error is evaluated by using Equation 2.10 and Equation 2.9 to regroup the gain and receiver noise error terms of Equation 2.3 as follows:

$$< T_A > \delta_T \cong (< T_A > + < T_r >)\delta_{g'} + (< T_A > + < T_r >)\delta_A$$
$$+ < T_r > \left[-\delta_r + \delta_{ro} \frac{< T_A > + < T_r >}{d_o + d_N} \left(\frac{d_o}{< T_r > + T_o} + \frac{d_N}{< T_r > + T_{ND} + T_o} \right) \right]. \qquad (2.12)$$

Note that the "o" subscript of δ_{ro} is retained from Equation 2.9 to distinguish it from δ_r ; these errors differ because of the different observation intervals that apply. In Equations 2.8 and 2.9 δ_{ro} represents the measurement error with respect to expected value of T_r averaged over the gain integration time, τ_o- not the antenna integration time τ_A which applies to δ_r in Equation 2.3. The 1/f component of these errors will differ when Equation 1.15 is evaluated for the different observation times, $\tau=\tau_A$ or $\tau=\tau_o$. For the range of possible gain integration time, $\tau_A<\tau_o<\tau_r$, the 1/f component of δ_{ro} will vary between $\delta_r=\delta_{ro}$ when $\tau_o=\tau_A$, and zero when $\tau_o=\tau_r$; for the general case we need to examine the partial correlation of δ_r and δ_{ro}. Each error shares the same white noise component, so

$$\delta_r = \delta_{rw} + \delta_{rf}$$
$$\delta_{ro} = \delta_{rw} + \delta_{rfo} \qquad (2.13)$$

where δ_{rf} and δ_{rfo} now represent the 1/f noise in each measurement. To evaluate the partial correlation of δ_{rf} and δ_{rfo} consider Figure 2.2 which depicts the time varying T_r in the absence of white noise, and the relation of the three different averages: the measured average over τ_r, the desired average over τ_o, and the desired average over τ_A. From Figure 2.2 we see that the 1/f errors of Equation 2.13 differ by δ_{Ao} so that with Equation 2.13 we have

$$\delta_r = \delta_{ro} + \delta_{Ao}. \qquad (2.14)$$

In Figure 2.2 we see that δ_{Ao} represents the difference between the short (τ_A-second) average from the intermediate (τ_o-second) average. Likewise, δ_{rfo} measures the difference between the intermediate (τ_o) average and the long (τ_r) average. Any given sample of T_r can not predict past or future changes in T_r, so δ_{Ao} can not predict T_r variations which occur outside of τ_o. Yet δ_{rfo} entirely depends on changes which occur outside of the intermediate (τ_o) average. Therefore, δ_{Ao} and δ_{rfo} are independent. δ_{Ao} and δ_{rfo} are also zero mean, so we find that δ_{Ao} and δ_{rfo} are uncorrelated; i.e that $<\delta_{Ao}\delta_{ro}>=0$. The variance of δ_{Ao} can be calculated from Equation 1.13 by letting $m=\tau_o/2\tau_A-1/2$.

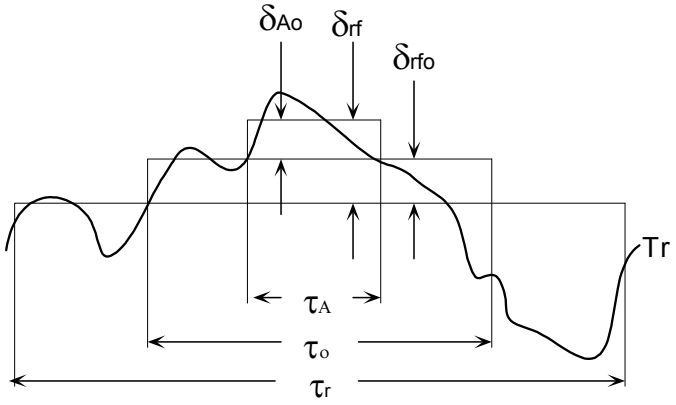

Figure 2.2: Errors associated with T_r when comparing various averages.

With Equation 2.14, Equation 2.12 becomes

$$< T_A > \delta_T \cong (< T_A > + < T_r >)\delta_{g'} + (< T_A > + < T_r >)\delta_A$$
$$+ < T_r > \left[\frac{< T_A > + < T_r >}{d_o + d_N} \left(\frac{d_o}{< T_r > + T_o} + \frac{d_N}{< T_r > + T_{ND} + T_o} \right) - 1 \right] \delta_{ro} + < T_r > \delta_{Ao}. \qquad (2.15)$$

Equation 2.15 equates the brightness temperature error to a sum of four errors: $\delta_{g'}$, δ_A, δ_{ro}, and δ_{Ao}. Each of these errors are zero-mean, and we wish to establish that they are independent. We have carefully constructed the equation so that the two receiver noise errors δ_{ro}, and δ_{Ao} are independent. The independence of the antenna noise

term, δ_A, is also given since the antenna counts, C_A, are measured independently (i.e. with no overlap with C_N or C_o). We can also assume that the white noise part of δ_{ro}, which from Equation 2.5 is proportional to difference δ_{or} -δ_{Nr}, is largely uncorrelated with the sum $d_o\delta_{oo}$+ $d_N\delta_{No}$ that constitutes the white noise of $\delta_{g'}$ in Equation 2.10. This is true if either d_o=d_N or τ_r>>τ_o.

The only remaining question is whether the 1/f noise of the receiver noise temperature and of the gain are independent. To establish this we refer to the fact the 1/f spectra of gain in Figures 1.6 and 1.7 were unaffected by application of the running average of T_r. Figure 1.7 was computed from noise diode deflections which are completely insensitive to changes in T_r, whereas Figure 1.6 depends heavily on a reliable estimate of T_r. If there was a significant correlation of gain and receiver noise within the time scales of interest, then the 1/f noise of Figures 1.6 and 1.7 would have shown it. We can also make a physical argument: the gain of a radiometer depend on the cumulative effects of many transistors, whereas the receiver noise temperature depends mostly on the first transistor. We can expect a partial correlation of gain and receiver noise due to the common first transistor, yet even that correlation may be weak given the complex and often opposing interactions of gain and noise figure with the input and output impedance match, bias, etc.. We therefore believe that the four errors of Equation 2.15 are indeed independent. The variance of the sum of these errors can therefore be computed from the sum of variances according to

$$\begin{aligned} &< T_A >^2 < \delta_T{}^2 > \cong (< T_A > + < T_r >)^2 < \delta_{g'}{}^2 > + (< T_A > + < T_r >)^2 < \delta_A{}^2 > \\ &+ < T_r >^2 \left[\frac{< T_A > + < T_r >}{d_o + d_N} \left(\frac{d_o}{< T_r > + T_o} + \frac{d_N}{< T_r > + T_{ND} + T_o} \right) - 1 \right]^2 < \delta_{ro}{}^2 > + < T_r >^2 < \delta_{Ao}{}^2 > \end{aligned} \tag{2.16}$$

where, summarizing Equation 1.15,

$$\begin{aligned} &< \delta_{g'}{}^2 > = b_g \theta(m) + \frac{a_g}{2\tau_A} \frac{1}{2m+1}, \\ &m = \frac{\tau_o - \tau_A}{2\tau_A} \end{aligned} \tag{2.17}$$

and θ(m) is from Equation 1.14. The gain variance is minimized by (from Equation 1.17)

$$\tau_o = \frac{a_g}{2b_g}, \tag{2.18}$$

where a_g is from Equation 2.11 and b_g is from Figures 1.6 or 1.7. The variance of the antenna measurement is, from the standard radiometer formula,

$$< \delta_A{}^2 > = \frac{1}{B\tau_A (1 - d_o - d_N)}, \tag{2.19}$$

and the receiver noise variance terms are

$$\begin{aligned} &< \delta_{ro}{}^2 > < T_r >^2 = b\theta(m) + \frac{a}{2\tau_o} \frac{1}{2m+1} \\ &m = \frac{\tau_r - \tau_o}{2\tau_o} \end{aligned} \tag{2.20}$$

and

$$\begin{aligned} &< \delta_{Ao}{}^2 > < T_r >^2 = b\theta(m) \\ &m = \frac{\tau_o - \tau_A}{2\tau_A} \end{aligned} \tag{2.21}$$

where a is from Equations 2.6 and 2.7, and b is from Figure 1.2.

Table 1 presents some test cases using the above algorithm. The duty cycles (reference and noise diode) were selected by generating errors on a 2-D grid versus duty cycle, then searching the resulting array for a minimum. The

computer program was written in IDL and is provided in the Appendix. Two test cases are presented: (1) the AWVR which observes brightness temperatures near 20K, and (2) the Aquarius radiometer which observes near 100K. The assumed system parameters are summarized in the table.

For each result in Table 1 the optimized noise equivalent delta-T (NEDT) predicted by Equation 2.16 is given along with a comparison to an "ideal" total power radiometer for a given antenna integration time, τ_A (/TP = NEDT/(T_{sys}/root(Bτ_A))). At least two results are given for each τ_A: the first case optimizes noise diode and reference duty cycles independently; the second constrains the duty cycles by d_N=d_o. In many cases the optimizations yield an unreasonably large τ_r, so all results were constrained by τ_r < 5,000 seconds, based on Figure 1.3. Neither of these constraints significantly affect the delta-T.

For the AWVR cases of Table 1 we see that the shortest observation intervals benefit the most from the above approach. At the longest interval τ_A, τ_o, and τ_r are nearly equal and the greatest fraction of the available time is spent measuring reference and noise diode counts. The delta-T in this case is almost 5x worse than that of a total power radiometer since, in effect, Equation 1.1 applies. The AWVR's are being used for the Cassini gravity wave experiment where 1,000 second timescales are the most important, so there is little to be gained with the algorithm presented above.

The Aquarius radiometer stands to benefit much more from the above approach than the AWVR. Two cases in Table 1, highlighted with bold characters, represents a reasonable estimates for Aquarius for the known observation time of 12 seconds. In the second of the two cases the receiver noise integration time has been cut to a conservative 500 seconds to limit the on-orbit systematic errors which might corrupt the receiver noise stability. The results indicate that the noise equivalent delta-T of the Aquarius radiometer will be between 0.033K and 0.039K, which is only about 1.5 times worse than the ideal total power radiometer.

I have assumed in Table 1 that the 1/f characteristics that I measured in the AWVR will scale to the Aquarius radiometer with receiver noise temperature. This is a very rough assumption, and I don't yet have data to show this. The net receiver noise temperature depends on passive losses that occur before the LNA the noise figure of the LNA. If the passive losses are constant and temperature is stable, one can expect that 1/f fluctuations caused by the LNA will scale as the inverse of the losses to antenna-referenced noise temperature. This is my only basis for such a scaling.

References

[1] Janssen, M.A., et al., "Direct imaging of the CMB from space," *ApJ*, 9602009, Feb. 1996, http://arxiv.org/PS_cache/astro-ph/pdf/9602/9602009.pdf

```
; Test case uses 1/f of AWVR#1,22.2GHz- where noise diodes are equal.
Tr=449.7 ; receiver noise temp (K)
To=308.1 ; reference temp (K)
Ta=20.  ; antenna brightness temperature (K)
Ts=Tr+Ta ; system noise temp
BW=500e+6 ; bandwidth (Hz)
Tnd=500.  ; noise diode deflection (K)
br=1.34e-10 ; 1/f spectra coefficient of normalized Tr (/Hz)
b=Tr*Tr*br  ; " not normalized (K^2/Hz)
bg=7.3e-10  ; normalized gain 1/f spectra coefficient (/Hz)
```

NEDT (K)	/TP (ratio)	τ_A (s)	τ_r (s)	τ_o (s)	d_o (fractions)	d_N
0.0773	1.16	0.1	5000.	68.5	0.03	0.01
0.0773	1.16	0.1	5000.	68.5	0.02	0.02
0.0341	1.62	1.0	5000.	11.0	0.21	0.04
0.0342	1.63	1.0	4470.	11.4	0.12	0.12
0.0144	2.17	10.0	5000.	10.0	0.45	0.06
0.0148	2.22	10.0	2146.	10.0	0.25	0.25
0.00616	2.93	100.0	3551.	100.0	0.47	0.09
0.00651	3.10	100.0	1850.	100.0	0.29	0.29
0.00307	4.62	1000.0	1665.	1000.0	0.49	0.24
0.00319	4.81	1000.0	1450.	1000.0	0.37	0.37

```
; test case for Aquarius
Tr=250. ; receiver noise temp (K)
To=295. ; reference temp (K)
Ta=100.  ; antenna brightness temperature (K)
BW=20e+6 ; bandwidth (Hz)
Tnd=500.  ; noise diode deflection (K)
br=1.34e-10 ; 1/f spectra coefficient of normalized Tr (/Hz)
b=Tr*Tr*br  ; " not normalized (K^2/Hz)
bg=7.3e-10  ; normalized gain 1/f spectra coefficient (/Hz)
```

NEDT	/TP	τ_A	τ_r	τ_o	d_o	d_N
0.253	1.02	0.1	5000.	3424.7	0.01	0.01
0.253	1.02	0.1	5000.	3424.7	0.01	0.01
0.0864	1.10	1.0	5000.	1369.9	0.03	0.02
0.0865	1.11	1.0	5000.	1141.6	0.03	0.03
0.0350	1.42	10.0	5000.	380.5	0.12	0.06
0.0351	1.42	10.0	5000.	380.5	0.09	0.09
0.0329	1.46	12.0	5000.	342.5	0.13	0.07
0.0330	**1.46**	**12.0**	**5000.**	**342.5**	**0.10**	**0.10**
0.0387	**1.71**	**12.0**	**500.**	**190.3**	**0.18**	**0.18**
0.0159	2.03	100.0	5000.	152.2	0.30	0.15
0.0160	2.04	100.0	5000.	148.9	0.23	0.23

Table 1

Appendix I: IDL code to evaluate delta-T versus duty cycle

```
pro dt_v_d,taua
; A.Tanner, JPL
; IIP study of running Tr and g averages vs duty cycle.
; Formula from 4/29- 5/10/2 notes
; Test case uses 1/f of AWVR#1,22.2GHz- where noise diodes are equal.
Tr=449.7       ; receiver noise temp (K)
To=308.1       ; reference temp (K)
Ta=20.         ; antenna brightness temperature (K)
Ts=Tr+Ta       ; system noise temp
BW=500e+6      ; bandwidth (Hz)
;taua=10.       ; observation time (s)
Tnd=500.       ; noise diode temperature (K)
Tn=Tnd+To      ; ND deflection plus ref
br=1.34e-10    ; 1/f spectra coefficient of normalized Tr (/Hz)
b=Tr*Tr*br     ; " not normalized (K^2/Hz)
bg=7.3e-10     ; normalized gain 1/f spectra coefficient (/Hz)
taurmax=5000.  ; receiver noise integration time limit, from Figure 1.3
n=49           ; grid size
dt=fltarr(n,n) ; to save delta-T results
taur=dt        ; Tr integration time
taug=dt        ; g integration time
vtr=dt         ; variance of Tr(K^2)
vg=dt          ; variance of gain (normalized gain ^2)
va=dt          ; variance of antenna counts (normalized count ^2)
vtg=dt         ; gain variance scaled by Ts
vta=dt         ; antenna counts variance scaled by Tsys
dr=(findgen(n)+1)/2/(n+1)  ; range of duty cycles to test- ref mode
dn=dr ; range of duty cycles to test- ref+ ND mode

arc=2./BW*((Tn+Tr)*(To+Tr)/Tr/(Tn-To))^2 ; common factor used below

for i=0,n-1 do begin  ; loop over reference mode duty cycle
  for j=0,n-1 do begin  ; loop over noise diode + reference mode duty cycle
; compute gain variance...
ag=2./BW/(dr(i)+dr(j))      ; from equation 2.11
; compute optimum integration time for gain estimate...
taug(i,j)=ag/2./bg          ; equation 1.17
if taug(i,j) lt taua then begin  ; don't let taua > taug...
  vg(i,j)=1./BW/taua/(dr(i)+dn(j)) ; compute variance from thermal noise
  taug(i,j)=taua            ; limit taug
endif else begin
  m=0.5*taug(i,j)/taua-0.5 ; used in following...
; compute variance of gain with 1/f and given taug...
  theta=2./(2*m+1)*((m+1)*(m+1)*alog(m+1)-m*m*alog(m))-alog(2.*m+1)
  vg(i,j)=bg*theta + ag/2./taug(i,j)  ; equation 2.17
endelse
; compute receiver noise temp variance...
ar=arc*(1./dr(i)+1./dn(j))  ; norm'd white noise Tr spectra /Hz, eq.2.6
a=ar*Tr*Tr                  ; " in K^2/Hz, as eq.2.7
taur(i,j)=ar/br/2.          ; integration time for min 1/f + white noise
if taur(i,j) gt taurmax then taur(i,j)=taurmax  ; limit
m=0.5*taur(i,j)/taug(i,j)-0.5    ; m for eq.2.20...
if m>0 then $
  theta=2./(2*m+1)*((m+1)*(m+1)*alog(m+1)-m*m*alog(m))-alog(2.*m+1)$
else theta=0.
vtr(i,j)=b*theta + a/2./taur(i,j) ; 1/f plus white noise
m=0.5*taug(i,j)/taua-0.5    ; m for eq. 2.21...
if m>0 then $
  theta=2./(2*m+1)*((m+1)*(m+1)*alog(m+1)-m*m*alog(m))-alog(2.*m+1)$
else theta=0.
va(i,j)=1./BW/taua/(1.-dr(i)-dn(j)) ; antenna noise by eq. 2.19
; final Ta variance by eq. 2.16...
```

```
dt(i,j)=Ts*Ts*(vg(i,j)+va(i,j)) $
  + vtr(i,j)*(1-Ts/(dr(i)+dn(j))*(dr(i)/(Tr+To)+dn(j)/(Tr+Tn)))^2$
  + b*theta

  endfor
endfor

l=(sort(dt))(0:1000)  ; get the 1000 smallest errors
lde=l((where(dn(l/n) eq dr(l mod n)))(0))  ; find first case dt=dn
print,"    NEDT     /TP     tA       tr       tg      do      dn"
print,format='(g9.3," ",g7.3," ",f6.1," ",f9.0," ",f7.1," ",f7.2," ",f7.2)',$
      sqrt(dt(l(0))),sqrt(dt(l(0)))/Ts*sqrt(BW*taua),$
      taua,taur(l(0)),taug(l(0)),dr(l(0) mod n),dn(l(0)/n)
print,format='(g9.3," ",g7.3," ",f6.1," ",f9.0," ",f7.1," ",f7.2," ",f7.2)',$
      sqrt(dt(lde)),sqrt(dt(lde))/Ts*sqrt(BW*taua),$
      taua,taur(lde),taug(lde),dr(lde mod n),dn(lde/n)

return
end
```

Appendix 5 Spectral Analysis of Testbed Data

JET PROPULSION LABORATORY INTEROFFICE MEMORANDUM

TO: USR team
FROM: Alan Tanner
DATE: 12/14/2004
SUBJECT: Spectral analysis of JPL and GSFC testbed data

I have computed a large number of power spectra from a total of six testbed experiments performed here at JPL and at Goddard. These spectral analysis show how the running averages of receiver noise and of gain improve the brightness temperature estimates- in spite of the fact that the antenna brightness temperature is not always stable. In Section 1 I describe how the spectra were calculated. In Section 2 I make some assertions about why I don't think we need an accurate noise diode calibration- or for that matter an accurate set of temperature coefficients with which to correct such things as front end losses, gain, or noise diode output- to make the demonstration. In Section 3 I present the data, and in Section 4 I discuss the results.

1. Notes regarding power spectral density plots

The power spectral density plots of gain, receiver noise, or antenna brightness temperature presented in this report are subject to the following processing steps: (1) the time series of radiometer data are de-trended by subtracting a linear fit versus time; (2) an FFT of the entire series is computed; and (3) the magnitude of the complex spectra from 0 Hz to one half of the sample frequency is computed and scaled by the square root of the sample period to produce a spectrum with units of pre-detected power (e.g. Kelvin or power gain) per root Hz. The square of these spectra (which would have units proportional to post-detected-power-per-Hz) are actually the true "power spectral densities" of the radiometer's output voltage, but we normally plot them in the square root to be linear on a Kelvin scale. In the case of gain spectra, the gain measurements are all scaled to a unit mean value. Note that the linear de-trending of step (1) removes a 1/f component from the spectra which cannot be accurately estimated from a finite time series (since the power density depends on the length of the time series). This is a subjective choice, and conventions may differ as to how to deal with such problems. It should also be noted that the scaling of step (2) should result in a white noise spectral density of T_{sys}*sqrt(2/B) for the specific case of an ideal total power radiometer with pre-detection bandwidth B[9].

An example of a gain spectra produced by the above steps is plotted with the black trace in Figure 1. This 'raw' spectra is very noisy since the FFT generates as many frequency samples as there are time samples. The noise is most pronounced at the higher frequencies of a log/log plot such as Figure 1. To reduce the noise, a logarithmic averaging scheme has been applied which produces an even distribution of samples on a logarithmic frequency scale. The green trace of Figure 1 is the result of this algorithm: to the left of this plot there is no frequency averaging and the noise of the spectra is identical to the sample noise of the black curve; to the right an exponentially increasing number of samples are averaged together, which leads to less scatter. This averaging is performed in an RSS sense (i.e. the green trace of Figure 1 is square root of the average of the square of the black trace).

In addition to the above spectra, it is also possible to calculate a 'co-spectra' which will isolate noise which is uncorrelated from one time series sample to the next (i.e. isolate the white noise). This 'co-spectrum' is computed by separating alternate samples into even and odd time series, computing the FFT's of each, and then multiplying one spectrum by the conjugate of the other spectrum. Such a spectra is plotted in Figure 1 as the red curve. This co-spectra is identical to the power spectral density at low frequencies where the drift in gain or receiver noise is slow compared to the sample frequency. At the higher frequencies the co-spectra suppresses the white noise- which is

[9] Note that the spectral density of the *square* of a band-limited noise process of unit variance is sqrt(2/B) (not sqrt(1/B) as one might think) for frequencies <<B. For higher frequencies the spectrum falls off linearly to zero power density at f=2B. The integral of this spectra equals 2, which equals to the variance of the square of a Gaussian random variable of unit variance, and satisfies Parseval's theorem.

uncorrelated between adjacent samples. The red trace in Figure 1 is fragmented at the higher frequencies by the plotting software- which ignores the logarithm of negative valued spectra.

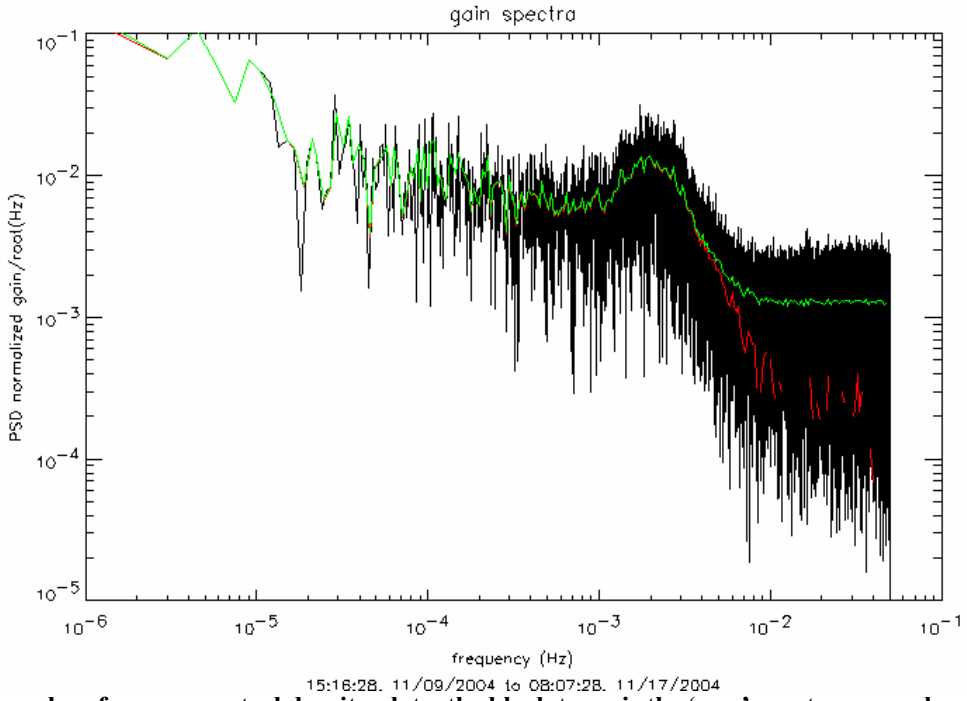

Figure 1: Examples of power spectral density plots: the black trace is the 'raw' spectra as produced by the FFT, the green trace is a 'logarithmically averaged' curve, and the red trace is the 'co-spectra', as explained in the text. All three spectra were computed from a time series of gain data- as discussed in Section 3.

2. Notes regarding the absolute calibration of the testbed data

Figure 2 shows two versions of a radiometric data set which was measured on October 24 using the GSFC testbed. These data were collected while connected to a cold load of approximately 40 K, and are calibrated in two ways: Figure 2a assumes a noise diode temperature of T_N=667 K, and Figure 2b assumes T_N=2600K in the following equation:

$$T_B = T_o - \frac{C_o - C_A}{C_N - C_o} T_N \quad (1)$$

where C_o, C_A, and C_N, are the reference, antenna, and reference plus noise diode counts from the radiometer, T_o is the reference ambient temperature of the radiometer as measured at the Dicke switch load. T_N is an equivalent noise temperature which is referenced to some arbitrary point in the system. In Figure 2a, this reference point is after the Dicke switch, and in Figure 2b this reference point is the coaxial input of the radiometer where it attaches to the cold load. Between these points there is a lot of electrical loss (due to several couplers, isolators, coaxial cable, etc.). If all temperatures within the radiometer assembly are equal to T_o, then (1) is valid for both cases. To a large extent this is the case in the testbed data. Figures 2a and 2b differ primarily by an offset (equal to the noise added by all the losses) and a scale factor (equal to the loss factor). Relatively minor differences are otherwise present, and these can be traced to thermal gradients which exist among the front end components. These gradients are measured (to a limited extent) in the testbeds so that corrections to (1) can be made. For the present analysis, however, these corrections will not be considered. Instead, the analysis presented below will focus on how the different averaging schemes affect various spectra, and it will be shown that these analysis do not require such corrections. The absolute calibration- and for that matter the absolute stability of the "antenna" noise temperature measurement- are not critical to these analysis.

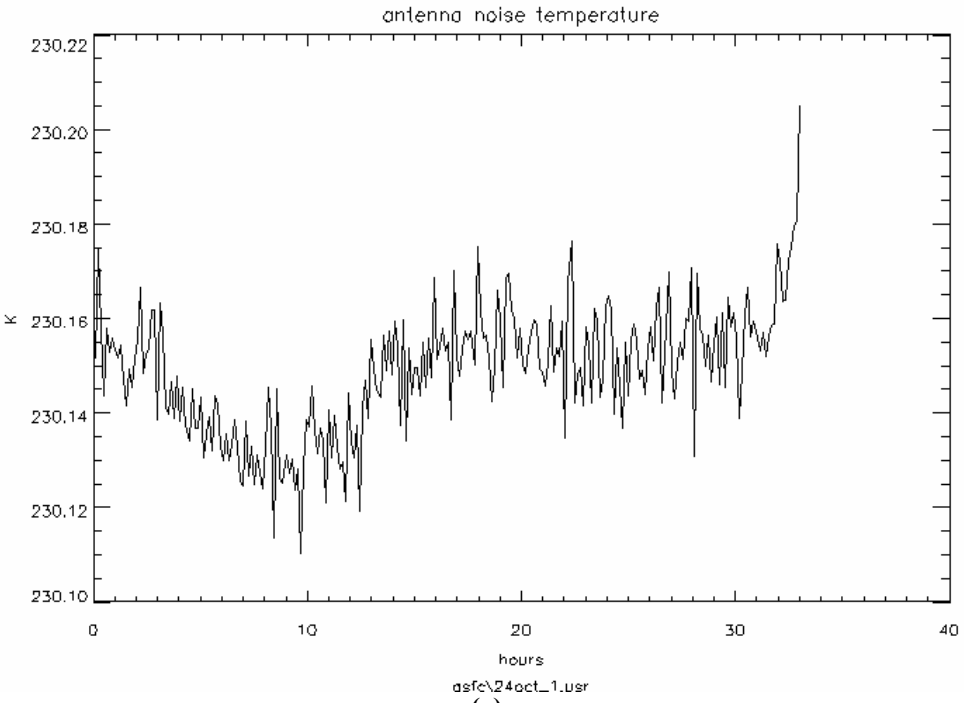

(a)

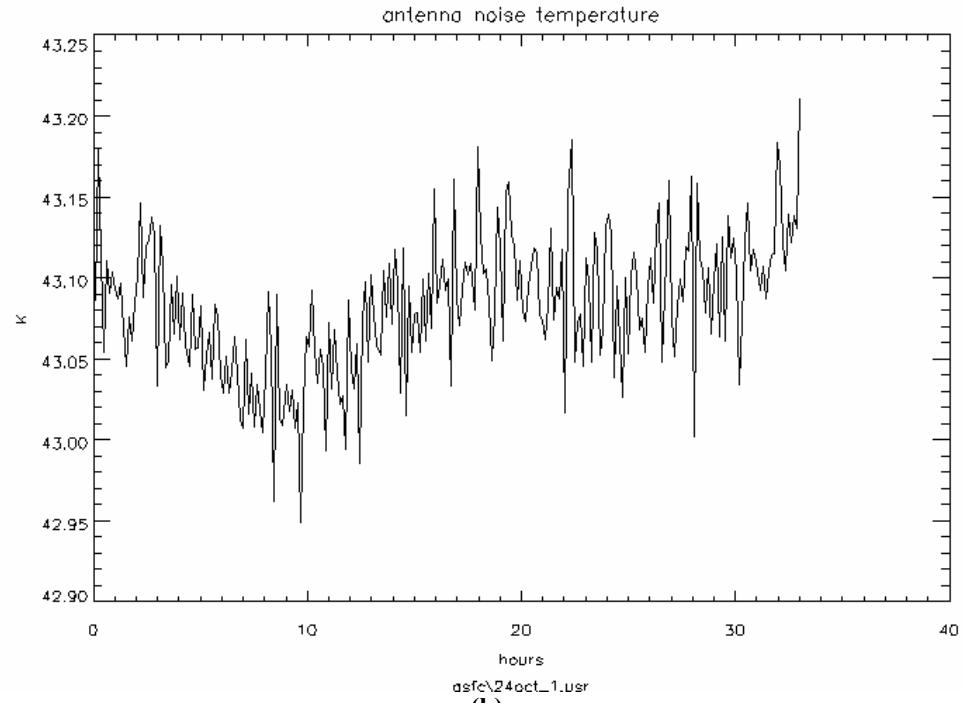

(b)

Figure 2: Brightness temperatures from 24 October using the GSFC testbed with two assumed noise diode temperatures of 667k (a), and 2600K (b), in Equation 1.

3. Spectral analysis of the testbed data

Table 1 summarizes six data sets collected at JPL and at GSFC. The following notes and observations apply to these experiments:

1. In tests #1 and #2 the JPL testbed had the thermoelectric cooler (TEC) switched on an set to 23 C. The temperature controller was not of a very good quality, and it was observed that the temperature control tended to randomly bounce back and fourth by about 0.1 to 0.2 C on a time scale of 100 to 200 seconds or so.
2. In tests #2 and #3 we switched off the temperature controller. In these cases, the radiometer temperature followed the ambient room temperature- which happened to be quite stable- with only 2 or 3 Kelvin changes from day to night. More significantly, the short term stability of the radiometer was greatly improved.
3. The JPL hot load of tests #1 and #4 was a 100 C Maurey laboratory standard.
4. The JPL active cold load of tests #2 and #3 consisted of an LNA which was placed on its own TEC, and operated in reverse with an isolator pointed away from the LNA input to send the cold noise temperature towards the testbed.
5. The GSFC data of tests #5 and #6 exhibited far superior stability in the temperature controller- at the level of just a few millikelvin in some cases- than that of the JPL tests. There were some temperature sensors that did indicate a sensitivity to ambient room temperature- but these sensitivities amounted to less than 0.1 C of slow varying temperature.
6. The GSFC test #5 was made with a deliberate +/1 C sinusoidal oscillation applied to the back-end RF temperatures (including second LNA, bandpass filter, and detector) at a frequency of one cycle per 4000 seconds. This oscillation was intended to simulate orbital variations of a 'split' Aquarius instrument where the temperature control is only applied to front-end components (Dicke switch, noise diode, first LNA). In the testbed the oscillations were inadvertently coupled into the front-end, however, at a level of 0.1 C as indicated by several temperature sensors.

Table 1 also summarizes the measurement timing. All of these data were collected with high antenna duty cycle and relatively low reference load and noise diode duty cycles in order to simulate the timing that we expect to apply to Aquarius. Receiver noise temperature was calculated from the reference load temperature and the noise diode deflection according to

$$T_R = \frac{C_o T_N}{C_N - C_o} - T_o \tag{2}$$

where the various terms are from (1). Gain was then calculated from an equal weighting of the reference load and the reference load plus noise diode counts according to

$$G = \frac{1}{2}\frac{C_o}{T_o + T_{Ry}} + \frac{1}{2}\frac{C_N}{T_o + T_{Ry} + T_N} \tag{3}$$

where the "y" subscript has been added to T_R to indicate that it is formed from a y-second running average of receiver noise of (2). Antenna brightness temperatures were then calculated according to

$$T_B = \frac{C_A}{G_z} - T_{Ry}\,. \tag{4}$$

where the "z" subscript denotes a z-second running average of gain from (3). In all cases, the 'counts' have been corrected against detector nonlinearity, and null offsets have been removed. Note that if no running averages of gain or receiver noise are performed, then the y and z subscripts are dropped, and (2) thru (4) reduce to (1).

Figures 3 thru 20 present the complete summary of receiver noise, gain, and brightness temperatures, and their spectra for all six experiments of Table 1. In all instances the time series data accompany the spectra, and it should be noted that boxcar integrations are typically applied to the time series plots- as indicated- which do not apply to the spectra. All spectra have a maximum frequency of 1/20th Hz (JPL data) or 1/24th Hz (GSFC data).

In the case of receiver noise spectra, a dashed line indicates a reference level spectral density of root($2\text{x}10^{-5}$/f) (K/root-Hz) which corresponds to the stability of the Advance Water Vapor Radiometer (AWVR). The co-spectra

has also been plotted in red in an attempt to resolve the true receiver noise spectra in the presence of the white noise measurement error.

Likewise, all gain spectra include a standard a dashed line of root($8x10^{-10}$/f) (normalized-gain/root-Hz) corresponding to the gain stability observed in the AWVR. I use the AWVR here as a kind of 'gold standard' since I know that these levels are possible when the temperature control is extremely precise (the AWVR stability was just a few millikelvin).

The horizontal dashed lines in the gain and antenna brightness temperature spectra represent theoretical white noise values as follows:

1. Theoretical gain white noise = $\sqrt{2/BD}$, where B is the bandwidth of 25 MHz, and D is the duty cycle of the reference load and reference load plus noise diode measurements in (3), which from Table 1 are D=0.2 for JPL data and D=0.4 for the GSFC data.
2. Theoretical T_B noise = $(T_B + T_R)\sqrt{2/BD}$ where D is the antenna duty cycle which has been plotted in each case with D=0.6 (which applies to both GSFC and JPL data) and D=1 which is the ideal total power radiometer performance.

The different color traces in the gain spectra correspond to different running averages of receiver noise. Time constants of either 400 seconds or 4000 seconds were applied. The black traces correspond to the case of no running average.

The different color traces in he brightness temperature spectra correspond to various assumed time constants for both receiver noise and gain running averages, as indicated. Again, the black traces correspond to the case of no running average.

Table 1

Testbed data sets:
1. JPL Testbed; 11/9-11/17/2004; 100C hot load; TECs set to 23C
2. JPL Testbed; 11/19-11/29/2004; active cold load; TECs set to 23C
3. JPL Testbed; 12/2-12/7/2004; active cold load; TEC control switched off
4. JPL Testbed; 12/7-12/13/2004; 100C hot load; TEC control switched off
5. GSFC Testbed; 10/24/2004; cryostat load; steady state temperatures
6. GSFC Testbed; 10/27/2004; cryostat load; back-end temperatures varied

JPL testbed timing (each cycle takes 10 ms to complete, and multiple repetitions are compiled in software before recording) :
1 cycle reference,
1 cycle reference+ NDA
1 cycle antenna + NDB
6 cycles antenna
1 cycle null

GSFC timing:
3 cycles antenna
1 cycle reference load
1 cycle reference load + NDA

JPL noise diode-A calibration:
T_N=415 K

This value produces the correct temperature while observing the 100 C hot load.

GSFC noise diode-A calibration:
T_N=1568 K

This equals the 669K estimated after the Dicke switch times the 2.344 (=3.7 dB) loss estimated between LNA in an e-mail from Fernando as follows:

Loss thru NDA coupler: 0.3 dB
Filter Insertion Loss: -2.0 dB
NDB coupler: 0.3 dB
Dicke Switch: 0.4 dB
Isolator: 0.3
NDC coupler: 0.4
Total: 3.7 dB

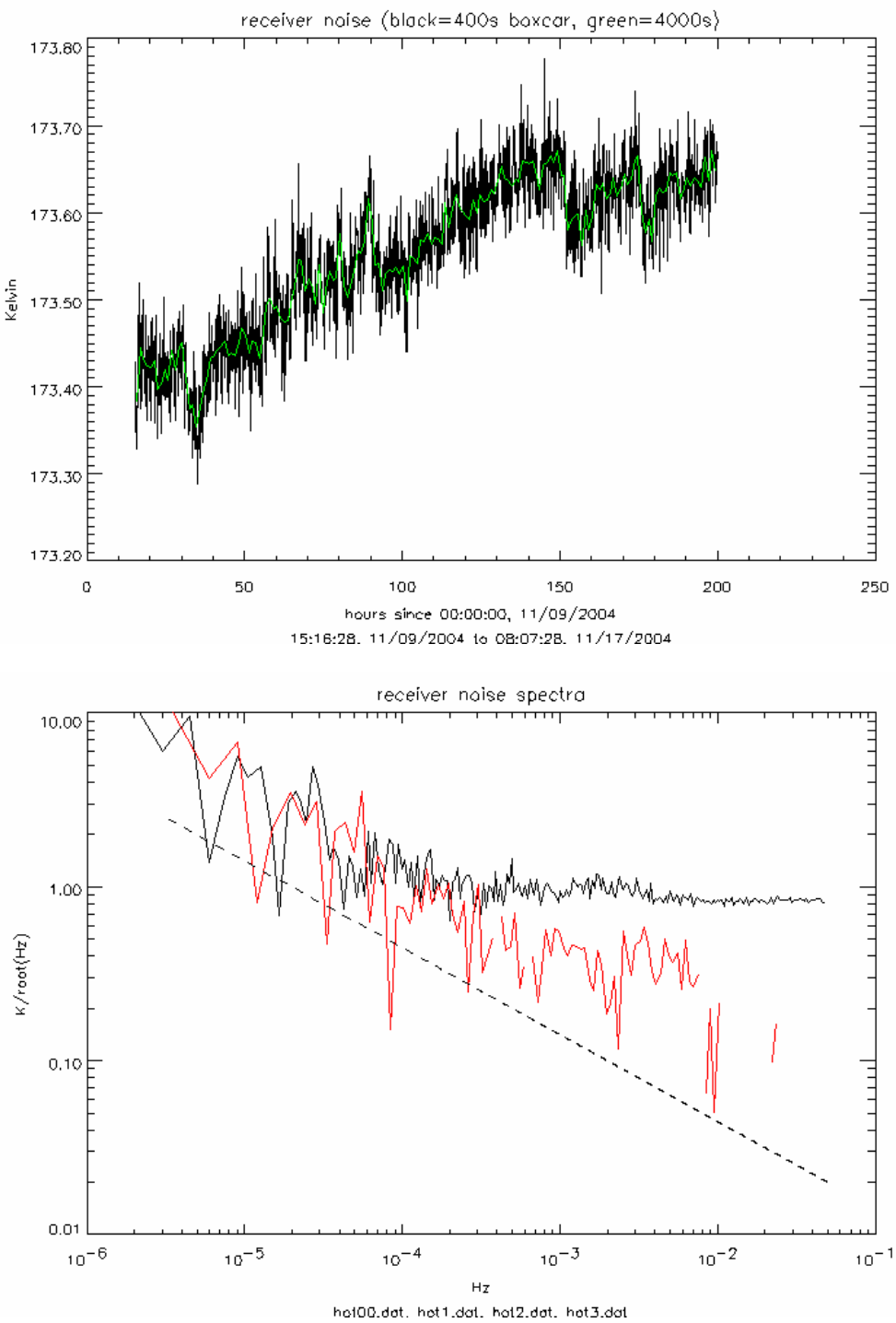

Figure 3: Test #1; receiver noise temperature from (2) and spectra; red line is co-spectra as discussed in text; dashed line represents 1/f noise of AWVR (=sqrt(2x10^{-5}/f)).

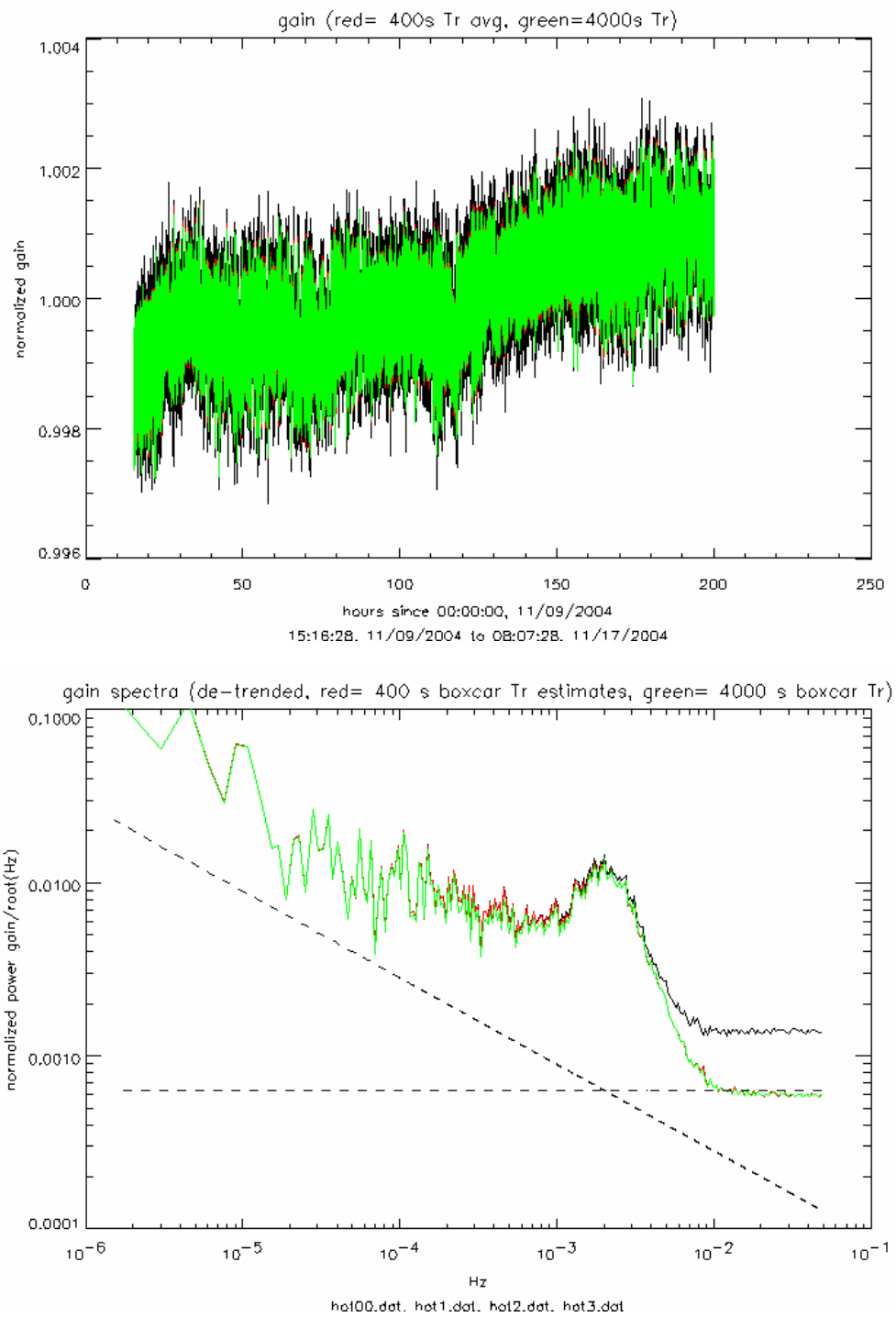

Figure 4: Test #1; gain and gain spectra for various running averages of receiver noise temperature in (3); dashed lines represent theoretical noise limit of (3) and 1/f noise of AWVR (=sqrt($8x10^{-10}$/f))

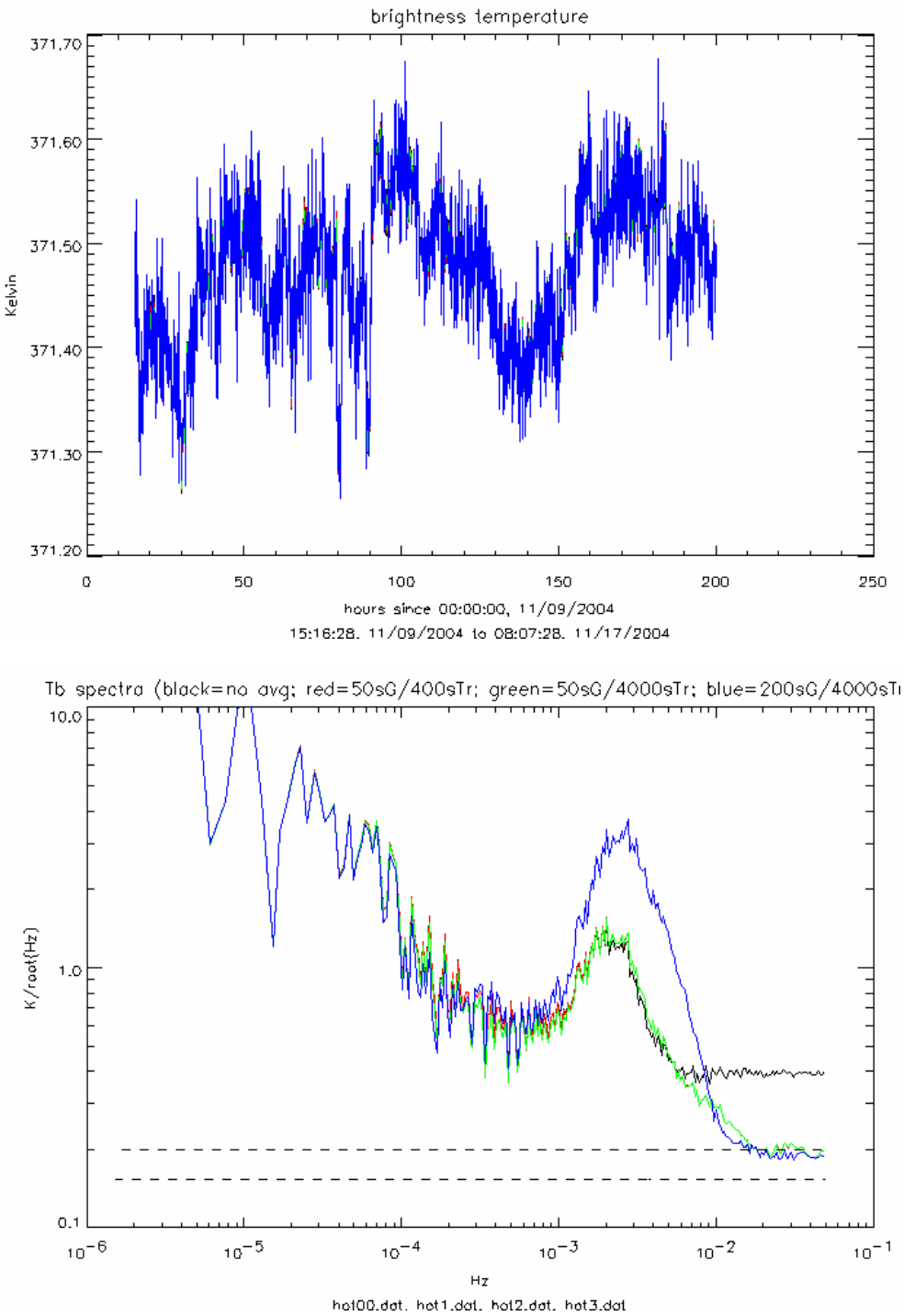

Figure 5: Test #1; Antenna noise temperature and spectra for various running averages of receiver noise temperature in (2) and gain in (3); upper dashed line represents the theoretical white noise limit of (4) given a duty cycle of 0.6, and the lower dashed line is the theoretical limit for a total power radiometer. A boxcar integration of 400 seconds applies to the time series plot.

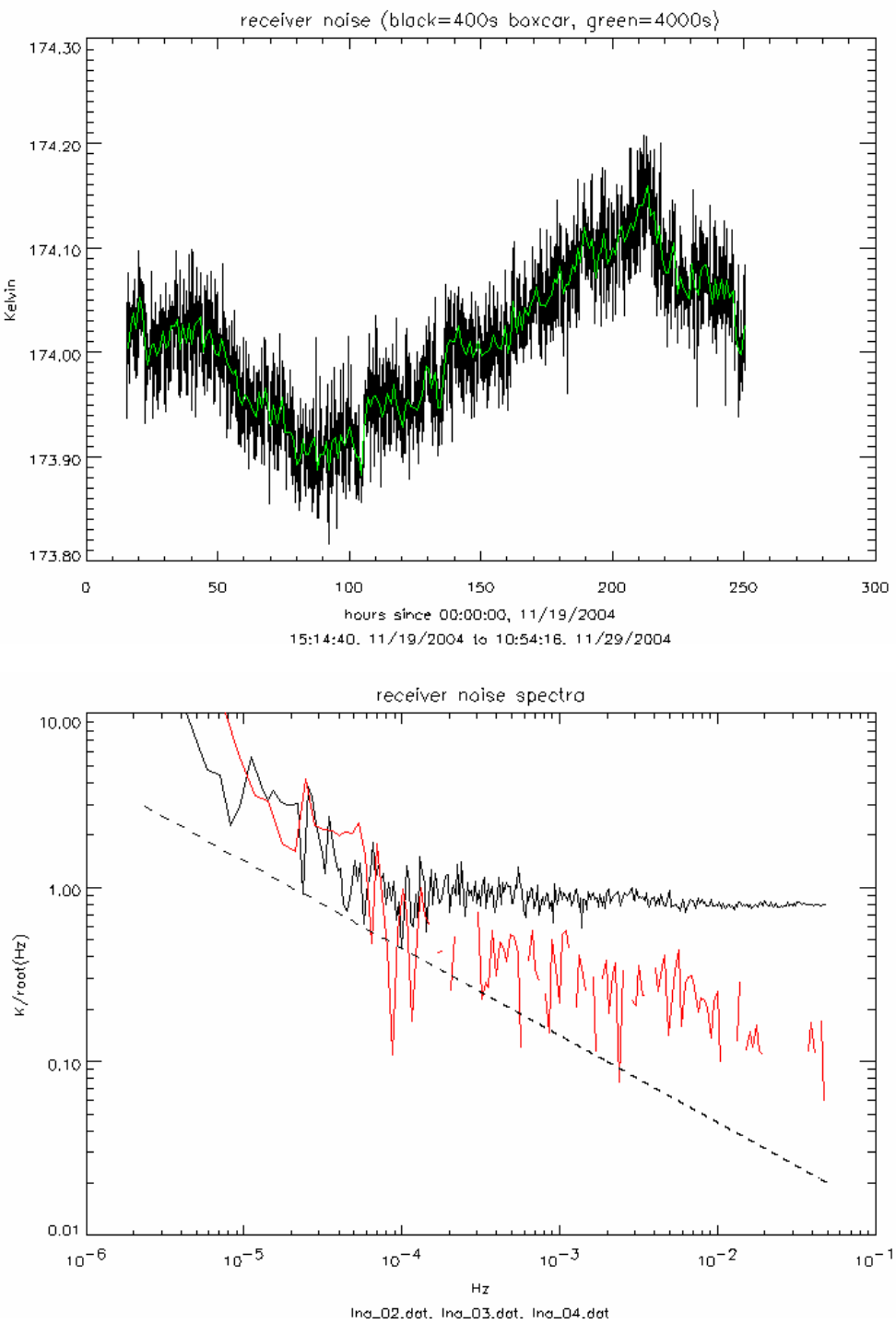

Figure 6: Test #2; receiver noise temperature from (2) and spectra; red line is co-spectra as discussed in text; dashed line represents 1/f noise of AWVR (=sqrt(2x10^{-5}/f)).

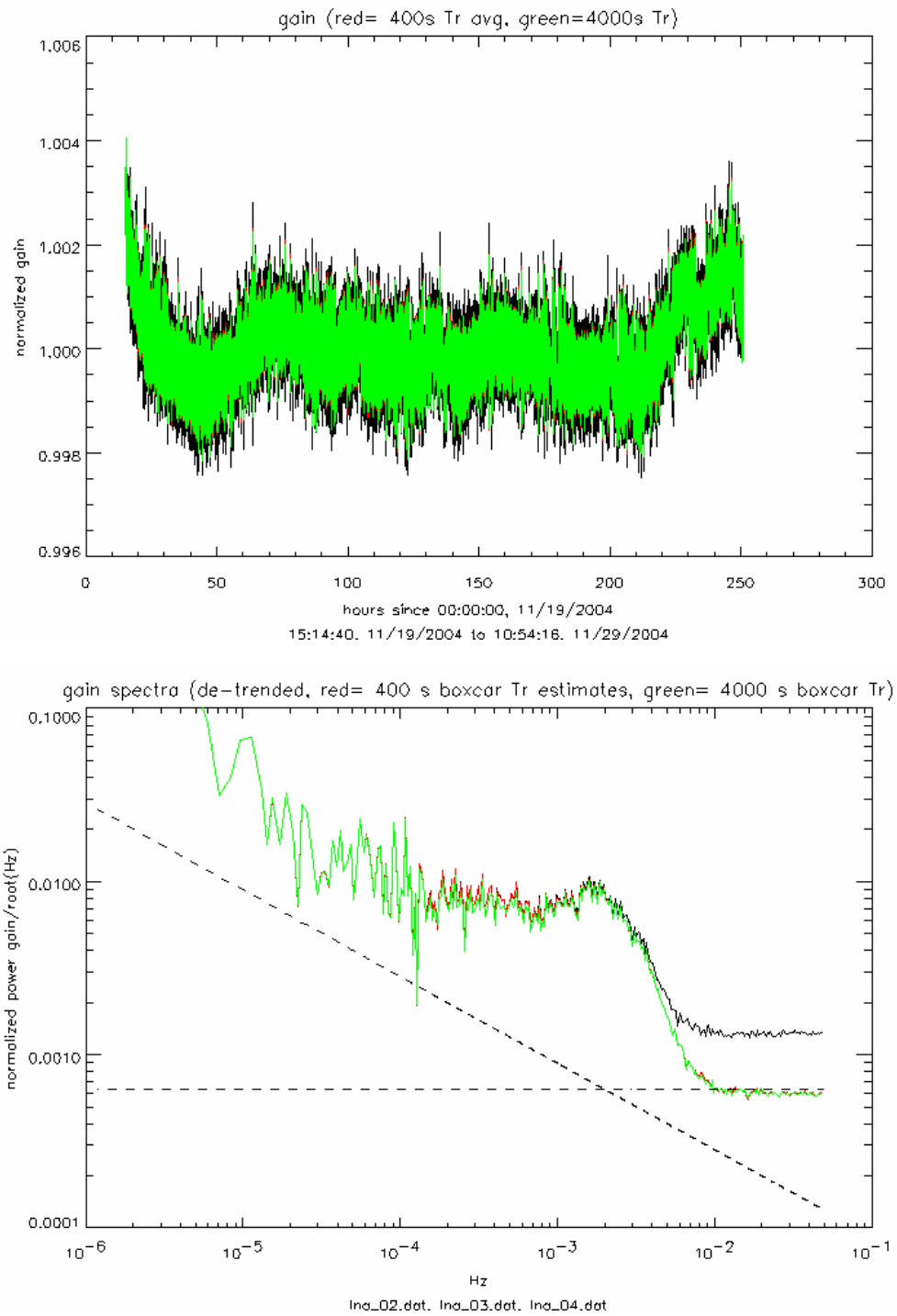

Figure 7: Test #2; gain and gain spectra for various running averages of receiver noise temperature in (3); dashed lines represent theoretical noise limit of (3) and 1/f noise of AWVR (=sqrt($8x10^{-10}$/f))

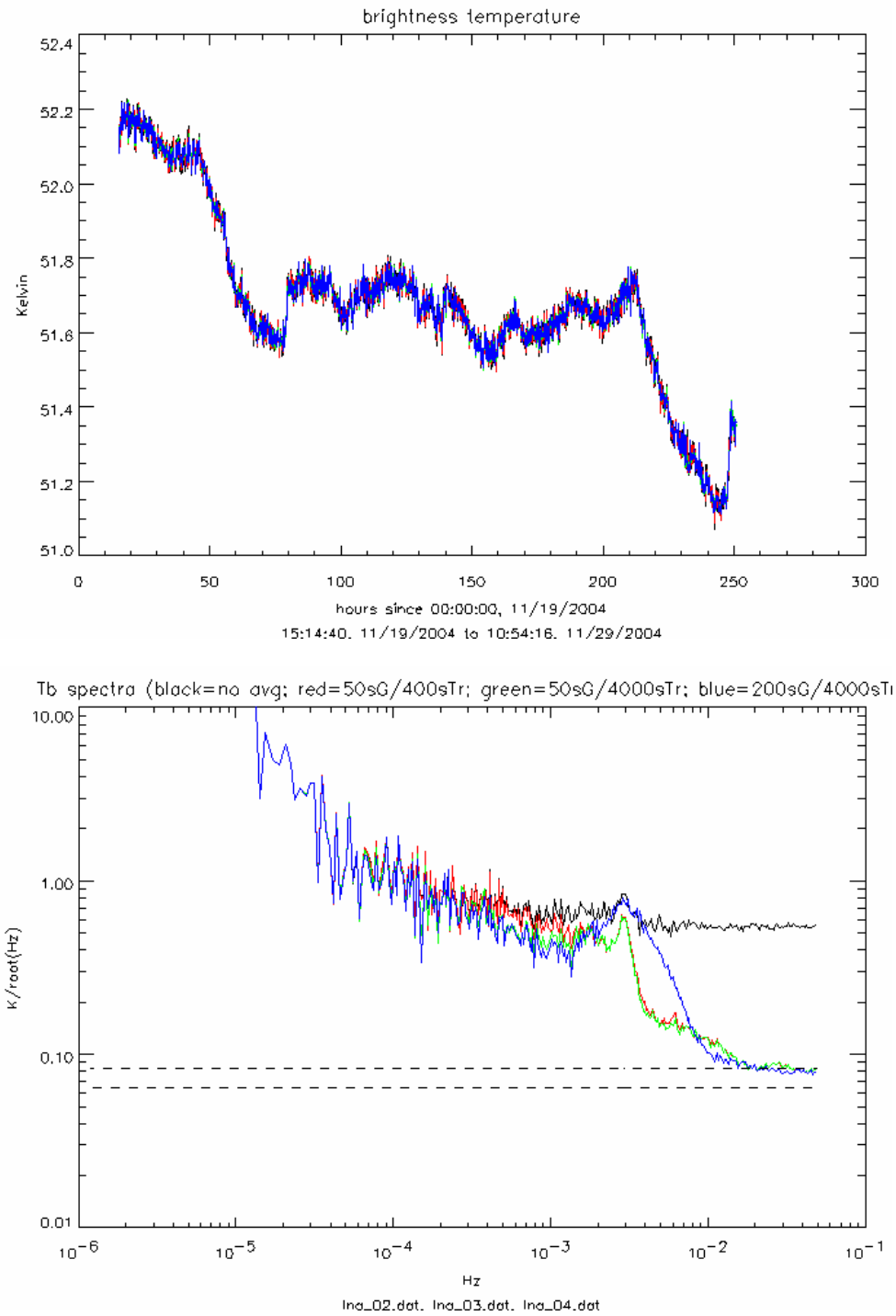

Figure 8: Test #2; Antenna noise temperature and spectra for various running averages of receiver noise temperature in (2) and gain in (3); upper dashed line represents the theoretical white noise limit of (4) given a duty cycle of 0.6, and the lower dashed line is the theoretical limit for a total power radiometer. A boxcar integration of 400 seconds applies to the time series plot.

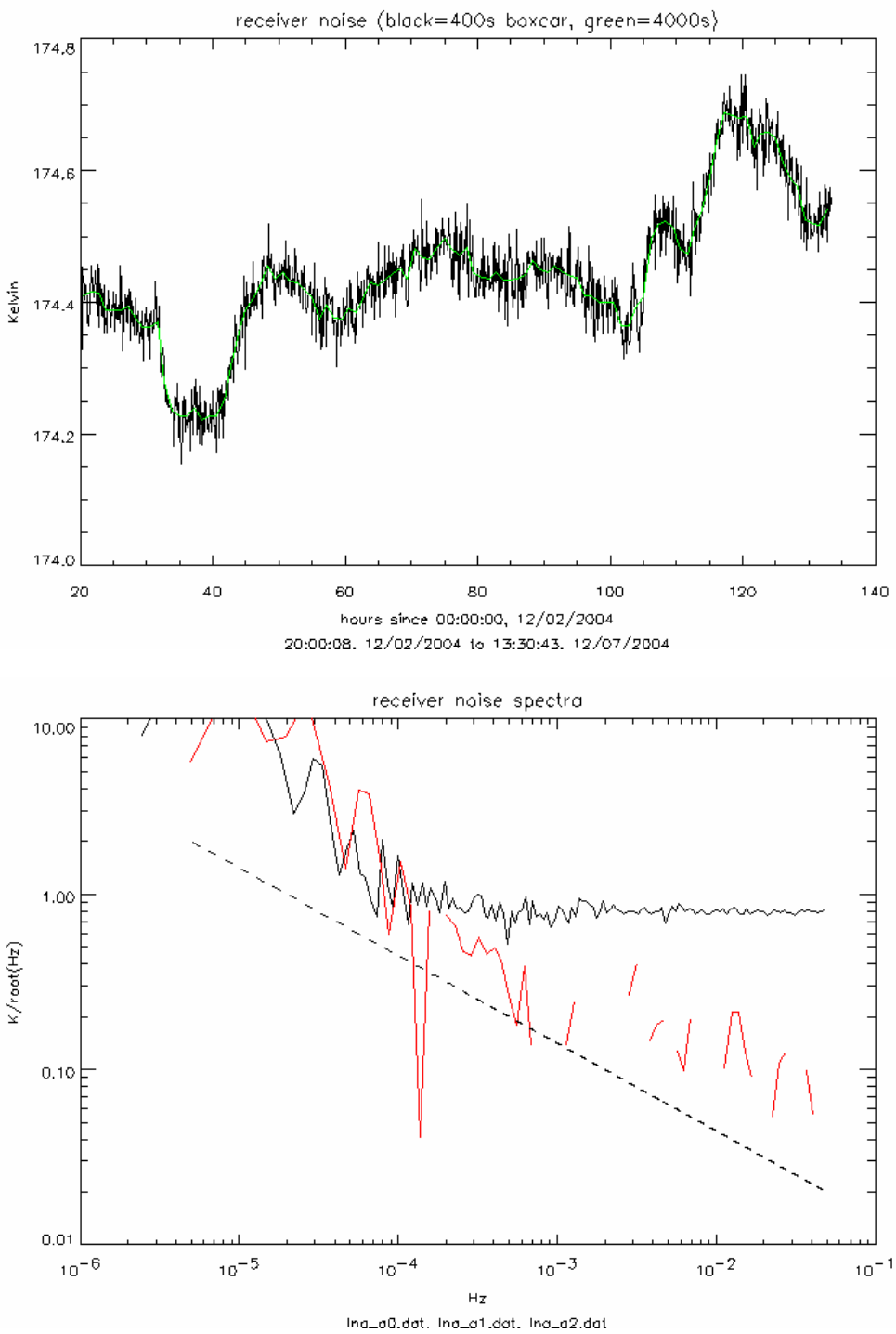

Figure 9: Test #3; receiver noise temperature from (2) and spectra; red line is co-spectra as discussed in text; dashed line represents 1/f noise of AWVR (=sqrt(2x10^{-5}/f)).

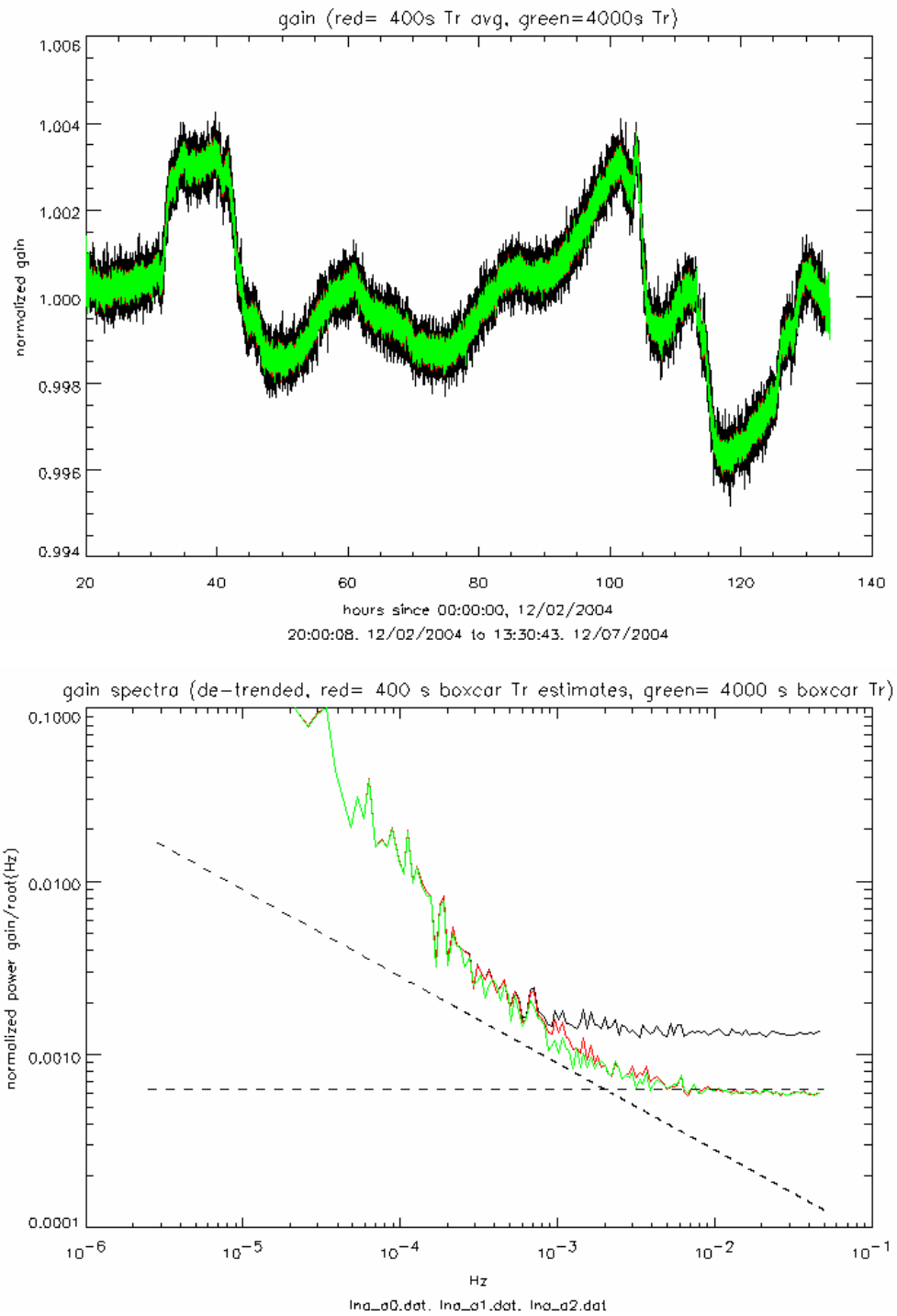

Figure 10: Test #3; gain and gain spectra for various running averages of receiver noise temperature in (3); dashed lines represent theoretical noise limit of (3) and 1/f noise of AWVR (=sqrt($8x10^{-10}$/f))

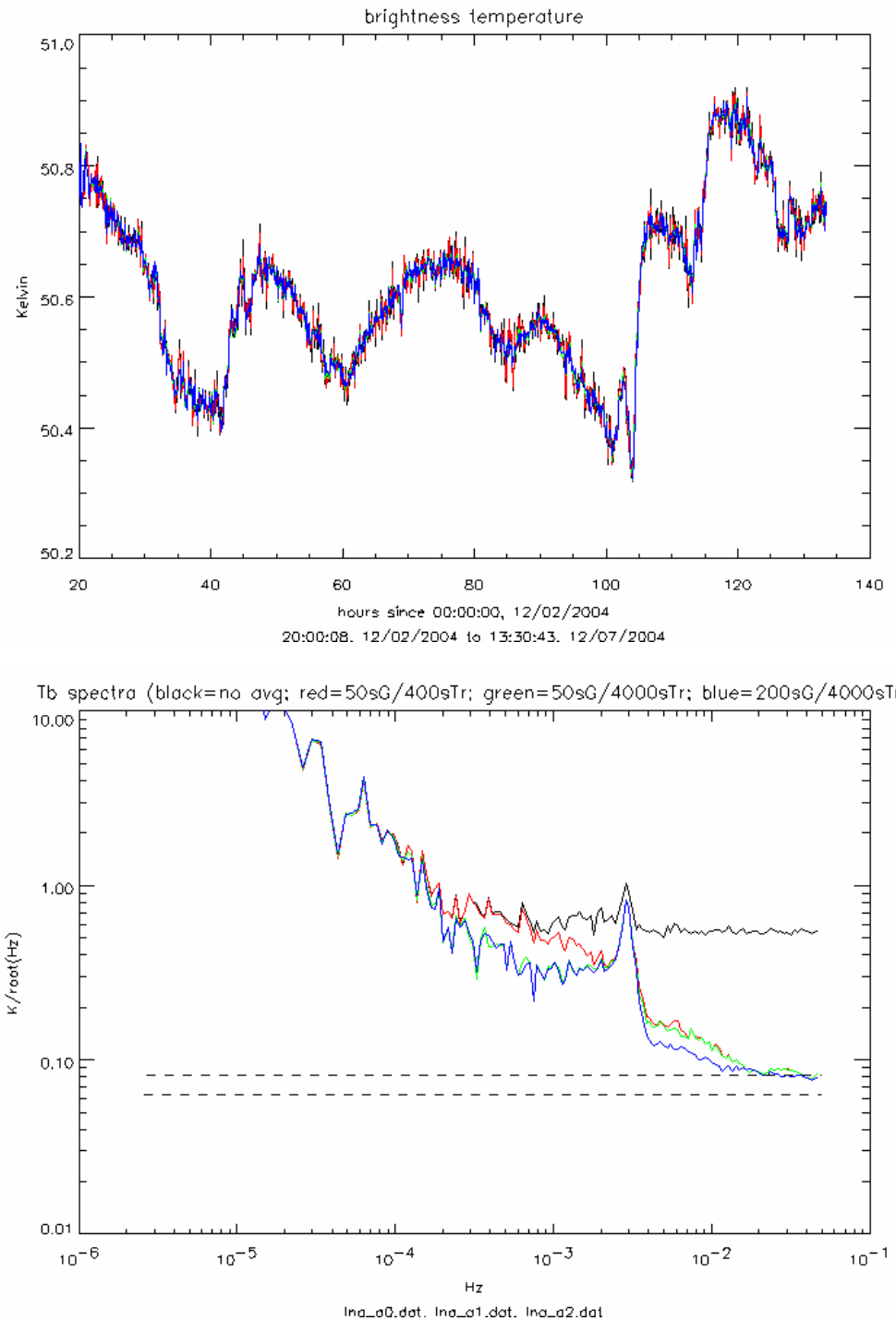

Figure 11: Test #3; Antenna noise temperature and spectra for various running averages of receiver noise temperature in (2) and gain in (3); upper dashed line represents the theoretical white noise limit of (4) given a duty cycle of 0.6, and the lower dashed line is the theoretical limit for a total power radiometer. A boxcar integration of 400 seconds applies to the time series plot.

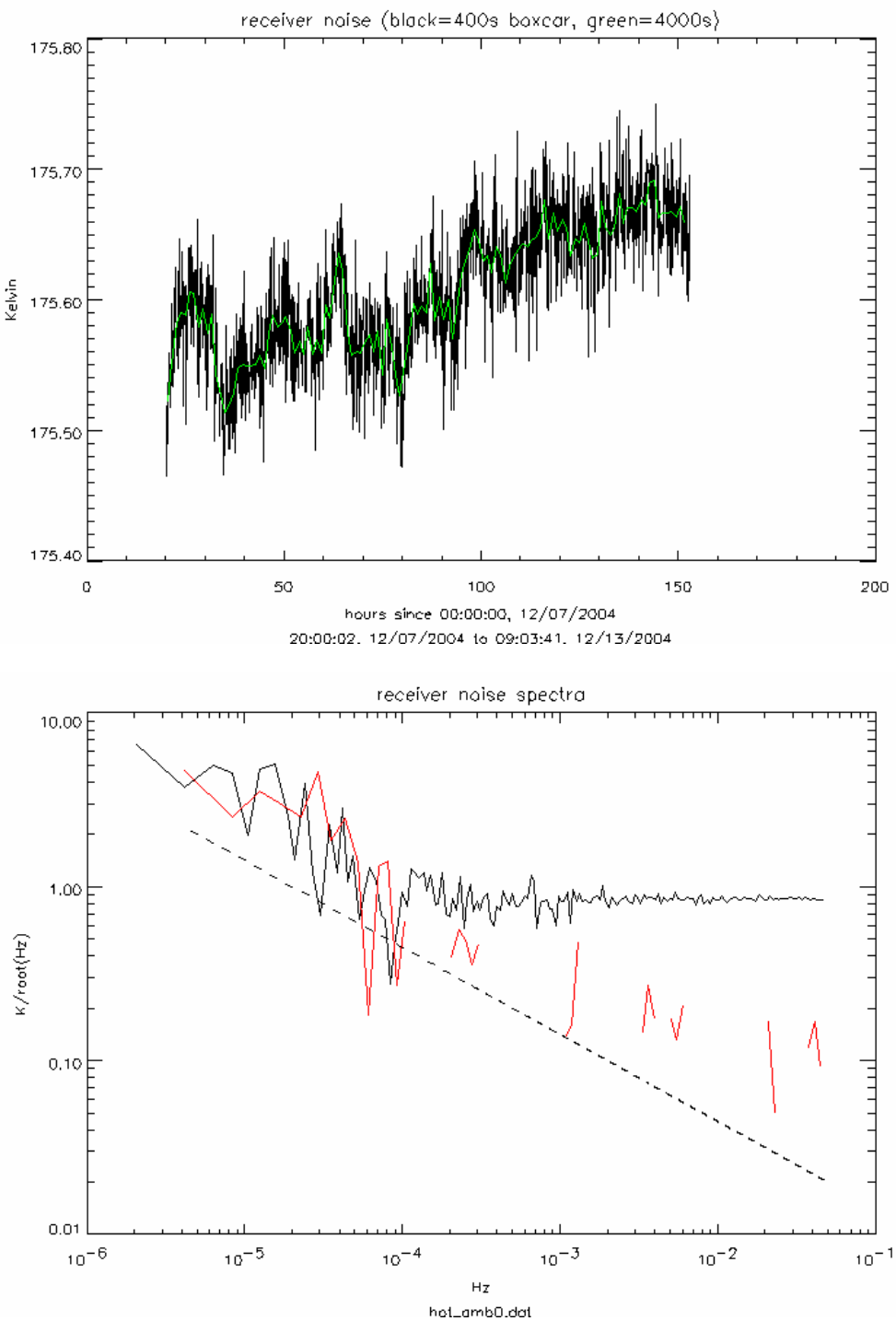

Figure 12: Test #4; receiver noise temperature from (2) and spectra; red line is co-spectra as discussed in text; dashed line represents 1/f noise of AWVR (=sqrt(2x10^{-5}/f)).

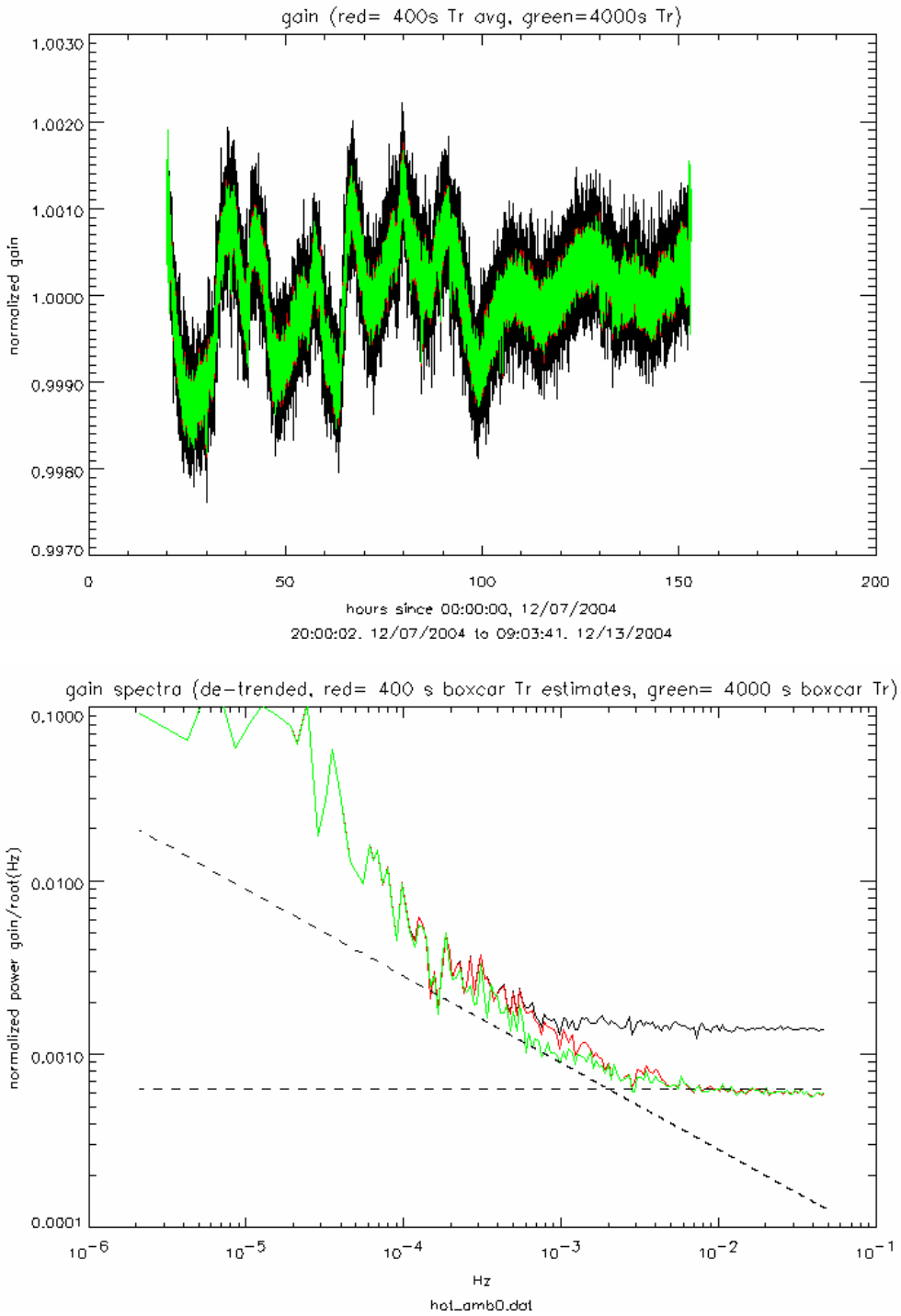

Figure 13: Test #4; gain and gain spectra for various running averages of receiver noise temperature in (3); dashed lines represent theoretical noise limit of (3) and 1/f noise of AWVR (=sqrt($8x10^{-10}$/f))

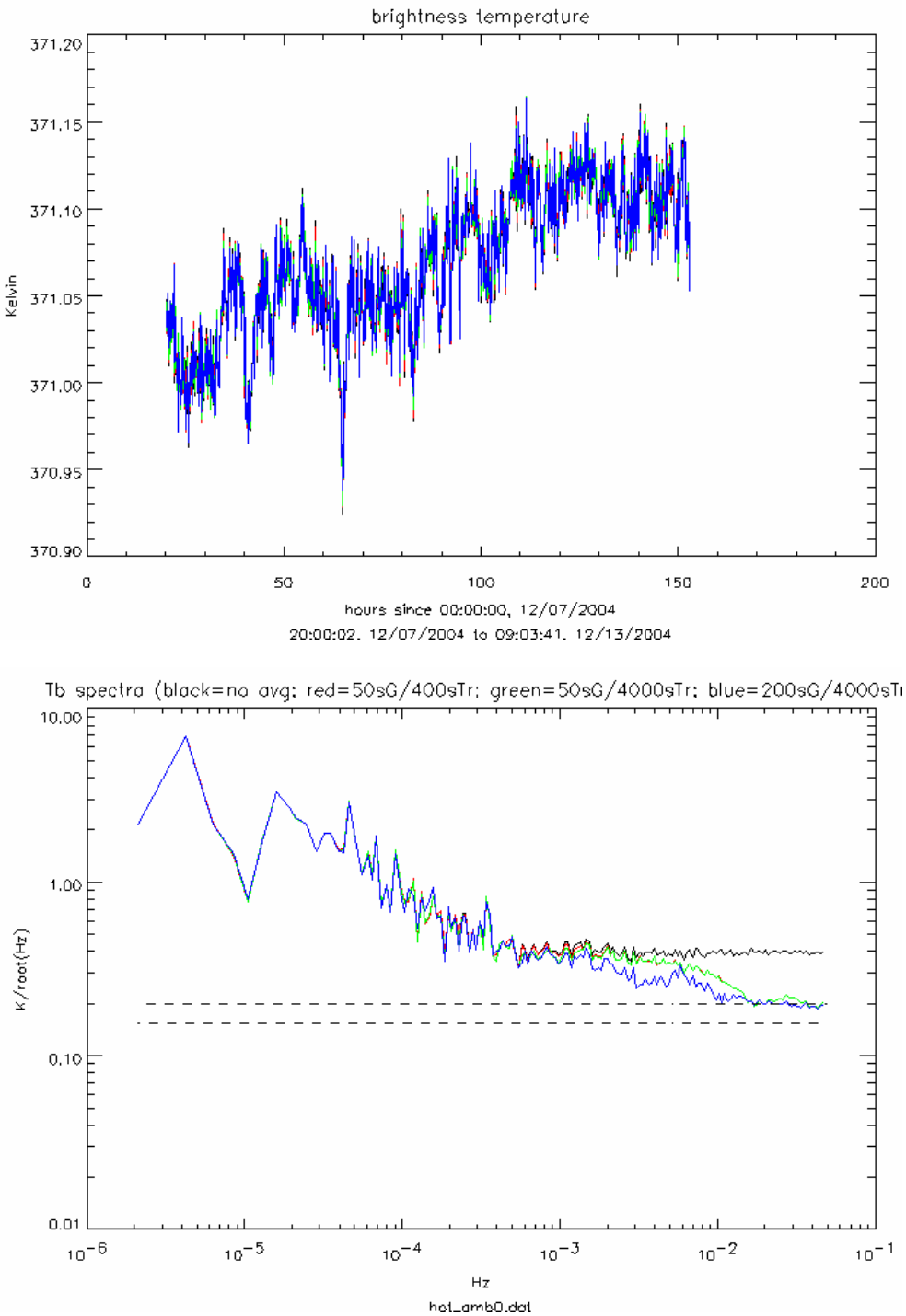

Figure 14: Test #4; Antenna noise temperature and spectra for various running averages of receiver noise temperature in (2) and gain in (3); upper dashed line represents the theoretical white noise limit of (4) given a duty cycle of 0.6, and the lower dashed line is the theoretical limit for a total power radiometer. A boxcar integration of 400 seconds applies to the time series plot.

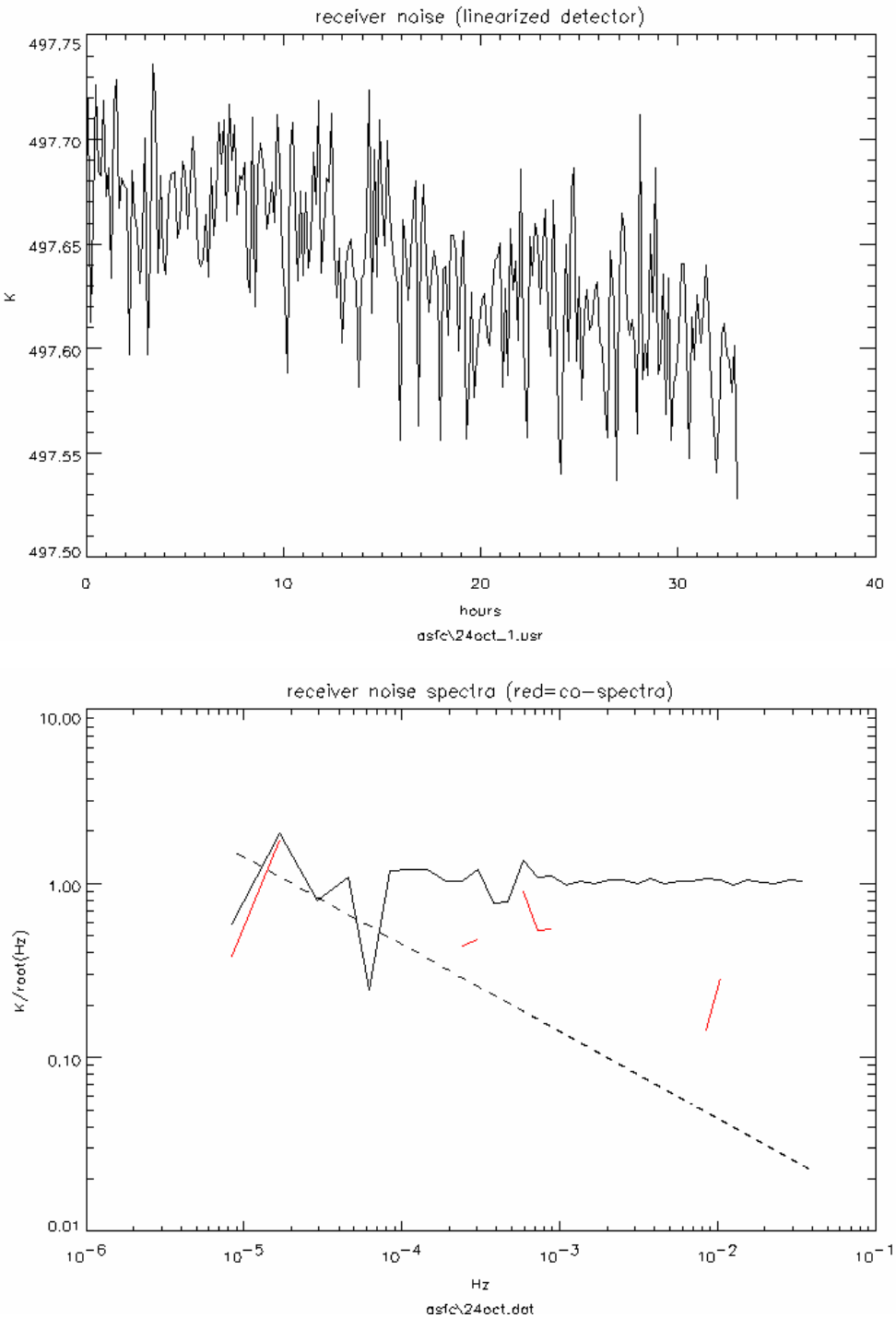

Figure 15: Test #5; receiver noise temperature from (2) and spectra; red line is co-spectra as discussed in text; dashed line represents 1/f noise of AWVR (=sqrt(2x10^{-5}/f)).

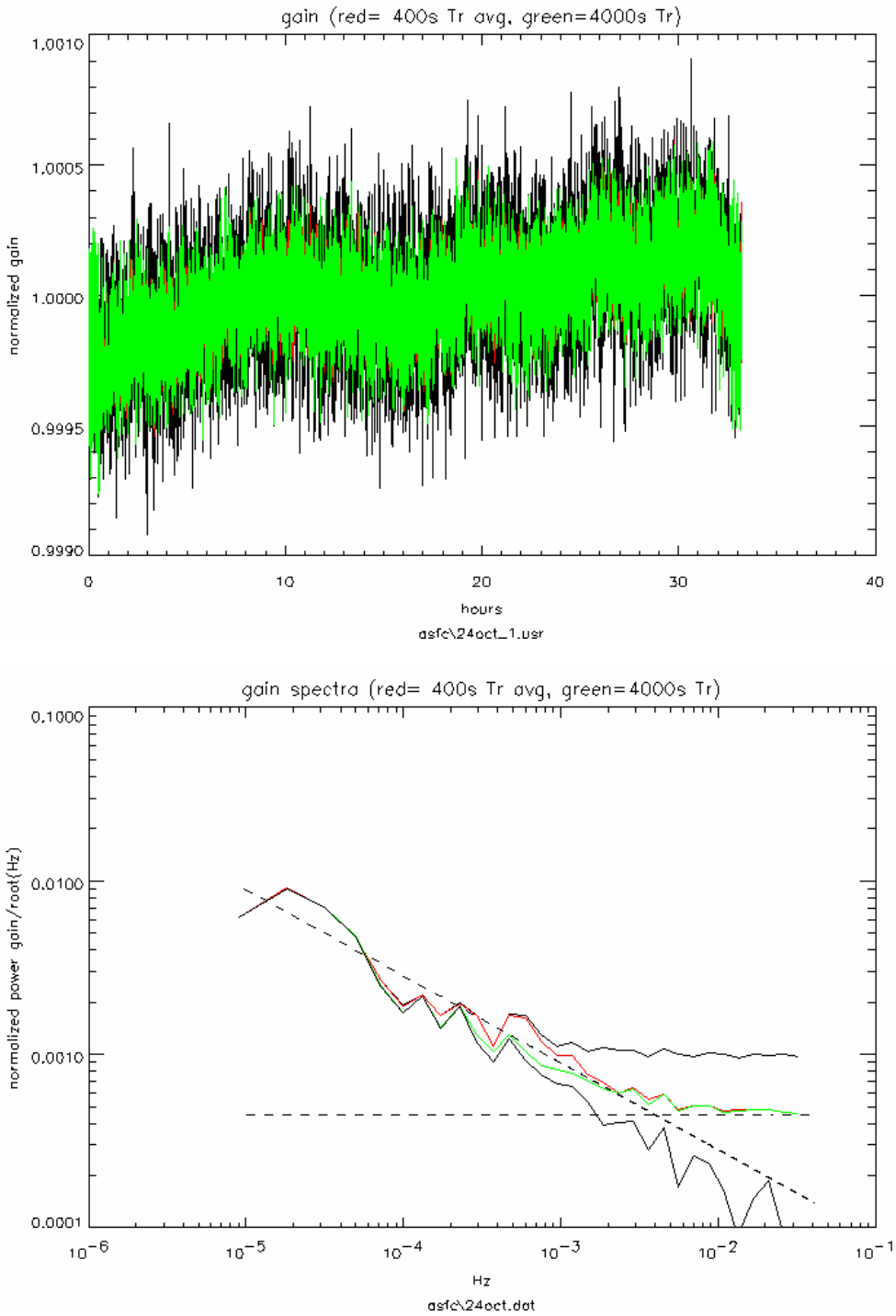

Figure 16: Test #5; gain and gain spectra for various running averages of receiver noise temperature in (3); dashed lines represent theoretical noise limit of (3) and 1/f noise of AWVR (=sqrt($8x10^{-10}$/f)). The lower of the two black traces is the co-spectra.

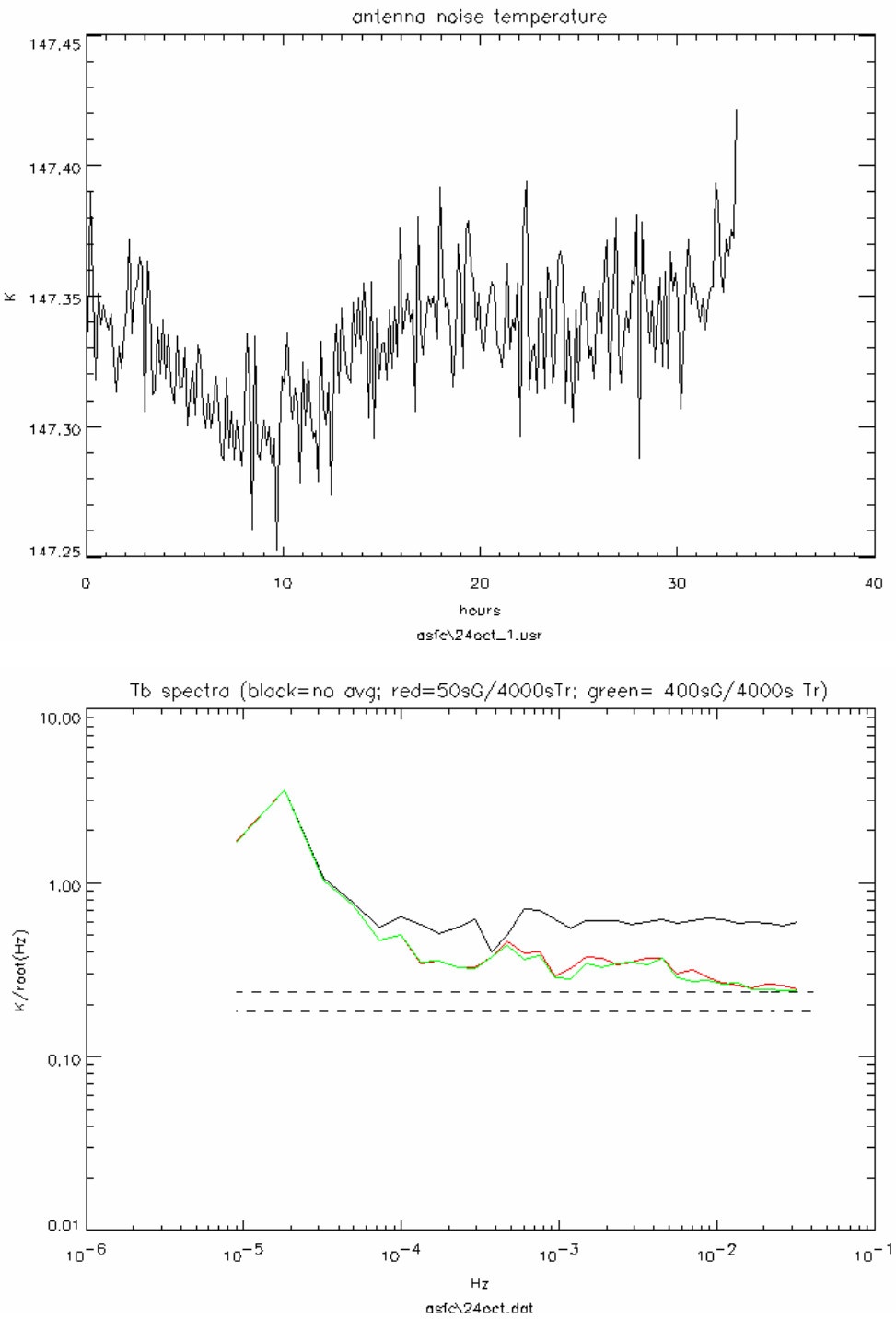

Figure 17: Test #5; Antenna noise temperature and spectra for various running averages of gain in (3); upper dashed line represents the theoretical white noise limit of (4) given a duty cycle of 0.6, and the lower dashed line is the theoretical limit for a total power radiometer. A boxcar integration of 480 seconds applies to the time series plot.

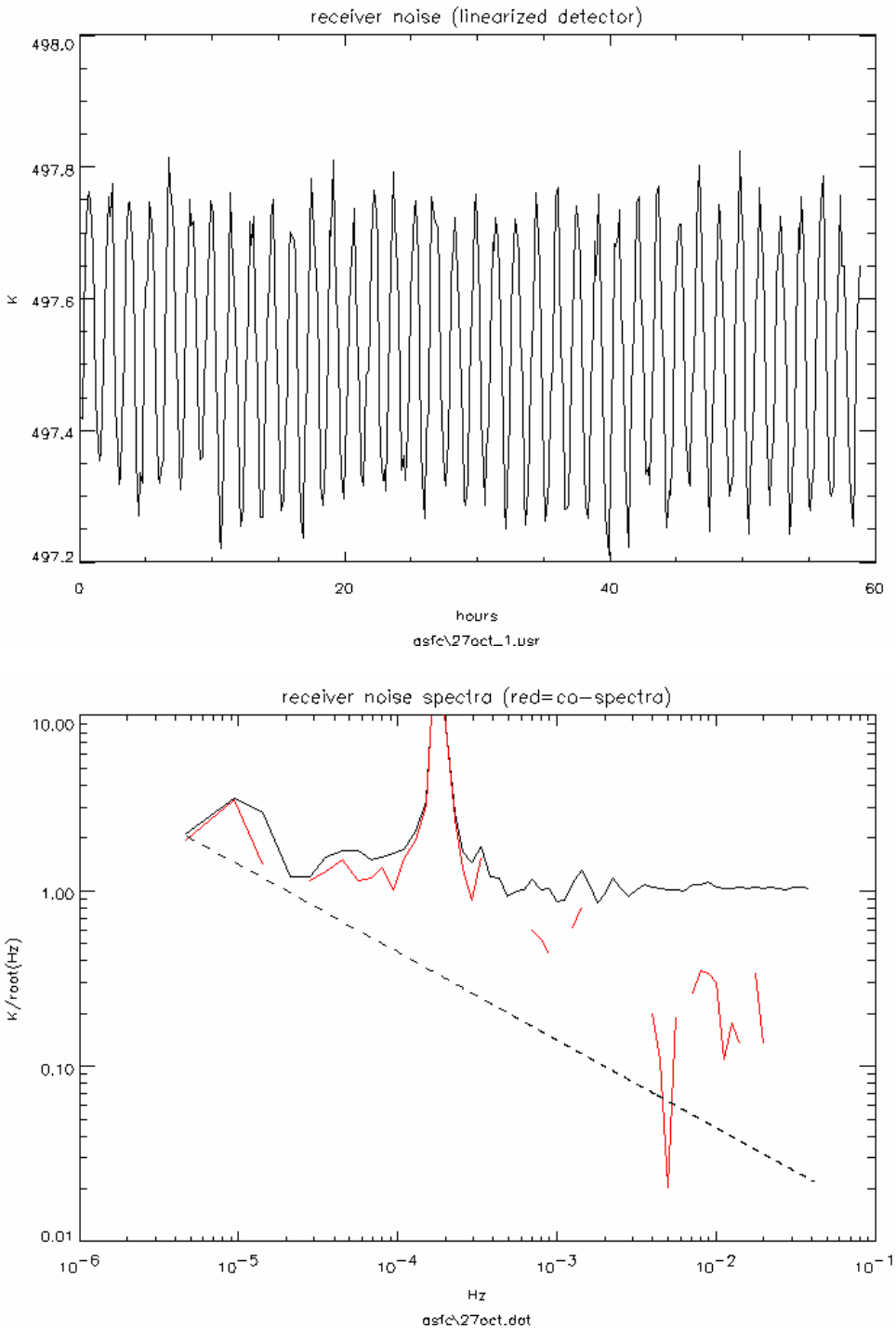

Figure 18: Test #6; receiver noise temperature from (2) and spectra; red line is co-spectra as discussed in text; dashed line represents 1/f noise of AWVR (=sqrt(2x10^{-5}/f)).

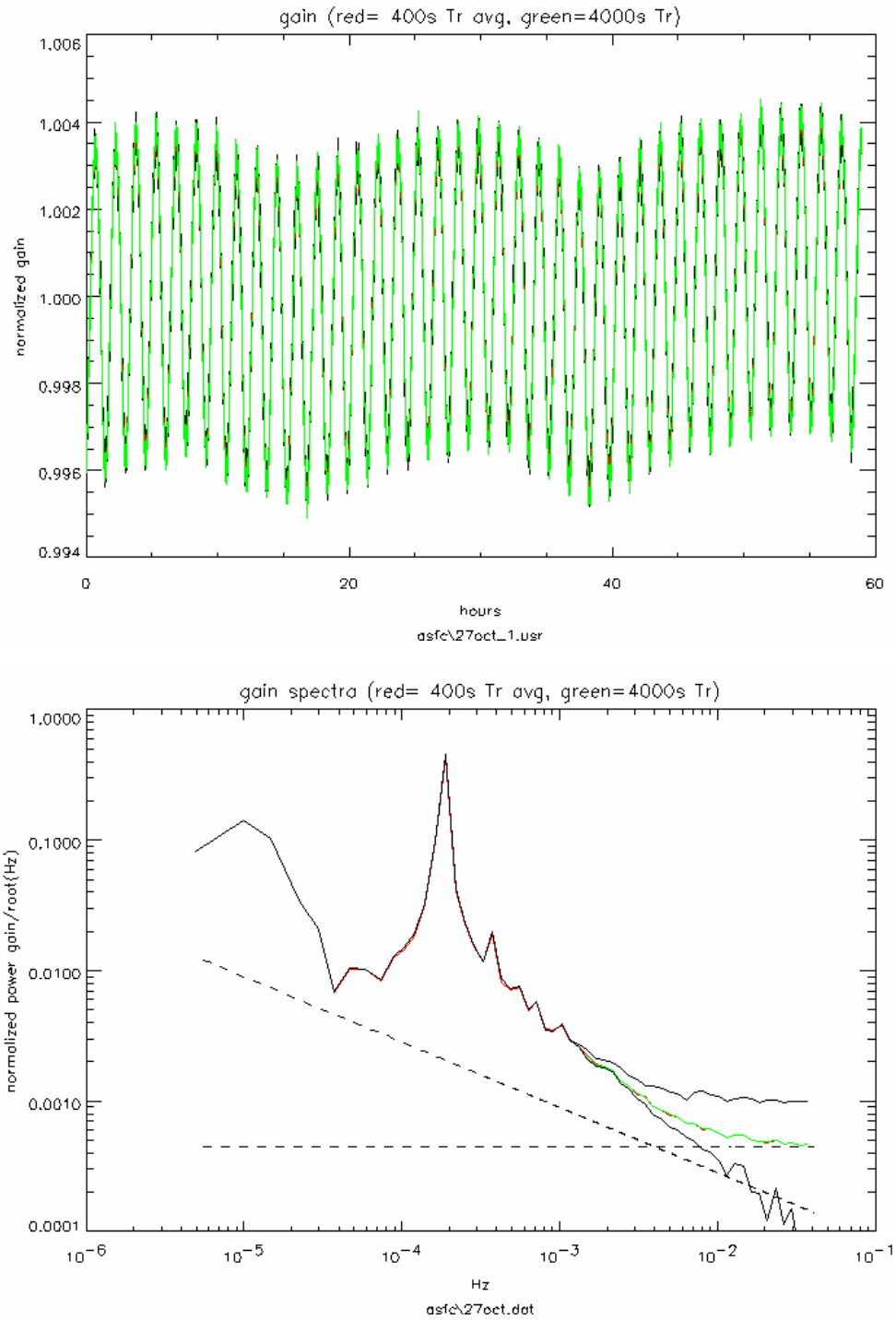

Figure 19: Test #6; gain and gain spectra for various running averages of receiver noise temperature in (3); dashed lines represent theoretical noise limit of (3) and 1/f noise of AWVR (=sqrt($8x10^{-10}$/f)). The lower of the two black traces is the co-spectra.

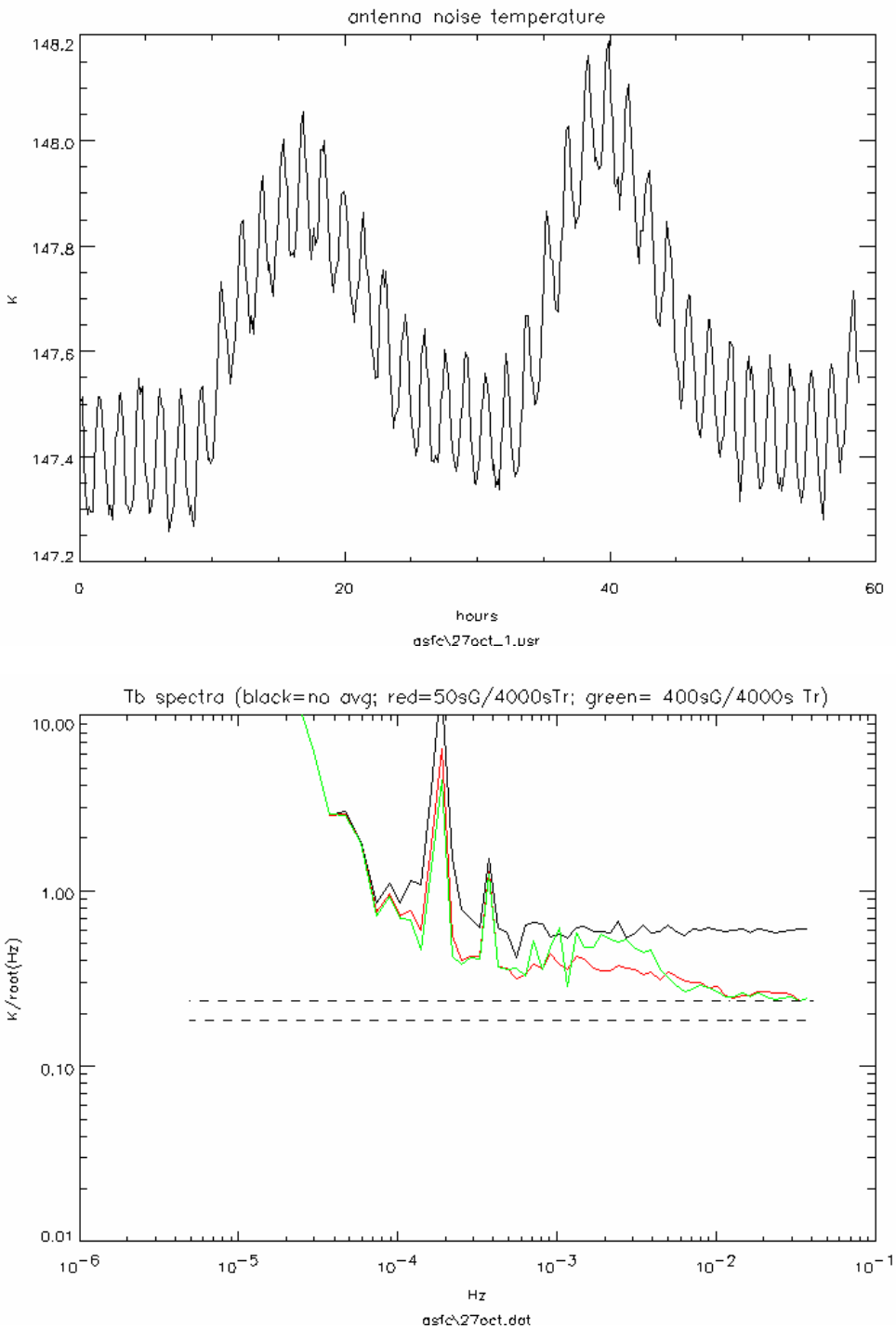

Figure 20: Test #6; Antenna noise temperature and spectra for various running averages of gain in (3); upper dashed line represents the theoretical white noise limit of (4) given a duty cycle of 0.6, and the lower dashed line is the theoretical limit for a total power radiometer. A boxcar integration of 480 seconds applies to the time series plot.

4. Discussion of test results

Tests #1 and #2 exhibited the worst stability due to TEC controller deficiencies noted above. These are evident in the gain spectra of Figures 4 and 7, where we see a large 'hump' in the spectra near 2 mHz. This hump disappears when the controllers were switched off for tests #3 and #4 in Figures 10 and 13. The penalty for switching off the controllers, however, is a large increase in noise below about 0.1 mHz. This makes sense since the testbed was subject to the slow varying room temperature.

In Figures 3, 6, 9 and 12 we see that the spectra of receiver noise in all cases is not bad: the 1/f spectra indicate a stability that is only about 2 times worse than the AWVR standard, and it doesn't seem to be badly affected by the temperature control since there doesn't appear to be a significant 'hump' at 2 mHz. This suggests that we should be able to apply long running averages to the receiver noise. And indeed, the gain spectra of Figures 4, 7, 10, and 13 all show a great improvement as running averages of 400 seconds (red) and 4000 seconds (green) are applied. In all cases the 4000 second average has reduced the gain noise above 0.1 mHz, and nowhere does the running average of receiver noise degrade the stability.

The Brightness temperature spectra of Figures 5, 8, 11, and 14 show how various running averages of gain and receiver noise affect the brightness temperature stability. In Figures 5 and 8 we see that a 50 second running average of gain reduces the noise to the theoretical limit above 20 mHz. We also see a slight advantage to a 4000 second receiver noise average (green) over the 400 second receiver noise average (red) between about 0.1mHz and 1 mHz. The blue trace, on the other hand, corresponds to a 200 second running average of gain and in Figures 5 and 8 we see that this is too long since the noise spectra has increased sharply between 1 and 10 mHz. If the gain is more stable- as it was in Figures 11 and 14 when the TEC was switched off- then a 200 second running average of gain might make sense- although the improvement is marginal.

In Figures 8 and 11 we see that the active cold load shows a sharp peak near 3 mHz which doesn't appear in the hot load data of Figure 14. This can be traced to the TEC temperature controller of the cold load: that controller was of an identical design to the one supporting the testbed radiometer, and it exhibited a similar 0.1 C oscillation near 3 mHz.

In the GSFC testbed, test #6 shows that the receiver noise exhibited an undetectable 1/f spectra in Figure 15, and a gain stability in Figure 16 which is even better than the AWVR standard. Again, in Figure 16 we see how the running average of receiver noise improves the stability, and we again see a slight advantage to the longer 4000 second time constant in the 0.1 to 1 mHz range. In Figure 17 we see how these averages have lowered the brightness temperature noise. It is also interesting that there appears to be very little difference between a 50 second and a 400 second running average of the gain between 1 mHz and 10 mHz, as evident in the narrow margin between the red and green traces of Figure 17. This can be explained in part by the fact that the GSFC testbed gain is measured with a duty cycle of 0.4 in (3), which is higher than the JPL testbed with a duty cycle of 0.2. This will tend to narrow the margin between the red and green traces. Also, the brightness temperature spectra below 10 mHz is evidently dominated by other instabilities in the system, and this will further diminish the advantage of a longer average.

In Figures 18, 19, and 20 we see the very significant impact of the sinusoidal temperature oscillations described in the previous section. Clearly, the time series data indicate a need to better thermally isolate the front end components. More elaborate temperature correction schemes would also help. Yet in spite of these large oscillations, we see that the receiver noise and gain spectra are reasonable outside of the one excitation frequency, and that the running averages of receiver noise and gain still reduce the noise of the brightness temperature spectra in Figure 20. We also see in Figure 20 that it would again be best to limit the gain average to 50 seconds due to gain fluctuations between 1 and 4 mHz.

5. Conclusions

The great advantage to the power spectral density plots as an analysis tool is that we can see how the various running averages of receiver noise and gain improve or degrade the brightness temperature stability- in spite of the fact that we don't have a stable target. In essence, all we need to show is that these running averages *reduce* the

spectral density curves by the anticipated amount without increasing the noise in any part of the spectrum. I think that this is a much better approach than looking at the overall RMS brightness temperature fluctuations.

Overall, the above results show that there is a consistent improvement in radiometer stability when receiver noise is averaged for 400 to 4000 seconds, and the gain is averaged for about 50 seconds. When temperatures are stable, the time constants of about 4000 and 200 seconds for receiver noise and gain, respectively, seem to work even better. This essentially confirms the predictions presented in the May 10, 2002 memo, "delta-T and duty cycle optimizations".

There are two areas where I think the testbed data analysis can be further refined: (1) temperature corrections can be applied. There are clear correlations- which have not been presented- between the various parameters presented above and the temperatures which were measured. (2) Even without those corrections, we could quantify the NEDT of our systems as follow: I think that an NEDT *spectrum* could be calculated by integrating the above noise spectral *density* between a variable lower bound frequency and an upper bound frequency fixed by the mission sample interval of 12 seconds. This would provide a direct measure of NEDT- in Kelvin- on a curve that has time-scale-of-interest on its x-axis. I think that Bill has already figured out the temperature corrections- so that work may already be done. I hope to follow up on the latter idea as I think this NEDT spectrum is just what we need.